



TECHNISCHE  
UNIVERSITÄT  
WIEN  
Vienna University of Technology

DISSERTATION

**Korrelative *in situ* Mikroskopie der Wasserstoff-Oxidation auf  
Rhodium-basierten Modellkatalysatoren**

ausgeführt zum Zwecke der Erlangung des akademischen Grades eines Doktors der  
technischen Wissenschaften unter der Leitung von

**Univ.Prof. Mag.rer.nat. Dr.rer.nat. Günther Rupprechter  
und Dipl.-Phys. Dr.rer.nat. Yuri Suchorski**

E165

Institut für Materialchemie

eingereicht an der Technischen Universität Wien  
Fakultät für Technische Chemie

von

**Dipl.-Ing. Philipp Winkler, BSc**

Matrikelnummer 1226363

Wien, am 08.12.2022





TECHNISCHE  
UNIVERSITÄT  
WIEN  
Vienna University of Technology

DOCTORAL THESIS

***In Situ* Correlative Microscopy of Hydrogen Oxidation on  
Rhodium-Based Model Catalysts**

carried out for fulfilment of the requirements for the degree of Doctor of  
Technical Sciences under the supervision of

**Univ.Prof. Mag.rer.nat. Dr.rer.nat. Günther Rupprechter  
and Dipl.-Phys. Dr.rer.nat. Yuri Suchorski**

E165

Institute of Materials Chemistry

submitted to TU Wien

Faculty of Technical Chemistry

by

**Dipl.-Ing. Philipp Winkler, BSc**

Matriculation Number 1226363

Vienna, Austria, 8<sup>th</sup> of December, 2022



GUTACHTER/THESIS ASSESSORS:

**Maya Kiskinova, Sc.D. Ph.D. BS**

Elettra Sincrotrone Trieste S.C.p.A.

**Privatdoz. Dipl.-Ing. Dr.techn. Michael Stöger-Pollach**

TU Wien, University Service Centre for Transmission Electron Microscopy

PRÜFUNGSSENAT/EXAMINATION BOARD:

**Ao.Univ.Prof. Dipl.-Ing. Dr.techn. Peter Gärtner**

TU Wien, Institute of Applied Synthetic Chemistry

**Univ.Prof. Mag.rer.nat. Dr.rer.nat Günther Rupprechter**

TU Wien, Institute of Materials Chemistry

**Privatdoz. Dipl.-Ing. Dr.techn. Michael Stöger-Pollach**

TU Wien, University Service Centre for Transmission Electron Microscopy

EIDESSTATTLICHE ERKLÄRUNG: Ich erkläre hiermit an Eides statt, dass ich die vorliegende Arbeit selbstständig verfasst, andere als die angegebenen Quellen/Hilfsmittel nicht benutzt, und die den benutzten Quellen wörtlich und inhaltlich entnommenen Stellen als solche kenntlich gemacht habe.

STATUTORY DECLARATION: I hereby declare that I have authored this thesis independently, that I have not used other than the declared sources/resources, and that I have explicitly marked all material which has been quoted either literally or by content from the used sources.



---

# Kurzfassung

Die katalytische Wasserstoff-Oxidation ist in vielen Technologiebereichen eine wichtige Reaktion und könnte eine der wichtigsten Reaktionen für die Entwicklung von neuen Energieerzeugungs- und -speichertechnologien sein. Mit ihrer Hilfe kann Energie aus erneuerbaren Quellen in den chemischen Bindungen von  $H_2$  gespeichert und bei Bedarf durch katalytische Oxidation wieder freigesetzt werden. Besonders Platingruppen-Metalle, unter anderen Rhodium, haben sich als geeignete Katalysatoren für diese Reaktion erwiesen. Die katalytische  $H_2$ -Oxidation wurde bereits mit vielen Oberflächenanalysemethoden untersucht und kann daher als Test-Reaktion zur Untersuchung verschiedener Katalysatorsysteme dienen.

Aufgrund der Adsorptionseigenschaften der Reaktanten  $H_2$  und  $O_2$ , und des Ablaufs der Reaktion über einen Langmuir-Hinshelwood-Mechanismus, kann sich ein solches System in zwei unterschiedlichen Zuständen (katalytisch aktiv und inaktiv) befinden und Bistabilität aufweisen. Das bedeutet, dass sich das System bei den selben Umgebungsbedingungen in beiden Zuständen befinden kann, wobei der tatsächliche Zustand nur von der Vorgeschichte des Systems abhängt. Die Parameterbereiche für diese Zustände und die Bistabilität können ermittelt und in kinetischen Phasendiagrammen zusammengefasst werden. Die katalytische  $H_2$ -Oxidation auf Rh kann zudem selbsterhaltende kinetische Oszillationen aufweisen, wobei in diesem Fall bei konstanten Umgebungsbedingungen die katalytische Aktivität periodisch zwischen dem aktiven und dem inaktiven Zustand wechselt. Die Bildung und der Verbrauch von eingelagertem Sauerstoff fungieren dabei als Rückkopplungsmechanismus.

Die meisten vorhergehenden Arbeiten zu diesem Thema wurden entweder auf wohldefinierten einkristallinen Oberflächen oder ohne räumliche Auflösung auf Pulverkatalysatoren durchgeführt. Einkristalle sind im Vergleich zu typischen Industriekatalysatoren stark vereinfachte Systeme. Örtlich mittelnde Untersuchungen erschweren es wiederum, den Einfluss der *lokalen* atomaren Struktur auf die katalytischen Eigenschaften zu untersuchen. Um die daraus erwachsenen Probleme zu umgehen wurden erst kürzlich polykristalline Folien, welche eine Vielzahl an unterschiedlichen wohldefinierten Oberflächenstrukturen aufweisen, als Oberflächenstrukturbibliotheken benutzt und mit verschiedenen Mikroskopien untersucht. Oft ist jedoch die Benutzung einer einzelnen Technik nicht ausreichend um alle nötigen Informationen zu erhalten und mehrere Techniken werden in einem korrelativen Mikroskopie-Ansatz vereinigt. Dabei werden die selben Stellen der selben Probe unter den selben Bedingungen mit verschiedenen Mikroskopien abgebildet.

Bisher gab es jedoch einige Aspekte der katalytischen  $H_2$ -Oxidation auf Rh, die unzureichend untersucht waren: Beispielsweise gab es keine spektroskopischen Daten zum Rückkopplungsmechanismus der kinetischen Oszillationen. Deshalb wurden die kinetischen Oszillationen auf einer polykristallinen Folie *in situ* mittels Rasterphotoelektronenmikroskopie (SPEM) untersucht und orts aufgelöste chemische Information in Form von Röntgenphotoelektronenspektren (XPS) erhalten, wobei die atomare Struktur der einzelnen Körner der Folie vorhergehend mittels Elektronenrückstreubeugung (EBSD) charakterisiert wurde. Zusätzlich zu weiteren Indizien, dass Bildung und Verbrauch von eingelagertem Sauerstoff tatsächlich als Rückkopplungsmechanismus der Oszillationen dienen, konnte eine vorher nie beobachtete Koexistenz von katalytisch inaktivem, katalytisch aktivem Zustand und kinetischen Oszillationen auf benachbarten, unterschiedlich strukturierten Körnern der selben Probe beobachtet werden. Dieses Verhalten konnte mit Unterschieden in Bildung und Verbrauch von eingelagertem Sauerstoff, abhängig von der atomaren Struktur, erklärt werden.

In Übereinstimmung mit vorhergehenden Untersuchungen war das beobachtete Verhalten stets charakteristisch für die einzelnen Körner in ihrer Gesamtheit. Während UV-Photoemissionselektronenmikroskopie-Experimenten (UV-PEEM) konnte jedoch in der Folge ein ungewöhnlicher Zustand beobachtet werden: Auf einem einzigen Korn wurden sowohl oszillierende als auch nicht oszillierende Bereiche festgestellt. Deshalb wurden Mikroskopie mit langsamen Elektronen (LEEM) und Röntgen-Photoemissionselektronenmikroskopie (X-PEEM) benutzt um in diese Bereiche auf eine korrelative Weise "hineinzuzoomen". Diese Experimente zeigten die Bildung von räumlich-zeitlichen Strukturen auf deutlich kleineren Größenskalen als zuvor beobachtet und verschiedene Arten von Strukturen (beispielsweise Spiralen, Dendritstrukturen oder elliptische Inseln) konnten in Abhängigkeit der Proben temperatur festgestellt werden. Des Weiteren wurde ein ungewöhnlicher inselbasierter Ausbreitungsmechanismus für Sauerstofffronten entdeckt.

Ein weiterer in der vorliegenden Arbeit untersuchter Aspekt war die Abhängigkeit der Oxidation von Rh von der atomaren Struktur sowie ihr Einfluss auf die katalytische Aktivität. Solche Untersuchungen sind für die Katalysatorforschung von besonderem Interesse, da eine ursprünglich metallische Katalysatoroberfläche im Verlauf der Reaktion oxidieren und damit die katalytische Aktivität beeinflusst werden kann. Erneut wurde die selbe polykristalline Rhodiumfolie unter Anwendung von korrelativer Mikroskopie untersucht, wobei SPEM orts aufgelöste chemische Analyse ermöglichte und mittels UV-PEEM die ablaufende Reaktion abgebildet werden konnte. Die Bildung von Rh-Oberflächenoxiden wurde in einer Oxidations-Karte zusammengefasst und Anisotropie des Oxidationsprozesses aufgezeigt. Die *in situ* Abbildung mittels UV-PEEM ermöglichte den direkten Vergleich zwischen metallischen und oxidierten Oberflächen und zeigte den Effekt von Rh-Oberflächenoxiden in der Katalyse. Durch Verwendung der Ausbreitungsgeschwindigkeit von Reaktionsfronten als Indikator für die Oberflächenreaktivität wurde eine hohe vorübergehende Aktivität der Rh-Oberflächenoxide für die katalytische  $H_2$ -Oxidation festgestellt.

Um die "Materiallücke", daher den Unterschied zwischen Ergebnissen die für einfache Modellsysteme und für komplexe industrielle Katalysatoren erhalten werden, zu überbrücken wurde die Komplexität der Modellsysteme erhöht und eine Probe bestehend aus  $\mu\text{m}$ -großen Rh-Partikeln auf verschiedenen Trägermaterialien erzeugt. Das katalytische Verhalten eines quasi-trägerfreien



Systems (Rh/Rh), eines Systems mit Ähnlichkeit zu metallmodifizierten Katalysatoren (Rh/Au) sowie eines Systems mit Ähnlichkeit zu Metallkatalysatoren auf Oxidträgermaterial (Rh/ZrO<sub>2</sub>) wurde *in situ* mittels korrelativer Anwendung von UV-PEEM und SPEM untersucht. Kinetische Phasendiagramme wurden ermittelt und selbsterhaltende kinetische Oszillationen auf Rh-Partikeln auf Trägermaterial wurden für diese Reaktion zum ersten Mal beobachtet. Die Abhängigkeit der katalytischen Aktivität von Trägermaterial und Rh-Partikelgröße konnte gezeigt werden. Mithilfe der SPEM-Daten konnte für Rh/Au die Bildung einer Oberflächenlegierung als Ursache für dieses Verhalten identifiziert werden, während bei Rh/ZrO<sub>2</sub> die Bildung von unterstöchiometrischen Zr-Oxiden, verbesserte Sauerstoffbindung, die Oxidation von Rh und Wasserstoffübertragung auf die ZrO<sub>2</sub>-Unterlage verantwortlich waren.

Zusammenfassend wurden in der vorliegenden Arbeit einige bisher nicht untersuchte oder nicht bekannte Aspekte der katalytischen H<sub>2</sub>-Oxidation auf mehreren Rh-basierten Modellkatalysatorsystemen untersucht und damit bei einigen für die Entwicklung von besseren Industriekatalysatoren relevanten Fragen Licht ins Dunkel gebracht. Eine Reihe von neuen Phänomenen wurde für diese Reaktion zum ersten Mal beobachtet. Diese Phänomene konnten durch die korrelative Anwendung von mehreren Mikroskopen erklärt werden, was die Stärke dieses Ansatzes bei der Verbindung von lokaler Struktur, Zusammensetzung und katalytischer Aktivität demonstriert.



---

# Abstract

Catalytic hydrogen oxidation is important in many areas of technology and may even be one of the key reactions in developing new energy generation and storage devices, because energy from renewable sources can be stored in the chemical bonds of  $H_2$  and released on demand via catalytic oxidation. Especially platinum group metals, including rhodium, have been shown to be effective catalysts in  $H_2$  oxidation. Catalytic  $H_2$  oxidation on Rh has been extensively studied using a wide range of surface science techniques and can therefore serve as well-understood test reaction for probing different catalyst systems.

Due to the adsorption properties of the reactants  $H_2$  and  $O_2$ , and the reaction proceeding via a Langmuir-Hinshelwood mechanism, such a system can exist in two distinct states of catalytic activity (active and inactive) and exhibits bistability. This means that the system can be in both states at the same set of external parameters, where the actual state depends solely on the system prehistory. The parameter spaces for these states and bistability can be mapped and summarized in kinetic phase diagrams. Comparison of such diagrams for different systems then allows designing better catalysts. Catalytic  $H_2$  oxidation on Rh has also been shown to exhibit self-sustained kinetic oscillations, i.e., at constant external parameters the state of catalytic activity can change periodically between active and inactive, whereby the formation and depletion of subsurface oxygen act as feedback mechanism.

Most of the previous work has been performed on either well-defined single crystal surfaces or in a spatially-averaging way on powder catalysts. Single crystals, on one hand, are strongly simplified systems in comparison to typical industrial catalysts. Spatially-averaging experiments, on the other hand, impair determining, e.g., the influence of the *local* catalyst atomic structure on its catalytic properties. In an attempt to overcome these limitations, just recently, polycrystalline foils, exposing plenty of domains of differing well-defined atomic structure, have been used as surface structure libraries in combination with various microscopy techniques. Often, however, a single technique alone cannot provide all necessary information and several techniques are combined in a correlative microscopy approach, i.e., the same areas of the same sample are imaged at identical conditions by different microscopies.

So far, several aspects of catalytic  $H_2$  oxidation on Rh had not yet been adequately explored: For example, spectroscopic evidence on the feedback mechanism of the kinetic oscillations was lacking. Therefore, kinetic oscillations on a polycrystalline foil, with the atomic structure of the individual domains characterized beforehand by electron backscatter diffraction (EBSD), were *in situ* monitored by scanning photoelectron microscopy (SPEM), providing spatially resolved

chemical information via x-ray photoelectron (XPS) spectra. Besides providing indications for subsurface oxygen indeed acting as feedback species, a previously unobserved coexistence of catalytically inactive state, catalytically active state and kinetic oscillations on neighboring, differently structured, domains of the same sample could be observed and explained by peculiarities of subsurface oxygen formation and depletion, depending on the atomic surface structure.

In accordance with previous studies, the observed behavior was characteristic for all domains in their entirety. During UV photoemission electron microscopy (UV-PEEM) experiments, however, a peculiar situation was later observed: Within a single domain, both oscillating and non-oscillating areas were present. Therefore, low energy electron microscopy (LEEM) and x-ray photoemission electron microscopy (X-PEEM) were used to “zoom in” on these areas in a correlative way. The experiments revealed the formation of spatio-temporal patterns on length scales smaller than previously observed and different types of patterns (e.g., spirals, dendritic structures or elliptic islands) were present, dependent on the sample temperature. Furthermore, an unusual island-mediated propagation mechanism for oxygen fronts could be detected.

Another aspect explored in the present work was the dependence of Rh oxidation on the atomic surface structure and its influence on catalytic activity. Such studies are of particular interest for catalysis, because an initially metallic surface may oxidize during the ongoing reaction, possibly changing its catalytic activity. Again, the same polycrystalline Rh foil was used as sample for a correlative microscopy study, with SPEM allowing spatially resolved chemical analysis and UV-PEEM providing visualization of the ongoing chemical reaction. Surface oxide formation was summarized in an oxidation map, revealing anisotropy of the oxidation process. *In situ* UV-PEEM imaging enabled directly comparing the local reactivity of metallic and oxidized surfaces, demonstrating the effect of Rh surface oxides on catalysis. Using the velocity of propagating reaction fronts as indicator for surface reactivity, a high transient activity of Rh surface oxides in H<sub>2</sub> oxidation was detected.

In an attempt to bridge the materials gap, i.e., the gap between the results obtained from simple model systems and complex industrial catalysts, the model system’s complexity was increased and a sample comprising μm-sized Rh particles of different sizes and on different support materials was prepared. The catalytic behavior of a quasi-unsupported system (Rh/Rh), a system resembling metal-modified catalysts (Rh/Au) and a system resembling oxide supported metal catalysts (Rh/ZrO<sub>2</sub>) was studied *in situ* by correlative UV-PEEM and SPEM. Kinetic phase diagrams were obtained and self-sustaining kinetic oscillations on supported Rh particles were observed for this reaction for the first time. The catalytic performance could be shown to be dependent on the support material and Rh particle size. Using the SPEM data, for Rh/Au, the formation of a surface alloy could be identified as being responsible for these effects, whereas for Rh/ZrO<sub>2</sub> the formation of substoichiometric Zr oxides on the Rh surface, enhanced oxygen bonding, Rh oxidation and hydrogen spillover onto the ZrO<sub>2</sub> support were identified as the causes.

In summary, several previously not explored or known aspects of catalytic H<sub>2</sub> oxidation were studied on several Rh-based model catalyst systems in the present work, shedding light on questions relevant for designing better industrial catalysts. A series of novel phenomena was observed for this reaction for the first time. These phenomena were explained by using several microscopic techniques in a correlative way, demonstrating the power of this approach in linking local structure, composition and catalytic performance.

---

# Acknowledgment

I would like to express my thanks to all the people who have supported me during my studies. Particularly I would like to thank...

- ... my supervisors **Prof. Günther Rupprechter** and **Prof. Yuri Suchorski**, for their advice and support, and for taking the time to guide me since starting as a trainee at the Institute of Materials Chemistry.
- ... my colleagues **Sebastian Buhr**, **Maximilian Raab**, **Lea Rois** and **Johannes Zeininger**, for the fruitful collaboration and a really great time.
- ... our collaboration partners at Elettra-Sincrotrone Trieste S.C.p.A. **Matteo Amati**, **Luca Gregoratti**, **Rahul Parmar** and **Patrick Zeller**, for their support and the nice environment during several beamtimes.
- ... our collaboration partners at the University Centre for Transmission Electron Microscopy of TU Wien **Andreas Steiger-Thirsfeld** and **Prof. Michael Stöger-Pollach** for the characterization of the polycrystalline Rh sample and their help with getting crystallography right.
- ... our collaboration partners at the Department of Interface Science at the Fritz-Haber-Institute of the Max-Planck-Gesellschaft **Mauricio Prieto**, **Thomas Schmidt**, **Lucas de Souza Caldas**, **Liviu Tănase**, and **Aarti Tiwari** for their support during our beamtime at BESSY II.
- ... the **Fonds zur Förderung der wissenschaftlichen Forschung** for financially supporting my research.
- ... **all the other colleagues** at the Institute of Materials Chemistry, for providing such a nice working environment in often difficult times.
- ... and of course **my friends and family** for their encouragement, patience and support.



---

# Contents

<b>1</b>	<b>Introduction</b>	<b>1</b>
1.1	Introduction to catalysis . . . . .	1
1.2	The importance of catalytic H <sub>2</sub> oxidation . . . . .	4
1.3	The surface science approach . . . . .	5
1.4	Rhodium and rhodium crystallography . . . . .	7
1.5	Adsorption of the reactants H <sub>2</sub> and O <sub>2</sub> and the product H <sub>2</sub> O on Rh . . . . .	8
1.6	The Langmuir-Hinshelwood mechanism of H <sub>2</sub> oxidation on Rh . . . . .	12
1.7	Bistability and kinetic phase diagrams for H <sub>2</sub> oxidation on Rh . . . . .	13
1.8	Kinetic oscillations in H <sub>2</sub> oxidation on Rh . . . . .	15
1.9	The initial oxidation of Rh . . . . .	17
1.10	A short overview of metal/support interactions . . . . .	18
<b>2</b>	<b>Methods and concepts</b>	<b>21</b>
2.1	X-ray photoelectron spectroscopy (XPS) . . . . .	21
2.2	Scanning photoelectron microscopy (SPEM) . . . . .	27
2.3	UV photoemission electron microscopy (UV-PEEM) . . . . .	29
2.4	Low energy electron microscopy (LEEM) and x-ray photoemission electron microscopy (X-PEEM) . . . . .	31
2.5	Electron backscatter diffraction (EBSD) . . . . .	34
2.6	The kinetics by imaging approach . . . . .	35
2.7	The surface structure library concept . . . . .	37
2.8	Correlative microscopy . . . . .	38
<b>3</b>	<b>Coexisting multi-states in catalytic hydrogen oxidation on rhodium</b>	<b>41</b>
<b>4</b>	<b>Pattern formation in catalytic H<sub>2</sub> oxidation on Rh: Zooming in by correlative microscopy</b>	<b>61</b>
<b>5</b>	<b>How the anisotropy of surface oxide formation influences the transient activity of a surface reaction</b>	<b>85</b>
<b>6</b>	<b>Imaging interface and particle size effects by <i>in situ</i> correlative microscopy of a catalytic reaction</b>	<b>109</b>

<b>List of Figures</b>	<b>135</b>
<b>List of Tables</b>	<b>137</b>
<b>Bibliography</b>	<b>139</b>
<b>Curriculum Vitae</b>	<b>153</b>



# 1

---

## Introduction

The principles of catalysis and the development of catalytic processes have led to major scientific and technological breakthroughs in the history of mankind and without catalysis many aspects of our everyday lives would not be possible. Therefore, section 1.1 is dedicated to a brief history of and an introduction to the principles of catalysis. In the present thesis, catalytic H<sub>2</sub> oxidation was used as a test reaction for probing catalytic properties, therefore its relevance to science and daily life will be discussed in section 1.2. One way of studying catalytic processes in order to improve the used catalysts is the *surface science approach*, which has been used in this work and will be described in section 1.3. Sections 1.4, 1.5 and 1.6 will then deal with the properties of the metal rhodium, on which the present catalytic studies were performed, and its crystallography, the adsorption properties of the reactants H<sub>2</sub> and O<sub>2</sub> and the product H<sub>2</sub>O, and the mechanism of catalytic H<sub>2</sub> oxidation on Rh, respectively. Catalytic H<sub>2</sub> oxidation on Rh exhibits several phenomena such as bistability, kinetic transitions and mono- as well as multifrequential oscillations, which will be discussed in sections 1.7 and 1.8. Sections 1.9 and 1.10 will then give a brief literature overview on the initial oxidation of rhodium and on metal/support interface effects in catalysis.

### 1.1 Introduction to catalysis

The deliberate use of catalytic processes, e.g., in form of enzymatic processes such as fermentation of sugar to alcohol or alcohol to acetic acid, dates back to about 7000 B.C., when fermented beverages were produced in early neolithic china [1]. Thousands of years later, in 1552, Valerius Cordus recorded the use of sulfuric acid to catalyze the conversion of alcohol to ether, representing the first known use of an inorganic catalyst. At the end of the 18<sup>th</sup> and the beginning of the 19<sup>th</sup> century, many scientists systematically studied the influence of the presence of metals and oxides on several chemical reactions, e.g., decomposition of alcohol or ammonia, and thus catalytic processes [2]. All this was, however, done without explicit knowledge of the principles of catalysis or even the word *catalyst*, which was only coined in 1836 by Jöns Jakob Berzelius [3],

describing substances which facilitate a chemical process but themselves remain unaffected by the process. Strongly connected with the discovery of catalytic surface reactions are the names of Humphry Davy, Johann Wolfgang Döbereiner, Michael Faraday and William Henry. During development of his miner's safety lamp, an apparatus which prevented coal gas explosions in underground mines by inhibiting uncontrolled spread of the combustion zone, Davy discovered in 1817 that oxygen and coal gas in contact with a platinum or palladium wire could combine without a flame at temperatures way below the ignition temperature of the mixture, which may be considered the first clear evidence of a *catalytic surface reaction* [4], i.e., a heterogeneously catalyzed reaction. In 1823, Döbereiner found that directing hydrogen gas at a platinum sponge in the presence of oxygen will result in the metal becoming hot and igniting the hydrogen jet as a result of the catalytic reaction [5]. This first example of catalytic hydrogen oxidation on platinum group metals was developed into a simple way to produce fire, the Döbereiner Feuerzeug, which remained in use until the development of the phosphorous match 100 years later. By studying the deactivation of platinum-based catalysts and discovering that the presence of certain substances could inhibit the catalytic activity, Henry in 1824 established the concept of *catalytic poisoning* [6], which will play an important role throughout this thesis. In 1834, Faraday published a thorough analysis of various previous works on platinum catalysts and laid the first stone towards a mechanistic understanding of catalytic surface reactions by proposing that the reactants have to *adsorb to the catalyst surface* in order to react [7].

In the following years, a framework for mathematically describing the thermodynamics of chemical reactions and the concept of the chemical equilibrium was developed by Jacobus Henricus van 't Hoff [8]. This enabled Wilhelm Ostwald to formulate his still valid definition of a catalyst as a substance which "accelerates a chemical reaction without affecting the position of the chemical equilibrium" in 1894 [9]. Paul Sabatier in 1913 then concluded from his research on catalysis in organic chemistry, that every chemical reaction involves the formation of unstable chemical compounds as *intermediate species*, which determine the course and rate of the reaction, and that addition of a catalyst can change the nature of these intermediates [10]. These principles are illustrated by energy diagrams in Fig. 1.1 for a hypothetical uncatalyzed and catalyzed bimolecular reaction  $A + B \rightarrow AB$ .

The release of the amount of  $\Delta E$  in energy indicates the thermodynamically favored formation of the product  $AB$  from  $A$  and  $B$ , regardless of the use of a catalyst. However, the reaction might still not take place at a significant rate because the activation energy  $E_{A,AB}$  for formation of the transition state  $A \cdots B$  has to be overcome before formation of the product can take place. By introducing a suitable catalyst  $C$ , a new pathway for the reaction is opened up via the intermediate  $AC$ . The corresponding transition states  $A \cdots C$  and  $A \cdots B \cdots C$  are of lower energy, and therefore only a reduced activation energy of  $E_{A,AC}$  has to be overcome (Fig. 1.1). Nonetheless, the energy  $\Delta E$  released by the reaction remains the same and, as the overall energetics of the reaction govern the position of the chemical equilibrium, the position of the equilibrium remains unchanged.

The change in the speed of the reaction can then be explained by use of the Arrhenius equation:

$$k = A \cdot e^{-\frac{E_{Act}}{k_B T}} \quad (1.1)$$

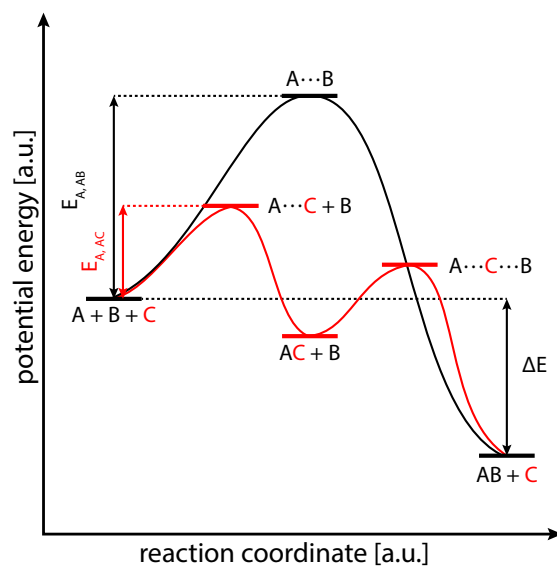


Figure 1.1: Working principle of a catalyst. The energy diagrams for a hypothetical bimolecular reaction illustrate the reaction paths and activation energy with (red) and without (black) use of a catalyst.

where  $k$  denominates the rate of the chemical reaction,  $A$  a pre-exponential factor,  $E_{Act}$  the activation energy (e.g.,  $E_{A,AB}$  or  $E_{A,AC}$ ),  $k_B$  the Boltzmann constant and  $T$  the temperature. Following from the equation, two methods exist for increasing the speed of the reaction: (i) increasing the temperature and (ii) lowering the activation energy. Usually the second approach is chosen, e.g., by introducing a catalyst, as an increase in temperature can shift the chemical equilibrium unfavorably and involves cost in endothermic processes, illustrating the importance of catalysis research.

These concepts of catalysis enabled the systematic, scientifically based search for better catalysts and catalytic processes for various applications were developed in the following, e.g., coal liquefaction using nickel catalysts, the Ostwald process for making nitric acid from ammonia using platinum catalysts, Fischer-Tropsch synthesis using iron and cobalt catalysts or catalytic cracking using clay-based catalysts [2]. An especially important milestone in the history of catalysis was the development of ammonia synthesis by Fritz Haber and Carl Bosch: Haber developed the idea of using atmospheric nitrogen and reacting it with hydrogen under extreme temperatures and pressures using osmium as catalyst [11], which was scaled to industrial production levels by Bosch and earned them Nobel Prizes in 1919 and 1931, respectively. The Haber-Bosch process resulted in a steep increase in world ammonia production, fertilizer production and thus food production during the 20<sup>th</sup> century, without which the exponential growth of the world population in the last 100 years would not have been possible [12].

With the increase of the world population and technological advancement, however, came not only benefits but also challenges. For example, due to the increased use of fossil fuels for electricity generation or mobility, increasing atmospheric pollution and depletion of natural resources became a huge problem, especially in big cities. Once again, catalysis was able to provide solutions to these problems: The development of the three-way automotive catalytic converter

enabled reducing the emission of harmful carbon monoxide, hydrocarbons and nitric oxides from combustion engines from over 60 g/km in the 1960s to below 1 g/km in the 2000s by treating the exhaust gas with a mixture of precious metals and ceria as catalyst, supported on an oxidic washcoat and a ceramic substrate [13, 14]. Other key developments in catalysis over the last several decades included the catalysts for production of several types of plastics, improvement of catalysts used for fuel reforming and catalytic cracking, and new, more energy efficient, catalytic processes for the production of base chemicals, such as methanol or acetic acid [2], highlighting the importance of catalytic processes for our current everyday lives.

The development of fuel cell technology could be another key step on the way to diminish depletion of natural resources and harmful emissions: In such a cell, the chemical energy stored in the fuel (e.g., hydrogen, small hydrocarbons or methanol) is directly, i.e., electrochemically, converted to electric energy via electrocatalytic reaction. If the fuel is generated in an environmentally friendly way by using renewable energy sources, such as biomass, solar or wind energy, such a system is entirely free of harmful emissions. While the development of fuel cell technology has greatly advanced in the last decade, general replacement of combustion engines by fuel cell is still hardly viable or even possible at the moment [15]. Therefore, further research on the catalytic processes going on in a fuel cells can be part in tackling one of the biggest challenges mankind currently has to face.

## 1.2 The importance of catalytic H<sub>2</sub> oxidation

The first commercial use of catalytic H<sub>2</sub> oxidation in form of Döbereiners Feuerzeug has already briefly been mentioned above. Since that time, a wide range of applications for catalytic H<sub>2</sub> oxidation has been developed: One area of applications is related to hydrogen itself and the energy stored in its chemical bond, which can be released in order to generate electricity or heat. Generation of electricity from hydrogen gas is possible via a fuel cell, where the chemical energy stored in hydrogen is directly converted to electric energy, eliminating the need to convert the chemical energy first to thermal energy, then to mechanical energy and finally to electric energy (as in a traditional combustion engine based power generator), significantly improving the efficiency of the conversion. Many different types of fuel cells exist, most of them using hydrogen as a fuel. In combination with a pre-reformer, however, also other fuels such as small hydrocarbons or methanol can be used by catalytically converting the primary fuel to H<sub>2</sub>, CO and CO<sub>2</sub> and using the resulting hydrogen-rich gas stream as input for the fuel cell [15]. Typically, some form of catalytic H<sub>2</sub> oxidation is one of the electrode reactions in such a cell, often using noble metals [16] or platinum group metals [17] as catalyst. By converting excess electric energy (e.g., from photovoltaics during sunny summer days) to chemical energy stored in hydrogen via water hydrolysis and back-conversion to electric energy in times of higher electricity demands, fuel cell technology could be one of the ways to solve the main problem of renewable electricity generation [18]. For applications where the generation of heat from hydrogen gas is the desired use, flame-less catalytic combustion devices have been developed, increasing the efficiency of the conversion and safety in comparison to flame-based combustion [19].

The other area of applications for catalytic H<sub>2</sub> oxidation is related to cases, where the presence

of hydrogen is undesirable and any present hydrogen needs to be safely disposed of. This includes for example the elimination of hydrogen traces from the off-gas of a fuel cell, which could otherwise lead to explosive environments in poorly ventilated rooms [20], or increasing the safety of nuclear power plants. In case of a severe accident in such a facility, several scenarios exist, where significant amounts of hydrogen could be produced, potentially leading to explosions and release of radioactive substances. By reacting off all traces of hydrogen in a safe way via catalytic oxidation on platinum group metal based catalysts, these risks can significantly be reduced [21]. Also, for some industrial processes, such as the dehydrogenation of organic compounds, removal of hydrogen from the reaction mixture via catalytic oxidation can lead to an increasing product yield [22]. Furthermore, catalytic  $H_2$  oxidation is also used in hydrogen gas sensors, where the catalytic reaction in the presence of hydrogen leads to an increase of the catalyst temperature, which can then be detected [23, 24].

Besides being technologically relevant, catalytic  $H_2$  oxidation is also interesting from a scientific perspective: Due to it being one of the simplest possible reactions, it can serve as a testbed for generating knowledge on heterogeneously catalyzed processes in general. Altogether, catalytic  $H_2$  oxidation is a reaction employed in various scientific and technological use cases and therefore interesting to study in order to further improve these processes and technologies and our knowledge about heterogeneous catalysis.

### 1.3 The surface science approach

Development of new and improved catalysts for technologically relevant processes usually takes place by combining two different strategies: The first one is the *screening approach*, where different mixtures of possibly suitable compounds are prepared, often in several different ways, and their catalytic performance is probed in experiments until a new composition exhibiting the desired catalytic properties is found. Even though this approach has yielded some of the most important technologically relevant catalysts such as the one for the industrial Haber-Bosch process, it is usually a costly and time-demanding strategy as huge amounts of compositions (often up to several thousands) have to be tested. The second strategy aims at uncovering the details of the mechanism of the catalytic process and its elemental steps, enabling tailored design of a new catalyst by modifying specific properties in order to improve or modify a specific step in the catalytic reaction. The development of computational chemistry and suitable experimental techniques has led to increasing knowledge on the individual steps of the reaction, often even on the atomic scale, demonstrating the power of this fundamental science approach.

As already hinted at in the previous section, a typical industrially employed catalyst does not only consist of the catalytically active component but is usually a complex system of catalyst nanoparticles, sometimes on an oxide support crucial for the catalytic activity, usually a substrate for mechanical stability and often additional compounds, e.g., promoters, for tuning specific properties. Additionally, typical industrial processes take place at pressures of several bars and elevated temperatures in a specially engineered reactor. Due to the complexity of these systems, resulting in a huge number of possibly interacting influences, and the lack of suitable experimental techniques which are able to cope with the elevated pressures while still remain-

ing sensitive only to processes going on at the catalyst surface, direct studying of an industrial process from a fundamental science perspective is hardly ever possible. It is therefore useful to reduce the complexity of the system along two paths: (i) reducing the pressures from several bars to the (ultra) high vacuum region ( $< 10^{-5}$  mbar) allows disregarding, e.g., heat and mass transfer limitations, which are crucial to consider in an industrial reactor, and enables the use of various surface sensitive techniques which require (ultra) high vacuum due to their working principle and (ii) reducing the complexity of the studied catalyst. Taken to the extremes, this leads to studying single crystals under ultra high vacuum conditions in a *surface science approach* [25–28].

Pioneered in the 1920s for example by Irving Langmuir, who suggested to focus research on reactions on planar surfaces until the principles in this case were well understood before extending the theories towards porous bodies [29], this approach has even led to Nobel Prizes for Langmuir in 1932 and Gerhard Ertl in 2007. When using such a strategy, it is however of crucial importance to remember that the results obtained for such simplified systems might not always match those obtained for real catalytic systems due to the pressure and materials gap resulting from the simplifications (Fig. 1.2a). Nonetheless, most of our current knowledge about chemical reactions taking place on surfaces has been obtained by using the surface science approach.

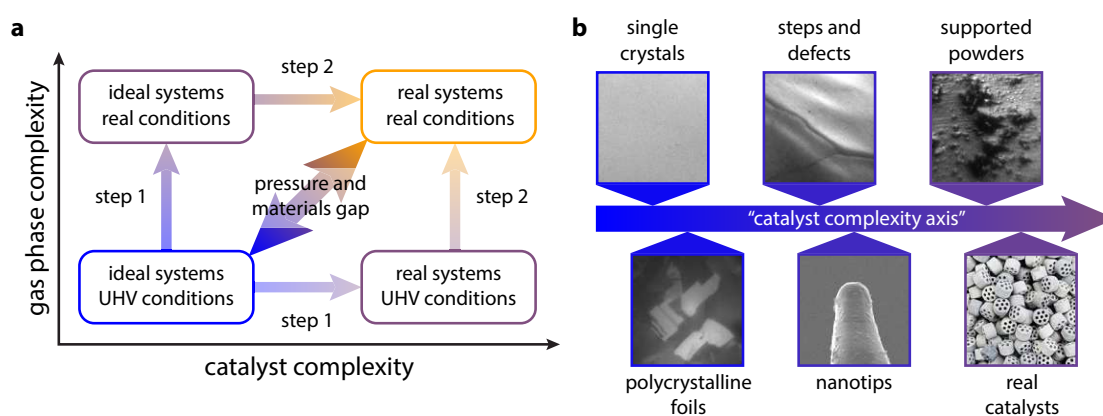


Figure 1.2: The pressure and materials gap. **(a)** pathways to overcome the pressure and materials gap; **(b)** the “catalyst complexity axis”, illustrating a way to increase the sample complexity from single crystals to real catalysts via several model systems.

As detailed above, increasing both the gas phase and sample complexities at the same time is unrewarding in terms of a better understanding of the catalytic reaction. Therefore, two strategies exist for bridging the pressure and materials gap: (i) the gas phase complexity is increased by increasing the pressure, while the complexity of the studied sample remains low (e.g., single crystals are studied) or (ii) the complexity is increased step-wise along the so-called “catalyst complexity axis” (1.2b), while the gas phase complexity remains low (i.e., the studies are performed under (ultra) high vacuum conditions). The “catalyst complexity axis” ranges from single crystals over polycrystalline metal foils and apexes of nm-sized tips towards supported metal powders and finally ends at real word catalysts, where each step along the axis introduces another feature present in such a catalyst. This second strategy was chosen for the present work and polycrystalline foils as well as powders supported on different materials were studied, representing two important steps along the “catalyst complexity axis”.

## 1.4 Rhodium and rhodium crystallography

All studies in the present work have been performed using rhodium as active metal in the various catalytic model systems. Rhodium is a platinum group metal with the atomic number of 45, a standard atomic weight of 102.9 u and with its electronic configuration of  $[Kr]4d^8 5s^1$  belongs to the platinum group metals. Its melting point is 2239 K, its boiling point 3968 K and below 9 K Rh becomes superconductive [30]. At standard conditions, Rh has a high thermal and electric conductivity [31]. Platinum group metals are especially known for their high corrosion resistance and their pronounced catalytic properties. Despite its rarity (Rh makes up only 0.2 ppb of earths crust), its difficult extraction from ores and the resulting high price, rhodium is essential for many industrial catalytic processes [32, 33], corrosion resistant coatings [34] or high temperature thermocouples [35]. The primary application, where 81% of world Rh production are used for, is, however, the production of three-way automotive catalytic converters, where Rh provides the  $NO_x$  reduction functionality in combination with ceria [36, 37].

Rhodium crystallizes in face-centered cubic (*fcc*) structure and belongs to space group number 225 ( $Fm\bar{3}m$  in Hermann-Mauguin notation) with a lattice constant of 3.804 Å. The unit cell, depicted in Fig. 1.3a, thus contains four Rh atoms. Cutting through the unit cell along an arbitrarily chosen plane yields a corresponding Rh surface with a well-defined surface structure. One way to characterize such a surface is the use of Miller indices  $h$ ,  $k$  and  $l$ , which are written as  $(hkl)$  and represent the family of planes orthogonal to the vector  $[hkl]$ . Depending on the exposed Rh( $hkl$ ) surface, different densities of surface atoms and adsorption sites are present, influencing the properties, e.g., the work function, and possibly the catalytic properties. For *fcc* structures, there are three main low-Miller-index surfaces: The Rh{100} surfaces are characterized by cubic primitive symmetry, a square unit cell and every Rh atom having eight nearest neighbors. In contrast, Rh{110} surfaces are the most loosely packed surfaces with a buckled structure, a rectangular unit cell and the upper layer of atoms having only seven nearest neighbors. Rh{111} surfaces, the most densely packed surfaces, display hexagonal symmetry, thus a rhombic unit cell, and nine nearest neighbors for each surface atom. These low-Miller-index surfaces are shown along with their corresponding plane in the *fcc* unit cell in Fig. 1.3b.

Usually, the formation of low-Miller-index surfaces is energetically favored for *fcc* systems. However, typical catalyst nanoparticles exhibit rounded or irregular shapes and thus expose high-Miller-index structures as well. Such structures are characterized by terraces of one of the low-Miller-index surfaces, bordered by monoatomic steps, which can either be of low-Miller-index structure or kinked in addition. The Miller indices of such surfaces are a linear combination of the three low-Miller-index surfaces: If only two components are present, the surface is stepped with terraces of the type corresponding to the “bigger” component and steps of the type corresponding to the “smaller” component. The ratio of the components then describes the terrace width. If all three components are present, the step edges are kinked. Examples of such structures are displayed in Fig. 1.3c: Rh(11 2 2) is characterized by (100)-type terraces of on average 3.25 atomic rows width and (111)-type flat step edges. Rh(7 5 5) is in contrast composed from (111)-type terraces and (100)-type flat step edges every 6<sup>th</sup> atomic row. Rh(10 5 5) has the same terrace and step edge structure, but a step edge every 3<sup>rd</sup> atomic row. Finally, Rh(10 6 5) has the same

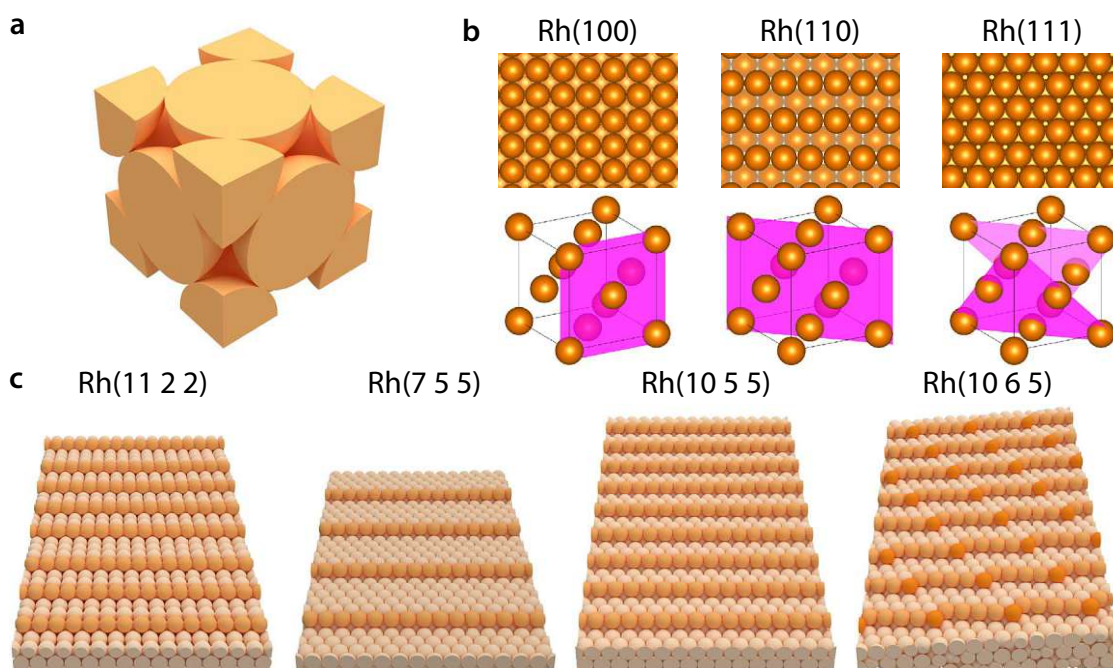


Figure 1.3: Crystal structures of rhodium and Rh(hkl) surfaces. **(a)** the *fcc* unit cell of rhodium; **(b)** atomic ball models of the Rh(100), Rh(110) and Rh(111) surface structures and their corresponding planes in the *fcc* unit cell; **(c)** atomic ball models of exemplary high-Miller-index surface structures (terrace atoms: beige, step edge atoms: light orange; kink atoms: dark orange).

terraces of the same width, but kinked (5 1 0)-type step edges, i.e., the (100)-type step edges are interrupted by a kink atom every 5<sup>th</sup> atom. Due to the lower coordination number of the atoms at step edges or kinks, such sites are especially favorable for reactant adsorption and chemical reaction. Highly stepped and kinked surfaces are therefore of special interest for surface science studies. On one hand, they better resemble the coordination geometries and binding environments of catalyst nanoparticles and, on the other hand, their catalytic properties are often improved in comparison to low-Miller-index surfaces.

## 1.5 Adsorption of the reactants H<sub>2</sub> and O<sub>2</sub> and the product H<sub>2</sub>O on Rh

As detailed in section 1.6 below, the catalytic hydrogen oxidation on rhodium takes place via the Langmuir-Hinshelwood mechanism, i.e., both reactants have to adsorb to the metal surface before reacting. Therefore it is of great importance to study the adsorption properties of the reactants H<sub>2</sub> and O<sub>2</sub> as well as the product H<sub>2</sub>O in order to understand the surface reaction. When a H<sub>2</sub> or O<sub>2</sub> molecule from the gas phase impinges on the metal surface it can adsorb to the surface via a molecular precursor and dissociation into two individual atoms that directly bind to the metal surface if two adjacent free adsorption sites are available. The probability of such an adsorption event upon impinging (i.e., the sticking coefficient) is dependent on several factors, including



the temperature, the energy gain by adsorption and the already existing surface coverage. The surface coverage  $\Theta_i$  for a species  $i$  is defined as the ratio of adsorption sites occupied by species  $i$  to the total number of possible adsorption sites for species  $i$ . Due to repulsive interactions between the individual adsorbed atoms, the equilibrium coverage is often significantly below 1 and dependent on the external parameters. In order to minimize the total energy, adsorbates can also form complicated two-dimensional structures, which can exhibit long-range ordering, where each structure can only be found in a certain range of external parameters, as the optimal energy minimum changes.

Such superstructures can be represented in Woods notation, which describes the symmetry of the adsorbate unit cell with respect to the substrate unit cell. Exemplary adsorbate structures on *fcc* substrates are given in Fig. 1.4 with their corresponding description in Woods notation: The numbers in the parentheses indicate the ratio of the size of the adsorbate unit cell relative to the substrate unit cell, the letter before the parentheses indicate the type of the adsorbate unit cell (e.g., p: primitive, c: centered) while a rotation of the adsorbate unit cell with respect to the substrate unit cell is indicated after the parentheses by the letter R followed by the angle of rotation.

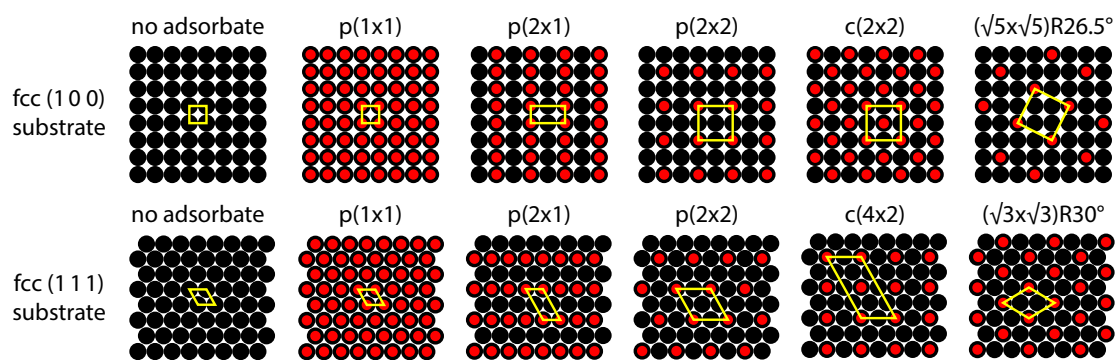


Figure 1.4: Woods notation for exemplary adsorbate structures on *fcc* substrates. Black circles indicate the substrate atoms while red circles indicate the adsorbate atoms. The corresponding unit cell is indicated in yellow.

The adsorption of  $\text{H}_2$ ,  $\text{O}_2$  and  $\text{H}_2\text{O}$  on rhodium has extensively been studied by various techniques such as Auger electron spectroscopy (AES), field emission microscopy (FEM), field ion microscopy (FIM), low energy electron diffraction (LEED) or thermal desorption spectroscopy (TDS) and the results have been complemented by theoretical calculations. Most of these studies have however been performed on low-Miller-index surfaces (i.e., Rh(111), Rh(110) or Rh(100)), while data on stepped and kinked high-Miller-index surfaces are scarce. In the following, literature data on the sticking coefficient, desorption temperatures, desorption energies and observed adsorbate structures will briefly be summarized for  $\text{H}_2$ ,  $\text{O}_2$  and  $\text{H}_2\text{O}$  on rhodium.

For the adsorption of  $\text{H}_2$  on Rh, the available data is very limited due to the formation of disordered adsorbate structures and the relatively low desorption temperatures below 400 K. For example, on Rh(100) a desorption temperature of around 400 K was determined by AES and LEED [38]. On Rh(110), an initial sticking coefficient of 0.97 was determined at  $T = 80$  K and TDS indicated three different atomic binding states. Two desorption maxima at  $T = 138$  K and

$T = 216$  K do not change with the surface coverage, while the third desorption maximum shifts from  $T = 280$  K at low coverage to  $T = 245$  K at saturation coverage. The corresponding desorption energies were calculated as 0.34, 0.55 and 0.93 eV [39]. On Rh(111), the initial sticking coefficient is 0.65 and a single desorption maximum was observed at low coverages at  $T = 390$  K, shifting to  $T = 275$  K with coverages approaching saturation coverage. The corresponding desorption energy was calculated as 0.81 eV [40]. For Rh(311) a sticking coefficient of 0.3 has been observed in the temperature range from 90 to 220 K at a coverage below 0.5 ML, which decreases to 0.05 at a coverage of 0.75 ML. TDS shows a desorption maximum at  $T = 175$  K independent of the surface coverage; a second maximum at  $T = 250$  K at low coverages becomes a double maximum at  $T = 250$  K and  $T = 320$  K at coverages increasing to 0.8 ML with the corresponding desorption energy calculated as 2.64 eV [41, 42]. Some of the adsorbate structures observed during these studies are summarized in table 1.1. Even though the adsorption behavior and binding energies are different for all the above Rh(hkl) surfaces, the hydrogen surface coverage above 400 K is minimal for all Rh(hkl) surfaces due to the fast desorption of hydrogen at these temperatures.

Table 1.1: Adsorption phases observed for hydrogen on various Rh(hkl) surfaces

Rh(hkl) surface	T [K]	$\Theta_{\text{H}}$ [ML]	Adsorbate structure	Reference
Rh(100)	< 400	< 1.00	(1 x 1) or disordered	[38]
Rh(110)	80	0.33	p(1 x 3)	[39]
	80	0.50	p(1 x 2)	[39]
	80	0.67	(1 x 3)-2H	[39]
	80	1.50	(1 x 2)-2H	[39]
	80	2.00	(1 x 1)-2H	[39]
Rh(111)	< 400	< 1.00	disordered	[40]
Rh(332)	90 - 220	0.33	p(1 x 3)	[41, 43]
	90 - 220	0.50	p(1 x 2)	[41, 43]
	90 - 220	0.66	p(1 x 3)-2H	[41, 43]
	140	0.25	p(1 x 4)	[42]

For the adsorption of  $\text{O}_2$  on Rh, the picture is significantly more complicated: On Rh(100) the sticking coefficient for oxygen was determined in the temperature range from 130 to 500 K as 0.8 - 1.0 at coverages below 0.4 ML, rapidly decreasing at higher coverages and approaching 0.001 at 1.0 ML [44, 45]. The TDS spectra show two desorption maxima, one at  $T = 1300$  K at low coverages, which shifts to lower temperatures with increasing coverage, and the second one appearing at coverages above 0.5 ML at  $T = 900$  K and remaining unchanged with higher coverage, giving desorption energies of 2.18 - 2.33 and 2.90 eV, correspondingly [45]. For Rh(110), the initial sticking coefficient is 0.7 to 0.95 at  $T = 125$  K and 0.62 at  $T = 310$  K and diminishes at coverages above 0.65 ML [46–48]. Three desorption maxima were observed using TDS, one at  $T = 1180$  K at low coverages, shifting to  $T = 1100$  K with the coverage increasing to 0.5 ML, the second one appears at coverages above 0.5 ML at  $T = 910$  K, while the third one appears at coverages above 0.7 ML at  $T = 830$  K. The corresponding desorption energies are 3.11, 2.76 and 2.12 eV, respectively [48, 49]. The initial sticking coefficient of oxygen on Rh(111) is 0.2

at  $T = 100$  K and is constant at temperatures below 170 K [50]. For oxygen adsorption at low temperatures, a single broad maximum from 900 to 1400 K is observed in TDS, while for adsorption at temperatures above 450 K, a sharper desorption maximum at 893 K can be observed, corresponding to a calculated desorption energy of 2.43 eV [50, 51]. A broad variety of adsorbate structures has been observed for various Rh(hkl) surfaces, which have been summarized in table 1.2.

Table 1.2: Adsorption phases observed for oxygen on various Rh(hkl) surfaces

Rh(hkl) surface	T [K]	$\Theta_{\text{O}}$ [ML]	Adsorbate structure	Reference
Rh(100)	130 - 450	0.25	p(2 x 2)	[52, 53]
	130	0.50	(2 x 2)p2mg	[52]
	370 - 550	0.50	(2 x 2)p4g	[53–55]
Rh(110)	125 - 300	0.40 - 1.00	(2 x 1)p2mg	[56, 57]
	470	0.35 - 0.50	(2 x 2)pg	[56]
	470	0.60 - 1.00	c(2 x 2n)	[48, 56]
	470	1.00	c(2 x 8)	[48, 56]
	500 - 650	0.15	p(2 x 3)	[46]
	500 - 650	0.25	np(2 x 3)	[46]
	500 - 650	0.30	np(2 x 3)	[46]
	500 - 650	0.40	c(2 x 6)	[46]
	500 - 650	0.45	c(2 x 10)	[46]
Rh(111)	120 - 400	0.50	p(2 x 2)	[50]
	325	0.25	p(2 x 2)	[58, 59]
	325	0.50	p(2 x 1)	[58, 59]
Rh(332)	430 - 510	0.60	p(1 x 1)	[60]
Rh(711)	675	0.15	c(2 x 2)	[61]
	675	0.50	(1 x n)	[61]

An essential feature of the adsorption of oxygen on rhodium is the ability to induce reconstructions of the corresponding underlying Rh surfaces, i.e., the structure of the surface is changed by relocating Rh atoms in order to minimize the total energy. For example, for Rh(100) surfaces can reconstruct in a “clock” like fashion at  $T = 370$  K and an oxygen coverage of 0.5 ML, where the surface metal atoms move tangentially in-plane in alternate clockwise and anticlockwise rotations [54, 55]. Similarly, for Rh(110) surfaces, row pairing of up to five adjacent atomic rows (i.e., missing-row-type reconstruction) has been observed at temperatures from 400 to 560 K at very low oxygen exposures, both on single crystals [47, 62–64] and the [110] facets of a nanotip [65]. Surface reconstructions have also been observed for high-Miller-index surfaces such as Rh(332), which undergoes a step-doubling reconstruction, where the density of atomic steps is halved in favor of doubling the height of the individual atomic steps, at  $T = 500$  K and very low oxygen exposures [60]. For Rh nanotips, it was also shown that the reconstruction of certain nano-facets on the nanotip can also result in other nano-facets appearing and disappearing, changing the morphology of the whole specimen [66], possibly also changing the catalytic behavior.

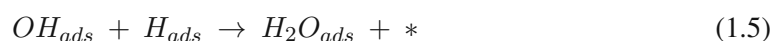
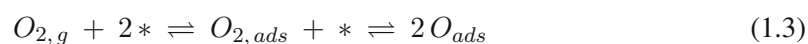
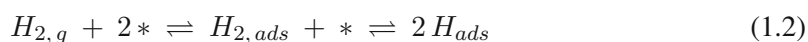
This already complex behavior is further complicated by the possibility of oxygen to penetrate the topmost Rh atomic layer and diffuse into the area directly beneath it, forming subsurface

oxygen. While adsorbed oxygen is hardly mobile due to the high binding energy of up to 3 eV, subsurface oxygen atoms are located in the interstitial octahedral sites and quite mobile in comparison. Due to the occupation of subsurface sites by oxygen, the lattice of the topmost Rh layer is distorted, in some cases resulting in changes in the most energetically favorable surface sites [67] and therefore possibly influencing the catalytic behavior of the surface. The existence and formation of subsurface oxygen has been studied using various surface sensitive techniques such as photoemission electron microscopy (PEEM), high resolution electron energy loss spectroscopy (HREELS), x-ray photoelectron spectroscopy (XPS) and TDS on several Rh surfaces such as Rh(110) [66], Rh(111) [67–69] or Rh(711) [61]. Also, theoretical studies have been performed to estimate whether the formation of subsurface oxygen is favorable for different Rh surfaces and oxygen coverages [70]. The probability of oxygen diffusion into the subsurface region is dependent on the surface structure, with rougher surfaces (i.e., with higher step and kink density) enhancing the formation of subsurface oxygen [61], and on the surface oxygen coverage. Although the formation of subsurface oxygen can in principle happen at any surface coverage, the formation of significant amounts of subsurface oxygen is only likely at higher surface oxygen coverages, as only then the repulsion between adsorbed oxygen atoms is high enough to make the occupation of subsurface sites energetically favorable [71]. In contrast to oxygen, a similar behavior is not to be expected for hydrogen, as the hydrogen surface coverage is very low as detailed above and the stability of subsurface hydrogen is much lower in comparison to surface hydrogen [72–74].

For the reaction product  $H_2O$ , the situation is more similar to hydrogen: Water adsorbed on Rh(100) readily desorbed at  $T = 180$  K in temperature programmed electron energy loss spectroscopy experiments [75] and at  $T = 150$  K on Rh(110), determined by work function measurements [39]. For Rh(111), literature data is a little more elaborate and has shown the formation of a  $(\sqrt{3}) \times (\sqrt{3})$ -R30° adsorbate structure upon water exposure at 100 K. Corresponding TDS spectra show two desorption maxima at  $T = 184$  K and  $T = 160$  K, with calculated desorption energies of 0.47 and 0.45 eV [76, 77]. Therefore, the expected  $H_2O$  coverage can be considered negligible and the product immediately desorbing at realistic reaction temperatures above 400 K.

## 1.6 The Langmuir-Hinshelwood mechanism of $H_2$ oxidation on Rh

Catalytic hydrogen oxidation on rhodium follows the Langmuir-Hinshelwood mechanism [78, 79], i.e., both reactants have to adsorb to the Rh surface before the reaction can take place, similarly to other platinum group metals [80, 81]. The mechanism can be described by six elementary steps, which are shown in equations (1.2) to (1.7) and where  $*$  denotes an unoccupied adsorption site:





The first step, described by equations (1.2) and (1.3) for  $H_{2,g}$  and  $O_{2,g}$ , respectively, is the dissociative adsorption on the Rh surface via a molecular precursor state, forming  $H_{ads}$  and  $O_{ads}$ .  $H_{ads}$ , which is more loosely bound in comparison to  $O_{ads}$  (see section 1.5), has the higher mobility and can diffuse along the surface. Upon encountering more strongly bound  $O_{ads}$ , an  $OH_{ads}$  intermediate can form (1.4). In the following,  $H_2O_{ads}$  can be produced either via reaction of  $OH_{ads}$  with  $H_{ads}$  (1.5) or via disproportioning of two  $OH_{ads}$  intermediates (1.6). The loosely bound product  $H_2O_{ads}$  then desorbs from the surface (1.7). The reaction mechanism is graphically illustrated in Fig. 1.5.

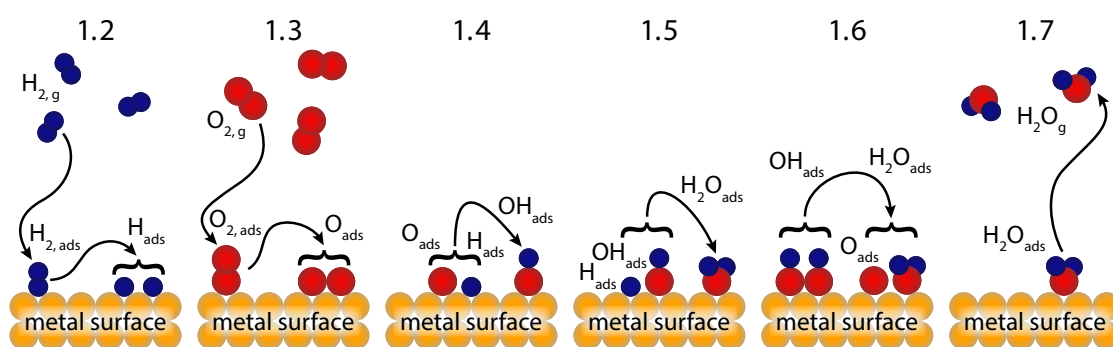


Figure 1.5: The Langmuir-Hinshelwood mechanism of catalytic  $H_2$  oxidation on platinum group metals. The individual panels correspond to the reaction steps in equations (1.2) to (1.7).

## 1.7 Bistability and kinetic phase diagrams for $H_2$ oxidation on Rh

As discussed in section 1.6 above, the catalytic  $H_2$  oxidation on Rh follows the Langmuir-Hinshelwood mechanism, where both reactants have to adsorb to the Rh surface before the reaction can take place. As a result, the adsorption behavior, in detail discussed in section 1.5, determines the course of the catalytic reaction. The competitive coadsorption of  $H_2$  and  $O_2$  is nonequivalent and varies depending on the specific external parameters (e.g.,  $T$ ,  $p_{H_2}$ ,  $p_{O_2}$ ). Therefore, the composition of the adsorbate layer changes with changing external parameters and the reaction can be in two different states of catalytic activity.

For example, if the adsorption probability for oxygen (i.e., the combination of sticking coefficient and impinging rate/partial pressure) is significantly higher than the one for hydrogen at a certain set of external parameters, the surface will predominantly be covered by oxygen. Oxygen adsorption and the resulting surface coverage is however a dynamic equilibrium: At any given time some oxygen will associatively desorb, while, due to the higher adsorption probability of oxygen, nearly all freed surface sites will immediately be occupied again by adsorbing oxygen. The surface coverage of hydrogen is very low, due to the lacking hydrogen supply the rate of water formation is also low and the surface is in the “poisoned” catalytically inactive steady state. If,

on the other hand, the adsorption probability for hydrogen is significant at another set of external parameters (e.g., due to increased  $p_{\text{H}_2}$  and thus increased impinging rate), some of the surface sites freed by desorption of oxygen will also be occupied by adsorbing hydrogen, which immediately reacts with neighboring oxygen and forms water desorbing from the surface. As a result, more free adsorption sites will be generated where both hydrogen and oxygen can adsorb. Due to the fast consumption of both reactants by water formation, both surface coverages are low, the water formation rate is high and the surface is in a catalytically active state. These steady states of catalytic activity are illustrated by schematic atomic ball models in Fig. 1.6a.

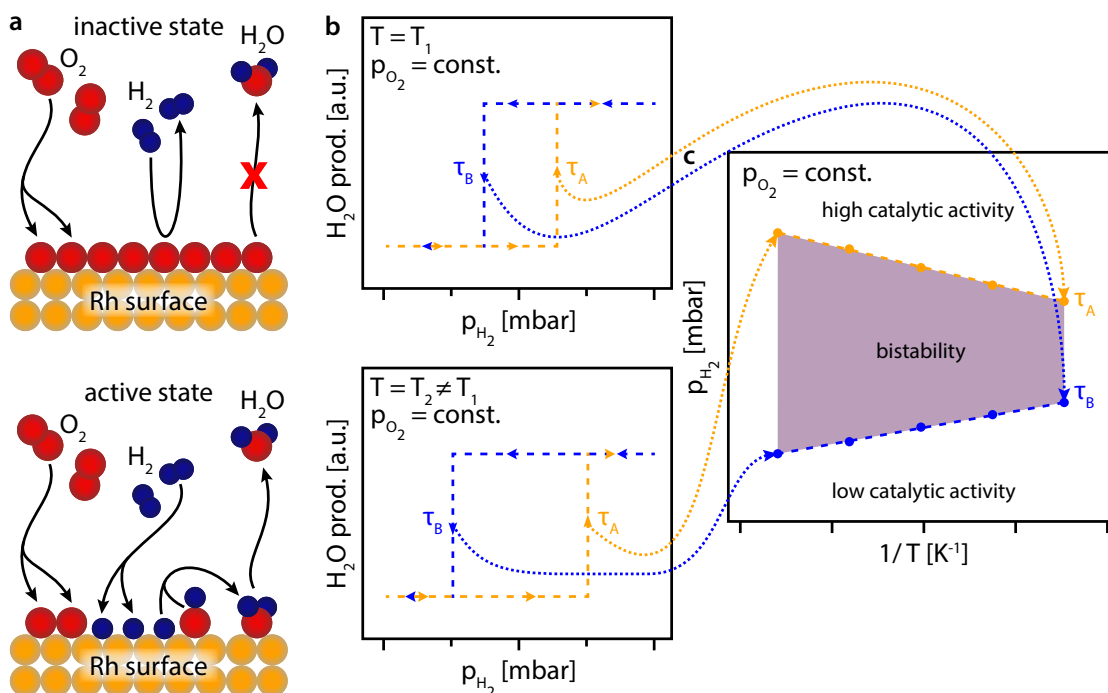


Figure 1.6: The steady states of catalytic activity, bistability and kinetic phase diagrams in catalytic  $\text{H}_2$  oxidation on Rh. (a) schematic atomic ball models of the catalytically inactive (top) and active (bottom) steady states; (b) idealized hysteresis curves of the water production upon cycle-wise variation of  $p_{\text{H}_2}$  at two different temperatures; (c) construction of the kinetic phase diagram from hysteresis measurements.

If the external parameters are changed, an abrupt change of the kinetic behavior can take place due to the changing adsorption equilibrium and the system switches from one steady state to the other steady state of catalytic activity. This *kinetic phase transition* [82] is usually accompanied by the propagation of reaction fronts [83, 84]. Keeping two parameters, e.g.,  $T$  and  $p_{\text{O}_2}$ , constant while varying the third parameter,  $p_{\text{H}_2}$  in this case, the kinetic behavior of the reaction system can be studied. Starting at low  $p_{\text{H}_2}$ , the system is in the catalytically inactive steady state. Upon increasing  $p_{\text{H}_2}$ , the partial pressure will at a certain point reach a critical value, where a kinetic transition to the catalytically active state will take place and the water production rate increases abruptly. The necessary  $p_{\text{H}_2}$  for this kinetic transition point, labeled  $\tau_A$ , is characteristic for the studied system and the other constant external parameters. When now  $p_{\text{H}_2}$  is decreased again, the inverse process will take place at a certain  $p_{\text{H}_2}$ , where the water production rate will drop and

the system switches to the catalytically inactive state. This  $p_{\text{H}_2}$  is once again characteristic and the kinetic transition labeled  $\tau_{\text{B}}$ . Due to the asymmetry in the adsorption properties of hydrogen and oxygen, the transition  $\tau_{\text{B}}$  occurs at a  $p_{\text{H}_2}$  which is significantly lower than  $\tau_{\text{A}}$ . Therefore, catalytic  $\text{H}_2$  oxidation on Rh exhibits *bistability*, i.e., the system can be in two different states of catalytic activity at the same set of external parameters, with the actual state of the system solely depending on its prehistory [71]. Plotting the water production rate against  $p_{\text{H}_2}$  yields a hysteresis-like looped shape (Fig. 1.6b).

Repeating such experiments for different temperatures but the same  $p_{\text{O}_2}$  (illustrated exemplarily for  $T_2 \neq T_1$  in the lower panel of Fig. 1.6b) yields a collection of kinetic transition points. These transition points can be plotted in the  $p_{\text{H}_2}$  vs.  $1/T$  parameter space, creating a kinetic phase diagram [85], which characterizes the areas of low and high catalytic activity and bistability of the studied system (Fig. 1.6c). As the kinetic transition points are characteristic for the studied system, kinetic phase diagrams can be used to characterize the kinetic behavior and to compare different systems, where changes, e.g., in composition or structure, are reflected in different kinetic state spaces [86, 87].

## 1.8 Kinetic oscillations in $\text{H}_2$ oxidation on Rh

Typically, catalytic reactions operated in a flow regime exhibit a constant reaction rate at constant external parameters. Since the beginning of the 20<sup>th</sup> century, it is, however, known, that the production rates of some chemical reactions can also oscillate at stationary external conditions. Already in 1921, the oscillating decomposition of hydrogen peroxide was observed [88], while in 1928 the oscillating electrodisolution of iron in aqueous sulfuric acid was studied for the first time [89]. The probably most famous example for an oscillating chemical reaction stems from the 1950s, where the Belousov-Zhabotinski reaction (i.e., the reaction of bromine and malonic acid) was shown to form spiral patterns in a petri dish [90, 91]. In the field of heterogeneous catalysis, oscillations in catalytic CO oxidation [92, 93] and NO reduction [94] on platinum have been observed since the 1970ies.

From a surface science perspective, the oscillating catalytic CO oxidation on platinum has been well studied on various single crystal surfaces, nanotips or supported catalysts and the mechanism of the oscillations uncovered [95–100]. Catalytic  $\text{H}_2$  oxidation was shown to exhibit oscillations on platinum [101–103], on bimetallic Rh/Ni catalysts [104, 105], silica-supported Rh powder catalysts [106] and on unsupported, pure Rh nanotips in high external electric fields [107]. Only recently, oscillations in catalytic  $\text{H}_2$  oxidation on Rh under field-free conditions were observed on the individual domains of a polycrystalline Rh foil [108] and individual facets of nanotips [109, 110].

In order for oscillatory phenomena to take place, two prerequisites need to be fulfilled: First, the reaction needs to exhibit bistability, i.e., two steady states have to be stable at the same external parameters. Second, a feedback mechanism is needed, inducing the periodic switches between these two states [111]. Examples of such feedback mechanisms include the periodic occurrence and lifting of adsorbate induced reconstruction (e.g., in the oscillating CO oxidation [112, 113] or  $\text{H}_2$  oxidation reactions [103] on Pt), the formation of subsurface oxygen (e.g., in the oscillating

CO oxidation reaction on Pd [97]) or the reversible segregation of one component in bimetallic alloys (e.g. in the oscillating  $\text{H}_2$  oxidation reaction on bimetallic Rh/Ni catalysts [104, 105]). While bistability in catalytic  $\text{H}_2$  oxidation on Rh has been discussed in section 1.7, the feedback mechanism of the kinetic oscillations will be discussed in the following.

Figure 1.7 schematically illustrates the feedback mechanism of catalytic  $\text{H}_2$  oxidation on Rh, based on the formation and depletion of subsurface oxygen, which was identified in photoemission electron microscopy studies of the oscillating reaction on individual grains of a polycrystalline foil and corroborated by micro-kinetic model simulations [108, 114]. Further evidence for the feedback mechanism is presented in chapters 3 and 6.

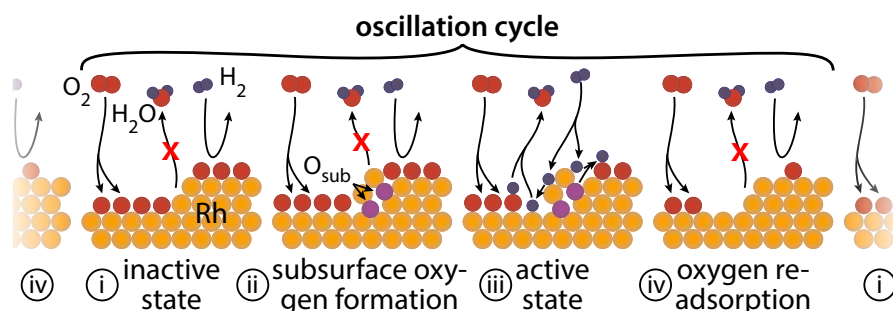


Figure 1.7: The feedback mechanism in the oscillating catalytic  $\text{H}_2$  oxidation on Rh. The atomic ball models schematically illustrate the four stages of the feedback mechanism.

The cycle starts from a catalytically inactive state (i), where, similar to the catalytically inactive steady state, the preferential adsorption of oxygen, especially at the step edges, hinders the dissociative adsorption of hydrogen and thus prevents catalytic activity. Because of the dense oxygen coverage, oxygen starts to penetrate the surface at the most loosely bound Rh atoms at step edges or kinks, forming subsurface oxygen (ii). As a result, some Rh atoms get slightly dislocated, increasing the local surface “roughness”, forcing a change of the adsorption geometry of the oxygen adsorbed in the vicinity and preventing further adsorption of oxygen at the step edge. This enables hydrogen to dissociatively adsorb and a switch to a catalytically active state (iii) takes place. Both hydrogen and oxygen can adsorb and form water, similar to the catalytically active steady state. Eventually all surface oxygen will have reacted and subsurface oxygen starts to diffuse to the surface and react. As a result the increase of the surface “roughness” will be reversed and oxygen will again preferentially adsorb at the step edges. Because of the resulting lack in hydrogen supply, the surface switches back to a catalytically inactive state. During the last stage (iv), oxygen at the surface is replenished and the cycle starts again.

Besides being of academic interest, studying oscillating chemical reactions also makes sense from a practical point of view: A system exhibiting non-steady behavior may perform better than the same system remaining in a steady state regime [115]. In addition, the local catalytic activity of such reaction systems can be tuned to fit temporally changing demands, e.g., by external stimuli [116].



## 1.9 The initial oxidation of Rh

Surface oxides and partially oxidized surfaces are important in many areas of technology, including catalytic reforming, syn-gas production, fuel cells, electrolysers, sensors and batteries, and play a decisive role in processes such as exhaust gas cleaning or corrosion [117–121]. Surface oxides have also received significant interest in heterogeneous catalysis because, depending on the reaction conditions, an initially metallic surface may oxidize in the presence of oxygen, possibly changing its catalytic activity [122–124]. When studying catalytic  $H_2$  oxidation on rhodium, it is therefore important to consider the possible oxidation of Rh and its influence on the catalytic properties.

Experimental and theoretical studies in the past decade have led to the discovery that the transition from metals to bulk oxides is not a simple process but often involves an intermediate step, where ultra-thin oxide films are formed, which have been termed *surface oxides* [125]. Such surface oxides have been found on various platinum group metals, including Rh [57, 124, 126–128], Ru [129], Pd [123, 125, 130] and Pt [130] and are characterized by the topmost metal layer being sandwiched between two atomic layers of oxygen. Due to their specific structures, such oxides can even be considered a new class of materials, as they may exhibit novel unexpected properties [57, 128, 131] and practical impact on the above-mentioned technologies. They are also significantly different from subsurface oxygen (section 1.5), which, in contrast to surface oxides, does not exhibit long ranging ordered structures.

The initial oxidation and the surface oxides of Rh have been studied using various techniques such as x-ray photoelectron spectroscopy (XPS), surface x-ray diffraction (SXR) or scanning tunneling microscopy (STM), complemented by ab-initio calculations. Most of these studies were, however, focused on low-Miller-index surfaces and single crystals [57, 126, 127, 132]. The surface oxidation of Rh starts at the lower coordinated Rh atoms at atomic steps and especially at kink sites by formation of  $RhO_2$  mono- and dimers [133]. In the following, a chain of such  $RhO_2$  units is formed along the step edges and Rh ridges [134, 135] and oxygen starts to penetrate the surface by diffusion under the step edges [126, 135, 136]. After reaching a distance of several atomic layers from the step edge, further oxide growth is kinetically hindered at intermediate oxygen partial pressures ( $10^{-5} < p_{O_2} < 10^{-3}$  mbar) and no bulk oxides are formed even under continued oxygen exposure. Only significant increase of the oxygen partial pressure [51, 137, 138] or oxidation by atomic oxygen [64, 132, 139] yields thicker bulk-oxide-like films. Furthermore, it was shown that the atomic structure of the step edges determines the kinetic barrier for oxygen penetration and thus the amount of formed surface oxide [135]. As a result, different surface structures are differently susceptible to oxidative modification during an ongoing catalytic reaction and thus changing catalytic properties, highlighting the importance of studies of the initial oxidation.

The structures of the surface oxides themselves, in contrast, have been shown to be largely similar on all low-Miller-index structures and thus, due to the mechanism of the oxidation, also on the terraces of stepped high-Miller-index structures. The surface oxide structure consists of a hexagonal arrangement of Rh atoms sandwiched between two atomic layers of oxygen atoms. The upper layer is located in half of the three-fold hollow sites formed by the Rh atoms, while

the lower layer is located in the other half. The structures for Rh(100), Rh(110) and Rh(111) just differ by slight variations of the lattice constants (3.07/3.09 Å, 3.02 Å and 3.04 Å, respectively) and a slight distortion in the case of Rh(100) [57, 126, 127]. To complement these studies focused on low-Miller-Index surfaces, a part of chapter 5 will deal with the oxidation of high-Miller-index surfaces, which play a crucial role in the structures of many catalyst nanoparticles.

## 1.10 A short overview of metal/support interactions

In section 1.3 it was already mentioned that catalysts employed in industrial processes rarely consist just of the catalytically active metal, but usually are a multi-component system: Such a catalyst typically consists of the nanoparticulate active metal, a support material, and often additional components (e.g., promoters) for tuning the catalytic properties. Besides ensuring mechanical stability, the support material often plays a decisive role for the catalytic activity due to various interactions possible between metal and support. The most important of these interactions for tuning catalytic properties [140] will briefly be discussed below:

**(i) Structural changes in nanoparticles induced by the support:** The support material can play a decisive role in controlling size, shape and stability of the catalyst nanoparticles. For example, by choosing the right support material, sintering (i.e., the loss of active surface due to formation of bigger aggregates from several nanoparticles), one of the key processes in catalyst degradation, can be diminished due to the increased adhesion energy between nanoparticle and support in comparison to unsupported particles [141–143]. Tuning the oxidation state and (in case of reducible oxides) the degree of reduction of the supporting oxide results in altered metal/oxide bonding and increased stability via formation and stabilization of oxygen vacancies, acting as strong anchoring sites for metal nanoparticles [142, 144, 145], or via formation of additional interfacial metal/oxide bonds [146]. Not only the chemical nature but also the atomic structure of the support material can influence the stability of the nanoparticles, either due to the presence or absence of specific metal/oxide binding sites [147] or due to strain effects. Because of lattice mismatch between the nanoparticle and the support materials, strain in the nanoparticle lattice is a common observation [148, 149], which can alter the electronic and therefore chemical properties of a metal [150–152] and could also modify the equilibrium shape of the nanoparticles [149, 153, 154].

**(ii) Electronic changes in nanoparticles induced by the support:** Metal/oxide interactions can also affect the electronic structure of the nanoparticle. The electron density jump across the metal/oxide interface and the resulting charge transfer can influence the reactivity, structure and stability of the nanoparticles. Electronic effects lead, for example, to stabilization of adsorbed OH and H species on supported Pt nanoparticles in comparison to unsupported nanoparticles [155], or interface promoted CO<sub>2</sub> adsorption and activation on Au nanoparticles [156], in both cases significantly increasing the catalytic activity. Besides affecting the binding of reactants or intermediates, charge transfer can also alter the morphology of the nanoparticles [157–159]. Several strategies to tune the interfacial charge transfer, and thus the catalytic properties, have been developed, e.g., modifying the density of oxygen vacancies on oxide supports [160], changing the support termination and structure [161], doping the support [159] or altering the size of the

nanoparticles [162].

**(iii) Chemical changes in nanoparticles induced by the support:** The support can also influence the reactivity of the catalytic system by changing the chemical properties, e.g., the composition, of the metal nanoparticles. The most prominent example of such effects is the strong metal-support interaction (SMSI), i.e., the modulation of catalytic activity resulting from decoration of the nanoparticle surface with substrate atoms. Initially demonstrated for metal clusters on  $\text{TiO}_2$  substrate becoming deactivated at elevated temperatures under a reducing environment [163, 164], the effect has since been observed for various combinations of metals and oxide supports [165, 166] and was shown to be reversible in some cases [167–169]. Besides deactivation of the catalyst due to blocking of the active sites or electronic effects, also cases exist, where the SMSI effect causes an enhancement of the catalytic activity due to the changed electronic structure of the nanoparticle [170, 171] or by stabilizing reaction intermediates [172]. Another example of chemical changes induced by the support is the affecting of the nanoparticle chemical stability, e.g., by diminishing surface poisoning [173–175].

**(iv) Synergistic interactions between nanoparticles and support:** Many cases exist, where the catalytic activity of the nanoparticle is not just enhanced by support-induced modifications of structure, electronic environment or chemistry but rather just made possible by the unique combination of both components. One mechanism behind such cases is the spillover of reactants, i.e., the migration of an adsorbate molecule or atom from one surface (e.g., the metal nanoparticle) to another surface (e.g., the oxide support), where it would not be able to adsorb by itself at all or at a significantly slower rate. The spillover of hydrogen or oxygen, for example, can have an enormous impact on the reactivity and stability of catalysts [176–178]. In some cases also a bi-functional mechanism may occur in which the metal nanoparticle provides active sites for one particular step of the catalytic reaction, while the oxide support provides active sites for another one. This was, e.g., demonstrated for methane dry reforming on ceria-supported nickel catalysts, where  $\text{CH}_4$  and  $\text{CO}_2$  are activated on the ceria support and spill over onto the nickel nanoparticles to react [179], or for ethanol steam reforming on similar catalysts, where the ethanol adsorbs on the nickel nanoparticles and the adsorption of water takes place on the ceria support [180]. Another mechanism in which nanoparticles and support play a combined role in enhancing of the catalytic activity is the creation of highly reactive perimeter sites at the boundary between the nanoparticle and the support, e.g., in CO oxidation on  $\text{Au/TiO}_2$  catalysts [181], methanol synthesis on  $\text{Cu/ZnO/Al}_2\text{O}_3$  catalysts [182] or the water gas shift reaction on  $\text{Au/Ce}_4\text{Pr}_1\text{O}_x$  catalysts [183].

**(v) Changes in the support induced by the nanoparticles:** While most of the studies show how different supports affect the metal nanoparticles, also the inverse phenomenon has been observed, where the nanoparticles change the structure of the support. Nanoparticles may catalyze the reduction of the support material, for example resulting in Au on  $\text{SiO}_2$  digging channels into the support, which hinders mobility and sintering of the nanoparticles [184] or Pt nanoparticles catalyzing the reaction of  $\text{Fe}_3\text{O}_4$  lattice oxygen with CO and  $\text{H}_2$ , facilitating diffusion of Fe into the oxide bulk and formation of holes in the substrate [185].

In summary, a wide range of effects exists, due to which the presence of a metal/support interface can alter the reactivity of a whole catalytic system. It is clear, that whenever reactivity

trends in nanocatalysts are discussed, also the support has to be considered. Furthermore, using support-dependent phenomena is a powerful strategy for optimizing existing and engineering new catalyst materials. While most observations of the above effects have been made on supported nanoparticles, they, in principle, also apply to the interfacial regions of bigger supported particles. They are therefore important to consider when studying any supported catalyst and are key to understanding the observations of catalytic H<sub>2</sub> oxidation on supported Rh particles in chapter 6.

---

## Methods and concepts

The studies on catalytic H<sub>2</sub> oxidation on Rh were performed using several surface science experimental techniques, each providing different types of information, which are briefly discussed in the following. Chemical information was provided by x-ray photoelectron spectroscopy (XPS, section 2.1), spatially averaging over mm-sized sample areas, and by scanning photoelectron microscopy (SPEM, section 2.2) with a lateral resolution down to the sub- $\mu\text{m}$ -range. Complementing spatio-temporal kinetic data were obtained by photoemission electron microscopy (UV-PEEM, section 2.3, and X-PEEM, section 2.4) and by low energy electron microscopy (LEEM, section 2.4). Some of the samples used in the present work expose different areas of differing well-defined surface structure, which were characterized by electron backscatter diffraction (EBSD, section 2.5). In addition, the concepts of *kinetics by imaging*, *surface structure libraries* and *correlative microscopy*, which have all been applied in the present thesis, will be presented in sections 2.6, 2.7 and 2.7, correspondingly.

### 2.1 X-ray photoelectron spectroscopy (XPS)

The working principle of x-ray photoelectron spectroscopy (XPS) and scanning photoemission microscopy (SPEM) is based on the *photoelectric effect*, i.e., on the emission of electrons from a surface upon irradiation with electromagnetic radiation. First discovered by Hertz and Hallwachs, where a metal sample emitted photoelectrons upon illumination with UV-light [186, 187], the phenomenon was explained by Einstein in 1905 [188], who was awarded with a Nobel Prize for his work in 1922. The most important equation of his work is the so-called Einstein equation, describing photoemission:

$$E_{kin} = h\nu - \phi - E_B \quad (2.1)$$

where  $E_{kin}$  is the kinetic energy of the emitted photoelectron,  $h\nu$  is the energy of the incident photon,  $\phi$  is the work function of the sample and  $E_B$  is the binding energy of the electron being photoemitted. The work function  $\phi$  of the sample depends on several factors, including the

studied element, the surface structure or adsorbed species and is defined as the energy difference between the Fermi level  $E_F$  of the sample and the vacuum level  $E_{vac}$  (Fig. 2.1a). By illuminating the sample with monochromatic radiation and analyzing the kinetic energy distribution of the emitted photoelectrons, information on the electronic structure of the sample can thus be collected. Plotting the number of photoelectrons at each kinetic energy then yields a photoelectron spectrum.

If now, for example, UV-light is used, the energy of the incident photons is just enough to overcome the work function and the binding energy of the most loosely bound electrons, i.e., electrons in the valence band, and valence band spectra can be obtained by UV photoelectron spectroscopy (UPS). The binding energy of valence band electrons is highly dependent on the chemical environment and the electronic structure of the sample. UPS spectra are therefore hard to interpret quantitatively. Increasing the energy of the incident photons, e.g., by using x-ray radiation, also more strongly bound, i.e., core level, electrons can undergo photoemission. In contrast to the valence band electrons, the variations in the binding energies of core level electrons are much smaller due to shielding by electrons in the outer shells. Therefore, the binding energies of core level electrons are characteristic for each element and allow identification of the elemental composition. The small variations in the core level binding energies still present, in turn, are characteristic for the chemical environment of the studied element, allowing also the detection and interpretation of its chemical state (e.g., metallic or oxidized). Schematic energy diagrams for UPS and XPS and a corresponding resulting schematic XPS spectrum are given in Fig. 2.1.

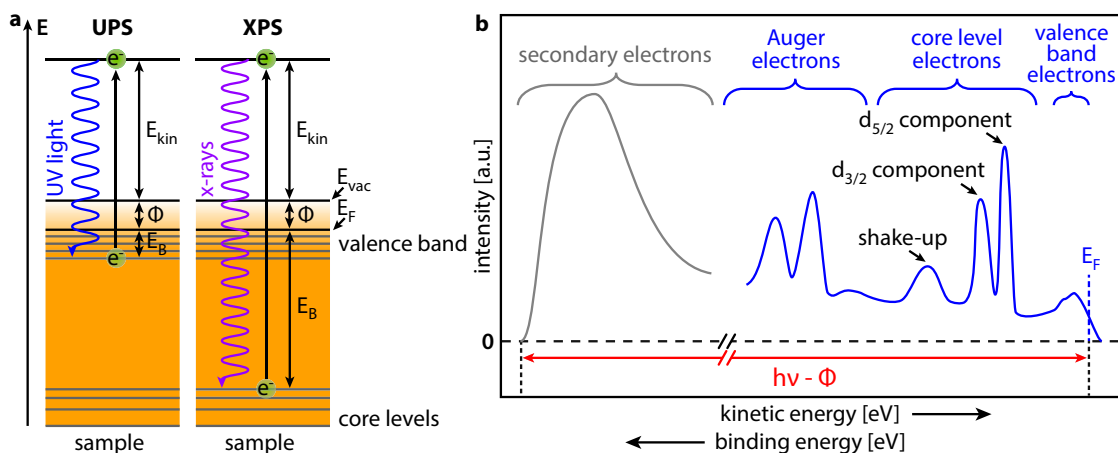


Figure 2.1: The photoelectric effect and its application in UPS and XPS. (a) schematic energy diagrams for the photoemission of electrons by UV-light and x-ray radiation; (b) schematic XPS spectrum.

Besides peaks due to the photoemission of core level or valence band electrons, other features can be present in an XPS spectrum: (i) inelastic scattering of a photoemitted electron can result in the emission of secondary electrons due to the energy absorbed in the scattering process, resulting in a broad and strong signal in the low kinetic energy region of the spectrum; (ii) the hole left behind in the core shell after photoemission of a core level electron can be filled by an electron from a higher energy level, with the energy gain resulting in the emission of a photon, which, in turn, can induce photoemission of another electron. These so-called *Auger electrons*

can easily be identified as their kinetic energy position in the XPS spectrum remains the same even upon changing the energy of the incident radiation, as it only depends on the energy differences between the involved energy levels and the incident radiation only serves the purpose of generating the initial hole; (iii) depending on the source of the x-ray radiation, which in many cases is not (perfectly) monochromatic, satellite peaks can appear in the spectrum due to the minor components present in the x-ray radiation. These satellite peaks always appear at a constant energy difference from the corresponding main photoelectron peaks; (iv) shake-up lines can result from the excitation of another electron in the same atom upon photoemission of a core level electron, resulting in a well-defined energy loss of the photoelectron and an additional component at higher binding energy in comparison to the main photoelectron peak.

Photoelectron peaks of energy levels where the angular momentum quantum number  $l$  of the corresponding orbital is not zero (i.e.,  $p$ ,  $d$  and  $f$  orbitals) in addition show up having two distinct components in the spectrum. This is a result of two energy states existing due to spin-orbit coupling with different probability of occupation. The multiplicity  $M$ , i.e., the occupation probability and thus peak area ratio, of these two components can be described by

$$M = 2(l + s) + 1 \quad (2.2)$$

where  $l$  is the angular momentum quantum number and  $s$  the spin quantum number (i.e.,  $\pm\frac{1}{2}$ ). For  $p$ -type orbitals, this results in a peak area ratio of  $p_{1/2} : p_{3/2} = 1 : 2$ , for  $d$ -type orbitals in a peak area ratio of  $d_{3/2} : d_{5/2} = 2 : 3$  and for  $f$ -type orbitals in a peak area ratio of  $f_{5/2} : f_{7/2} = 3 : 4$ . All these additional features are schematically shown in the XPS spectrum in Fig. 2.1b.

Besides providing qualitative information on the elemental composition and chemical state of the involved elements, XPS can also provide quantitative information. For this, the peak area of the individual spectrum components has to be determined, which in turn can be described by

$$I = n \sigma \lambda f T \phi \quad (2.3)$$

where  $I$  is the total area of the spectrum component, including any satellite or shake-up lines,  $n$  is the atomic concentration of the species corresponding to the spectrum component,  $\sigma$  is the photoionization cross-section for electrons in the orbital corresponding to the spectrum component, i.e., the probability, that an incident photon causes a photoelectron to be emitted,  $\lambda$  is the inelastic mean free path (see below),  $f$  is the incident photon flux,  $T$  is the instrument transmission factor, i.e., the probability that a photoelectron reaching the analyzer will indeed correctly be detected, and  $\phi$  is the angular distribution factor, which depends on the setup geometry, the studied element and the type of orbital. For typical XPS experiments,  $f$  is constant within the experimental timeframe or can be measured,  $T$  as a function of the kinetic energy of the emitted photoelectrons is known for a given analyzer and  $\phi$  can be assumed to be nearly unity (while the variation for gas phase atoms and molecules has been well understood [189], there is not much evidence for significant variation in solids). When calculating elemental compositions from peak area ratios, thus, only  $\sigma$  and  $\lambda$  need to be considered, their product having been tabulated as sensitivity factors in several databases. When only different chemical states of the same element are to be quantified,

even the variations of  $\sigma$  and  $\lambda$  can be neglected, allowing quantification by calculating simple peak area ratios.

Typical x-ray radiation used in XPS penetrates the sample up to several hundreds of nanometers, potentially inducing photoemission. The photoemitted electron, however, can lose energy on its way to the sample surface due to scattering, rendering it useless for energy analysis, as the kinetic energy does not correspond to the originating core level anymore. On average, an electron will inelastically scatter after traveling its inelastic mean free path  $\lambda$  in a material, which is dependent on the material and its kinetic energy and can be described by the *universal mean free path curve*, shown in Fig. 2.2.

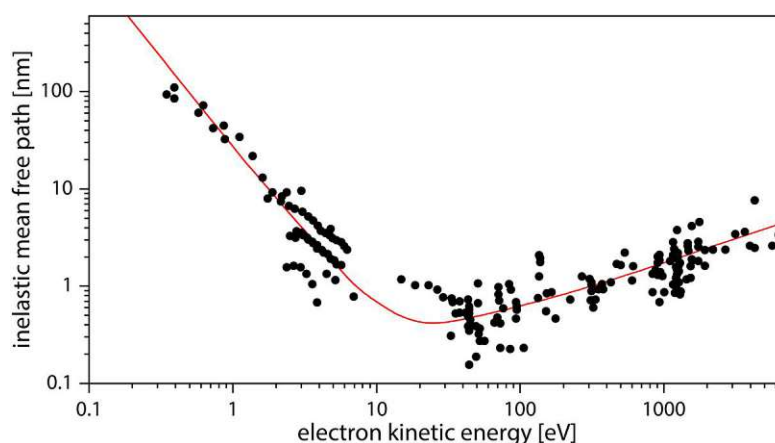


Figure 2.2: The universal mean free path curve. Black circles indicate experimental data, while the red line indicates a least squares fit using the equation  $\lambda = A/E^2 + BE^{1/2}$ , with  $A$  and  $B$  as constants. Reproduced using the data in Ref. [190].

The probability  $P$  of an electron to travel a certain distance without being inelastically scattered can be described by

$$P(d) \propto e^{-\frac{d}{\lambda}} \quad (2.4)$$

where  $d$  is the traveled distance and  $\lambda$  the inelastic mean free path. Therefore, approximately 63% of the useful emitted photoelectrons come from a depth smaller than  $\lambda$ , 86% come from a depth smaller than  $2\lambda$  and 95% come from a depth smaller than  $3\lambda$ . For typical kinetic energies in XPS of several hundred eV, this corresponds to the topmost several atomic layers, making XPS a surface sensitive technique in comparison to other x-ray based techniques (e.g., x-ray fluorescence) and ideally suited to study surface processes. By tilting the sample relative to the entrance of the energy analysis instrumentation, the surface sensitivity can be increased even more.

Although the first report of photoelectron emission due to illumination by x-rays was already recorded in 1907 [191], the first high-energy resolution XPS spectrum was obtained in 1957 by Kai Siegbahn [192], who was also awarded a Nobel prize for his work. Since then x-ray photoelectron spectroscopy, which was originally called electron spectroscopy for chemical analysis (ESCA), has been developed into a powerful surface analysis technique, used in many fields



of science such as biology, catalysis metallurgy, microelectronics, nanotechnology or polymer chemistry.

From an experimental perspective, three main components are necessary for performing XPS: an x-ray source, the sample, and an energy analyzer for determining the energy distribution of the emitted photoelectrons. Several methods for generation of the incident x-ray radiation for XPS exist, with the two relevant to the present work being briefly described. Typical laboratory x-ray sources (Fig. 2.3a) are based on the principle of a hot cathode vacuum tube. The heated cathode (typically a tungsten filament) emits electrons, which are accelerated towards the anode by a voltage of several kV, where they impinge and cause the emission of secondary electrons from the core levels of the anode material. The holes left behind in the core energy levels will get refilled by electrons from outer shells, producing x-ray photons of an energy characteristic for the anode material. Most of the impinging electrons however do not produce an x-ray photon and just cause heating of the anode, necessitating water-cooling. The most commonly used anode materials are Al and Mg, producing Al  $K_{\alpha 1/2}$  and Mg  $K_{\alpha 1/2}$  x-ray radiation with energies of 1486.6 and 1253.8 eV, correspondingly. The second method is the generation of synchrotron x-ray radiation (Fig. 2.3b). In a synchrotron storage ring, high kinetic energy electrons (in the order of several GeV) travel in vacuum along a fixed closed-loop path with relativistic speeds. Travel along the quasi-circular path is ensured by bending the electron trajectories using magnetic fields, which causes the emission of radiation as a direct consequence of the acceleration perpendicular to their direction of motion. Similarly, in insertion devices, which are placed in straight sections of the beam path, spatially periodic magnetic fields exert forces perpendicular to the electron beam path, causing undulating electron trajectories, again generating electromagnetic radiation. The spectrum of the emitted synchrotron radiation is a function of the electron energy and the strength of the used magnetic fields and usually spans several orders of magnitude in terms of wavelength from hard x-rays to visible light and infrared. The desired incident x-ray photon energy for XPS is then selected from the collected synchrotron radiation by a monochromator based on cylindrical x-ray reflective mirrors or curved single crystals [193]. In comparison to laboratory x-ray sources, the brilliance of synchrotron x-ray radiation is higher by several orders of magnitude, allowing shorter data acquisition times, e.g., for studies of dynamic processes, and drastically improved sensitivity. Furthermore, a typical synchrotron x-ray beam is of much smaller size in comparison to illumination by a laboratory x-ray source, making it more suitable for spatially resolved studies, and the monochromaticity is significantly increased, resulting in a smaller linewidth of the observed photoelectron peaks and thus better energy resolution. As a downside, performing research with a synchrotron x-ray source requires a access to a dedicated facility (of which there are only about 65 in the world), while lab-XPS is a standard technique available in nearly any surface science laboratory.

The photoemitted electrons generated from the interaction of the x-ray beam with the sample are then collected and analyzed with respect to their kinetic energy distribution. This is usually done with a hemispherical energy analyzer (HSA), schematically depicted in Fig. 2.3c. The multi-stage electrostatic lens system at the entrance of the HSA serves multiple purposes: First, the size of the sample area and the angular range, from which photoelectrons are collected, can be adjusted. Second, the photoelectron beam is focused onto the entrance slit of the analyzer and

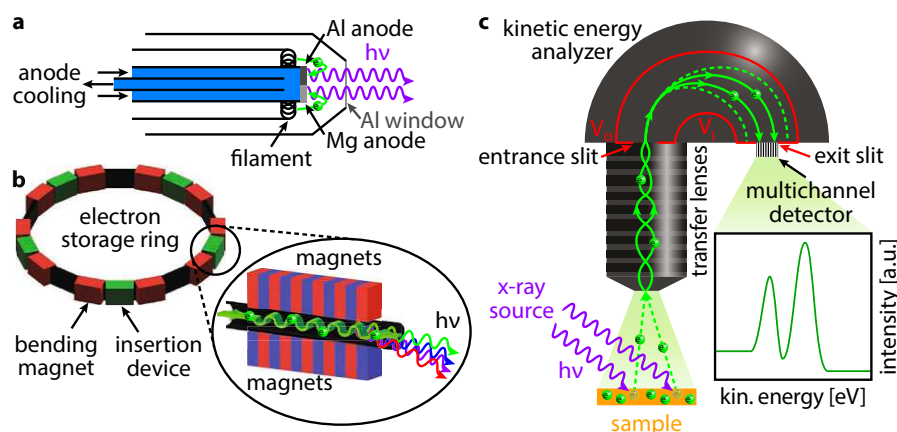


Figure 2.3: Working principles of the essential components of an XPS setup. **(a)** schematic drawing of a laboratory x-ray source; **(b)** schematic drawing of synchrotron x-ray generation; **(c)** schematic drawing of a hemispherical energy analyzer.

third, the kinetic energy of the photoelectrons is adjusted to ensure optimum functioning of the energy analyzer and detector. After passing through the entrance slit, the photoelectrons enter the hemispherical section of the analyzer. Two voltages  $V_i$  and  $V_o$  are applied to the inner and outer hemisphere, forcing the electrons on a semicircular path in the constant electrostatic field. Only electrons having the correct kinetic energy for the chosen voltages  $V_i$  and  $V_o$  will be able to pass through the hemisphere to the exit slit, while electrons having too low kinetic energy will collide with the inner and electrons having too high kinetic energy will collide with the outer hemisphere. Typically the choice of  $V_i$  and  $V_o$  will allow a certain limited range of kinetic energies for electrons, the so-called pass energy in the order of tens of eV, to successfully reach the exit slit. These electrons are separated by their kinetic energy along the so-called energy dispersive axis within the exit slit. Using a multi-channel detector for detecting the number of electrons along the energy-dispersive axis of the analyzer allows quick collection of a “mini-spectrum” spanning several eV in a single snapshot without varying  $V_i$  and  $V_o$ . For bigger energy ranges and better resolution,  $V_i$  and  $V_o$  are varied step-wise and the corresponding numbers of electrons are recorded, forming the XPS spectrum. Two main strategies for detecting the photoelectrons at the analyzer exit exist: The photoelectron current is amplified by a multichannel plate and then either directed onto a fluorescent screen, where the electrons cause the emission of photons, and the image on the screen is recorded by a CCD camera, or the amplified photoelectron current is directly converted to spatially and temporally resolved electric signals in a delay-line detector.

Following from equation (2.1), in order to determine the correct binding energy of the photoemitted electrons, the work function of the sample has to be known, which is hardly ever the case for unknown materials. Therefore, the sample and the energy analyzer are electrically connected, leading to equalization of their Fermi levels. Due to the resulting contact potential, the kinetic energy of the photoelectrons changes during their flight from the sample surface to the entrance of the analyzer exactly by the difference between the samples and the analyzers work function. This allows determining the correct binding energies of the photoelectrons by using the known work function of the energy analyzer and avoids determining the work function of the

sample.

Summarizing, XPS yields chemical information on the sample composition and chemical state of the sample by x-ray illumination and analysis of the photoemitted electrons and is therefore one of the most used surface science techniques. Due to constraints arising from the limited brilliance of laboratory x-ray sources and technical limitations, XPS spectra in lab environments are obtained in a spatially averaging way with only limited lateral resolution (several 100  $\mu\text{m}$  at best). Also most XPS setups operated at synchrotron light sources focus primarily on improving energy and/or time resolution in comparison to lab-XPS, while their lateral resolution remains limited. This makes XPS an ideal technique to study uniform samples but, on its own, not well suited to perform laterally resolved studies on heterogeneous samples. XPS has nonetheless been applied in virtually every area, where surface properties are important, including biomaterials, catalysis, ceramics and glasses, corrosion, micro- and optoelectronics, nanomaterials, polymers and composite materials, thin films and coatings or tribology [194].

## 2.2 Scanning photoelectron microscopy (SPEM)

The working principle of scanning photoelectron microscopy (SPEM) is strongly related to the working principle of XPS. Also in the case of SPEM, the sample is illuminated by x-rays, causing the emission of photoelectrons. Again, their kinetic energy distribution is analyzed, creating XPS spectra. In contrast to conventional XPS, the sample is, however, not uniformly illuminated on a large scale (in the order of several 100  $\mu\text{m}^2$  to several  $\text{mm}^2$ ) but only a tiny sample spot (below 1  $\mu\text{m}^2$ ) is illuminated at any given time by an x-ray micro-probe. A specimen positioning and scanning system then allows recording of XPS spectra for individual spots or grids of spots on the sample surface, creating spatially resolved XPS data.

In order to generate a decent number of photoelectrons, which allows reliable detection and quantification, from such a small illuminated sample area requires a high brilliance x-ray source. Therefore, SPEM is only possible at synchrotron light sources. All SPEM studies in the present work have been performed at the “ESCA Microscopy” beamline at the Elettra Synchrotron in Trieste, Italy, which has been described in detail in Ref. [195] and will be summarized below.

The “ESCA Microscopy” beamline uses an undulator photon source (briefly described in section 2.1) shared with another beamline, which provides radiation in the range of 100-1500 eV. The emitted synchrotron radiation travels through a section common for both branch beamlines, including beam position monitors for diagnostic purposes and a feedback-controlled slit system to keep the photon beam centered on its way to the experimental chamber. A switching mirror then allows switching between the two branch beamlines, followed by a prefocusing chamber, the monochromator and the experimental chamber. The purpose of the prefocusing chamber is to focus the photon beam with a toroidal mirror into the entrance slit of the monochromator along the sagittal plane and into the exit slit of the monochromator along the tangential plane. Monochromatization of the photon beam is then achieved by using a spherical grating monochromator, having two selectable gratings with 600 and 1200 grooves/mm. By varying the exit slit size of the monochromator, the photon beam can be tailored to the right conditions for sample illumination, where increasing the width of the exit slit results in higher photon flux but wider

photon energy distribution and vice versa.

The experimental end station consists of several UHV sub-chambers, one for introducing the sample into vacuum via a fast-entry lock, one for sample preparation and one hosting the SPEM itself. The SPEM is based on three main components: (i) an optic system, which provides the x-ray micro-probe, (ii) a specimen positioning and scanning system and (iii) a hemispherical energy analyzer (HSA) equipped with a multi-channel detector, which are shown in a schematic drawing in Fig. 2.4a. The optic system consists of a zone plate (ZP) and a pinhole serving as order-selecting aperture (OSA). The zone plate, manufactured by gold coating a thin  $\text{Si}_3\text{N}_4$  membrane, comprises a set of alternating opaque and transparent concentric rings (Fresnel zones). Due to spacing the Fresnel zones in a specific way, the incident x-ray beam is diffracted and the diffracted x-rays exhibit constructive interference only at specific focus points. As typical for diffraction-based systems, several focus points exist for the several possible diffraction orders. Only the first order diffracted x-ray beam is used for illuminating the sample, selected by the OSA, providing an x-ray micro-probe having a diameter in the sub- $\mu\text{m}$  range (150 nm in the present case [195]). The specimen positioning and scanning system, including a sample stage, stepper motors for coarse positioning (accuracy of  $\sim 5 \mu\text{m}$ ) and piezoelectric motors for fine positioning (accuracy of  $\sim 0.1 \mu\text{m}$ ), allows positioning the sample in front of the x-ray micro-probe and selecting the precise spot on the sample surface being illuminated, allowing spatially resolved studies with a resolution in the sub- $\mu\text{m}$  range. By raster-scanning over the sample surface and recording a data point for each of the grid-points, even synthetic images can be produced. As already mentioned above, SPEM is closely related to XPS, i.e., also here the energy distribution of the photoemitted electrons is analyzed, which is achieved by the HSA. The working principle of such an analyzer is detailed in Fig. 2.3c. Due to the highly monochromatic x-ray illumination an energy resolution of  $\sim 0.3 \text{ eV}$  is typically achieved in the SPEM used in the present work [196].

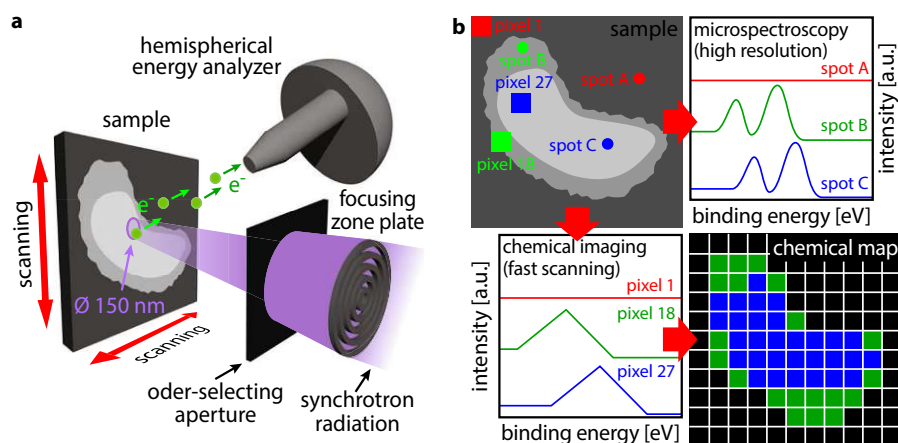


Figure 2.4: The working principle of SPEM. **(a)** schematic illustration of the essential components of a SPEM; **(b)** the SPEM micro-spectroscopy and spectromicroscopy modes.

The SPEM can be operated in two fundamentally different modes, which are shown in Fig. 2.4b. In the microspectroscopy mode, individual micro-spots on the sample surface are selected, the sample is positioned accordingly by the positioning and scanning system and a high-resolution XPS spectrum is collected for each micro-spot by scanning through the desired spectrum energy

range with the HSA. This provides the possibility to perform high-resolution XPS in a laterally resolved way, but each spectrum takes several minutes to record. In contrast, in the imaging mode, the sample surface is mapped pixel by pixel by raster-scanning with the positioning and scanning system, while for each micro-spot only a single snapshot from the multi-channel detector is collected with the HSA remaining set at a constant kinetic energy. Due to the analyzer pass energy of several tens of eV and the multi-channel detector along the energy dispersive axis of the detector, this nonetheless allows collecting a “mini-spectrum” for each micro-spot. Acquiring such a “mini-spectrum” only takes below 100 msec, and typical 64 x 64 pixel maps can be recorded in several minutes. Of course, the energy resolution and quality of each “mini-spectrum” is significantly reduced in comparison to spectra obtained in the micro-spectroscopy mode, but nonetheless allows discerning different chemical species [197]. By processing the “mini-spectra” for each pixel in one or several subsequently obtained raster-scans, chemical maps, spatial profiles and spectral time series can be created.

In summary, SPEM is a scanning electron microscopy technique based on electrons photoemitted due to x-ray illumination. It can provide both chemical information due to the information encoded in the photoelectron spectra and, in contrast to typical laboratory XPS, lateral resolution in the sub- $\mu\text{m}$  range. As a result, SPEM has been used in the last decades to study a broad variety of both individual nano-objects, e.g., catalyst particles [198], and mesoscopic structurally heterogeneous samples, e.g., individual domains of polycrystalline foils (showcased, e.g., in chapters 3 and 5). By using the SPEM as a catalytic flow reactor, even *in situ* studies of ongoing reactions can be performed (shown, e.g., in chapter 3). Due to its working principle being closely related to XPS, SPEM can be applied wherever XPS is a suitable technique, provided that the additional lateral resolving power suits the specific problem.

## 2.3 UV photoemission electron microscopy (UV-PEEM)

Similar to XPS and SPEM, UV photoemission electron microscopy (UV-PEEM) is also based on the photoelectric effect. The sample is illuminated by UV-light, causing the photoemission of valence band electrons. In contrast to XPS and SPEM, however, not their kinetic energy is analyzed, but an electrostatic lens system is used to form a magnified image of the sample projected onto a multichannel plate and then a fluorescent screen. As detailed in section 2.1, most of the photoemitted electrons will inelastically scatter on their way to the sample surface. While these electrons are lost for spectroscopic purposes because of the change in their kinetic energy, they still can be used for UV-PEEM imaging, since the UV-PEEM image brightness depends only on the number of photoemitted electrons.

The total number of photoelectrons emitted from a given sample area can be described by the Fowler theory [199], yielding the following expression

$$j \propto (h\nu - \phi)^2 \quad (2.5)$$

where  $j$  is the photoelectron flux,  $h\nu$  the energy of the incident UV-light and  $\phi$  the local work function of the respective sample area. As a result, the number of photoemitted electrons (and

thus the UV-PEEM image brightness) is a very sensitive probe for the local work function and its changes. The working principle of UV-PEEM and its contrast formation are illustrated in Fig. 2.5a. The schematically depicted sample consists of three regions exhibiting three distinct work functions  $\phi_A$ ,  $\phi_B$  and  $\phi_C$ . The photoemission spectra for exemplary points within those three regions differ not only in their width, but also in their overall area (i.e., the total number of photoemitted electrons differs, as per the Fowler theory). As a result, three areas of different brightness are formed in the UV-PEEM image.

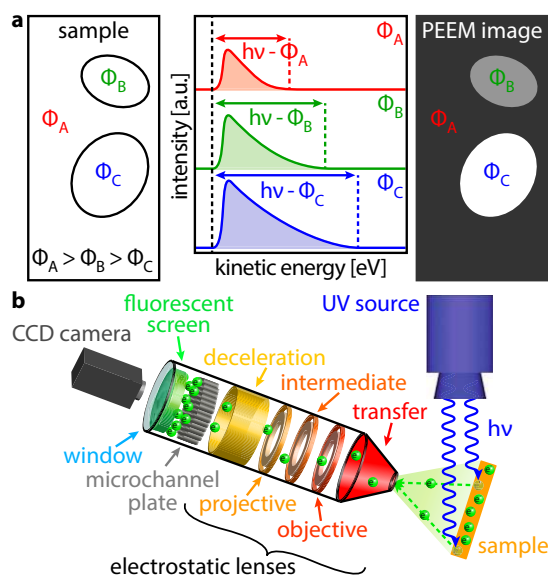


Figure 2.5: The working principle of UV-PEEM. **(a)** schematic illustration of the UV-PEEM working principle and contrast formation; **(b)** schematic drawing of a UV-PEEM.

The first report of photoelectrons being used to image a metal surface stems already from the 1930s [200], but only the development of UHV compatible systems 60 years later enabled applying the concept to surface science [201]. A typical UV-PEEM setup comprises three essential components: A UV-light source, the sample and the PEEM instrument itself, schematically depicted in Fig. 2.5b. Typical light sources include mercury or deuterium gas-discharge lamps with maximum energies of 4.9 eV and 6.8 eV, respectively, while the sample is illuminated at angles of around 60 to 75° from the surface normal. The sample is placed a few millimeters away from the entrance cone of the PEEM instrument, with the surface normal aligned with the optical axis. The electrostatic lens system of the PEEM typically consists of five lenses: The transfer lens acts as anode for the photoemitted electrons, accelerating them away from the sample and into the lens column. The objective, intermediate and projective lenses then form a magnified real image of the sample surface. Depending on the specific set of lens voltages, the system works either as a two lens (intermediate lens at similar voltage as the transfer lens, low magnification mode) or as a three lens system (intermediate lens at voltage close to ground level, high magnification mode). As the number of emitted photoelectrons is too low to directly form a usable image, the photoelectron current has to be amplified by a multichannel plate acting as image intensifier. As the sensitivity of the multichannel plate is highest for electrons impinging with a kinetic energy between 200 and 2000 eV, a drift tube (the deceleration lens) is used to decrease

the photoelectron kinetic energy to be within that range before amplification. After amplification of the photoelectron current, the electron beam is directed at a fluorescent screen, converting the electron image to visible light. The screen is then monitored from outside the vacuum system by a high-speed CCD camera, which can be used to record images and videos of the sample surface and any ongoing processes (e.g., adsorption, oxidation or chemical reactions), provided there are differences in the local work function and therefore image contrast.

Since its development, UV-PEEM has been used to *in situ* study a wide range of dynamic processes, including adsorption, diffusion or layer growth [202, 203]. UV-PEEM has also successfully been applied in catalysis for imaging ongoing surface reactions, with the first examples being related to CO oxidation on Pt and Pd single crystal surfaces [204–206] and the most prominent example probably being the oscillating reaction mode of CO oxidation on Pt by Gerhard Ertl [207]. Summarizing, UV-PEEM is a very powerful technique for imaging ongoing surface processes, demonstrated, e.g., in chapters 4, 5 and 6). The spatial resolution is typically in the range of several  $\mu\text{m}$ , while the temporal resolution is only limited by the sensitivity and maximum frame rate of the CCD camera and the decay time of the fluorescent screen. In contrast to XPS and SPEM, UV-PEEM does not provide any direct chemical information, but rather just work function differences, which, however, can often be related to the chemical state of the surface (see section 2.6). On the other hand, the temporal resolution of UV-PEEM is significantly improved in comparison to SPEM due to the parallel imaging principle of UV-PEEM in contrast to the scanning imaging principle of SPEM.

## 2.4 Low energy electron microscopy (LEEM) and x-ray photoemission electron microscopy (X-PEEM)

Similar to UV-PEEM, both, low energy electron microscopy (LEEM) and x-ray photoemission electron microscopy (X-PEEM), are two surface science microscopic imaging techniques based on the parallel imaging principle. They are, in fact, so similar from a technical viewpoint, that often all three microscopies are combined in a single experimental setup and can be used for correlative microscopy studies (section 2.8). The contrast mechanism, and thus the information encoded in the recorded images, is, however, fundamentally different for the three techniques: In the LEEM mode of the instrument, the sample is illuminated by a beam of low energy electrons (kinetic energy in the range of several eV), which will be elastically backscattered at the sample surface and undergo backscatter diffraction in case of crystalline samples. An aperture is then used to select either the specularly reflected electrons (bright field imaging) or one of the diffracted electron beams (dark field imaging), which is accelerated and used for further imaging. A multi-stage lens system provides a magnified image of the backscattered electrons on a multichannel plate image intensifier, which amplifies the electron current. The electrons exiting the multichannel plate form an image on a fluorescent screen, which is monitored by a CCD camera. The dominating diffraction contrast in LEEM is caused by non-uniform diffraction within the specimen, e.g., due to different surface structure, surface composition or adsorbates present at the surface [208]. For otherwise uniform samples, however, also geometric phase contrast due to the different optical path length of electrons reflected from two terraces next to a step edge

(Fresnel diffraction), may play a significant role and allows imaging, e.g., atomic steps [209]. Especially in thin film samples, also quantum size contrast can be observed, i.e., contrast due to the interference of electrons reflected from the parallel top and bottom faces of the thin film [210].

In the UV-PEEM mode, the sample is illuminated by UV-light and the photoemitted electrons are used for imaging by the same electron optical and detection system as in the LEEM mode. The image contrast has in detail already been described in section 2.3 and is provided by the different number of secondary electrons generated for areas of differing work function.

In the X-PEEM mode, the sample is illuminated by monochromatic x-rays and again the photoemitted electrons are used for imaging by the same electron optical and detection system as in the other two modes. The addition of a kinetic energy filter before the imaging optics, however, now allows selecting only photoelectrons of specific kinetic energy to be used for imaging. As the kinetic energy distribution of the photoelectrons depends on the sample composition and chemical state (section 2.1), by using a suitable kinetic energy window, the X-PEEM image contrast results from variations in elemental composition or chemical state.

The LEEM and X-PEEM studies in the present work have been performed using the “Spectromicroscope for All Relevant Techniques” (SMART), currently operating at the synchrotron light source BESSY-II of the Helmholtz Center Berlin, which has in detail been described in literature [211, 212], no studies using the UV-PEEM mode of the instrument were conducted. A brief summary of the essential features is given below, along with a schematic drawing in Fig. 2.6.

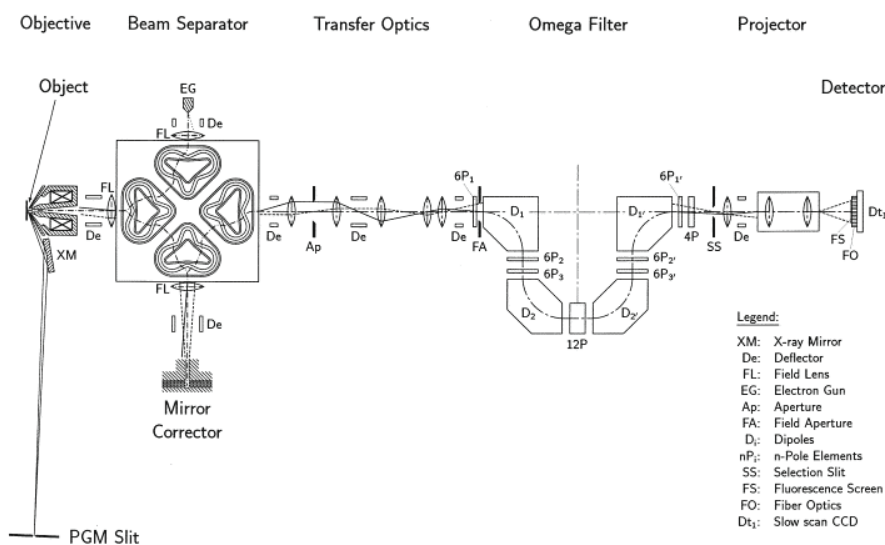


Figure 2.6: Schematic layout of the “Spectromicroscope for All Relevant Techniques” (SMART). Reproduced from Ref. [211] with permission of Elsevier BV. Permission conveyed through Copyright Clearance Center, Inc.

In the LEEM mode, the electron beam is provided by an electron gun (EG, beam separator section of the drawing) and illuminates the sample via the magnetic beam separator (square unit, beam separator section), two electrostatic field lenses (FL, one before and one after the beam separator) and the objective lens (objective section). In X-PEEM mode, the sample is illuminated by monochromatic soft x-rays in the energy range between 100 and 2000 eV, provided by an



undulator synchrotron radiation source (see section 2.1) in combination with a monochromator comprising two cylindrical mirrors, one plane mirror, one sphere mirror and a grating [212]. The x-ray beam from the monochromator (PGM slit, objective section) is projected onto the sample by a plane mirror (XM, objective section), illuminating an area of about  $5 \times 10 \mu\text{m}^2$  at an angle of  $70^\circ$  from the surface normal. The objective lens is designed as an electrostatic-magnetic compound lens using the sample as a cathode and, on one hand, provides illumination with low energy electrons in LEEM mode, while, on the other hand, also focuses the photoemitted, diffracted or reflected electrons onto the entrance of the magnetic beam separator. The magnetic beam separator provides both separation of incident and reflected/diffracted beams in LEEM mode and, in combination with the electrostatic tetrode mirror (mirror corrector, beam separator section), correction of spheric and chromatic aberrations of the objective lens. After the beam separator, a transfer system follows, consisting of five electrostatic lenses (transfer optics section), forming a magnified real-space image of the sample and a demagnified image of the electron diffraction pattern at two different positions in front of the imaging electron analyzer (omega filter section). The imaging electron analyzer consists of an omega-shaped configuration of dipole magnets ( $D_1$ ,  $D_2$ ,  $D_2'$  and  $D_1'$ , omega filter section) and can be used to select photoelectrons of certain kinetic energy for imaging in X-PEEM mode or inelastically scattered and secondary electrons in LEEM mode. Several sextupole magnets are used for correction purposes ( $6P_1$ , omega filter section). The final projection and magnification is provided by a three-lens system (projector section), projecting either the real-space image or the electron diffraction pattern onto the two-dimensional detector comprising a multichannel plate, a fluorescent screen (FS, detector section) and a CCD detector ( $Dt_1$ , detector section). Due to the possibility to change the focal length of the projector system, also structural analysis by low energy electron diffraction (LEED) of selected small sample areas can be performed. For this, the first focal point of projector system is adjusted to the diffraction plane instead of the real space image plane, resulting in the electron diffraction pattern being imaged on the screen and CCD detector. Several deflection elements ( $De$ ) along the electron path in the microscope allow for correction and, in combination with several apertures ( $Ap$ , transfer optics section;  $FA$  and  $SS$ , omega filter section), selecting limited sample areas for imaging and diffraction or performing dark-field imaging.

Since its development in the 1980ies [209], LEEM has been used to study a wide range of surface processes, including surface phase transitions, adsorption, diffusion, crystal growth or chemical reactions [208, 209, 213]. Due to the smaller energy distribution of the electrons used for imaging, the spatial resolution in LEEM is significantly better than in UV- or X-PEEM, resulting from the reduced chromatic aberration, and a spatial resolution of 2.6 nm can be achieved by the SMART in LEEM mode [214]. In addition, no work function differences are necessary for the image contrast, allowing also studies of processes where the work function does not change significantly. The combination with chemical information, which can be obtained in X-PEEM mode (resolution of 18 nm, [215]), and local surface structure determination by LEED allows powerful correlative studies of various surface processes in real time in a single experimental setup, showcased, e.g., in chapter 4.

## 2.5 Electron backscatter diffraction (EBSD)

In order to study effects of the catalyst atomic structure on its catalytic properties, often a sample consisting of different areas of differing atomic structure is studied (i.e., a surface structure library is used, section 2.7). Before studying the catalytic properties, it is therefore necessary to characterize the sample with respect to its atomic structure. For polycrystalline foils, which have partly been used as samples in the present work (see chapters 3, 4 and 5), electron backscatter diffraction (EBSD) can provide such analysis.

EBSD allows obtaining crystallographic information from small volumes of material by directing a focused electron beam at the sample surface, e.g., in a scanning electron microscope (SEM), as schematically illustrated in Fig. 2.7. Due to the interaction with the sample surface, some of the impinging electrons will be backscattered from the sample. These electrons can be collected by a detector, typically comprising a scintillator screen coupled to a photon sensitive imaging detector (e.g., a CCD camera), where they form an electron backscatter diffraction pattern. Usually, the sample is highly tilted ( $60^\circ$  to  $80^\circ$ ) with respect to the detector in order to reach the best possible pattern contrast. Each backscatter diffraction pattern, which can then be observed on the imaging detector, consists of many pairs of bright and dark lines, termed Kikuchi bands, which correspond to each of the diffracting crystal lattice planes [216, 217]. These bands are the backscattered equivalent of Kikuchi bands that can also be observed in a transmission electron microscope, initially discovered in 1928 when studying the diffraction of electrons passing through a thin film of mica [218]. The patterns are then transferred from the camera to a computer for indexing and determination of the crystallographic orientation of the volume illuminated by the incident electron beam.

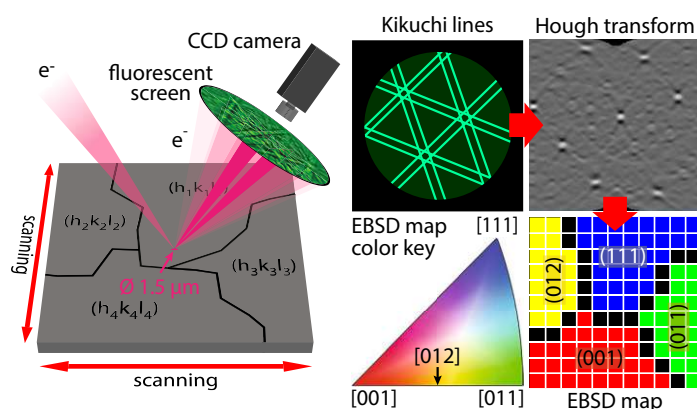


Figure 2.7: The working principle of EBSD. By raster-scanning the sample with a focused electron beam and analysis of the electron backscatter diffraction patterns maps of the sample crystallography can be created.

Briefly, the line pattern is transformed to a point pattern by Hough transform [219], as points can more easily be located by automated image processing routines than lines. With knowledge of the experimental geometry, the locations of the peaks in the Hough transform image are then converted to a table of interplanar angles and automatically compared to look-up-tables of expected angles in order to identify the crystallographic orientation of the illuminated sample

volume. By raster-scanning the focused electron beam over the sample surface and determination of the crystallographic orientation from each backscatter diffraction pattern, EBSD maps of the sample crystallography can then be constructed.

The first recordings of large-angle electron backscatter Kikuchi diffraction patterns used film directly exposed to the backscattered electrons and date from 1954 [220]. In the 1970s the technique was first implemented in a SEM, using either film within the experimental chamber or an externally mounted film camera and it was demonstrated, that the patterns correspond to the orientations of micro-crystals selected with the scanning electron beam [221–223]. Further improvements were made to the camera design and methods were devised for systematic analysis of diffraction patterns recorded from the seven crystal systems [224]. Initially, the recorded data had to be evaluated by hand, but by the development of low-light-level digital cameras and increasing computational power allowed increasing the throughput in pattern indexing and orientation measurements. By adding computer control of the SEM beam position and image processing routines, fully automated EBSD mapping became possible [219, 225]. Since then, EBSD has become a commonly used technique to study crystalline or polycrystalline materials, e.g., in metallurgy to understand recrystallization or grain-growth processes [226, 227], in electrochemistry, where the local micro-structure was correlated with electrochemical properties [228], or in catalysis, where structural features were correlated with catalytic properties [108, 229, 230].

## 2.6 The kinetics by imaging approach

As already discussed in section 1.7 for catalytic H<sub>2</sub> oxidation on Rh, surface reactions can typically be in different states of catalytic activity depending on the chosen set of external parameters. Routinely, e.g., mass spectrometry (MS) is applied to measure the consumption of reactants and presence of reaction products in order to determine the state of catalytic activity. The downside of this approach is, however, that it only yields data spatially averaging over the whole sample. While this is not a problem for homogeneous samples such as single crystal surfaces or for determining the overall catalytic activity of powder catalysts in a test reactor, spatially heterogeneous samples can not be analyzed with respect to the local catalytic activity using this approach. To mitigate these issues, scanning MS has been developed [231], where a small nozzle is used to allow only gas molecules from a certain defined sample area to enter the mass spectrometer and the nozzle can be moved over the sample surface for raster scanning. Even though this approach is a huge improvement in comparison to spatially averaging over the whole sample, parallel measurements of several sample regions are not possible due to the scanning working principle and the spatial resolution is still quite low due to the high mobility of gas atoms, so reactants and products from neighboring sample areas will still enter the nozzle to some extent.

One way to overcome these limitations is to use a chemically sensitive microscopy technique, ideally based on a parallel imaging principle (e.g., LEEM, UV- or X-PEEM) or with a scanning time significantly faster than the studied surface processes (e.g., SPEM). In all cases, some physical quantity characteristic for the surface coverage is imaged: In LEEM, the local image brightness is dependent on the local diffraction of the sample surface [211], which is locally modified by the presence and amount of adsorbates on the sample surface. In UV-PEEM, the

local image brightness is dependent on the local work function of the surface, which is, again, determined by the adsorbates on the sample surface [232]. In X-PEEM, the local image brightness corresponds to the number of photoelectrons emitted within a certain kinetic energy range. Thus the local presence and intensity of certain adsorbate-induced XPS spectrum components gives rise to the image contrast if a suitable kinetic energy window is chosen. Similarly, in SPEM, the local presence of such spectral components is represented in the signal of some of the energy channels of the multi-channel detector for the corresponding image pixels.

Following from the Langmuir-Hinshelwood kinetics of catalytic  $H_2$  oxidation on Rh (section 1.6), the surface adsorbate coverage will, in turn, determine the state of catalytic activity: A surface covered primarily by adsorbed oxygen will be in the catalytically inactive state due to the impeded hydrogen adsorption, while a nearly adsorbate-free or hydrogen covered surface will be in the catalytically active state. Therefore, the detector signal of all of the above-mentioned techniques can directly be linked to the state of catalytic activity via the adsorbate coverage. As this relationship holds true for each of the individual pixels in a microscopy image, analysis of images and video-sequences allows the determination of the local reaction kinetics from the local detector signals.

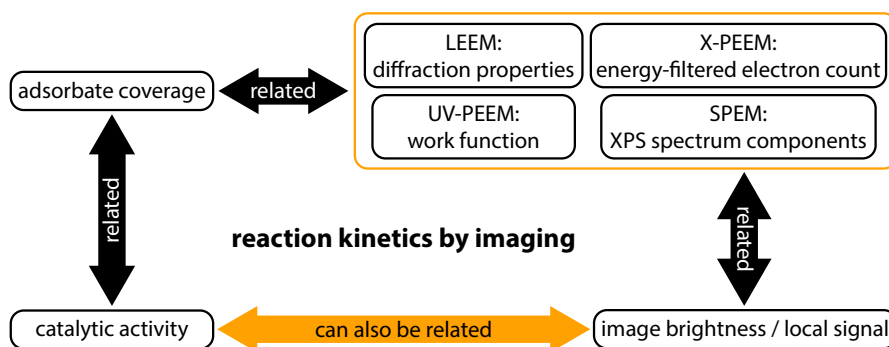


Figure 2.8: The kinetics by imaging approach. The catalytic activity can directly be deduced from a suitable microscopy detector signal (e.g., image brightness or spectrum component intensity) as both result from the specific adsorbate coverages of the catalyst surface.

This local reaction kinetics by imaging approach (Fig. 2.8), developed by Suchorski and Rupprechter [233, 234], has successfully been applied to *in situ* study several surface reactions on various platinum group metals, e.g., CO oxidation on Pd and Pt surfaces [86, 235] or CO [87] and  $H_2$  oxidation on Rh [236]. For catalytic  $H_2$  oxidation, recently a number of spatio-temporal phenomena was detected using this approach: Multifrequential oscillations in  $\mu\text{m}$ - [108] and nm-sized [109] systems, frequency transformation by grain boundaries [114] and atomic rows [109], coexisting multi-states (chapter 3) and nm-scale reaction pacemakers [110]. The approach also appears promising for studying individual catalyst particles in supported catalyst powder samples (see chapter 6). In summary, the kinetics by imaging approach provides access to local kinetic data by using the detector signal in microscopic techniques for determining the local surface coverages and thus local catalytic activity. While the resulting data is lacking quantitative information (e.g., turnover frequencies), the combination with techniques providing such information

(e.g., scanning MS) appears to be promising, and important quantitative information (e.g., kinetic transition points, see section 1.7) can be determined by applying the kinetics by imaging approach.

## 2.7 The surface structure library concept

In heterogeneous catalysis, the rate of the catalytic reaction rate depends on various parameters. This, on one hand, includes external parameters (e.g., temperature or reactant pressures) and, on the other hand, properties of the catalyst itself. Of course, the choice of the catalyst material plays a decisive role, while often also size of the catalytically active particle or the atomic structure of the catalyst is of great importance. For example, the low-Miller-index densely packed surfaces are often less active than high-Miller-index surfaces (i.e., surfaces having step edges and kinks and thus low-coordinated surface atoms) of the same material. This structure-dependence has been demonstrated for many heterogeneous catalytic reactions in various surface science studies [237–239].

In order to assess such structure dependence of the catalytic properties, experiments at identical conditions have to be performed for a set of differently structured catalyst surfaces. Typically, surface science experiments are performed on structurally well-defined catalyst surfaces and often on homogeneous single crystal surfaces. Usually, several such samples are measured in sequence for this purpose, inherently making it difficult to achieve the necessary identicalness of the external parameters. If instead a structurally heterogeneous sample, with different areas of well-defined known surface structures, is composed and used in combination with a spatially resolving technique, these problems are overcome, as each part of the sample is at inherently identical conditions and the microscopy technique still allows monitoring each of the individual areas of the sample, often even simultaneously.

Such a sample then acts as a kind of “surface structure library” [240]. Various kinds of such surface structure libraries exist: Already in 1992 a cylindrical Pt crystal was used to investigate the structure sensitivity of CO oxidation on Pt [241] as such a cylindrical sample has a systematic arrangement of surface structures and varying step and kink densities ordered along the line of curvature. Combining two samples cut from a Ag(111) single crystal along two different axes allowed studying the effects of step edges, different step edge structures and kinks on the electronic properties of different Ag surfaces [242]. In order to cover a wider range of surface structures, dome-shaped crystal samples can be prepared by cutting along two orthogonal axes of the same single crystal. Using a set of six dome-shaped crystals, prepared to represent a complete surface structure library (i.e., including all possible surface orientations), the oxidation of different Cu surfaces was systematically studied [243, 244]. All these surface structure libraries nonetheless often require studying a number of several samples to cover the entire range of possible surface structures. By fabricating a hemispherical tip-shaped curved crystal specimen with a radius of curvature in the nm- to  $\mu\text{m}$ -range, all possible surface structures are present in a single sample. This approach was, e.g., used to study the oscillating catalytic  $\text{H}_2$  oxidation Rh and allowed discovering structure-dependent oscillation behavior [109] or regions of well-defined surface structure acting as pacemakers for the oscillations [110].

Another approach for combining several surface structures in a single sample is the use of polycrystalline foils as surface structure libraries. In contrast to cut single crystals or hemispherical apexes of tip-shaped specimens, the surface structures present in polycrystalline foil samples are not systematically arranged but rather randomly distributed among all possible surface structures. A polycrystalline foil is, however, typically flat and thus readily accessible by all surface science techniques, while curved samples often pose experimental problems, especially in combination with microscopic techniques. Using such polycrystalline foils, with the atomic structure of the individual domains beforehand characterized by EBSD (section 2.5), for example the structure-sensitivity of the oscillating  $\text{H}_2$  oxidation reaction on Rh [108, 114], the kinetic transition points in CO oxidation [87], the simultaneous presence of different states of catalytic activity in  $\text{H}_2$  oxidation on Rh (see chapter 3) or the anisotropy of Rh surface oxide formation (see chapter 5) have been probed.

The concept can then also be extended towards more realistic systems, e.g., differently sized catalytically active particles on different support materials, which can then simultaneously be studied. A sample can, e.g., be composed from different support materials (e.g., different metal or oxidized metal foils) and the powdered catalytically active metal, having a certain particle size distribution, can be deposited onto this combined sample, turning it into a particle size and support materials library. Using such a sample, particle size and interface effects can be studied (see chapter 6) and the importance of metal/oxide interfaces for the catalytic properties has been demonstrated for  $\text{ZrO}_2$ -supported Pd agglomerates in CO oxidation [245] or  $\text{ZrO}_2$ -supported Rh agglomerates in  $\text{H}_2$  oxidation [246].

In summary, the surface structure library concept allows eliminating one of the crucial problems of the traditional sequential-analysis approach for studying effects of the catalyst structure, size or support material on its properties. By combining several known surface structures, particle sizes or support materials into a single sample, all parts of the sample can be studied at inherently identical conditions, enabling direct comparison of the results. The power of this approach has been demonstrated for a wide range of catalysts and catalytic reactions and was widely employed in the present work.

## 2.8 Correlative microscopy

As detailed in sections 2.1 to 2.5, discussing the experimental techniques used in the present work, each of these yields different kinds of information. In order to fully understand the observed phenomena, often using a single experimental technique is not enough and a combination of several techniques is necessary. If the same phenomena on the same areas of the same samples are studied under identical conditions, ideally in the same experimental setup and even simultaneously, the results can directly be compared and correlated, giving the full picture of the studied processes.

While using several, e.g., spectroscopic, diffractive or imaging techniques on the same or identically prepared samples and combining their information is common practice in catalysis [247–249], using several microscopic techniques in a correlative way originally stems from biology. Already in the 1970ies the first efforts were made to study the same cell/tissue structures by cor-

relative light and electron microscopy (CLEM) in a correlative microscopy approach [250, 251]. In the meantime, CLEM was developed into a broad range of methods, where various types of light and electron microscopies are combined and used on the same sample [252]. Also other imaging techniques, such as atomic force microscopy (AFM), x-ray tomography and scanning electron microscopy (SEM) have successfully been used for correlative microscopy [253, 254]

In the last decades, correlative microscopy has also been applied in materials research, where correlative information from microscopic volumes of the studied material can be obtained by using, e.g., transmission electron microscopy (TEM) and atom probe tomography (APT) [255] or Raman microscopy and SEM [256, 257]. The approach has also made huge impact in catalysis [258], where, e.g., APT and scanning transmission x-ray microscopy (STXM) were combined to study elemental distributions in industrial zeolite catalysts [259], APT and SPEM were combined to study oxygen evolution reaction catalysts for use in fuel cells [260] or optical microscopy was combined with confocal and x-ray fluorescence microscopy to study aging of catalysts for fluid catalytic cracking [261].

One of the most crucial points to consider when performing correlative microscopy studies in different experimental setups is the possible changes in the sample induced by transferring the sample through air between the experiments. Therefore, rigorous and tested cleaning procedures are necessary. Also, protective coatings have been developed to assure identical conditions before and after the sample transfer [260]. Such problems can also be overcome by performing the experiments using different microscopies within the same experimental setup. In the ideal case, the different microscopies are even applied simultaneously, as then perfect comparability of the obtained results is inherent to the experiment. Due to the involved complexity, reports from this supreme discipline of correlative microscopy, are, however, scarce. For example, TEM and single-molecule fluorescence (SMF) were combined to study catalysts for fluid catalytic cracking simultaneously in a single experimental setup [262].

Catalytic reactions on Rh, e.g., H<sub>2</sub> oxidation or NO reduction, have previously been studied by correlative microscopy using LEEM and UV-PEEM [263], LEEM and X-PEEM [264] or PEEM and SPEM [265], in all cases using alkali metals as promoters, as well as by PEEM and metastable impact electron emission microscopy (MIEEM) [266] or field electron microscopy (FEM) and field ion microscopy (FIM) [109]. In the present work, combinations of UV-PEEM, X-PEEM and LEEM (see chapter 4) or UV-PEEM and SPEM (see chapter 6) were used to image several aspects of catalytic H<sub>2</sub> oxidation on Rh in a correlative way.





---

# Coexisting multi-states in catalytic hydrogen oxidation on rhodium

Catalytic hydrogen oxidation on rhodium may exhibit kinetic oscillations even at constant external parameters, as detailed in section 1.8. These oscillations were first observed on Rh nanotips under the influence of strong electric fields [107], on bimetallic Rh/Ni catalysts [104, 105] and just recently on individual domains of a polycrystalline Rh foil [108, 114] and Rh nanotips under field-free conditions [109, 110]. Most of these studies were however lacking direct chemical information during the ongoing oscillations and thus direct experimental evidence for the feedback mechanism of the oscillations. Therefore, studies of the catalytic hydrogen oxidation on a polycrystalline foil used as a surface structure library (section 2.7) were performed using scanning photoelectron microscopy (SPEM, section 2.2) in the  $10^{-6}$  mbar pressure range, yielding spatially resolved chemical information. Besides giving spectroscopic indications for the formation and depletion of subsurface oxygen acting as feedback mechanism for the oscillations, a previously unknown coexistence of all different states of catalytic activity at the same external parameters was observed in the experiments. Simultaneously, some domains of the polycrystalline foil were constantly in the catalytically active state, while others exhibited kinetic oscillations, exposing different oscillation frequencies, and some even remained in the catalytically inactive state. This highly unusual behavior could be explained on the basis of peculiarities of the formation and depletion of subsurface oxygen in relation to the atomic structure of the respective surfaces, which was previously determined by electron backscatter diffraction (EBSD, section 2.5), and demonstrated the general possibility of multi-states in a catalytic reaction. The experimental findings could be supported by micro-kinetic model simulations.

The results of these studies were published in *Nature Communications* as given below. For this work, I performed the SPEM experiments in collaboration with J. Zeininger, M. Raab, M. Amati, L. Gregoratti and G. Rupprechter, analyzed the SPEM data and prepared the manuscript in collaboration with J. Zeininger, M. Raab, Y. Suchorski and G. Rupprechter.









The following pages give an unmodified reproduction of the manuscript “Coexisting multi-states in catalytic hydrogen oxidation on rhodium” by P. Winkler, J. Zeininger, M. Raab, Y. Surchorski, A. Steiger-Thirsfeld, M. Stöger-Pollach, M. Amati, L. Gregoratti, H. Grönbeck and G. Rupprechter, published in 2021 in *Nature Communications*, vol. 12, article no. 6517, and its supplementary material. The article and supplementary material are licensed under a Creative Commons Attribution 4.0 International License, available at <http://creativecommons.org/licenses/by/4.0/>.

## ARTICLE


<https://doi.org/10.1038/s41467-021-26855-y>

OPEN

# Coexisting multi-states in catalytic hydrogen oxidation on rhodium

P. Winkler <sup>1</sup>, J. Zeininger <sup>1</sup>, M. Raab <sup>1</sup>, Y. Suchorski <sup>1</sup>, A. Steiger-Thirsfeld<sup>2</sup>, M. Stöger-Pollach <sup>2</sup>, M. Amati <sup>3</sup>, L. Gregoratti <sup>3</sup>, H. Grönbeck<sup>4</sup> & G. Rupprechter <sup>1</sup>✉

Catalytic hydrogen oxidation on a polycrystalline rhodium foil used as a surface structure library is studied by scanning photoelectron microscopy (SPEM) in the  $10^{-6}$  mbar pressure range, yielding spatially resolved X-ray photoemission spectroscopy (XPS) measurements. Here we report an observation of a previously unknown coexistence of four different states on adjacent differently oriented domains of the same Rh sample at the exactly same conditions. A catalytically active steady state, a catalytically inactive steady state and multi-frequential oscillating states are simultaneously observed. Our results thus demonstrate the general possibility of multi-states in a catalytic reaction. This highly unusual behaviour is explained on the basis of peculiarities of the formation and depletion of subsurface oxygen on differently structured Rh surfaces. The experimental findings are supported by mean-field micro-kinetic modelling. The present observations raise the interdisciplinary question of how self-organising dynamic processes in a heterogeneous system are influenced by the permeability of the borders confining the adjacent regions.

Die approbierte gedruckte Originalversion dieser Dissertation ist an der TU Wien Bibliothek verfügbar. The approved original version of this doctoral thesis is available in print at TU Wien Bibliothek.

<sup>1</sup>Institute of Materials Chemistry, TU Wien, Getreidemarkt 9, 1060 Vienna, Austria. <sup>2</sup>University Service Center for Transmission Electron Microscopy, TU Wien, Wiedner Hauptstraße 8-10, 1040 Vienna, Austria. <sup>3</sup>Elettra-Sincrotrone Trieste S.C.p.A., SS14 - km 163.5 in Area Science Park, 34149 Trieste, Italy. <sup>4</sup>Department of Physics and Competence Center for Catalysis, Chalmers University of Technology, 412 96 Göteborg, Sweden. Dedicated to Prof. Gerhard Ertl on the occasion of his 85th birthday. ✉email: [guenther.rupprechter@tuwien.ac.at](mailto:guenther.rupprechter@tuwien.ac.at)

Spatiotemporal self-organisation may lead to spontaneous formation of patterns in many biological, chemical and physical systems far from equilibrium<sup>1</sup>. Such patterns have been observed for heart<sup>2</sup> and brain tissues<sup>3</sup>, liquid crystals<sup>4</sup>, semiconductors<sup>5</sup> and even for the geographical spread of pandemics<sup>6</sup> or malware propagation<sup>7</sup>. In chemistry, apart from the well-known Belousov–Zhabotinsky reaction<sup>8</sup>, a wide range of spatiotemporal dynamics has been observed in catalytic surface reactions, such as H<sub>2</sub> and CO oxidation<sup>9</sup>. Steady-state patterns, travelling waves, moving pulses and oscillating patterns have been detected using surface microscopies, and modelled theoretically<sup>9–12</sup>. Usually, just one type of spatiotemporal behaviour is observed at a time, whereas a coexistence of both steady states and oscillations or travelling waves on the very same sample was not yet observed. However, using a polycrystalline Rh foil consisting of hundreds of  $\mu\text{m}$ -sized Rh(hkl) domains, multifrequential oscillations in catalytic H<sub>2</sub> oxidation were previously detected: the reaction oscillated simultaneously on crystallographically different surface domains exhibiting different frequencies related to the domain structures<sup>13</sup>. On the nanoscale, this phenomenon was also visualised on a Rh curved crystal with the curvature in the range of  $10^{-3} \text{ nm}^{-1}$ , allowing detection of the reconstruction-driven transition from synchronised to multifrequential oscillations along with entrainment, frequency-locking and collapse of spatial coupling<sup>14</sup>.

Using polycrystalline samples and curved crystals allowed establishing the surface structure library concept: surface processes are simultaneously monitored on crystallographically different  $\mu\text{m}$ -sized domains or nanofacets of the same sample<sup>15</sup>. This automatically allows identical reaction conditions for all crystallographic orientations, a condition which is hard to fulfil in a conventional “one sample after another” type of measurement<sup>16–18</sup>.

The advantages of surface structure libraries can be exploited only when spatially-resolving methods based on parallel imaging, such as photoemission electron microscopy (PEEM) or field emission/field ion microscopies (FEM/FIM), are applied<sup>19,20</sup>. A limitation with these techniques is that only the local intensity of the recorded image is analysed, whereas chemical sensitivity is lacking. This prevents a straightforward investigation of the atomistic mechanism of the observed effects. In contrast, SPEM, applied in the present work, can—besides imaging the sample surface with sub-micrometre resolution—chemically resolve the surface distribution of individual species via locally resolved XPS (see further details in the Methods section). The use of a technique with chemical information is essential when studying catalytic oxidation reactions on Rh, because the formation of subsurface oxygen and surface oxides may strongly obscure the reaction kinetics<sup>21</sup>.

The experimental approach is illustrated in Fig. 1: the crystallography of each Rh(hkl) domain of the polycrystalline surface was characterised by electron backscatter diffraction (EBSD; Fig. 1a, see further details in the SI). The ongoing catalytic H<sub>2</sub> oxidation reaction was visualised in situ by SPEM (Fig. 1b), providing chemical maps, spatial profiles and time series of different spectral components.

In the present work, catalytic hydrogen oxidation is studied by SPEM in the  $10^{-6}$  mbar pressure range on a polycrystalline rhodium foil acting as a surface structure library. Due to the combination of chemical imaging and spatially resolved XPS measurements provided by SPEM, a coexistence of a catalytically active steady state, a catalytically inactive steady state and of multifrequential oscillating states on adjacent domains of the same Rh sample is observed for the first time. This unique behaviour is explained on the basis of the distinguishing behaviour of differently structured Rh surfaces with respect to the

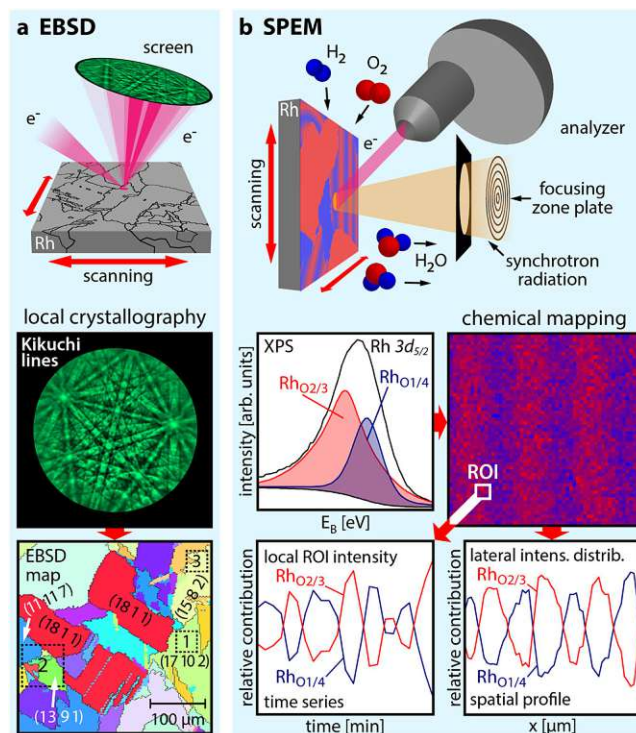


**Fig. 1 Experimental approach.** **a** EBSD: the backscattered electrons of a focused electron beam form Kikuchi lines on a phosphorous screen, enabling determination of the crystallographic orientation of each  $\mu\text{m}$ -sized Rh domain; the square regions marked in the EBSD map correspond to those shown in Fig. 2a (region 1) and Fig. 3a (regions 2 and 3); **b** SPEM: the Rh surface is in situ raster-scanned by a sub- $\mu\text{m}$ -sized X-ray spot during H<sub>2</sub> oxidation, with the emitted photoelectrons providing local XPS spectra. The local adsorbate coverage obtained from the XPS data is displayed as a chemical map. Real-time monitoring reveals both temporal and spatial periodicity of individual spectral components.

mechanism of the kinetic oscillations. The present findings support the formation and depletion of subsurface oxygen as a feedback mechanism for the observed kinetic oscillations. The experimental data are complemented by mean-field micro-kinetic modelling.

## Results and discussion

**Spectromicroscopy of kinetic oscillations.** The experiments, in which the SPEM chamber was operated as a flow reactor in the  $10^{-6}$  mbar pressure range, were performed at the “ESCA Microscopy” beamline of the Elettra synchrotron facility<sup>22</sup>.

Figure 2a shows as an example the Rh  $3d_{5/2}$  SPEM chemical map formed on the Rh(17 10 2) domain (cf. region 1 in the EBSD map in Fig. 1a) during oscillations at  $T = 453 \text{ K}$ ,  $p_{\text{O}_2} = 1.1 \times 10^{-6}$  mbar and  $p_{\text{H}_2} = 1.2 \times 10^{-6}$  mbar. The energy windows (blue and red shaded areas in Fig. 2b) for constructing the map were chosen to reflect different rhodium-oxygen-binding environments. Using reference spectra, these can be related to the state of catalytic activity, as detailed below: the red colour in Fig. 2a corresponds to a catalytically inactive state, while blue corresponds to a catalytically active state. Examples of Rh  $3d_{5/2}$  spectra of both active and inactive surface regions marked in Fig. 2a are given in Fig. 2b, c, respectively.

Deconvolution of the spectra reveals three essential components: Rh<sub>b</sub>, related to bulk rhodium, and Rh<sub>O2/3</sub> and Rh<sub>O1/4</sub> which are related to Rh bound to oxygen. In the notation Rh<sub>O*i*/j</sub>, *i* and *j*

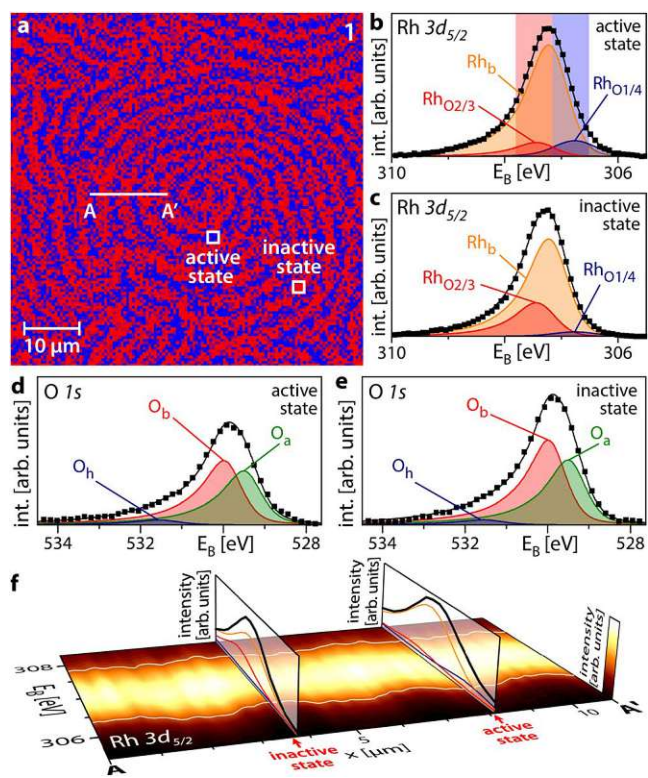


**Fig. 2** Oscillating pattern in  $\text{H}_2$  oxidation on Rh ( $T = 453 \text{ K}$ ,  $p_{\text{O}_2} = 1.1 \times 10^{-6} \text{ mbar}$ ,  $p_{\text{H}_2} = 1.2 \times 10^{-6} \text{ mbar}$ ). **a** Rh  $3d_{5/2}$  SPEM map of region 1 in Fig. 1a showing the distribution of 2/3 (red) and 1/4 (blue) oxygen-bound Rh states on the Rh(17 10 2) domain; **b** Rh  $3d_{5/2}$  XPS spectrum corresponding to the catalytically active state.  $\text{Rh}_b$ , bulk Rh;  $\text{Rh}_{\text{O}_{2/3}}$  and  $\text{Rh}_{\text{O}_{1/4}}$  correspond to Rh bound to oxygen; further details are given in the text. Squares: measured values; black solid line: sum of the deconvoluted components. The energy windows for constructing the SPEM map are shaded red and blue; **c** the same as in **(b)** but for the catalytically inactive state; **d** O  $1s$  XPS spectrum corresponding to the catalytically active state.  $\text{O}_a$  and  $\text{O}_b$  are associated with adsorbed atomic oxygen species, while  $\text{O}_h$  corresponds to the OH reaction intermediate. Squares: measured values; black solid line: sum of the deconvoluted components; **e** the same as in **(d)** but for the catalytically inactive state; **f** XPS spectral line profile along the line A-A' marked in **(a)**, with the colour code shown at the right edge. Vertical slices show exemplary spectra for the catalytically inactive and active states. The oscillating white lines serve as a guide for the eye.

refer to the number of O atoms each Rh surface atom is bound to and the number of Rh surface atoms each O atom is bound to, respectively. The deconvolution procedure and notation are based on previous studies, reporting the Rh  $3d_{5/2}$  spectral components characteristic for adsorption of oxygen on different Rh single crystal surfaces<sup>23–26</sup>.

The corresponding O  $1s$  spectra are shown in Fig. 2d, e, where  $\text{O}_a$  and  $\text{O}_b$  correspond to differently adsorbed oxygen species, while  $\text{O}_h$  belongs to the reaction intermediate OH<sup>27,28</sup>. In addition to varying amounts of different oxygen species, the total amount of oxygen (reflected in the total peak area) changes significantly between the two states.

Figure 2f illustrates, using colour-coded photoemission signal intensity, the oscillatory behaviour: the spectral line profile along the line A-A' marked in Fig. 2a exhibits a sinus-like shape, with the white lines serving as a guide for the eye. Two vertical slices show examples of spectra characterising the catalytically active and inactive states. The switching between catalytically active and

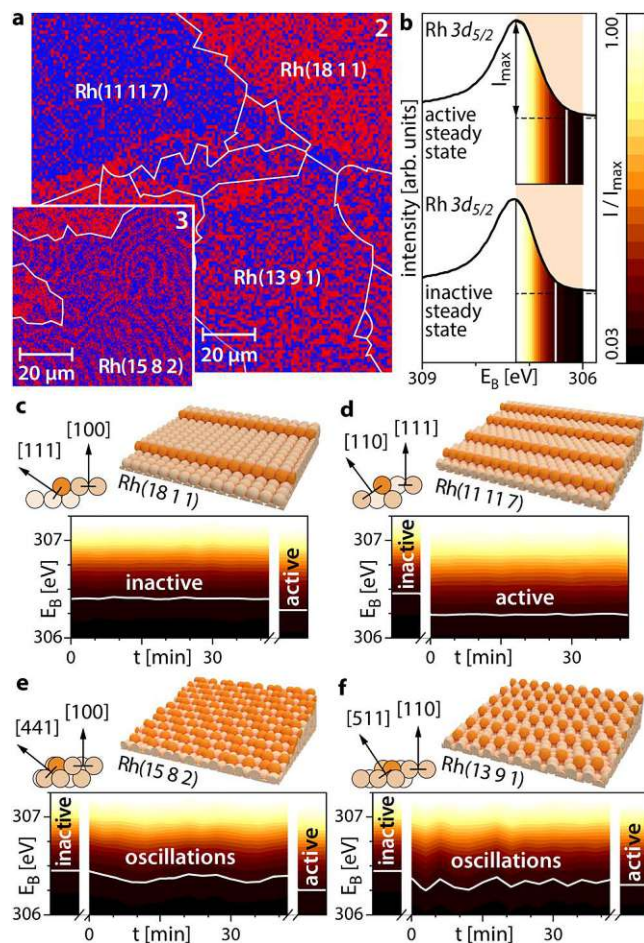


**Fig. 3** Coexisting multistates in catalytic  $\text{H}_2$  oxidation on Rh. **a** Rh  $3d_{5/2}$  SPEM map of 2/3 (red) and 1/4 (blue) oxygen-bound Rh states of regions 2 and 3 in Fig. 1a during  $\text{H}_2$  oxidation at  $T = 453 \text{ K}$ ,  $p_{\text{O}_2} = 1.1 \times 10^{-6} \text{ mbar}$ ,  $p_{\text{H}_2} = 1.2 \times 10^{-6} \text{ mbar}$ ; **b** reference Rh  $3d_{5/2}$  XPS spectra for the catalytically active and inactive steady states on Rh(13 9 1) at  $T = 453 \text{ K}$ ,  $p_{\text{O}_2} = 1.1 \times 10^{-6} \text{ mbar}$ ,  $p_{\text{H}_2} = 1.6 \times 10^{-6}$  and  $0.9 \times 10^{-6} \text{ mbar}$ , respectively. The XPS signal intensity in the energy window 306–307.25 eV is colour-coded; **c** atomic ball model of the Rh(18 1 1) surface and colour-coded spectral time series in the multi-state regime. The colour-coded active steady state reference spectrum from **(b)** is shown on the right hand side; **d** the same as in **(c)** but for the Rh(11 11 7) surface, with a reference spectrum of the inactive steady state on the left-hand side; **e** the same as in **(c)** but for the Rh(15 8 2) surface, with two reference spectra on both sides; **f** the same as in **(e)** but for Rh(13 9 1).

inactive states occurs via kinetic transitions, which resemble equilibrium phase transitions, due to the crucial role of cooperative phenomena<sup>29,30</sup>, but take place in a non-equilibrium thermodynamical situation<sup>1,31</sup>. Kinetic transitions in catalytic  $\text{H}_2$  oxidation on Rh were discussed in our previous work<sup>32</sup>.

**Coexisting multistates.** The use of a Rh surface structure library allows us to simultaneously visualise the ongoing reaction in situ on Rh(hkl) domains with different atomic surface structures. This is demonstrated in Fig. 3a with Rh  $3d_{5/2}$  chemical maps constructed in the same way as in Fig. 2a, showing regions 2 and 3 from the EBSD map in Fig. 1a. The maps illustrate a unique situation, where different domains of the same sample (and thus at the exactly same  $p/T$  conditions) show oscillating patterns on

Rh(15 8 2) and Rh(13 9 1), while the Rh(18 1 1) and Rh(11 11 7) domains appear to be entirely in the catalytically inactive and active steady states, respectively. Supplementary Video 1, created from consecutively obtained Rh  $3d_{5/2}$  chemical maps of the Rh(13 9 1) domain, exemplarily shows the oscillating spatiotemporal patterns described above. Further details about the video are given in the SI.

In order to assign the local XPS spectra of a particular domain to a specific state of catalytic activity, reference spectra for the catalytically inactive (at identical  $T = 453$  K,  $p_{O_2} = 1.1 \times 10^{-6}$  mbar and  $p_{H_2} = 0.9 \times 10^{-6}$  mbar) and catalytically active steady states (at the same  $T$  and  $p_{O_2}$  and  $p_{H_2} = 1.6 \times 10^{-6}$  mbar) were acquired for each of the studied domains. Reference Rh  $3d_{5/2}$  spectra for Rh(13 9 1) are exemplarily shown in Fig. 3b with additionally colour-coded XPS signal intensity in the energy window from 306–307.25 eV.

Due to the temporal and spatial periodicity of the oscillation process, time series data can be used in addition to chemically resolved images to probe the oscillating spectral components. Representative spectral time series for the four Rh(hkl) domains mentioned above are shown in Fig. 3c–f using the same colour code for the XPS signal intensity as in Fig. 3b. For reference, spectra of the catalytically inactive and active steady states on the respective Rh(hkl) domain are shown on the sides of the spectral time series. The comparison of Fig. 3c, d again demonstrates that simultaneously some domains remain in the catalytically inactive (e.g. Rh(18 1 1)) or catalytically active (e.g. Rh(11 11 7)) steady states, while others oscillate with differing frequencies (e.g. Rh(15 8 2),  $f = 0.8$  mHz; Rh(13 9 1),  $f = 2.4$  mHz). To our knowledge, this behaviour, i.e. the simultaneous presence of oscillations and both steady states on the same sample at the exactly same external parameters, has not yet been observed for a catalytic surface reaction.

The multiplicity of states observed herein is, however, not a transient state that occurs only temporarily during a kinetic transition, but results from stationary patterns formed under reaction conditions as non-equilibrium (dissipative) structures<sup>33,34</sup>. Since the extension of patterns formed by adsorbates is confined by domain boundaries, such patterns can be treated solely as Turing-like and not as true Turing-structures possessing intrinsic dimensions<sup>35,36</sup>. In addition, the domain boundaries play the role of coherence terminators, disturbing the spatial coupling via hydrogen diffusion which provides the coherence of oscillations within individual domains. This leads to abrupt changes of the oscillation frequencies from one domain to another (frequency transforming) as previously observed<sup>13,37</sup> or even to a full collapse of the entrainment of the oscillations and their termination as, e.g. in the case of the boundary between Rh(18 1 1) and Rh(13 9 1) visible in Fig. 3a.

This unique behaviour demonstrates the role of the catalyst surface structure in  $H_2$  oxidation, as illustrated by atomic ball models in Fig. 3c–f: Rh(18 1 1) and Rh(11 11 7), i.e. both domains in the steady state, exhibit step edges of a low-Miller-index type ([111] and [110]), whereas for both oscillating domains, i.e. Rh(15 8 2) and Rh(13 9 1), the step edges include kink sites. Although the presence of certain “atomic roughness” has been previously identified as a prerequisite for the occurrence of oscillations in  $H_2$  oxidation (oscillations do not occur on a smooth Rh(111) surface<sup>37</sup>), the present study reveals how the atomic structure of the step edges influences the behaviour of particular Rh(hkl) domains.

**Insights into the feedback mechanism.** The presence of coexisting multistates can be rationalised by considering the feedback

mechanism governing the oscillations (Fig. 4). The top row in Fig. 4 shows ball models of the four stages of the oscillating cycle, while the middle and bottom rows display corresponding Rh  $3d_{5/2}$  and O  $1s$  XPS spectra acquired during a single cycle of the oscillations on Rh(15 8 2). As the particular atomic structure of Rh(15 8 2) exhibits occupancies of oxygen binding sites differing from those of the other studied surfaces, a fourth component containing Rh<sub>O1/3</sub> and Rh<sub>O2/4</sub>, i.e. corresponding to another type of oxygen-bound Rh, was included in the Rh  $3d_{5/2}$  spectra<sup>24</sup>. The pie diagrams show the respective peak area contributions.

The Langmuir–Hinshelwood kinetics of catalytic  $H_2$  oxidation on Rh, including its oscillating mode, is primarily governed by the adsorption properties of the reactants oxygen and hydrogen<sup>38</sup>. The oscillation cycle starts from the catalytically inactive state (I), characterised by oxygen occupying primarily the energetically favoured threefold-hollow sites<sup>26</sup>. The higher binding energy of oxygen compared to hydrogen<sup>39</sup> and preferential oxygen adsorption at the step edges<sup>40</sup> hinder the dissociative adsorption of hydrogen on the step edges<sup>41</sup>, and thus catalytic activity. Due to the resulting dense oxygen coverage, oxygen atoms start to penetrate the Rh surface (stage II of the cycle). The process probably starts at a kink or edge sites which exhibit a larger structural flexibility<sup>42</sup>. While this can be considered the first step towards Rh surface oxidation, the resulting subsurface species should not be considered an ordered surface oxide, which is characterised by a far-ranging O–Rh–O trilayer structure and different XPS spectral signatures<sup>18</sup>. Following this incorporation of oxygen into the surface and the still dense oxygen coverage, some Rh atoms get slightly dislocated, increasing the local surface “roughness”<sup>41</sup> and changing the binding geometry of adsorbed oxygen<sup>43</sup>. The changes in the binding geometry result in altered Rh  $3d_{5/2}$  spectra, while the total amount of oxygen remains unchanged.

The increased surface “roughness” and the freed threefold-hollow sites create favourable conditions for the dissociative adsorption of hydrogen. Once enough hydrogen is available at the surface, a switch to the catalytically active state (III) takes place, where both hydrogen and oxygen adsorb dissociatively, and hydrogen can diffuse along the step edges and form water via an OH intermediate. This is reflected in a lower amount of oxygen-bound Rh and the corresponding diminished total peak area in the O  $1s$  spectra. Eventually, also oxygen from subsurface sites will diffuse to surface sites and react. As a result, the rest of the adsorbed oxygen will switch back to the energetically more favourable adsorption sites and oxygen will once again be preferred at the step edges, resulting in a lack of hydrogen supply and the surface switching back to the catalytically inactive state. During the last stage (IV), oxygen at the surface is replenished and the cycle starts again.

Using this description, the peculiarities of the Rh(18 1 1) and Rh(11 11 7) surfaces can also be explained: as already mentioned, the Rh(18 1 1) surface has a relatively low amount of step edges ([111]-type). Due to the kinetic limitations for oxygen penetration into the subsurface<sup>40</sup>, the amount of subsurface oxygen is not sufficient to create surface conditions for dissociative hydrogen adsorption. This domain thus remains in an inactive state. On the contrary, the Rh(11 11 7) surface exhibits plenty of step edges of [110] type, which owing to their structure allow for dissociative hydrogen adsorption at the present conditions. As a result, the Rh(11 11 7) surface maintains its catalytically active state.

While previous studies have provided a few hints about the feedback mechanism based on the formation/depletion of subsurface oxygen<sup>13,37</sup>, the present observations by chemically sensitive SPEM yield the first spectroscopic confirmation of the validity of the subsurface oxygen model.

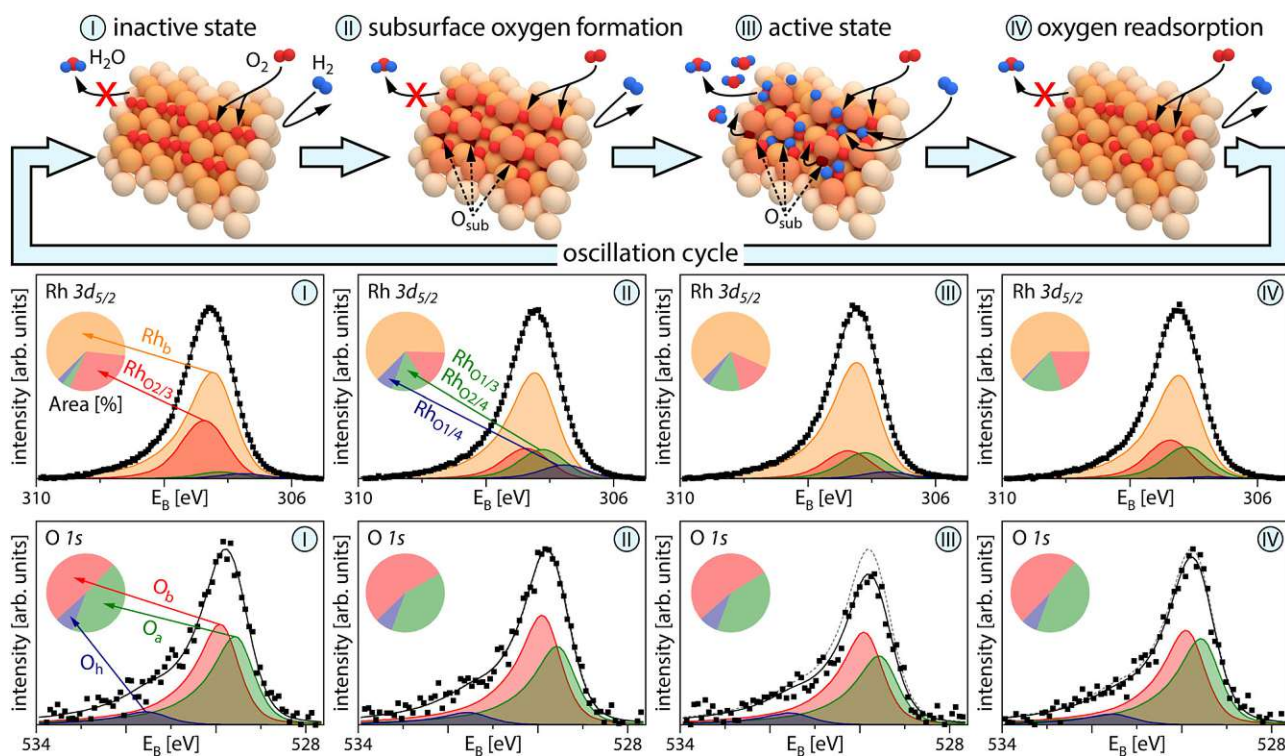


**Fig. 4** Oscillating components in catalytic  $\text{H}_2$  oxidation on Rh. Upper row: schematic ball models of the four stages of the oscillation cycle,  $\text{O}_{\text{sub}}$  indicates subsurface oxygen species; middle row: deconvoluted  $\text{Rh } 3d_{5/2}$  XPS spectra obtained during one cycle of oscillations on  $\text{Rh}(15\ 8\ 2)$ . The  $\text{Rh}_b$  component relates to bulk Rh, while the  $\text{RhO}_{2/3}$ ,  $\text{RhO}_{1/3}/\text{RhO}_{2/4}$  and  $\text{RhO}_{1/4}$  components correspond to differently oxygen-bound Rh states; further details are given in the text. Squares: measured values; black solid line: sum of the deconvoluted components. The corresponding peak area contributions are given in the pie diagrams; bottom row: deconvoluted  $\text{O } 1s$  XPS spectra obtained during one cycle of oscillations.  $\text{O}_a$  and  $\text{O}_b$  components are associated with adsorbed atomic oxygen species, while  $\text{O}_h$  corresponds to the OH reaction intermediate. Squares: measured values; black solid line: sum of the deconvoluted components. The dashed grey lines in steps II–IV indicate the measured data from step I as a reference. The corresponding peak area contributions are given in the pie diagrams.

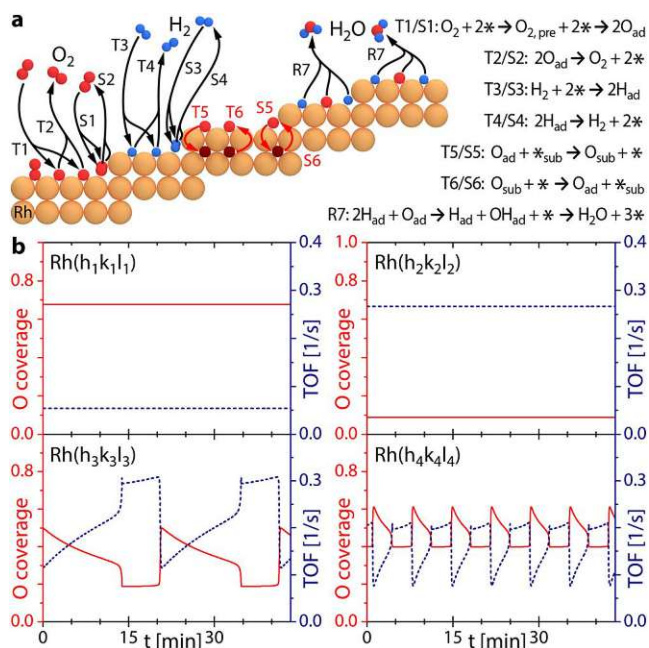
**Micro-kinetic modelling.** To provide a rationale for the observed phenomena, micro-kinetic model simulations based on the Langmuir–Hinshelwood mechanism of  $\text{H}_2$  oxidation on Rh were carried out. The present model version is a field-free-case adaptation of a model originally developed by McEwen et al. to simulate field-induced oscillations<sup>44,45</sup>. The adapted model has already been applied in our previous studies of  $\text{H}_2$  oxidation on Rh<sup>13,37</sup>. In order to account for the role of the step edges in the formation and depletion of subsurface oxygen, the present version was additionally modified to include two different types of sites, namely terrace and step edge sites. The terrace sites are characterised by a higher barrier for the formation and reduction of subsurface oxygen species than the step edge sites. We use the step density resulting from the crystallographic orientation to model the relation of amounts of the two types of sites. Further details on the micro-kinetic model and the used parameters are given in the SI.

Figure 5a schematically depicts the reaction steps considered in the present model, where the letter T refers to terrace sites and the index S to step edge sites: the dissociative adsorption (T1/S1) and associative desorption (T2/S2) of oxygen and hydrogen (T3/S3 and T4/S4), formation (T5/S5) and depletion (T6/S6) of subsurface oxygen species and catalytic water formation (via an  $\text{OH}_{\text{ad}}$  intermediate) and desorption (R7). In contrast to hydrogen, dissociative adsorption of oxygen takes place via a molecular precursor state (T1/S1).

Figure 5b presents the oxygen coverages and reaction rates (turnover frequency; TOF) calculated for the experimental conditions of Fig. 3 for four differently structured Rh(hkl)

surfaces, as modelled by terrace and step sites with the corresponding step density. The top left panel shows the results for a surface having [100]-type terraces and 13% non-kinked [111]-type step edges (i.e. similar to the  $\text{Rh}(18\ 1\ 1)$  surface), the top right panel for [111]-type terraces and 39% non-kinked [110]-type step edges (i.e. the  $\text{Rh}(11\ 11\ 7)$  surface), the bottom left panel for [100]-type terraces and 23% highly kinked [110]-type step edges (i.e. the  $\text{Rh}(15\ 8\ 2)$  surface) and the bottom right panel for [110]-type terraces and 50% highly kinked [100]-type step edges (i.e. the  $\text{Rh}(13\ 9\ 1)$  surface). The results of the calculations simulate the experimental behaviour well: the realistic variations of the step density and different basic terrace (i.e. [100]-, [110]- and [111]-structured) and step edge types (i.e. kinked and non-kinked) is sufficient to generate multistates simultaneously present on the differently structured adjacent domains of polycrystalline Rh at identical external parameters.

In summary, the presented study provides an unambiguous demonstration of how the surface structure may influence the local catalytic performance of small surface areas on the very same sample. At certain reaction conditions, adjacent crystallographically different regions of a catalyst are able to coexist in multiple states of catalytic activity. In the present case of catalytic hydrogen oxidation on rhodium, all possible states, i.e. high activity, low activity and multifrequent self-sustained oscillations, were observed simultaneously for  $\mu\text{m}$ -sized differently oriented  $\text{Rh}(hkl)$  domains of a polycrystalline Rh foil. The structure-related peculiarities of the formation and depletion of subsurface oxygen were identified as the key factor for such unusual behaviour. Depending on the specific configuration of



**Fig. 5** Micro-kinetic simulations of coexisting steady states and oscillations in catalytic  $\text{H}_2$  oxidation on  $\text{Rh}(hkl)$  domains of different atomic structure for  $T = 453 \text{ K}$ ,  $p_{\text{O}_2} = 1.1 \times 10^{-6} \text{ mbar}$ ,  $p_{\text{H}_2} = 1.2 \times 10^{-6} \text{ mbar}$ . **a** Reaction steps of  $\text{H}_2$  oxidation on a stepped Rh surface included in the micro-kinetic model and corresponding reaction equations, the denominations T and S refer to terrace sites and step edge sites, respectively. The index ad indicates adsorbed species, while the index sub refers to subsurface species and  $\cdot$  denotes an empty site; **b** calculated results of the oxygen coverage (red solid line, left ordinate axis) and reaction rate (TOF, blue dotted line, right ordinate axis) for four differently structured Rh surfaces.

terraces and step edges, the rate of formation of subsurface oxygen can either hinder the dissociative adsorption of hydrogen (i.e. the surface is in the catalytically inactive state) on some surfaces or, on other surfaces, promote the hydrogen adsorption (i.e. yielding the catalytically active state). In the range of “intermediate” formation rates of subsurface oxygen, self-sustaining oscillations occur at the same conditions. The present observations support the formation and depletion of subsurface oxygen as a feedback mechanism, which governs the frequency of the oscillations. Mean-field micro-kinetic calculations within a model distinguishing between terrace and step edge surface sites, which differ in their adsorption properties and activation energies for the formation of subsurface oxygen, corroborate the experimental observations.

The observed multistates are made possible because the grain boundaries confining the individual domains are permeable for the propagation of reaction fronts, but still effectively attenuate the spatial coupling. Attenuation of coupling impedes the transfer of a particular state that prevails on one domain to the adjacent regions, i.e. it prevents entrainment effects. Such entrainment was e.g. observed on a curved crystal, where the crystal edges separating different facets are more permeable for reaction fronts than grain boundaries on a polycrystalline sample<sup>14</sup>. Stimulated by the present observations, the interdisciplinary question arises of how the characteristics of borders between adjacent regions, exhibiting different spatiotemporal behaviour, can influence the self-organising dynamic processes in a heterogeneous system.

## Methods

**Preparation and characterisation of the Rh sample.** A polished Rh foil ( $10 \times 12 \text{ mm}^2$ , 0.2 mm thickness, 99.99% purity, MaTeck) was used as a polycrystalline Rh sample. The sample was cleaned in UHV by repeated cycles of  $\text{Ar}^+$  ion sputtering at 1 keV at 300 K, annealing to 1073–1173 K and consecutive chemical treatment in oxygen ( $p_{\text{O}_2} = 5 \times 10^{-7} \text{ mbar}$  at 773 K) and hydrogen ( $p_{\text{H}_2} = 5 \times 10^{-6} \text{ mbar}$  at 773 K). The cleanliness of the sample was verified before each experiment and post-experimental analysis routinely performed after SPEM experiments did not indicate any changes in the surface composition.

The foil temperature was measured by a Type K thermocouple spot-welded to its front and regulated by a PID controller within a window of typically 0.25 K. The gas-phase composition was monitored by a mass spectrometer and the reactant partial pressures were constant within measurement accuracy. Previous work has demonstrated the absence of measurable temperature and pressure gradients at the present conditions<sup>46,47</sup>.

Characterisation of the sample crystallography was performed by electron backscatter diffraction (EBSD), providing the crystallographic orientation of each  $\mu\text{m}$ -sized domain by scanning the sample surface with a focused electron beam and recording the diffraction patterns generated by the backscattered electrons. EBSD measurements were performed in a field emission scanning electron microscope (FEI Quanta 200 F) using standard EBSD conditions and evaluation procedures<sup>48</sup>, more details are given in the SI.

**Spectromicroscopy of kinetic oscillations.** The experiments on the kinetic oscillations of catalytic hydrogen oxidation on Rh were performed with the scanning photoemission microscope (SPEM) hosted at the “ESCA Microscopy” beamline of the Elettra synchrotron facility, which has been described in detail elsewhere<sup>22</sup>. The end station consists of three UHV sub-chambers: the sample is introduced to the system via a fast-entry load lock attached to the first chamber. Using magnetic transfer arms and wobble sticks, the sample can be transferred in UHV to a preparation chamber, which is equipped with facilities for  $\text{Ar}^+$  ion sputtering, annealing, high purity gas supply ( $\text{H}_2$ : 99.999%,  $\text{O}_2$ : 99.999%) and Auger Electron Spectroscopy (AES) for checking sample composition and cleanliness. Afterwards, the sample is transferred in UHV to the SPEM chamber. A zone plate optical system provides a small focused photon probe (spot diameter 0.13  $\mu\text{m}$ ) used to illuminate the sample surface, while the analysed surface region is selected by a piezo specimen positioning and scanning system. The emitted photoelectrons are collected within an 8 eV kinetic energy window by a hemispherical energy analyser equipped with a 48 channel detector.

The SPEM was operated in two modes: in the microspectroscopy mode, an XPS spectrum from a microspot on the sample surface was collected, while in the imaging mode, the sample surface was mapped by synchronised-scanning the sample with respect to the photon probe. In the imaging mode, a 48 points XPS spectrum covering the 8 eV kinetic energy window was recorded for each pixel in the image, allowing determination of the spatial distribution of different chemical species and removal of the topography contribution<sup>49</sup>, and thus creating chemical maps, spatial profiles and time series. A single pixel in a typical SPEM image in the present work takes about 0.05 s to obtain, i.e. the whole image takes below 5 min, while the high-resolution Rh 3d or O 1s spectra take less than 1 min. The overall energy resolution is 0.3 eV<sup>50</sup>. Due to the setup geometry, electrons emitted at an angle of 60° to the surface normal were registered. Spectra were taken at a photon energy of 652.75 eV and the energy scales were calibrated against the energy of the Au 4f<sub>7/2</sub> peak with a binding energy of 84.0 eV. The absence of any drifts in photon energy and photon flux was verified by obtaining Ta 4f spectra of the chemically inert tantalum clips used for mounting the sample and by obtaining Au 4f spectra of a separate gold foil sample at regular intervals between the experiments.

All spectra in the present work are representative examples of the described states and were deconvoluted using a pseudo-Voigt line shape<sup>51</sup> in combination with a Shirley background<sup>52</sup>. The spectral components are based on literature data (see above) and were refined by considering the whole ensemble of spectra, including reference spectra of all clean, catalytically active and catalytically inactive surfaces.

**The micro-kinetic simulations.** The micro-kinetic simulations were carried out using a model based on the Langmuir–Hinshelwood mechanism of  $\text{H}_2$  oxidation on Rh. The reaction network included the dissociative adsorption and associative desorption of hydrogen, dissociative adsorption of oxygen via a precursor state and associative desorption of oxygen, formation and depletion of subsurface oxygen and catalytic water formation. In order to account for the role of the step edges in the formation and depletion of subsurface oxygen, in the present model, a distinction was made between two different types of adsorption sites, namely terrace and step edge sites. Details of the model and of the calculations as well as the used calculation parameters are given in the SI.

## Data availability

The data that support the findings of this study are available as zipped folders of annotated HDF4 files and text files in a Zenodo repository under <https://doi.org/10.5281/zenodo.5535787><sup>53</sup>.



Received: 14 July 2021; Accepted: 18 October 2021;  
Published online: 11 November 2021

## References

- Nicolis, G. & Prigogine, I. *Self-Organization in Nonequilibrium Systems: From Dissipative Structures to Order through Fluctuations* (Wiley, 1977).
- Winfree, A. T. Chemical waves and fibrillating hearts: discovery by computation. *J. Biosci.* **27**, 465–473 (2002).
- Bao, W. & Wu, J.-Y. Propagating wave and irregular dynamics: spatiotemporal patterns of cholinergic theta oscillations in neocortex in vitro. *J. Neurophysiol.* **90**, 333–341 (2003).
- Sasaki, Y. et al. Large-scale self-organization of reconfigurable topological defect networks in nematic liquid crystals. *Nat. Commun.* **7**, 13238 (2016).
- Schöll, E. *Nonlinear Spatio-temporal Dynamics and Chaos in Semiconductors* (Cambridge Univ. Press, 2001).
- Malchow, H., Petrovskii, S. V. & Venturino, E. *Spatiotemporal Patterns in Ecology and Epidemiology: Theory, Models, and Simulation* (Chapman and Hall, 2008).
- Kumari, S. & Upadhyay, R. K. Exploring the behavior of malware propagation on mobile wireless sensor networks: Stability and control analysis. *Math. Comput. Simul.* **190**, 246–269 (2021).
- Zaikin, A. N. & Zhabotinsky, A. M. Concentration wave propagation in two-dimensional liquid-phase self-oscillating system. *Nature* **225**, 535–537 (1970).
- Sachs, C., Hildebrand, M., Volkening, S., Wintterlin, J. & Ertl, G. Spatiotemporal self-organization in a surface reaction: From the atomic to the mesoscopic scale. *Science* **293**, 1635–1638 (2001).
- Ertl, G. Reactions at surfaces: from atoms to complexity (Nobel lecture). *Angew. Chem. Int. Ed.* **47**, 3524–3535 (2008).
- Wolff, J., Papathanasiou, A. G., Kevrekidis, I. G., Rotermund, H. H. & Ertl, G. Spatiotemporal addressing of surface activity. *Nature* **294**, 134–137 (2001).
- Imbihl, R. in *Handbook of Surface Science* (eds Hasselbrink, E. & Lundqvist, B. I.) Ch. 9 (Elsevier, 2008).
- Suchorski, Y. et al. Visualizing catalyst heterogeneity by a multifrequential oscillating reaction. *Nat. Commun.* **9**, 600 (2018).
- Suchorski, Y. et al. Resolving multifrequential oscillations and nanoscale interfacial communication in single-particle catalysis. *Science* **372**, 1314–1318 (2021).
- Suchorski, Y. & Rupprechter, G. Heterogeneous surfaces as structure and particle size libraries of model catalysts. *Catal. Lett.* **148**, 2947–2956 (2018).
- Vogel, D. et al. Local catalytic ignition during CO Oxidation on low-index Pt and Pd surfaces: a combined PEEM, MS and DFT study. *Angew. Chem. Int. Ed.* **51**, 10041–10044 (2012).
- Vogel, D. et al. The role of defects in the local reaction kinetics of CO oxidation on low-index Pd surfaces. *J. Phys. Chem. C* **117**, 12054–12060 (2013).
- Winkler, P. et al. How the anisotropy of surface oxide formation influences the transient activity of a surface reaction. *Nat. Commun.* **12**, 69 (2021).
- Rotermund, H. H. Real time imaging of catalytic reactions on surfaces: past, present and future. *Surf. Sci.* **603**, 1662–1670 (2009).
- Suchorski, Y. & Rupprechter, G. Catalysis by imaging: from meso- to nano-scale. *Top. Catal.* **63**, 1532–1544 (2020).
- von Oertzen, A., Mikhailov, A. S., Rotermund, H. H. & Ertl, G. Subsurface oxygen in the CO oxidation reaction on Pt(110): experiments and modeling of pattern formation. *J. Phys. Chem. B* **102**, 4966–4981 (1998).
- Casalis, L. et al. ESCA microscopy beamline at ELETTRA. *Rev. Sci. Instrum.* **66**, 4870–4875 (1995).
- Ganduglia-Pirovano, M. V. et al. Oxygen-induced Rh 3d<sub>5/2</sub> surface core-level shifts on Rh(111). *Phys. Rev. B* **63**, 205415 (2001).
- Gustafson, J. et al. Identification of step atoms by high resolution core level spectroscopy. *Phys. Rev. Lett.* **91**, 056102 (2003).
- Baraldi, A. et al. Spectroscopic link between adsorption site occupation and local surface chemical reactivity. *Phys. Rev. Lett.* **93**, 046101 (2004).
- Bianchettin, L. et al. Surface core level shift: high sensitive probe to oxygen-induced reconstruction of Rh(100). *J. Phys. Chem. C* **113**, 13192–13198 (2009).
- Comelli, G. et al. Real-time X-ray photoelectron spectroscopy study of dissociative oxygen adsorption on Rh(110). *Chem. Phys. Lett.* **261**, 253–260 (1996).
- Klikovits, J. et al. Kinetics of the reduction of the Rh(111) surface oxide: linking spectroscopy and atomic-scale information. *J. Phys. Chem. B* **110**, 9966–9975 (2006).
- Schlögl, F. Chemical reaction models for non-equilibrium phase transitions. *Z. Phys.* **253**, 174–161 (1972).
- Schlögl, F. What can we learn about dissipative structures by model reactions. *Ber. Bunsenges. Phys. Chem.* **84**, 351–357 (1980).
- Prigogine, I. & Glansdorff, P. *Thermodynamic Theory of Structure, Stability and Fluctuations* (Wiley, 1971).
- Datler, M. et al. Hydrogen oxidation on stepped Rh surfaces:  $\mu\text{m}$ -scale versus nanoscale. *Catal. Lett.* **146**, 1867–1874 (2016).
- Turing, A. M. The chemical basis of morphogenesis. *Philos. Trans. R. Soc. Lond. B. Biol. Sci.* **237**, 37 (1952).
- Nicolis, G. *Introduction to Nonlinear Science* (Cambridge Univ. Press, 1995).
- Kapral, R. & Showalter, K. (eds.) *Chemical Waves and Patterns*. (Kluwer Academic, 1995).
- Schütz, E. et al. Bimetallic catalysts as dissipative structures: stationary concentration patterns in the O<sub>2</sub> + H<sub>2</sub> reaction on a composite Rh(110)/Pt surface. *Catal. Lett.* **63**, 13–19 (1999).
- Suchorski, Y. et al. Surface-structure libraries: multifrequential oscillations in catalytic hydrogen oxidation on rhodium. *J. Phys. Chem. C* **123**, 4217–4227 (2019).
- Yates, J. T. Jr., Thiel, P. A. & Weinberg, W. H. The catalytic reaction between adsorbed oxygen and hydrogen on Rh(111). *Surf. Sci.* **82**, 45–68 (1979).
- Afliche, S., Natoli, V. & Cohen, M. H. Theoretical investigation of water formation on Rh and Pt Surfaces. *J. Chem. Phys.* **112**, 9986–9995 (2000).
- Klikovits, J. et al. Step-orientation-dependent oxidation: from 1D to 2D oxides. *Phys. Rev. Lett.* **101**, 266104 (2008).
- Africh, C. et al. Two-step reaction on a strained, nanoscale segmented surface. *Phys. Rev. Lett.* **93**, 126104 (2004).
- Derouin, J., Farber, R. G. & Killelea, D. R. Combined STM and TPD study of Rh(111) under conditions of high oxygen coverage. *J. Phys. Chem. C* **119**, 14748–14755 (2015).
- Köhler, L. et al. High-coverage oxygen structures on Rh(111): adsorbate repulsion and site preference is not enough. *Phys. Rev. Lett.* **93**, 266103 (2004).
- McEwen, J.-S., Gaspard, P., Visart de Bocarmé, T. & Kruse, N. Oscillations and bistability in the catalytic formation of water on rhodium in high electric fields. *J. Phys. Chem.* **113**, 17045–17058 (2009).
- McEwen, J.-S., Gaspard, P., Visart de Bocarmé, T. & Kruse, N. Nanometric chemical clocks. *Proc. Natl Acad. Sci. USA* **106**, 3006–3010 (2009). and SI therein.
- Suchorski, Y. et al. Local reaction kinetics by imaging: CO oxidation on polycrystalline platinum. *ChemPhysChem* **11**, 3231–3235 (2010).
- Spiel, C. et al. Catalytic CO oxidation on individual (110) domains of a polycrystalline Pt foil: local reaction kinetics by PEEM. *Catal. Lett.* **141**, 625–632 (2011).
- Humphreys, F. J. Grain and subgrain characterisation by electron backscatter diffraction. *J. Mat. Sci.* **36**, 3833–3854 (2001).
- Gregoratti, L. et al. 48-Channel electron detector for photoemission spectroscopy and microscopy. *Rev. Sci. Instrum.* **75**, 64–68 (2004).
- Zeller, P. et al. Scanning photoelectron spectro-microscopy: a modern tool for the study of materials at the nanoscale. *Phys. Status Solidi A* **215**, 180308 (2018).
- Evans, S. Curve synthesis and optimization procedures for X-ray photoelectron spectroscopy. *Surf. Interface Anal.* **17**, 85–93 (1991).
- Shirley, D. A. High-resolution X-ray photoemission spectrum of the valence bands of gold. *Phys. Rev. B* **5**, 4709–4714 (1972).
- Winkler, P. et al. Coexisting multi-states in catalytic hydrogen oxidation on rhodium - Supplementary Database 1. *Zenodo* <https://doi.org/10.5281/zenodo.5535787> (2021).

## Acknowledgements

This work was supported by the Austrian Science Fund (FWF) (P 32772-N; M.R., G.R., Y.S., P.W. and J.Z.) and the EU Framework Programme for Research and Innovation HORIZON 2020 by the project CALIPSOplus (730872; P.W.).

## Author contributions

A.S.-T. and M.S.-P. contributed to the EBSD characterisation. M.A., L.G., M.R., G.R., P.W. and J.Z. contributed the SPEM measurements. M.R. and H.G. contributed the micro-kinetic model simulations. G.R. and Y.S. supervised the experimental work and were involved in the analysis of the experimental data. M.R., G.R., Y.S., P.W. and J.Z. prepared the manuscript. All authors contributed to the discussion and approved the manuscript.

## Competing interests

The authors declare no competing interests.

**Additional information**

**Supplementary information** The online version contains supplementary material available at <https://doi.org/10.1038/s41467-021-26855-y>.

**Correspondence** and requests for materials should be addressed to G. Rupprechter.

**Peer review information** *Nature Communications* thanks the anonymous reviewers for their contribution to the peer review of this work.

**Reprints and permission information** is available at <http://www.nature.com/reprints>

**Publisher's note** Springer Nature remains neutral with regard to jurisdictional claims in published maps and institutional affiliations.



**Open Access** This article is licensed under a Creative Commons Attribution 4.0 International License, which permits use, sharing, adaptation, distribution and reproduction in any medium or format, as long as you give appropriate credit to the original author(s) and the source, provide a link to the Creative Commons license, and indicate if changes were made. The images or other third party material in this article are included in the article's Creative Commons license, unless indicated otherwise in a credit line to the material. If material is not included in the article's Creative Commons license and your intended use is not permitted by statutory regulation or exceeds the permitted use, you will need to obtain permission directly from the copyright holder. To view a copy of this license, visit <http://creativecommons.org/licenses/by/4.0/>.

© The Author(s) 2021

## Coexisting multi-states in catalytic hydrogen oxidation on rhodium

P. Winkler<sup>1</sup>, J. Zeininger<sup>1</sup>, M. Raab<sup>1</sup>, Y. Suchorski<sup>1</sup>, A. Steiger-Thirsfeld<sup>2</sup>, M. Stöger-Pollach<sup>2</sup>, M. Amati<sup>3</sup>, L. Gregoratti<sup>3</sup>, H. Grönbeck<sup>4</sup> and G. Rupprechter<sup>1\*</sup>

<sup>1</sup>*Institute of Materials Chemistry, TU Wien, Getreidemarkt 9, 1060 Vienna, Austria*

<sup>2</sup>*University Service Center for Transmission Electron Microscopy, TU Wien, Wiedner Hauptstraße 8-10, 1040 Vienna, Austria*

<sup>3</sup>*Elettra–Sincrotrone Trieste S.C.p.A., SS14 - km 163.5 in Area Science Park, 34149 Trieste, Italy*

<sup>4</sup>*Department of Physics and Competence Center for Catalysis, Chalmers University of Technology, 412 96 Göteborg, Sweden*

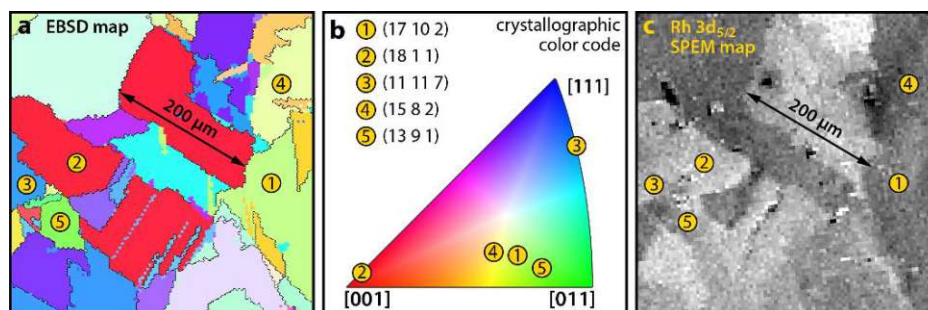
## Supplementary Information

### Supplementary Note 1: Determining the crystallographic orientation of Rh(hkl) domains

The determination of the crystallographic orientations of each of the surface domains is crucial when using a polycrystalline sample as a surface structure library [1], as done in the present work. Only then, surface processes such as adsorption, oxidation or ongoing catalytic reactions can be studied with respect to the local surface crystallography and surface structure effects can be uncovered. For samples in the meso-scale range, such as the polycrystalline Rh foil used in this work, electron backscatter diffraction (EBSD) is a suitable technique to determine the crystallographic orientations of each of the studied surface structures.

Based on scanning electron microscopy, EBSD is a well-established crystallographic microstructural characterisation technique, which is commonly used to study crystalline or polycrystalline materials, e.g., in catalysis [2-4], electrochemistry [5-7] or metallurgy [8, 9] and surface oxidation [10]. In the EBSD experiments, a diffraction pattern is formed on a fluorescent screen by the backscattered electrons of an electron beam focused onto a particular sample spot, showing up as so-called Kikuchi lines. As the formed diffraction pattern corresponds to each of the diffracting crystal lattice planes [11, 12], the crystallographic orientation of the particular sample spot can be determined, usually by computer-based image transformation [13, 14]. The concept is routinely applied and has been developed into a standard technique in scanning electron microscopy. In the present study, the EBSD measurements were performed by a FEI Quanta 200F field emission scanning electron microscope using standard EBSD conditions and evaluation procedures [15]. A comparison of pre- and post-reaction EBSD characterisation showed that the surface structures of particular domains remain conserved even after extended periods of ongoing chemical reaction.

The results of the EBSD characterisation are shown as a color-coded map in Supplementary Fig. 1a. The domains are numbered in the order of occurrence in the main text. In Supplementary Fig. 1b, the crystallographic orientations (Miller indices) of the domains are given, and their positions marked on the color-coded inverse pole figure of the cubic lattice (used for colouring the EBSD map in Supplementary Fig. 1a). A Rh  $3d_{5/2}$  SPEM map of the same region as in Supplementary Fig. 1a is given in Supplementary Fig. 1c, where the contrast results from the sample topography and the differing total photoelectron yield of each of the Rh(hkl) domains. The magnification of all of the used imaging techniques was calibrated by comparing the respective maps with optical micrographs of the same polycrystalline Rh sample.



**Supplementary Figure 1.** Determination of the crystallographic orientations of individual domains of the polycrystalline Rh foil. (a) EBSD color-coded map of the studied region; the individual studied Rh(hkl) domains are numbered; (b) Miller indices of the five Rh(hkl) domains studied in the present work and their location on the inverse pole figure; (c) Rh  $3d_{5/2}$  SPEM map of the same region as in (a). The image contrast results from the local photoelectron yield.

## Supplementary Note 2: Micro-kinetic model simulations

The mean-field microkinetic model applied in our simulations is based on the Langmuir-Hinshelwood mechanism, which is well established for H<sub>2</sub> oxidation on Rh surfaces [16]. The observed kinetic oscillations in this reaction result from the periodic formation/depletion of subsurface oxygen, which influences the adsorption behaviour of both reactants, thus serving as feedback mechanism [4, 17].

The oscillatory water formation is described by seven reactions (Fig. 5: S1/T1 – R7). The formation of water takes place via an OH<sub>ad</sub> intermediate, where the formation of the intermediate from O<sub>ad</sub> and H<sub>ad</sub> is the rate-limiting step in comparison to the subsequent reaction with a second H<sub>ad</sub> species. Alternative ways of water formation (e.g., by OH disproportionation) can be neglected at the present conditions [18]. We assume that water desorbs immediately after its formation at the considered reaction conditions (453 K), which is justified by the desorption temperature for water being about 300 K on Rh surfaces [19]. The coverages for oxygen ( $\theta_O$ ), subsurface oxygen ( $\theta_S$ ) and hydrogen ( $\theta_H$ ) are in the model described by the following kinetic equations:

$$\frac{d\theta_O}{dt} = \frac{2}{1+K\theta_*^2} (k_a^O K p_{O_2} \theta_*^2 - k_d^O \theta_O^2) - k_{ox} \theta_O (1 - \theta_S) + k_{red} \theta_S \theta_* - k_r \theta_H \theta_O \quad (S1)$$

$$\frac{d\theta_S}{dt} = k_{ox} \theta_O (1 - \theta_S) - k_{red} \theta_S \theta_* \quad (S2)$$

$$\frac{d\theta_H}{dt} = 2k_a^H p_{H_2} \theta_*^2 - 2k_d^H \theta_H^2 - 2k_r \theta_H \theta_O \quad (S3)$$

The empty sites are given by  $\theta_* = 1 - \theta_H - \theta_O$  and the rate constants by the expressions below, where  $\beta = 1/k_B T$ . The symbols are explained in Supplementary Tab. 2.

$$k_a^H = S_0^H a_s / \sqrt{2\pi m_{H_2} k_B T} \quad (S4)$$

$$k_a^O = S_0^O a_s / \sqrt{2\pi m_{O_2} k_B T} \quad (S5)$$

$$k_d^H = k_{d0}^O e^{-\beta E_d^H} \quad (S6)$$

$$K = K_0 e^{-\beta(E_K + A_K^O \theta_O + A_K^S \theta_S)} \quad (S7)$$

$$k_d^O = k_{d0}^O e^{-\beta(E_d^O + A_d^O \theta_O + B_d^O \theta_O^2)} \quad (S8)$$

$$k_{ox} = k_{ox}^0 e^{-\beta E_{ox}} \quad (S9)$$

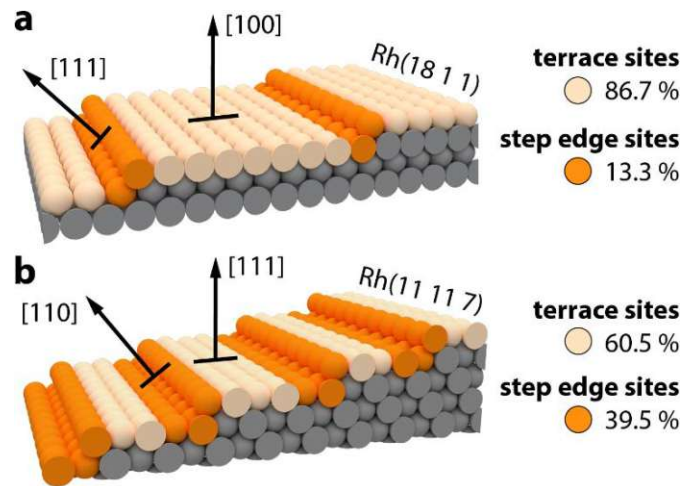
$$k_{red} = k_{red}^0 e^{-\beta(E_{red} + A_{red}^S \theta_S)} \quad (S10)$$

$$k_r = k_r^0 e^{-\beta(E_r + A_r^H \theta_H + A_r^O \theta_O)} \quad (S11)$$

A linear correlation between the activation energies for oxide formation ( $E_{ox}$ ) and reduction ( $E_{red}$ ) is assumed [4, 17], based on the results for Rh(100), Rh(110) and Rh(111) reported in Ref. [18], and used to calculate the  $E_{red}$  associated with each respective  $E_{ox}$  (listed in Supplementary Tab. 2):

$$E_{red} = 0.293 + 0.776 E_{ox} \quad (\text{S12})$$

The model applied herein is adapted from a version developed by McEwen et al. to simulate field-induced oscillations in  $\text{H}_2$  oxidation on Rh [18, 20, 21]. This model was modified to describe the field-free oscillations on stepped Rh surfaces observed by PEEM [4, 17] and, in the present study, by SPEM. While the original model considers field-induced effects such as a reduction of the activation barrier for oxygen incorporation [22], such effects are not present in our experiments and, therefore, not included in the simulations. The field-free version of the model was already successfully applied to simulate oscillations in the  $\text{H}_2$  oxidation on a polycrystalline Rh foil [4, 17] and on a  $\mu\text{m}$ -sized curved Rh crystal [23]. Since the present SPEM measurements demonstrated an important role of the step edges in the observed oscillations, we have extended the model in the present work to take effects of steps into account. In particular, the model is modified to include two different site types for each Rh(hkl) domain, namely terrace and step edge sites, as illustrated in Supplementary Fig. 2 for the Rh(18 1 1) and the Rh(11 11 7) surfaces. The two sites are not coupled by diffusion in the modelled reaction kinetics.



**Supplementary Figure 2.** (a) Atomic ball model of the stepped Rh(18 1 1) surface with terrace sites and step edge sites coloured in beige and orange, respectively. The bulk atoms are shown in grey; (b) atomic ball model for the Rh(11 11 7) surface. Atomic ball models for the other studied Rh(hkl) surfaces are given in Fig. 3 of the main text.

Each type of sites is assigned a set of kinetic parameters and a set of energy barriers for subsurface oxygen formation  $E_{ox}$  and reduction  $E_{red}$ . The three used sets of kinetic parameters are based on literature data for Rh(100), Rh(110) and Rh(111) [4, 18] and are listed in Supplementary Tab. 1.

**Supplementary Table 1.** Parameter sets for Rh(100), Rh(110) und Rh(111) used in the micro-kinetic simulations. Energies are given in eV, the area of a surface site ( $a_s$ ) in  $\text{\AA}^2$  and rate constants in 1/s. All simulations have been performed for the same conditions as in the SPEM experiments ( $T = 453$  K,  $p_{\text{O}_2} = 1.1 \times 10^{-6}$  mbar,  $p_{\text{H}_2} = 1.2 \times 10^{-6}$  mbar). The values are taken from Refs. [4, 18].

symbol	description	(100)	(110)	(111)
$a_s$	area of a surface site	10	10	10
$E_d^H$	desorption energy of H	0.75	0.64	0.70
$S_0^O$	initial sticking coefficient O	0.95	0.95	0.60
$A_K^S$	coverage dependence of sub-surface oxygen on oxygen dissociation	0.070	0.075	0.082
$E_d^O$	desorption energy of O	3.5	3.2	2.85
$A_d^O$	coverage dependence of oxygen desorption energy on adsorbed oxygen	-0.6	-0.5	-0.4
$B_d^O$	coverage dependence of oxygen desorption energy on molecular oxygen	-0.8	-0.7	-0.5
$E_r$	activation energy for water formation	0.79	0.79	0.75
$S_0^H$	initial sticking coefficient H	0.4	0.4	0.4
$k_{d0}^h$	pre-factor for hydrogen desorption	$3.0 \times 10^{10}$	$3.0 \times 10^{10}$	$3.0 \times 10^{10}$
$K_0$	pre-factor for oxygen dissociation equilibrium constant	0.2525	0.2525	0.2525
$E_k$	activation energy for oxygen dissociation equilibrium constant	-0.178	-0.178	-0.178
$A_K^O$	coverage dependence of adsorbed oxygen on oxygen dissociation	0.158	0.158	0.158
$k_{ox}^O$	pre-factor for oxygen diffusion from surface to sub-surface sites	$5.0 \times 10^{11}$	$5.0 \times 10^{11}$	$5.0 \times 10^{11}$
$k_{red}^O$	pre-factor for oxygen diffusion from sub-surface to surface sites	$1.85 \times 10^{13}$	$1.85 \times 10^{13}$	$1.85 \times 10^{13}$
$A_{red}^S$	coverage dependence of sub-surface oxygen on surface subsurface reduction	0.3	0.3	0.3
$k_{d0}^O$	pre-factor for oxygen desorption	$6.0 \times 10^{13}$	$6.0 \times 10^{13}$	$6.0 \times 10^{13}$
$k_r$	pre-factor for water formation	$7.0 \times 10^{12}$	$7.0 \times 10^{12}$	$7.0 \times 10^{12}$
$A_r^H$	coverage dependence of activation energy of water formation on H	-0.27	-0.27	-0.27
$A_r^O$	coverage dependence of activation energy of water formation on O	-0.145	-0.145	-0.145

The step edge sites are assigned lower energy barriers  $E_{ox,s}$  and  $E_{red,s}$  for subsurface oxygen formation and reduction than the corresponding energy barriers for terrace sites  $E_{ox,t}$  and  $E_{red,t}$ .

The barriers for the terraces were taken from literature [4, 18]. For kinked step edges (i.e., for the Rh(15 8 2) and Rh(13 9 1) surfaces),  $E_{ox,s}$  and  $E_{red,s}$  were reduced even further to achieve the experimentally observed oscillations. The energy barriers for oxidation and reduction should be considered as apparent barriers, given that the oxidation and reduction are complex processes at the atomic scale with several elementary steps.

The Miller indices of the stepped domains obtained by EBSD provide crystallographic orientations of the terrace and step edges (Supplementary Tab. 2), which are used for the choice of the kinetic parameter sets and energy barriers. The relative contributions of step edge and terrace sites result from the respective step densities. The chosen energy barriers and relative site type contributions are listed in Supplementary Tab. 2.

**Supplementary Table 2.** Description of terrace and step edge sites in the micro-kinetic model simulations for individual Rh(hkl) domains. The kinetic parameters associated with Rh(100), Rh(110) and Rh(111) are given in Supplementary Tab. 1; the activation energies for subsurface oxide formation ( $E_{ox}$ ) are given in eV; the relative contribution of terrace and step edge sites is based on the step density of the domains.

<i>domain orientation</i>	<b>terrace sites</b>			<b>step edge sites</b>		
	<i>terrace orientation</i>	$E_{ox,t}$	<i>relative contribution</i>	<i>main step edge orientation</i>	$E_{ox,s}$	<i>relative contribution</i>
(18 1 1)	(100)	1.520	0.867	(111)	1.300	0.133
(11 11 7)	(111)	1.680	0.605	(110)	1.300	0.395
(15 8 2)	(100)	1.520	0.232	(110)	1.236	0.768
(13 9 1)	(110)	1.630	0.504	(100)	1.174	0.496



### Supplementary Note 3: Construction of the Supplementary Video

Supplementary Video 1 shows the spatio-temporal patterns formed during catalytic hydrogen oxidation at  $T = 453$  K,  $p_{O_2} = 1.1 \times 10^{-6}$  mbar and  $p_{H_2} = 1.2 \times 10^{-6}$  mbar on Rh(13 9 1). The video was constructed from chemical maps ( $41 \times 41 \mu\text{m}^2$ ) obtained by SPEM consecutively, which were then used as individual video-frames. For the individual chemical maps, the same energy windows as those in Figs. 2 and 3 in the main text were used, reflecting two different rhodium-oxygen binding environments:  $\text{Rh}_{O_{2/3}}$  (energy window from 307.16 eV to 307.81 eV) and  $\text{Rh}_{O_{1/4}}$  (energy window from 306.51 eV to 307.16 eV) [24]. The image contrast in the chemical map results from the relative contribution of the two spectral components, i.e., bright contrast indicates predominance of the  $\text{Rh}_{O_{1/4}}$  binding geometry, associated with a catalytically active state (cf. Figs. 2 and 3 in the main text), while dark image contrast indicates predominance of the  $\text{Rh}_{O_{2/3}}$  binding geometry, associated with a catalytically inactive state. Periodic changes between bright and dark stripes in the video illustrate the spatial and temporal periodicity in the adlayer composition and thus in the catalytic activity during the multifrequential self-sustaining oscillations in  $\text{H}_2$  oxidation on Rh(hkl) domains.

## Supplementary References:

- [1] Suchorski, Y. & Rupprechter, G. Heterogeneous Surfaces as Structure and Particle Size Libraries of Model Catalysts. *Catal. Lett.* **148**, 2947–2956 (2018).
- [2] Vogel, D. *et al.* The Role of Defects in the Local Reaction Kinetics of CO Oxidation on Low-Index Pd Surfaces. *J. Phys. Chem. C* **117**, 12054–12060 (2013).
- [3] Weatherup, R. S. *et al.* In Situ Graphene Growth Dynamics on Polycrystalline Catalyst Foils. *Nano Lett.* **16**, 6196–6206 (2016).
- [4] Suchorski, Y. *et al.* Visualizing catalyst heterogeneity by a multifrequential oscillating reaction. *Nat. Commun.* **9**, 600-1–6 (2018).
- [5] König, U. & Davepon, B. Microstructure of polycrystalline Ti and its micro-electrochemical properties by means of electron-backscattering diffraction (EBSD). *Electrochim. Acta* **47**, 149–160 (2001).
- [6] Yule, L.C. *et al.* Nanoscale electrochemical visualization of grain-dependent anodic iron dissolution from low carbon steel. *Electrochim. Acta* **332**, 135267-1–12 (2020).
- [7] Daviddi, E. *et al.* Nanoscale electrochemistry in a copper/aqueous/oil three-phase system: surface structure–activity–corrosion potential relationships. *Chem. Sci.* **12**, 3055-1–15 (2021).
- [8] Dingley, D. J. & Randle, V. Microtexture determination by electron back-scatter diffraction. *J. Mater. Sci.* **27**, 4545–4566 (1992).
- [9] Schwartz, A. J., Kumar, M., Adams, B. L. & Field, D. P. (eds.) *Electron Backscatter Diffraction in Materials Science*. (Springer US, 2009).
- [10] Winkler, P. *et al.* How the anisotropy of surface oxide formation influences the transient activity of a surface reaction. *Nat. Commun.* **12**, 69-1–8 (2021).
- [11] Dingley, D. J., Baba-Kishi, K. Z. & Randle V. *Atlas of Backscattering Kikuchi Diffraction Patterns*. (IOP Publishing, 1995).
- [12] Baba-Kishi, K. Z. Electron backscatter Kikuchi diffraction in the scanning electron microscope for crystallographic analysis. *J. Mater. Sci.* **37**, 1715–1746 (2002).
- [13] Lasse, N.C.K. A New Procedure for Automatic High Precision Measurements of the Position and Width of Bands in Backscatter Kikuchi Patterns. *Mat. Sci. Forum* **273-275**, 201–208 (1998).
- [14] Engler, O. & Randle, V. *Introduction to Texture Analysis: Macrotecture, Microtexture and Orientation Mapping*. (CRC Press, Boca Raton, 2009).
- [15] Humphreys, F. J. Grain and subgrain characterisation by electron backscatter diffraction. *J. Mater. Sci.* **36**, 3833–3854 (2001).
- [16] Zum Mallen, M.P., Williams, W.R. & Schmidt, L.D. Steps in hydrogen oxidation on rhodium: hydroxyl desorption at high temperatures. *J. Phys. Chem.* **97**, 625–632 (1993) and references therein.
- [17] Suchorski, Y. *et al.* Surface-Structure Libraries: Multifrequential Oscillations in Catalytic Hydrogen Oxidation on Rhodium. *J. Phys. Chem. C* **123**, 4217–4227 (2019).
- [18] McEwen, J.-S., Gaspard, P., Visart de Bocarmé, T. & Kruse, N. Oscillations and Bistability in the Catalytic Formation of Water on Rhodium in High Electric Fields. *J. Phys. Chem.* **113**, 17045–17058 (2009).

- [19] Gregoratti, L. *et al.* Structural effects on water formation from coadsorbed H+O on Rh(100). *Surf. Sci.* **340**, 205–214 (1995).
- [20] McEwen, J.-S., Gaspard, P., Visart de Bocarmé, T. & Kruse, N. Nanometric chemical clocks. *Proc. Natl. Acad. Sci.* **106**, 3006–3010 (2009) and SI therein.
- [21] McEwen, J.-S., Gaspard, P. & Kruse, N. Electric field induced oscillations in the catalytic water production on rhodium: a theoretical analysis. *Surf. Sci.* **604**, 1353–1368 (2010).
- [22] McEwen, J.-S., Gaspard, P., Mittendorfer, F., Visart de Bocarmé, T., & Kruse, N. Field-assisted oxidation of rhodium. *Chem. Phys. Lett.* **452**, 133–138 (2008).
- [23] Suchorski, Y. *et al.* Resolving multifrequential oscillations and nanoscale interfacet communication in single-particle catalysis. *Science* **372**, 1314–1318 (2021).
- [24] Baraldi, A. *et al.* Spectroscopic Link between Adsorption Site Occupation and Local Surface Chemical Reactivity. *Phys. Rev. Lett.* **93**, 046101-1–4 (2004).



# 4

---

## Pattern formation in catalytic H<sub>2</sub> oxidation on Rh: Zooming in by correlative microscopy

Previous studies of the oscillating mode of catalytic hydrogen oxidation on rhodium (section 1.8) on polycrystalline foil samples revealed a strong dependence of the oscillation frequencies on the atomic structure [108, 114] and also the simultaneous presence of both steady states of catalytic activity and oscillations on individual domains of the polycrystalline sample at certain constant external parameters (chapter 3). In all these cases, the observed behavior was characteristic for areas of identical surface structure in their entirety and only a change in surface structure (e.g., due to a grain boundary) could result in different behavior. During following UV photoemission electron microscopy (UV-PEEM, section 2.3) studies, however, an unusual phenomenon was observed: Within a single domain of only slightly heterogeneous surface structure, both oscillating and non-oscillating areas were observed.

Therefore, low energy electron microscopy (LEEM, section 2.4) and x-ray photoemission electron microscopy (X-PEEM, section 2.4) were used to zoom in on the ongoing oscillations in the 10<sup>-6</sup> mbar pressure range in these areas, applying the correlative microscopy approach (section 2.8). LEEM and X-PEEM were even performed quasi-simultaneously in the same experimental setup under identical external parameters, representing the highest development stage of correlative microscopy. The experiments revealed the formation of spatio-temporal patterns on length scales below traditional UV-PEEM resolution and different types of patterns (e.g., spirals, dendritic structures or elliptic islands) could be observed dependent on the sample temperature. Furthermore, an unusual, previously not observed, island-mediated propagation mechanism for oxygen fronts could be detected. The origin of this island-mediated front propagation and the different observed patterns could be rationalized by model calculations based on a hybrid approach combining micro-kinetic modeling and Monte Carlo simulations.

The results of these studies were published in *ACS Catalysis* as given below. For this work, I performed the PEEM experiments, evaluated the PEEM data, performed the X-PEEM and LEEM experiments, as well as the  $\mu$ -LEED structural characterization, in collaboration with J. Zeininger, M.J. Prieto, L.C. Tănase, L. de Souza Caldas, A. Tiwari, T. Schmidt and G. Rupprechter, evaluated the X-PEEM and LEEM data in collaboration with J. Zeininger and M. Raab, evaluated the  $\mu$ -LEED data in collaboration with J. Zeininger, M. Raab and T. Schmidt and prepared the manuscript in collaboration with J. Zeininger, M. Raab, Y. Suchorski, and G. Rupprechter.

The following pages give an unmodified reproduction of the manuscript “Pattern Formation in Catalytic  $H_2$  Oxidation on  $Rh$ : Zooming in by Correlative Microscopy” by J. Zeininger, P. Winkler, M. Raab, Y. Suchorski, M.J. Prieto, L.C. Tănase, L. de Souza Caldas, A. Tiwari, T. Schmidt, M. Stöger-Pollach, A. Steiger-Thirsfeld, B. Roldan Cuenya, and G. Rupprechter, published in 2022 in *ACS Catalysis*, **vol. 12**, pages 11974-11983, and its supplementary material. The article and supplementary material are licensed under a Creative Commons Attribution 4.0 International License, available at <http://creativecommons.org/licenses/by/4.0/>.

# Pattern Formation in Catalytic H<sub>2</sub> Oxidation on Rh: Zooming in by Correlative Microscopy

Johannes Zeininger,<sup>||</sup> Philipp Winkler,<sup>||</sup> Maximilian Raab, Yuri Suchorski, Mauricio J. Prieto, Liviu C. Tănase, Lucas de Souza Caldas, Aarti Tiwari, Thomas Schmidt, Michael Stöger-Pollach, Andreas Steiger-Thirsfeld, Beatriz Roldan Cuenya, and Günther Rupprechter\*



Cite This: *ACS Catal.* 2022, 12, 11974–11983



Read Online

ACCESS |



Metrics & More

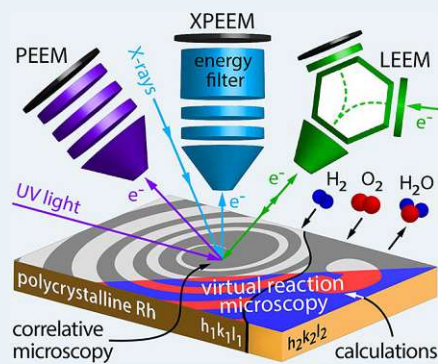


Article Recommendations



Supporting Information

**ABSTRACT:** Spatio-temporal nonuniformities in H<sub>2</sub> oxidation on individual Rh(*hkl*) domains of a polycrystalline Rh foil were studied in the 10<sup>-6</sup> mbar pressure range by photoemission electron microscopy (PEEM), X-ray photoemission electron microscopy (XPEEM), and low-energy electron microscopy (LEEM). The latter two were used for in situ correlative microscopy to zoom in with significantly higher lateral resolution, allowing detection of an unusual island-mediated oxygen front propagation during kinetic transitions. The origin of the island-mediated front propagation was rationalized by model calculations based on a hybrid approach of microkinetic modeling and Monte Carlo simulations.



**KEYWORDS:** catalytic hydrogen oxidation, correlative microscopy, photoemission electron microscopy, low-energy electron microscopy, microkinetic modeling, Monte Carlo modeling

## INTRODUCTION

Heterogeneous catalysis is one of the key enablers of sustainable energy generation and storage. For example, renewable energy can be stored in the chemical bonds of hydrogen and released on-demand via H<sub>2</sub> oxidation in a fuel cell,<sup>1</sup> rendering a fundamental understanding crucial for efficient operation.<sup>2</sup>

The interaction between active sites in a heterogeneous catalytic reaction may lead to spatial nonuniformities of the local reaction rates, which may also vary in time.<sup>3–5</sup> Such pattern formation has often been observed for reactions with oscillatory or multistable kinetics, such as H<sub>2</sub> or CO oxidation, NO reduction, or NO<sub>2</sub> reduction on noble metals,<sup>5–9</sup> and has been a subject of longstanding studies and several reviews.<sup>10–12</sup> Recently, single-crystal studies were extended to more realistic systems, and a number of effects were detected that influence the spatio-temporal structures: multifrequential oscillations, both in μm<sup>-13</sup> and nm-sized<sup>14</sup> systems, frequency transformation by grain boundaries<sup>15</sup> and by atomic rows,<sup>14</sup> coexisting multi-states<sup>16</sup> and nm scale reaction pacemakers.<sup>17</sup> These previous studies have demonstrated the plethora of novel effects that may occur in surface reactions. However, studying aspects such as communication between adjacent domains or facets acting as individual oscillators still remains a challenge. The same concerns the mechanisms of pattern formation on a heterogeneous surface with varying sample

topology. To address these challenges, it is necessary to significantly improve the lateral resolution, preferentially combined with chemical sensitivity. Still, conventional modeling approaches have typically been focused on either mean-field kinetic modeling well applicable to extended homogeneous systems<sup>13,15,16</sup> or Monte Carlo simulations on the traditional atomic length and time scales.<sup>11,18</sup> To combine both approaches for the simulation of processes on mesoscopic heterogeneous surfaces is another challenge in studying surface reactions.

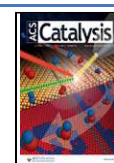
To reveal the mechanisms of spatio-temporal effects, it is advantageous to study these dynamic processes in situ at different length scales using different microscopy techniques. Such an approach was recently applied to monitor CO and H<sub>2</sub> oxidation at different length scales on rhodium samples with different morphologies, i.e., single crystals, μm-sized domains of a polycrystalline foil, and facets of a nanotip.<sup>19,20</sup>

The most straightforward way to draw correct conclusions from such studies is to apply different microscopies to the

Received: July 28, 2022

Revised: August 31, 2022

Published: September 19, 2022



same surface structure, if possible, under the same conditions. The approach stems from biological research, where the first efforts of correlative light and electron microscopy (CLEM) on the same cell/tissue structures were made already in the 1970s.<sup>21,22</sup> In the meantime, CLEM has been extended to a broad category of methods combining any type of light and electron microscopy on the same sample.<sup>23</sup> Actually, other imaging techniques such as atomic force microscopy (AFM), X-ray tomography, and scanning electron microscopy (SEM) are also successfully used in a correlative microscopy approach.<sup>24,25</sup> In the last few decades, correlative analysis has made a vast impact in materials research, combining, e.g., transmission electron microscopy (TEM) with atom probe tomography (APT)<sup>26</sup> or Raman with SEM.<sup>27,28</sup> Using protective coatings, changes in the sample resulting from transfer (air exposure) between different devices can be avoided.<sup>29</sup> In catalysis, the correlative microscopy approach, often applied in different setups,<sup>30–32</sup> has reached its highest development stage when different microscopies, e.g., single-molecule fluorescence microscopy (SMF) and TEM are combined in one instrument.<sup>33</sup> Dual microscopy combinations, such as LEEM/PEEM,<sup>34</sup> LEEM/XPEEM,<sup>35</sup> or PEEM/SPEM,<sup>36</sup> were also previously used to study potassium redistribution in alkali-promoted H<sub>2</sub> oxidation on Rh(110).

Here, we present a refinement of this concept, combining three different microscopic techniques (PEEM, XPEEM, and LEEM) for in situ imaging of catalytic H<sub>2</sub> oxidation on the same structures of the same Rh sample, i.e., in a correlative approach. Two of them, XPEEM (with chemical sensitivity) and LEEM (with a resolution of 2.6 nm, i.e., much better than in conventional PEEM), were even combined in a single setup and thus under truly identical conditions. Additionally, the selected small area (1.5 μm diameter) electron diffraction (μ-LEED) mode of LEEM was used for the determination of the local crystallography.

As a model system, individual differently oriented well-defined μm-sized Rh(*hkl*) domains of a polycrystalline Rh foil were used, all being automatically under identical reaction conditions. The ongoing catalytic reaction was monitored in situ by all three microscopies, and an analysis of the recorded video frames provides time-resolved data of the observed process (kinetics by imaging<sup>37</sup>).

The approach is illustrated in Figure 1a: an individual Rh(*hkl*) domain can be selected from the surface structure library (XPEEM, LEEM), or even a few different domains in the field of view can be studied simultaneously (PEEM). The different employed microscopy techniques vary in magnification, resolution, and origin of the information carriers: secondary (inelastically scattered) electrons form the image in PEEM with UV-light excitation (Figure 1b), core level electrons in XPEEM (Figure 1c), and backscattered low-energy electrons in LEEM (bright-field imaging mode was used, Figure 1d). All available Rh(*hkl*) domains were crystallographically characterized beforehand by electron backscatter diffraction (EBSD). No electron beam and X-ray beam effects were observed in the present experiments. This was directly proven by in situ switching between the XPEEM and LEEM modes in the present study and between LEEM and PEEM<sup>34</sup> as well as between PEEM and metastable impact electron microscopy (MIEEM), known as the least invasive surface analysis method,<sup>38</sup> in earlier experiments on H<sub>2</sub> oxidation on Rh.

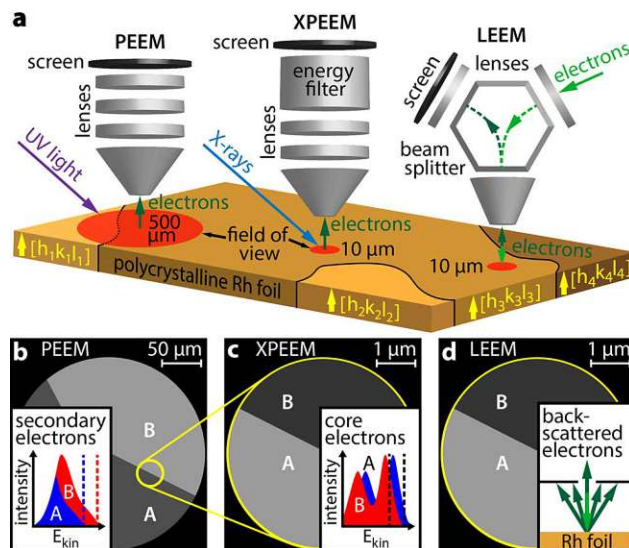


**Figure 1.** Correlative microscopy approach: (a) different information is collected in situ from the same individual domain of a polycrystalline Rh foil using different imaging techniques; (b) in PEEM with UV-light excitation, inelastically scattered photoemitted electrons create the image; (c) in XPEEM with X-ray excitation, energy-filtered core level electrons provide the image contrast; and (d) in LEEM, elastically backscattered electrons are utilized. The bright-field imaging mode with a contrast aperture selecting the specularly reflected electron beam was used.

In the present work, we have taken up the abovementioned pattern formation challenge by studying catalytic H<sub>2</sub> oxidation on Rh, an often-studied reaction that still keeps the mechanisms of spatial propagation hidden. Due to the well-known reaction mechanism, the reaction is well suited for the application of novel modeling approaches. A combined application of PEEM, LEEM, with its significantly higher resolution, and XPEEM, with its chemical sensitivity, all used in situ on the same surface regions, has allowed us to gain unprecedented insights into the mechanisms behind the formation of spatio-temporal patterns. A novel hybrid modeling approach combining microkinetic modeling and Monte Carlo simulations corroborated the experimental data well and allowed time-dependent simulations in a kind of virtual reaction microscopy.

## RESULTS AND DISCUSSION

**PEEM Studies.** The ongoing H<sub>2</sub> oxidation reaction on Rh was visualized in an ultrahigh vacuum (UHV) PEEM setup operated as a flow reactor. The setup is equipped with a deuterium discharge lamp (Heraeus D200F, photon energy ~6.5 eV) for UV illumination, a Staib Instruments PEEM 150 system, a high-speed CCD camera (Hamamatsu C11440-42U30), a quadrupole mass spectrometer (MKS e-Vison 2), gas dosing (Ar, H<sub>2</sub>, O<sub>2</sub>; purity 99.999%), and sample cleaning facilities. More details on the experimental procedures are given in the Supporting Information.

Figure 2a shows a PEEM snapshot from a video sequence recorded during the ongoing reaction at constant  $T = 468$  K,  $p_{\text{H}_2} = 4.5 \times 10^{-7}$  mbar,  $p_{\text{O}_2} = 5.0 \times 10^{-7}$  mbar. The image contrast results from the differences in the local work function, which in turn depends on the adsorbate coverage: the catalytically inactive (oxygen-covered) Rh(*hkl*) surface appears generally darker than the catalytically active (low



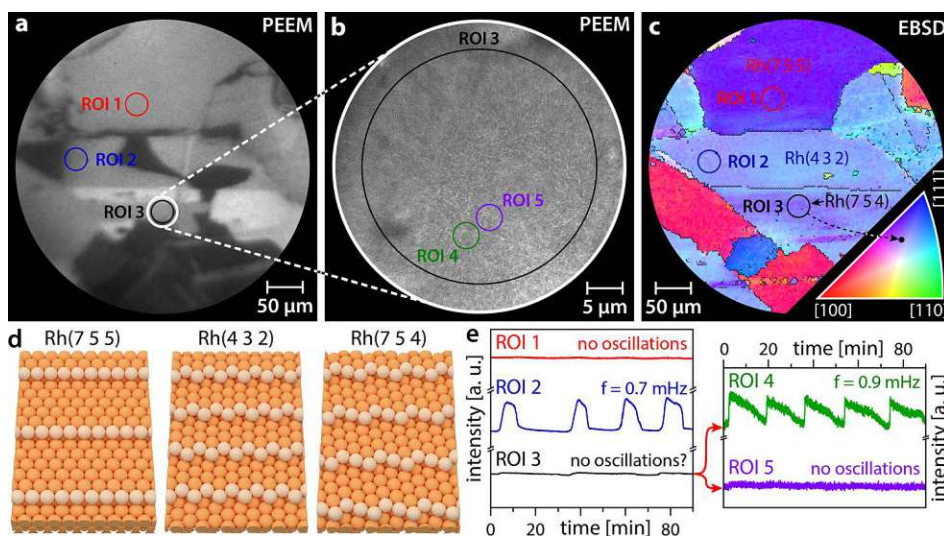


**Figure 2.** PEEM zoom-in on catalytic H<sub>2</sub> oxidation on a polycrystalline Rh foil at  $p_{\text{H}_2} = 4.5 \times 10^{-7}$  mbar,  $p_{\text{O}_2} = 5.0 \times 10^{-7}$  mbar, and  $T = 468$  K: (a) PEEM snapshot taken during the ongoing reaction with three regions of interest (ROIs) marked; (b) electron-optical zoom-in (10-fold higher magnification) PEEM snapshot of the region marked by a white circle in panel (a); (c) EBSD map and crystallographic orientations (Miller indices) of the same region with the same ROIs as in panel (a); the legend for the color code is given as an inset in the lower right corner; (d) ball models of the Rh(7 5 5), Rh(4 3 2), and Rh(7 5 4) surfaces; and (e) time series of the local PEEM intensities obtained for the structurally different ROIs marked in panels (a) and (b).

H<sub>ads</sub> and O<sub>ads</sub> coverage) surface due to the higher work function of the oxygen-covered Rh surface. An illustration of the catalytically active and inactive states is given in the Supporting Information (Figure S2).

To study the reaction behavior on structurally different Rh(*hkl*) domains, the local PEEM intensity was analyzed for different regions of interest (ROIs) on the surface. Three ROIs were placed on different Rh(*hkl*) regions, crystallographically defined by EBSD in a field emission scanning electron microscope (FEI Quanta 200F, further details are given in the Supporting Information). The corresponding local PEEM intensity time series are shown in Figure 2e, revealing cardinal differences in the kinetic behavior of different regions: ROI 1 constantly remains in the catalytically active state, whereas ROI 2 shows a self-sustaining oscillating mode of the reaction (frequency 0.7 mHz). The reaction course for ROI 3 is actually not clear: oscillatory behavior can neither be presumed nor excluded.

To explain the remarkable differences in the local reaction behavior, we refer to the color-coded EBSD map in Figure 2c, with the color code given as an inset in the lower right corner. The EBSD characterization reveals that ROIs 1 and 2 are located on homogeneous Rh(7 5 5) and Rh(4 3 2) domains, respectively, while ROI 3 was placed within a domain of a rather heterogeneous surface structure.

The reaction modes observed at the present conditions for the homogeneous Rh(7 5 5) and Rh(4 3 2) domains can be understood in view of recent studies in which different reaction modes of H<sub>2</sub> oxidation were simultaneously observed on adjacent crystallographically different regions.<sup>16</sup> The Rh(7 5 5) surface (ROI 1) is characterized by [1 1 1]-type terraces in combination with nonkinked [1 0 0]-type step edges. The Rh(4 3 2) surface (ROI 2) is also characterized by [1 1 1]-type terraces but combined with kinked [2 1 0]-type step edges. This is illustrated in atomic ball models in Figure 2d. The structural differences lead to differing kinetic behavior: as recently shown, the formation and depletion of subsurface

oxygen on the Rh(*hkl*) surfaces and the resulting enabling or inhibition of dissociative hydrogen adsorption may lead to self-sustaining oscillations in H<sub>2</sub> oxidation, with the activation energy of the oxygen incorporation governing the oscillation frequency.<sup>13–16</sup> An illustration of the oscillation cycle and further details of the mechanism of the oscillations are presented in the Supporting Information (Figure S2) and have been extensively discussed previously.<sup>13–16</sup> For Rh, the activation energy of subsurface oxygen formation strongly varies with the surface roughness, with the kink sites playing a particular role.<sup>39</sup> The Rh(4 3 2) surface exhibits kinked step edges, which accelerates the formation/depletion of subsurface oxygen compared to the nonkinked Rh(7 5 5) surface. This leads to the observed oscillatory reaction behavior on the Rh(4 3 2) surface, whereas the Rh(7 5 5) surface remains in the catalytically active state at the present conditions.

To evaluate the reaction behavior within ROI 3, where the discrimination between a possible steady state and oscillatory behavior seems difficult, the reaction was monitored at the same conditions but with an electron-optical magnification 10 times higher than that of Figure 2a. Figure 2b shows the corresponding PEEM video frame, revealing instable bright and dark spots that are invisible at lower magnification. Placing additional ROIs (ROIs 4 and 5) on such spots and evaluating the local PEEM intensities yield the two time series displayed in the right panel of Figure 2e. While the PEEM intensity read out from ROI 5 remains constant, the intensity within ROI 4 oscillates with a frequency of 0.9 mHz. Apparently, on a structurally heterogeneous Rh surface, similar phenomena as represented by the three curves in the left panel of Figure 2e take place but on a much smaller length scale, possibly due to a significantly smaller correlation length of individual oscillating regions due to structural peculiarities. The black curve (ROI 3) in Figure 2e thus represents a weighted sum of both oscillating and nonoscillating surface regions, which accounts for the difficulties in interpreting the behavior when averaging over the whole ROI. To understand these phenomena, alternative

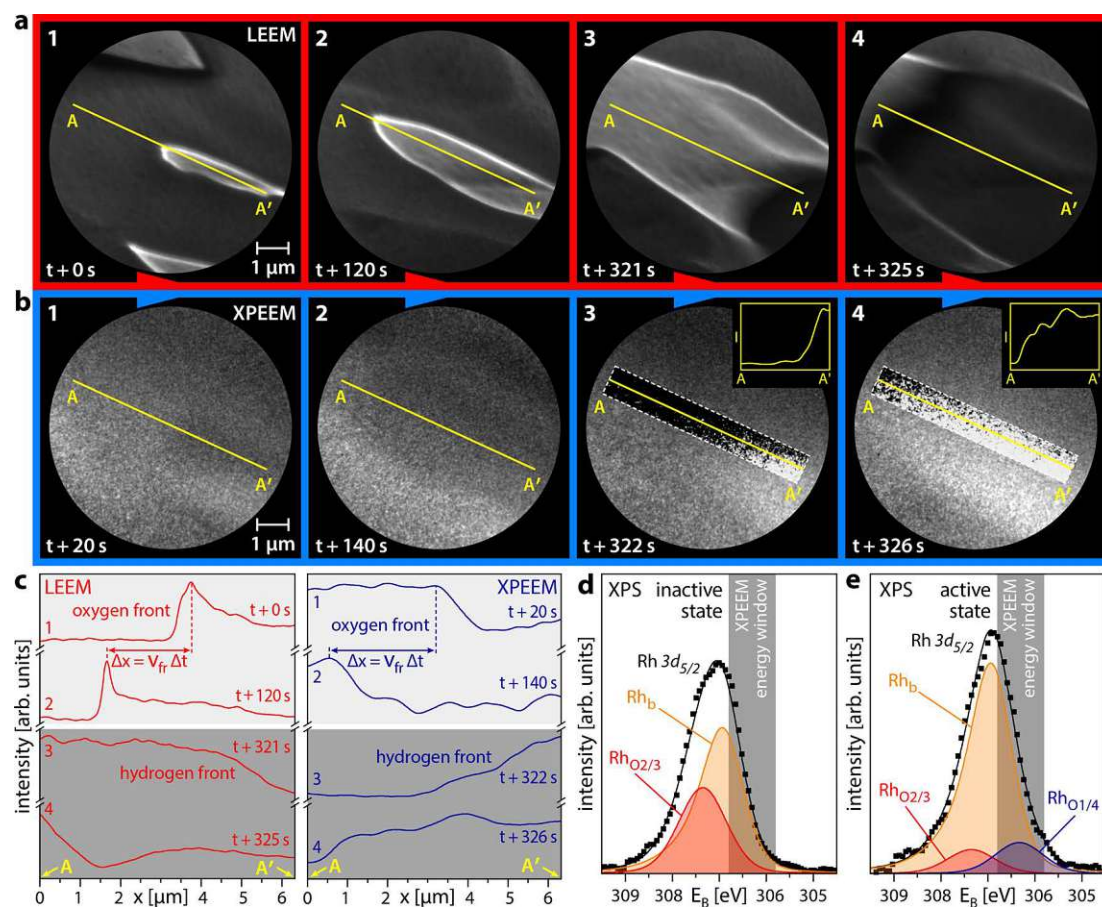


**Figure 3.** Reaction front identification using correlative microscopy: (a) bright-field LEEM images of oxygen front propagation (frames 1 and 2) and hydrogen front propagation (frames 3 and 4) on the Rh(7 5 4) domain at  $p_{\text{H}_2} = 4.5 \times 10^{-7}$  mbar,  $p_{\text{O}_2} = 5.0 \times 10^{-7}$  mbar,  $T = 468$  K, and electron energy = 2.5 eV; (b) the same, but imaged with XPEEM, the used binding energy window is shaded gray in panels (d) and (e). In the dashed rectangular regions, the image contrast is enhanced locally for better front visibility, the insets in frames 3 and 4 illustrate the front positions; (c) local LEEM (left) and XPEEM (right) image intensity profiles obtained from the original data along the A–A′ line in panels (a) and (b), the principle of the determination of the front propagation velocity is illustrated; (d) Rh 3d XPS spectra locally measured on the Rh(7 5 4) domain for the catalytically inactive state in H<sub>2</sub> oxidation. Deconvolution of the peaks provides the Rh<sub>b</sub> and Rh<sub>O<sub>2/3</sub></sub> components; (e) the same, but for the catalytically active state, with an additional Rh<sub>O<sub>1/4</sub></sub> component present in the deconvolution, identifying the hydrogen front.

imaging methods with much higher magnification, resolution, and chemical contrast appear promising.

**Correlative LEEM and XPEEM Studies.** As such alternative imaging methods, the LEEM and XPEEM modes of the aberration-corrected photoemission electron microscope equipped with an imaging energy analyzer (SMART) at the UE49-PGM beamline of the BESSY II synchrotron light source in Berlin were used (resolution limits of 2.6 and 18 nm for LEEM and XPEEM, respectively).<sup>40,41</sup> These modes of the SMART microscope, described in detail elsewhere,<sup>42,43</sup> were applied in a correlative microscopy approach, combining the imaging of the same sample by backscattered low-energy electrons (LEEM) and X-ray photoemitted electrons (XPEEM). A 7.5 μm field of view was chosen for the present studies to capture the processes of interest. The local surface crystallography was determined by μ-LEED (see the Supporting Information), while μ-XPS was used for local chemical analysis. The UHV chamber of the SMART microscope was used as a flow reactor for in situ visualization of catalytic H<sub>2</sub> oxidation on the same sample as in the PEEM studies. The bright-field LEEM mode using the (00)-diffracted electron beam for imaging was applied to monitor the reaction.

The LEEM image contains structural contrast but no direct chemical information, which can be gained by XPEEM, however.

Figure 3a shows selected LEEM video frames of the reaction front propagation during self-sustained oscillations on a Rh(7 5 4) domain at constant  $T = 468$  K,  $p_{\text{H}_2} = 4.5 \times 10^{-7}$  mbar,  $p_{\text{O}_2} = 5.0 \times 10^{-7}$  mbar. Two different types of reaction fronts were observed: a slow-moving front in frames 1 and 2 (time difference of 120 s) and a fast-moving front in frames 3 and 4 (time difference of 4 s). To understand the chemical information encoded in the image contrast in Figure 3a, similar series of Rh 3d XPEEM video frames ( $h\nu = 433$  eV) were acquired, as exemplarily shown in Figure 3b. The image contrast in Figure 3b results from an energy window for Rh 3d XPEEM imaging being chosen in the range 305.8–306.8 eV, marked in gray in Figure 3d,e. The choice of this energy window is based on the local Rh 3d μ-XPS spectra of the catalytically inactive and active states on the Rh(7 5 4) domain, shown in Figure 3d,e, respectively. Deconvolution of the measured XPS spectra was performed based on literature data and is discussed in refs 16, 44–47. The spectra include a Rh bulk component (Rh<sub>b</sub>) and two components for two different

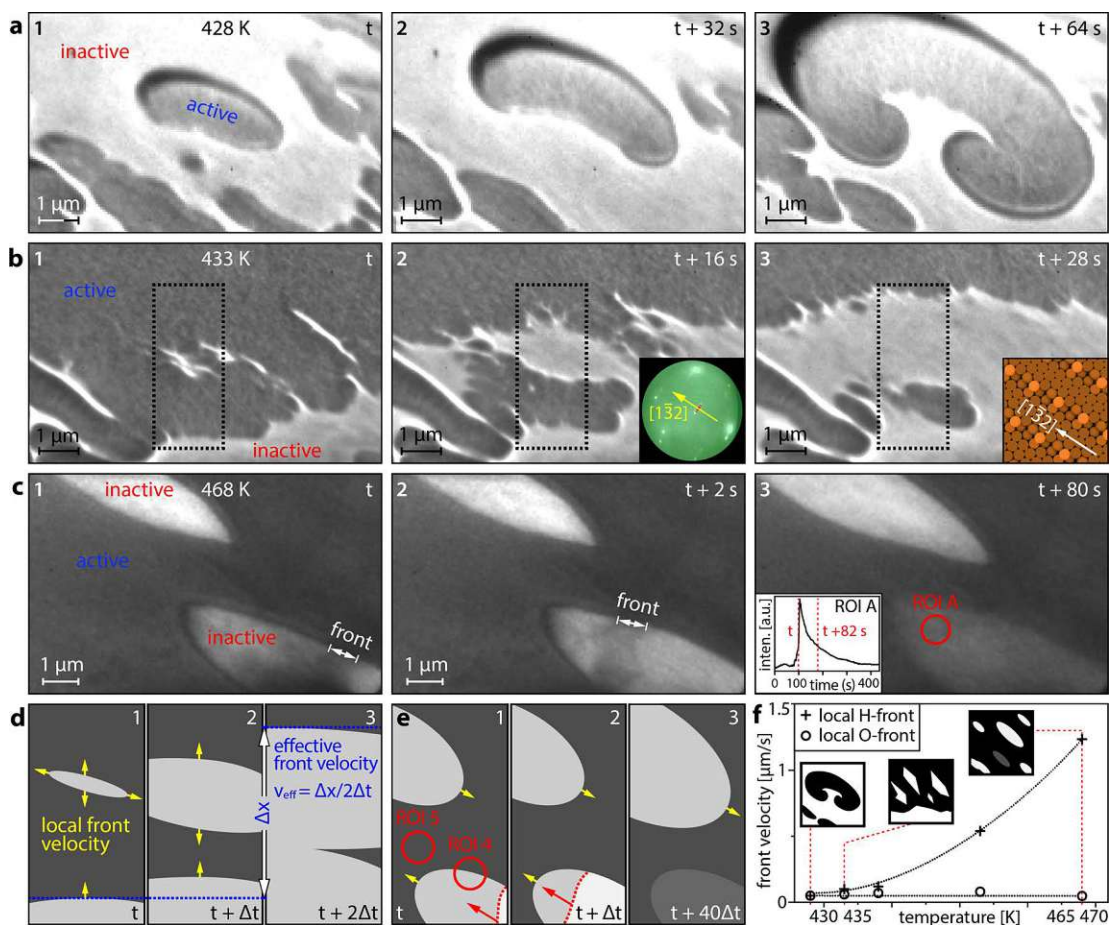


**Figure 4.** Pattern formation in catalytic H<sub>2</sub> oxidation on Rh(7 5 4) visualized by LEEM at constant  $p_{\text{H}_2} = 4.5 \times 10^{-7}$  mbar and  $p_{\text{O}_2} = 5.0 \times 10^{-7}$  mbar: (a) rotating double spiral formed at 428 K. Catalytically inactive regions appear bright, while active regions appear dark in the LEEM video frames (electron energy 2.5 eV); (b) island-assisted front propagation at 433 K. The inset in frame 2 shows a  $\mu$ -LEED image taken from the same region at  $E = 330$  eV, the red dotted line illustrates the spot splitting, and the yellow arrow shows the step direction. The inset in frame 3 shows the corresponding surface structure; (c) collapse of an oxygen island before it can coalesce with other islands at 468 K. The position of the hydrogen front is indicated in frames 1 and 2. The inset in frame 3 shows the intensity recorded in ROI A during the kinetic transition, the time points corresponding to frames 1 and 3 are indicated, all frames in panel (c) are recorded at an electron energy of 3.3 eV; (d) schematic illustration of the island-assisted front propagation, each third corresponds to the black dotted rectangles in frames 1–3 in panel (b); (e) schematic illustration of the oxygen island collapse, ROIs 4 and 5 schematically represent the corresponding ROIs in Figure 2b; (f) local velocities of the hydrogen (crosses) and oxygen (circles) fronts. The cartoon insets depict the different patterns shown in panels (a) to (c). The red dotted lines indicate the temperatures at which the sketched patterns are observed, and the black dotted lines serve as guides for the eye.

adsorbed oxygen species ( $\text{Rh}_{\text{O}_{2/3}}$  and  $\text{Rh}_{\text{O}_{1/4}}$ , where  $i$  and  $j$  in  $\text{Rh}_{\text{O}_{ij}}$  denote the number of O atoms each Rh surface atom is bound to and the number of Rh surface atoms each O atom is bound to, respectively).

The presence of the  $\text{Rh}_{\text{O}_{1/4}}$  component is unambiguously related to the active state in catalytic H<sub>2</sub> oxidation. The physical reasons for this relation are clarified in our previous XPS study.<sup>16</sup> By choosing the proper energy window, this component can thus be used as a basis for the contrast in XPEEM, imaging the extent of the active state on the surface. For better visualization of the reaction fronts, the image contrast of the original XPEEM video frames was locally enhanced within the white dashed rectangles in frames 3 and 4 of Figure 3b. Line profiles along the A–A' line, shown in the insets of frames 3 and 4 of Figure 3b, illustrate the determination of reaction front positions. Analysis of the front positions provides the velocities of the reaction fronts, as shown in Figure 3c.

Comparison of the front velocities in the video files then allows relating the image contrast in LEEM and XPEEM: at the used electron energies of 2.5–3.5 eV, the inactive state (high oxygen coverage) appears bright in LEEM but dark in XPEEM, whereas the active state (low hydrogen and oxygen coverage) is dark in LEEM but bright in XPEEM. This means that the transition from dark to bright in LEEM equals a transition from bright to dark in XPEEM and vice versa.

Understanding the image contrast in LEEM allows spatially resolved studies of local instabilities with  $\sim 20$  nm resolution (at the given magnification), which were merely time-resolved in PEEM (Figure 2e). Figure 4 shows the formation of spatio-temporal patterns at different temperatures in the range 428–468 K, with the reactant pressures kept constant at  $p_{\text{H}_2} = 4.5 \times 10^{-7}$  mbar and  $p_{\text{O}_2} = 5.0 \times 10^{-7}$  mbar. As an example, Figure 4a displays how during a kinetic transition at 428 K accompanying each oscillation cycle, the propagating hydrogen and oxygen fronts form a rotating double spiral pattern, a

phenomenon known from PEEM studies to occur on a much larger length scale.<sup>48</sup>

Figure 4b illustrates the propagation of the oxygen front at 433 K, which proceeds in an unusual way: ahead of the front, due to the anisotropy of the Rh(7 5 4) surface, plenty of elongated oxygen islands nucleate and grow (frame 1 in Figure 4b), forming oxygen archipelagos ahead of the traveling front (frame 2). Eventually, the archipelagos conglomerate via the development of dendritic structures and merge when the moving oxygen front reaches the oxygen islands (frame 3). To our knowledge, such an island-assisted propagation mechanism was not yet observed, neither in H<sub>2</sub> oxidation nor in any other heterogeneous catalytic reaction. Each nucleating island possesses its “local front” along the island perimeter, propagating with its local velocity  $v_{loc}$ , which is different from the effective velocity  $v_{eff}$  of the mesoscopically observed front (without resolving the nucleating islands). Figure 4d shows a schematic drawing of this concept, where  $v_{eff} = 3 \cdot v_{loc}$  by the formation of a singular island ahead of the moving front. For the hydrogen front, such island-assisted front propagation was not observed; therefore,  $v_{eff}$  is equal to  $v_{loc}$  for hydrogen.

The unique ability of the SMART microscope to directly correlate the orientation of real space images (LEEM) with diffraction patterns obtained for the reciprocal space ( $\mu$ -LEED)<sup>42,43</sup> allows us to identify the preferential direction of the front propagation. The latter appears to be along the [1 1 1]-type terraces of the stepped Rh(7 5 4) surface, i.e., in the [1 3 2]-direction, as illustrated by the insets in Figure 4b (details of the crystallographic analysis and  $\mu$ -LEED patterns of the studied surface regions are given in the Supporting Information). Such preferential front propagation along the terraces of stepped Rh surfaces was previously observed in H<sub>2</sub> oxidation and is caused by anisotropy of the diffusional hydrogen supply along vs across the atomic steps.<sup>19</sup>

At an even higher temperature of 468 K, kinetic transitions to the active state occur via fast “island-snapping” hydrogen fronts (Figure 4c and schematic illustration in Figure 4e) without island agglomeration. In video frames 1 and 2 of Figure 4c, the fast front appears as a stripe and not as a line due to the blurring caused by the exposure time of 2 s for each LEEM video frame. The origin of such island-mediated transition lies in the subsurface oxygen formation/depletion, which serves as a feedback and “clock” mechanism governing the frequency of the self-sustained oscillations in H<sub>2</sub> oxidation on Rh.<sup>13–16</sup> At rising temperatures, the formation/depletion of subsurface oxygen occurs faster and the clock frequency increases, eventually leading to kinetic transitions within the growing oxygen islands before they can coalesce with other islands. The LEEM videos of the three different types of pattern formation at 428, 433, and 468 K are given in the Supporting Information. Such transitions can be registered even in PEEM as sawtooth-like local oscillations (ROI 4 in Figure 2e).

The sawtooth shape of the intensity curves, shown in the inset of frame 3 in Figure 4c, reflects the fast “avalanche-like” snapping of the oxygen islands by hydrogen fronts and the following relatively slow relaxation due to subsurface oxygen depletion, as schematically shown in Figure 4e. The temperature dependence of the local front velocities for oxygen and hydrogen is displayed in Figure 4f. While the local hydrogen front velocity shows an exponential increase with rising temperature, the local velocity of the oxygen front remains approximately constant. The temperature-dependent differ-

ences in the local velocities of reaction fronts during self-sustained oscillations allow us to explain the formation of qualitatively different patterns at different temperatures. At 428 K, the local velocities of hydrogen and oxygen fronts are equal, which favors the formation of spiral patterns,<sup>48</sup> as observed in the present experiments (Figure 4a). At 433 K, the local hydrogen front is about two times faster than the local oxygen front, which can only partially be compensated by island-assisted propagation; thus, no spiral nuclei are formed anymore,<sup>49</sup> favoring the island-assisted oxygen front propagation in the form of a “frayed” inactive area (frame 3 in Figure 4b). At 468 K, the discrepancy of local velocities appears to be too high for the formation of a mesoscopic front: the growing oxygen islands are “snapped” by fast island-internal hydrogen fronts before they can merge. Therefore, mesoscopic fronts are not visible in PEEM within ROI 3 in Figure 2 despite plenty of local instabilities occurring on a smaller length scale at the present conditions. Since the nucleation of oxygen islands occurs most probably via reaction-induced fluctuations,<sup>18</sup> the nucleating/collapsing islands are stochastically distributed over the surface, occasionally leaving space for regions that also locally remain temporarily nonoscillating, as visible in ROI 5 in Figure 2e.

**Modeling.** To rationalize the experimental findings and to investigate the influence of differences between the front propagation of hydrogen and oxygen on the observed pattern formation, theoretical simulations were performed. Usually, a mean-field approach, which ignores the nonideality of surface rate processes and the stochastic components of adsorption, desorption, and reaction, is used for microkinetic modeling of pattern formation. The alternative use of the Monte Carlo method, which is superior for the simulation of pattern formation on the nm scale,<sup>11</sup> is still a challenge for simulation of patterns on the  $\mu$ m scale because of limitations in lattice size, rate constants, and calculations of the elementary steps of diffusion. Therefore, a novel model was developed based on a hybrid approach of complementary microkinetic modeling (MKM) and Monte Carlo (MC) simulations, with the goal of realistically describing the experimental microscopy observations. The Langmuir–Hinshelwood mechanism that is well established for catalytic hydrogen oxidation and the formation and depletion of subsurface oxygen as feedback mechanism of the oscillations were assumed. The calculations provide the time-dependent spatial distribution of the catalytically active and inactive states and, thus, allow monitoring the simulated pattern formation, in a kind of virtual reaction microscopy.

In the MC calculations, a hexagonal tiling MC-grid consisting of 160 000 tiles corresponding to a  $40 \times 34.6 \mu\text{m}^2$  area of the sample surface was used. A simplified MC approach was chosen, where the state of each of the tiles is either catalytically active (low O and H coverage) or catalytically inactive (high O coverage). Transitions between these states occur via two possible pathways: internally, by local oxygen or hydrogen adsorption, which is mediated by the local  $O_{sub}$  concentration, or externally, via reaction/diffusion fronts propagating from neighboring grid points. These events are governed by MC, while MKM is used to determine the local probabilities for each event to occur and to calculate the formation/depletion of  $O_{sub}$  based on the current local coverages (details of the calculations are given in the Supporting Information).

Simulations were performed for the same partial pressures of reactants as used in the experiment ( $p_{H_2} = 4.5 \times 10^{-7}$  mbar

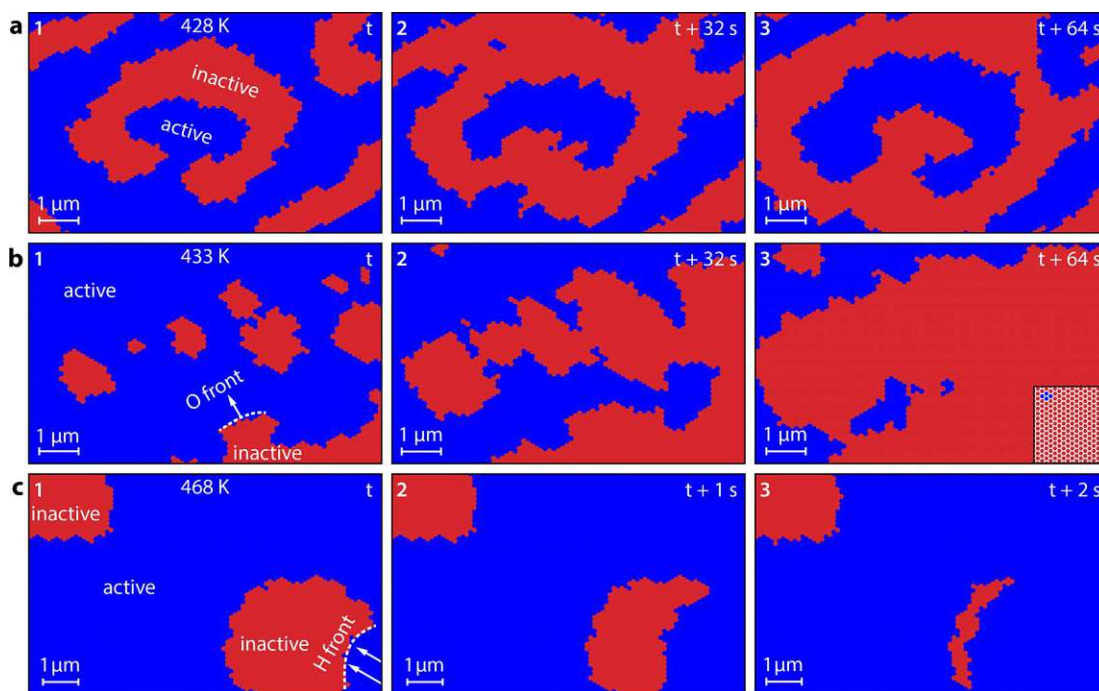


**Figure 5.** Virtual reaction microscopy of catalytic H<sub>2</sub> oxidation on Rh at constant  $p_{\text{H}_2} = 4.5 \times 10^{-7}$  mbar and  $p_{\text{O}_2} = 5.0 \times 10^{-7}$  mbar: (a) calculated pattern formation at 428 K. Catalytically active regions (low hydrogen and oxygen coverage) are colored blue, and catalytically inactive regions (oxygen-covered) are colored red. A double spiral is recognizably formed in the middle of the image; (b) island-assisted front propagation at 433 K: the white dotted line marks the main front position, the inset in frame 3 shows a part of the hexagonal tiling MC-grid; (c) simulation results at 468 K: the oxygen islands are snapped by hydrogen fronts (white dotted line) before the islands can grow together.

and  $p_{\text{O}_2} = 5.0 \times 10^{-7}$  mbar), only varying the temperature. For all calculations, the same set of MKM parameters was used (details are given in the Supporting Information). Results of the simulations are displayed in Figure 5. Figure 5a shows the formation of patterns at  $T = 428$  K, where characteristic double spirals are formed. Both hydrogen and oxygen fronts propagate with the same velocity. The simulations closely mirror the pattern formation observed in the experiment at the same temperature (Figure 4a).

At 433 K, hydrogen fronts propagate much faster, but oxygen fronts keep their velocity which is now about one-third of that of hydrogen. The simulations predict the formation and growth of additional small oxygen islands ahead of the main front in the right lower corner of frame 1 (Figure 5b). Eventually, the main oxygen front fuses with these islands (frames 2 and 3). Incorporation of islands contributes to the oxygen front propagation, thus increasing the effective front velocity, which therefore approaches the hydrogen front velocity. Indeed, such a front propagation mechanism was exactly observed in the experiments as island-assisted front propagation (Figure 4b,d).

When increasing the temperature parameter to 468 K, where the hydrogen front is about 2 orders of magnitude faster than the oxygen front, the calculations provide a very different behavior (Figure 5c). Oxygen islands slowly grow until, eventually, one nucleation spot, preferentially at the edge of the island, spontaneously undergoes a sudden transition to the active state, forming a fast hydrogen front that “devours” the whole oxygen island, preventing the fusion with other islands. Again, the calculations reproduce the specific experimentally observed behavior at the same conditions well (Figure 4c,e).

Since the size of the MC-grid and the dimensions of each grid tile can be chosen arbitrarily, both the size of the field of

view and the time interval between calculated images are not limited. This allows calculating a stack of surface snapshots (exemplary presented in Figure 5), which can be assembled to a virtual video file (calculated videos are given in the Supporting Information). By convoluting the adsorbate concentrations with a proper contrast mechanism, different imaging modes can be simulated without experimental limitations, such as the size of the field of view or the duration of the experiment. Additionally, such calculated virtual reaction microscopy videos can be processed using the same tools, which are applied to experimental video data complementing the insights into the observed phenomena.<sup>17,37,50</sup>

## CONCLUSIONS

In conclusion, we have performed a microscopic study of pattern formation in H<sub>2</sub> oxidation on Rh using PEEM, LEEM, and XPEEM in a correlative microscopy approach, taking up important challenges in studying this catalytic surface reaction. Due to their significantly higher lateral resolution, LEEM and XPEEM allowed zooming in on processes observed by PEEM, enabling the detection of an unusual island-mediated oxygen front propagation during kinetic transitions. To rationalize the experimental findings, theoretical simulations were performed using a novel model based on a hybrid approach of microkinetic modeling and Monte Carlo, which allows us to realistically simulate the spatio-temporal surface processes in a kind of virtual reaction microscopy on realistic length and time scales. The results of the calculations agree well with the experimental observations and provide novel insights into the mechanism of pattern formation in catalytic hydrogen oxidation on platinum group metals.

## ■ ASSOCIATED CONTENT

### SI Supporting Information

The Supporting Information is available free of charge at <https://pubs.acs.org/doi/10.1021/acscatal.2c03692>.

Details on experimental procedures, determination of the local crystallography by  $\mu$ -LEED, and model calculations (PDF)

Movie S1: In situ low-energy electron microscopy video at 428 K, showing an evolving double spiral pattern during the self-sustaining oscillations in hydrogen oxidation on a Rh(7 5 4) surface (MP4)

Movie S2: In situ low-energy electron microscopy video at 433 K, showing the island-assisted front propagation mechanism during the self-sustaining oscillations in hydrogen oxidation on a Rh(7 5 4) surface (MP4)

Movie S3: In situ low-energy electron microscopy video at 468 K, showing oxygen “island-snapping” by fast hydrogen fronts during the self-sustaining oscillations in hydrogen oxidation on a Rh(7 5 4) surface (MP4)

Movie S4: Model simulation as a virtual reaction microscopy video at 428 K, showing an evolving double spiral pattern during calculated oscillations of the simulated catalytic activity on a grid of 160 000 individual grid tiles (MP4)

Movie S5: Model simulation as a virtual reaction microscopy video at 433 K, showing the island-assisted front propagation mechanism during calculated oscillations of the simulated catalytic activity on a grid of 160 000 individual grid tiles (MP4)

Movie S6: Model simulation as a virtual reaction microscopy video at 468 K, showing oxygen “island-snapping” by fast hydrogen fronts during calculated oscillations of the simulated catalytic activity on a grid of 160 000 individual grid tiles (MP4)

## ■ AUTHOR INFORMATION

### Corresponding Author

**Günther Rupprechter** – Institute of Materials Chemistry, TU Wien, 1060 Vienna, Austria; [orcid.org/0000-0002-8040-1677](https://orcid.org/0000-0002-8040-1677); Email: [guenther.rupprechter@tuwien.ac.at](mailto:guenther.rupprechter@tuwien.ac.at)

### Authors

**Johannes Zeininger** – Institute of Materials Chemistry, TU Wien, 1060 Vienna, Austria

**Philipp Winkler** – Institute of Materials Chemistry, TU Wien, 1060 Vienna, Austria

**Maximilian Raab** – Institute of Materials Chemistry, TU Wien, 1060 Vienna, Austria

**Yuri Suchorski** – Institute of Materials Chemistry, TU Wien, 1060 Vienna, Austria; [orcid.org/0000-0002-6996-1745](https://orcid.org/0000-0002-6996-1745)

**Mauricio J. Prieto** – Department of Interface Science, Fritz-Haber-Institut der Max-Planck Gesellschaft, D-14195 Berlin, Germany; [orcid.org/0000-0002-5087-4545](https://orcid.org/0000-0002-5087-4545)

**Liviu C. Tănase** – Department of Interface Science, Fritz-Haber-Institut der Max-Planck Gesellschaft, D-14195 Berlin, Germany; [orcid.org/0000-0002-4177-5676](https://orcid.org/0000-0002-4177-5676)

**Lucas de Souza Caldas** – Department of Interface Science, Fritz-Haber-Institut der Max-Planck Gesellschaft, D-14195 Berlin, Germany; [orcid.org/0000-0002-5499-4712](https://orcid.org/0000-0002-5499-4712)

**Aarti Tiwari** – Department of Interface Science, Fritz-Haber-Institut der Max-Planck Gesellschaft, D-14195 Berlin, Germany

**Thomas Schmidt** – Department of Interface Science, Fritz-Haber-Institut der Max-Planck Gesellschaft, D-14195 Berlin, Germany; [orcid.org/0000-0003-4389-2080](https://orcid.org/0000-0003-4389-2080)

**Michael Stöger-Pollach** – University Service Center for Transmission Electron Microscopy, TU Wien, 1040 Vienna, Austria

**Andreas Steiger-Thirsfeld** – University Service Center for Transmission Electron Microscopy, TU Wien, 1040 Vienna, Austria

**Beatriz Roldan Cuenya** – Department of Interface Science, Fritz-Haber-Institut der Max-Planck Gesellschaft, D-14195 Berlin, Germany; [orcid.org/0000-0002-8025-307X](https://orcid.org/0000-0002-8025-307X)

Complete contact information is available at: <https://pubs.acs.org/doi/10.1021/acscatal.2c03692>

### Author Contributions

<sup>||</sup>J.Z. and P.W. contributed equally to this work. J.Z., P.W., M.J.P., L.C.T., L.d.S.C., A.T., T.S., and G.R. performed the XPEEM, LEEM, and  $\mu$ -LEED measurements. P.W. performed the PEEM measurements. A.S.-T. and M.S.-P. performed the EBSD characterization. J.Z., P.W., and M.R. evaluated the PEEM, XPEEM, and LEEM data. J.Z., P.W., M.R., and T.S. evaluated the  $\mu$ -LEED data. M.R. performed the model simulations. Y.S., T.S., B.R.C., and G.R. supervised the work. J.Z., P.W., M.R., Y.S., and G.R. prepared the manuscript. All authors contributed to the discussion and approved the manuscript.

### Funding

Open Access is funded by the Austrian Science Fund (FWF).

### Notes

The authors declare no competing financial interest.

## ■ ACKNOWLEDGMENTS

This work was supported by the Austrian Science Fund (FWF) (P 32772-N and F81-P08). The authors would also like to thank the Helmholtz-Center Berlin for Materials and Energy (HZB) for the allocation of beamtime 212-10440-ST. The SMART instrument was financially supported by the Federal German Ministry of Education and Research (BMBF) under contract 05 KS4WWB/4, as well as by the Max Planck Society.

## ■ REFERENCES

- (1) Nehrhr, M. H.; Wang, C. Fuel Cells. In *Electric Renewable Energy Systems*, Elsevier, 2016; pp 92–113.
- (2) Rego de Vasconcelos, B.; Lavoie, J.-M. Recent Advances in Power-to-X Technology for the Production of Fuels and Chemicals. *Front. Chem.* **2019**, *7*, No. 392.
- (3) Volford, A.; Simon, P. L.; Farkas, H.; Noszticzus, Z. Rotating Chemical Waves: Theory and Experiments. *Phys. Stat. Mech. Appl.* **1999**, *274*, 30–49.
- (4) Kiss, I. Z.; Hudson, J. L. Chemical Complexity: Spontaneous and Engineered Structures. *AIChE J.* **2003**, *49*, 2234–2241.
- (5) Ertl, G. Reactions at Surfaces: From Atoms to Complexity (Nobel Lecture). *Angew. Chem., Int. Ed.* **2008**, *47*, 3524–3535.
- (6) Jakubith, S.; Rotermund, H. H.; Engel, W.; von Oertzen, A.; Ertl, G. Spatiotemporal Concentration Patterns in a Surface Reaction: Propagating and Standing Waves, Rotating Spirals, and Turbulence. *Phys. Rev. Lett.* **1990**, *65*, 3013–3016.
- (7) Sachs, C.; Hildebrand, M.; Völkening, S.; Wintterlin, J.; Ertl, G. Spatiotemporal Self-Organization in a Surface Reaction: From the Atomic to the Mesoscopic Scale. *Science* **2001**, *293*, 1635–1638.
- (8) Barroo, C.; De Decker, Y.; Visart de Bocarmé, T.; Kruse, N. Emergence of Chemical Oscillations from Nanosized Target Patterns. *Phys. Rev. Lett.* **2016**, *117*, No. 144501.

- (9) Barroo, C.; Wang, Z.-J.; Schlögl, R.; Willinger, M.-G. Imaging the dynamics of catalyzed surface reactions by in situ scanning electron microscopy. *Nat. Catal.* **2020**, *3*, 30–39.
- (10) *Chemical Waves and Patterns* Kapral, R.; Showalter, K., Eds.; Springer Netherlands: Dordrecht, 1995.
- (11) Zhdanov, V. P. Monte Carlo Simulations of Oscillations, Chaos and Pattern Formation in Heterogeneous Catalytic Reactions. *Surf. Sci. Rep.* **2002**, *45*, 231–326.
- (12) Luss, D.; Sheintuch, M. Spatiotemporal Patterns in Catalytic Systems. *Catal. Today* **2005**, *105*, 254–274.
- (13) Suchorski, Y.; Datler, M.; Bespalov, I.; Zeininger, J.; Stöger-Pollach, M.; Bernardi, J.; Grönbeck, H.; Rupprechter, G. Visualizing Catalyst Heterogeneity by a Multifrequential Oscillating Reaction. *Nat. Commun.* **2018**, *9*, No. 600.
- (14) Suchorski, Y.; Zeininger, J.; Buhr, S.; Raab, M.; Stöger-Pollach, M.; Bernardi, J.; Grönbeck, H.; Rupprechter, G. Resolving Multifrequential Oscillations and Nanoscale Interfacet Communication in Single-Particle Catalysis. *Science* **2021**, *372*, 1314–1318.
- (15) Suchorski, Y.; Datler, M.; Bespalov, I.; Zeininger, J.; Stöger-Pollach, M.; Bernardi, J.; Grönbeck, H.; Rupprechter, G. Surface-Structure Libraries: Multifrequential Oscillations in Catalytic Hydrogen Oxidation on Rhodium. *J. Phys. Chem. C* **2019**, *123*, 4217–4227.
- (16) Winkler, P.; Zeininger, J.; Raab, M.; Suchorski, Y.; Steiger-Thirsfeld, A.; Stöger-Pollach, M.; Amati, M.; Gregoratti, L.; Grönbeck, H.; Rupprechter, G. Coexisting Multi-States in Catalytic Hydrogen Oxidation on Rhodium. *Nat. Commun.* **2021**, *12*, No. 6517.
- (17) Zeininger, J.; Suchorski, Y.; Raab, M.; Buhr, S.; Grönbeck, H.; Rupprechter, G. Single-Particle Catalysis: Revealing Intraparticle Pacemakers in Catalytic H<sub>2</sub> Oxidation on Rh. *ACS Catal.* **2021**, *11*, 10020–10027.
- (18) Suchorski, Y.; Beben, J.; Imbihl, R.; James, E. W.; Liu, D.-J.; Evans, J. W. Fluctuations and Critical Phenomena in Catalytic CO Oxidation on Nanoscale Pt Facets. *Phys. Rev. B* **2001**, *63*, No. 165417.
- (19) Datler, M.; Bespalov, I.; Buhr, S.; Zeininger, J.; Stöger-Pollach, M.; Bernardi, J.; Rupprechter, G.; Suchorski, Y. Hydrogen Oxidation on Stepped Rh Surfaces:  $\mu$ m-Scale versus Nanoscale. *Catal. Lett.* **2016**, *146*, 1867–1874.
- (20) Suchorski, Y.; Bespalov, I.; Zeininger, J.; Raab, M.; Datler, M.; Winkler, P.; Rupprechter, G. CO Oxidation on Stepped Rh Surfaces:  $\mu$ m-Scale Versus Nanoscale. *Catal. Lett.* **2020**, *150*, 605–612.
- (21) Osborn, M.; Webster, R.; Weber, K. Individual Microtubules Viewed by Immunofluorescence and Electron Microscopy in the Same PtK2 Cell. *J. Cell Biol.* **1978**, *77*, R27–R34.
- (22) Webster, R. E.; Osborn, M.; Weber, K. Visualization of the Same PtK2 Cytoskeletons by Both Immunofluorescence and Low Power Electron Microscopy. *Exp. Cell Res.* **1978**, *117*, 47–61.
- (23) Jun, S.; Ro, H.-J.; Bharda, A.; Kim, S. I.; Jeoung, D.; Jung, H. S. Advances in Cryo-Correlative Light and Electron Microscopy: Applications for Studying Molecular and Cellular Events. *Protein J.* **2019**, *38*, 609–615.
- (24) Carlson, D. B.; Gelb, J.; Palshin, V.; Evans, J. E. Laboratory-Based Cryogenic Soft X-Ray Tomography with Correlative Cryo-Light and Electron Microscopy. *Microsc. Microanal.* **2013**, *19*, 22–29.
- (25) Odermatt, P. D.; Shivanandan, A.; Deschout, H.; Jankele, R.; Nievergelt, A. P.; Feletti, L.; Davidson, M. W.; Radenovic, A.; Fantner, G. E. High-Resolution Correlative Microscopy: Bridging the Gap between Single Molecule Localization Microscopy and Atomic Force Microscopy. *Nano Lett.* **2015**, *15*, 4896–4904.
- (26) Povstugar, I.; Weber, J.; Naumenko, D.; Huang, T.; Klinkenberg, M.; Quadakkers, W. J. Correlative Atom Probe Tomography and Transmission Electron Microscopy Analysis of Grain Boundaries in Thermally Grown Alumina Scale. *Microsc. Microanal.* **2019**, *25*, 11–20.
- (27) Albu, M.; Fitzek, H.; Moser, D.; Kothleitner, G.; Hofer, F. Multiscale and Correlative Analytical Electron Microscopy of Extraterrestrial Minerals. *Front. Astron. Space Sci.* **2020**, *7*, No. 544331.
- (28) Fitzek, H.; Wewerka, K.; Schmidt, U.; Schröttner, H.; Zankel, A. The Combination of Raman Microscopy and Electron Microscopy – Practical Considerations of the Influence of Vacuum on Raman Microscopy. *Micron* **2021**, *143*, No. 103029.
- (29) Schweinar, K.; Nicholls, R. L.; Rajamathi, C. R.; Zeller, P.; Amati, M.; Gregoratti, L.; Raabe, D.; Greiner, M.; Gault, B.; Kasian, O. Probing Catalytic Surfaces by Correlative Scanning Photoemission Electron Microscopy and Atom Probe Tomography. *J. Mater. Chem. A* **2020**, *8*, 388–400.
- (30) Weckhuysen, B. M. Chemical Imaging of Spatial Heterogeneities in Catalytic Solids at Different Length and Time Scales. *Angew. Chem., Int. Ed.* **2009**, *48*, 4910–4943.
- (31) Schmidt, J. E.; Ye, X.; van Ravenhorst, I. K.; Oord, R.; Shapiro, D. A.; Yu, Y.; Bare, S. R.; Meirer, F.; Poplawsky, J. D.; Weckhuysen, B. M. Probing the Location and Speciation of Elements in Zeolites with Correlated Atom Probe Tomography and Scanning Transmission X-Ray Microscopy. *ChemCatChem* **2019**, *11*, 488–494.
- (32) Gambino, M.; Nieuwelink, A. E.; Reints, F.; Veselý, M.; Filez, M.; Ferreira Sanchez, D.; Grolimund, D.; Nesterenko, N.; Minoux, D.; Meirer, F.; Weckhuysen, B. M. Mimicking Industrial Aging in Fluid Catalytic Cracking: A Correlative Microscopy Approach to Unravel Inter-Particle Heterogeneities. *J. Catal.* **2021**, *404*, 634–646.
- (33) Hendriks, F. C.; Mohammadian, S.; Ristanović, Z.; Kalirai, S.; Meirer, F.; Vogt, E. T. C.; Bruijninx, P. C. A.; Gerritsen, H. C.; Weckhuysen, B. M. Integrated Transmission Electron and Single-Molecule Fluorescence Microscopy Correlates Reactivity with Ultrastructure in a Single Catalyst Particle. *Angew. Chem., Int. Ed.* **2018**, *57*, 257–261.
- (34) Marbach, H.; Lilienkamp, G.; Wei, H.; Günther, S.; Suchorski, Y.; Imbihl, R. Ordered Phases in Alkali Redistribution during a Catalytic Surface Reaction. *Phys. Chem. Chem. Phys.* **2003**, *5*, 2730–2735.
- (35) Günther, S.; Liu, H.; Menteş, T. O.; Locatelli, A.; Imbihl, R. Spectromicroscopy of Pulses Transporting Alkali Metal in a Surface Reaction. *Phys. Chem. Chem. Phys.* **2013**, *15*, 8752–8764.
- (36) Marbach, H.; Günther, S.; Neubrand, T.; Imbihl, R. Mass Transport of Alkali Metal with Pulses: Catalytic NO Reduction with Hydrogen on Rh(110)/K. *Chem. Phys. Lett.* **2004**, *395*, 64–69.
- (37) Suchorski, Y.; Rupprechter, G. Local Reaction Kinetics by Imaging. *Surf. Sci.* **2016**, *643*, 52–58.
- (38) Lilienkamp, G.; Wei, H.; Maus-Friedrichs, W.; Kempter, V.; Marbach, H.; Günther, S.; Suchorski, Y. Metastable Impact Electron Emission Microscopy of the Catalytic H<sub>2</sub> Oxidation on Rh(110). *Surf. Sci.* **2003**, *532–535*, 132–136.
- (39) Winkler, P.; Zeininger, J.; Suchorski, Y.; Stöger-Pollach, M.; Zeller, P.; Amati, M.; Gregoratti, L.; Rupprechter, G. How the Anisotropy of Surface Oxide Formation Influences the Transient Activity of a Surface Reaction. *Nat. Commun.* **2021**, *12*, No. 69.
- (40) Schmidt, Th.; Marchetto, H.; Lévesque, P. L.; Groh, U.; Maier, F.; Preikszas, D.; Hartel, P.; Spehr, R.; Lilienkamp, G.; Engel, W.; Fink, R.; Bauer, E.; Rose, H.; Umbach, E.; Freund, H.-J. Double Aberration Correction in a Low-Energy Electron Microscope. *Ultramicroscopy* **2010**, *110*, 1358–1361.
- (41) Schmidt, Th.; Sala, A.; Marchetto, H.; Umbach, E.; Freund, H.-J. First Experimental Proof for Aberration Correction in XPEEM: Resolution, Transmission Enhancement, and Limitation by Space Charge Effects. *Ultramicroscopy* **2013**, *126*, 23–32.
- (42) Fink, R.; Weiss, M. R.; Umbach, E.; Preikszas, D.; Rose, H.; Spehr, R.; Hartel, P.; Engel, W.; Degenhardt, R.; Wichtendahl, R.; Kühlenbeck, H.; Erlebach, W.; Ihmann, K.; Schlögl, R.; Freund, H.-J.; Bradshaw, A. M.; Lilienkamp, G.; Schmidt, Th.; Bauer, E.; Benner, G. SMART: A Planned Ultrahigh-Resolution Spectromicroscope for BESSY II. *J. Electron Spectrosc. Relat. Phenom.* **1997**, *84*, 231–250.
- (43) Wichtendahl, R.; Fink, R.; Kühlenbeck, H.; Preikszas, D.; Rose, H.; Spehr, R.; Hartel, P.; Engel, W.; Schlögl, R.; Freund, H.-J.; Bradshaw, A. M.; Lilienkamp, G.; Schmidt, Th.; Bauer, E.; Benner, G.; Umbach, E. SMART: An Aberration-Corrected XPEEM/LEEM with Energy Filter. *Surf. Rev. Lett.* **1998**, *5*, 1249–1256.
- (44) Ganduglia-Pirovano, M. V.; Scheffler, M.; Baraldi, A.; Lizzit, S.; Comelli, G.; Paolucci, G.; Rosei, R. Oxygen-Induced Rh 3d<sub>5/2</sub> Surface Core-Level Shifts on Rh(111). *Phys. Rev. B* **2001**, *63*, No. 205415.

(45) Gustafson, J.; Borg, M.; Mikkelsen, A.; Gorovikov, S.; Lundgren, E.; Andersen, J. N. Identification of Step Atoms by High Resolution Core Level Spectroscopy. *Phys. Rev. Lett.* **2003**, *91*, No. 056102.

(46) Baraldi, A.; Lizzit, S.; Comelli, G.; Kiskinova, M.; Rosei, R.; Honkala, K.; Nørskov, J. K. Spectroscopic Link between Adsorption Site Occupation and Local Surface Chemical Reactivity. *Phys. Rev. Lett.* **2004**, *93*, No. 046101.

(47) Bianchettin, L.; Baraldi, A.; de Gironcoli, S.; Vesselli, E.; Lizzit, S.; Comelli, G.; Rosei, R. Surface Core Level Shift: High Sensitive Probe to Oxygen-Induced Reconstruction of  $Rh(100)$ . *J. Phys. Chem. C* **2009**, *113*, 13192–13198.

(48) Bär, M.; Gottschalk, N.; Eiswirth, M.; Ertl, G. Spiral Waves in a Surface Reaction: Model Calculations. *J. Chem. Phys.* **1994**, *100*, 1202–1214.

(49) Mikhailov, A. S.; Krinsky, V. I. Rotating Spiral Waves in Excitable Media: The Analytical Results. *Phys. Nonlinear Phenom.* **1983**, *9*, 346–371.

(50) Spiel, C.; Vogel, D.; Schlögl, R.; Rupprechter, G.; Suchorski, Y. Spatially Coupled Catalytic Ignition of CO Oxidation on Pt: Mesoscopic versus Nano-Scale. *Ultramicroscopy* **2015**, *159*, 178–183.



## Supporting Information

# Pattern formation in catalytic H<sub>2</sub> oxidation on Rh: Zooming in by correlative microscopy

*Johannes Zeininger<sup>1, ‡</sup>, Philipp Winkler<sup>1, ‡</sup>, Maximilian Raab<sup>1</sup>, Yuri Suchorski<sup>1</sup>,  
Mauricio J. Prieto<sup>2</sup>, Liviu C. Tănase<sup>2</sup>, Lucas de Souza Caldas<sup>2</sup>, Aarti Tiwari<sup>2</sup>, Thomas Schmidt<sup>2</sup>,  
Michael Stöger-Pollach<sup>3</sup>, Andreas Steiger-Thirsfeld<sup>3</sup>, Beatriz Roldan Cuenya<sup>2</sup>,  
and Günther Rupprechter<sup>1, \*</sup>*

<sup>1</sup> Institute of Materials Chemistry, TU Wien, Getreidemarkt 9, 1060 Vienna, Austria

<sup>2</sup> Department of Interface Science, Fritz-Haber-Institut der Max-Planck Gesellschaft,  
Faradayweg 4-6, D-14195 Berlin, Germany

<sup>3</sup> University Service Center for Transmission Electron Microscopy, TU Wien,  
Wiedner Hauptstraße 8-10, 1040 Vienna, Austria

\* E-Mail: [guenther.rupprechter@tuwien.ac.at](mailto:guenther.rupprechter@tuwien.ac.at)

‡ These authors contributed equally to this work.

## Experimental Procedures

### Sample Preparation

A polished polycrystalline Rh foil ( $10 \times 12 \text{ mm}^2$ , 0.2 mm thickness, 99.99% purity, MaTecK) consisting of crystallographically different  $\mu\text{-sized Rh(hkl)}$  domains was used as sample. It was cleaned in UHV by repeated cycles of  $\text{Ar}^+$  ion sputtering (ion energy of 1 keV at 300 K), annealing to 1073–1173 K and consecutive chemical treatment in oxygen ( $p_{\text{O}_2} = 5.0 \times 10^{-7}$  mbar at 773 K) and hydrogen ( $p_{\text{H}_2} = 5.0 \times 10^{-6}$  mbar at 773 K). Cleanliness of the sample was verified before and after each experiment by X-ray photoelectron spectroscopy (XPS), with post-experimental analysis not indicating any changes in surface composition. The sample temperature was measured by a thermocouple via direct physical contact to the front of the sample (Type K in the PEEM experiments, Type C in the LEEM and XPEEM experiments) and regulated by a PID controller within a range of typically 0.25 K. Characterization of the local sample crystallography was performed by electron backscatter diffraction (EBSD) and spatially resolved low energy electron diffraction ( $\mu\text{-LEED}$ ), further details are given below.

### PEEM

The PEEM experiments were conducted in a multipurpose UHV setup containing a PEEM and an XPS chamber, interconnected by a sample transfer tunnel. The PEEM chamber is equipped with sample cleaning facilities, a PEEM (Staib Instruments PEEM 150), a deuterium discharge UV lamp (Heraeus D200F, photon energy  $\sim 6.5$  eV), a quadrupole mass spectrometer (MKS e-Vision 2) and a high purity gas supply system (Ar: 99.9999%,  $\text{H}_2$ : 99.9995%,  $\text{O}_2$ : 99.9999%). The XPS chamber is equipped with a hemispherical energy analyzer (Specs Phoibos 100), a twin anode X-ray source (Specs XR-50) and sample cleaning facilities and a high purity gas supply system analogous to those in the PEEM chamber. The ongoing  $\text{H}_2$  oxidation reaction, visualized in situ by PEEM, was video recorded by a high-speed CCD camera (Hamamatsu C11440-42U30). The PEEM magnification was calibrated by comparison of PEEM images with optical micrographs of individual domains of the polycrystalline Rh sample. The XPS spectra were acquired from circular areas of 100  $\mu\text{m}$  in diameter, using Mg  $K\alpha$  X-ray radiation, with the energy analyzer oriented perpendicular to the sample surface (take-off angle  $0^\circ$ ).

### LEEM/XPEEM

The LEEM/XPEEM experiments were carried out using the SMART microscope operating at the UE49-PGM beam line of the synchrotron light source BESSY-II of the Helmholtz Centre Berlin (HZB). The aberration corrected and energy filtered instrument, which has been described in detail elsewhere (*S1*, *S2*), combines microscopy (LEEM/XPEEM), low-energy electron diffraction ( $\mu\text{-LEED}$ ), and laterally resolved X-ray spectroscopy ( $\mu\text{-XPS}$ ). The SMART microscope achieves a maximal lateral resolution of 2.6 nm and 18 nm in LEEM and XPEEM mode, respectively. The system is equipped with gas dosing (Ar,  $\text{H}_2$ ,  $\text{O}_2$ ; purity 99.999%) and sample cleaning facilities.

In LEEM, the low-energy electrons elastically backscattered from the sample surface are exploited for imaging, whereby the bright-field imaging mode with a contrast aperture selecting the specularly reflected electron beam was used. In XPEEM, the sample surface is illuminated

with X-rays and photoemitted electrons are used for imaging. The imaging energy analyzer allows the selection of electrons having a binding energy within a window and using them to form the XPEEM image. The choice of energy windows (Figs. 3d, e of the main text) corresponding to the XPS peaks specific for particular elements and their chemical states provides the chemical contrast (Fig. 3b of the main text).

### EBSD

Electron backscatter diffraction (EBSD) is an additional characterization technique based on scanning electron microscopy (SEM), enabling crystallographic microstructural characterization of polycrystalline materials, including determination of individual grain orientations (S3–S5). The backscattered electrons of an electron beam, focused onto a particular sample spot, form a diffraction pattern consisting of Kikuchi bands, which correspond to each of the diffracting crystal lattice planes. Computer-based pattern transformation allows determination of the crystallographic surface orientation of the studied particular sample spot. In the present study, the EBSD characterization was performed by a FEI Quanta 200F field emission scanning electron microscope using standard EBSD conditions and evaluation procedures (S6). A comparison of pre- and post-reaction EBSD characterization has shown that the surface structures of the Rh(hkl) domains remain conserved even after extended periods of the ongoing hydrogen oxidation reaction.

### Determination of the local crystallography by $\mu$ -LEED

The local crystallographic orientation of a specific domain region of the polycrystalline Rh sample investigated in the LEEM studies was determined using  $\mu$ -LEED. The determination is based on the fact that any regular atomic stepped array found on a stepped surface produces a characteristic LEED pattern (S7, S8). For the  $\mu$ -LEED, first, a specific area of interest with 1.5  $\mu\text{m}$  in diameter was selected by LEEM. From this area, LEED patterns were obtained for different electron energies in the range of 20 to 350 eV. Figure S1a exemplarily displays the LEED pattern obtained at 330 eV, showing a six-fold symmetry which reflects the [1 1 1]-like nature of the surface. A closer look reveals the splitting of LEED spots, indicating a stepped surface. Such a stepped surface can be considered as consisting of two superimposed lattices: the short-period lattice associated with the atomic structure of the terraces and the long-period lattice (vicinal plane) associated with the atomic steps. In the corresponding Ewald construction, both of these lattices contribute with reciprocal rods which are tilted by the angle between the vicinal planes and the terraces and have a certain thickness due to the non-negligible terrace width (S9). This is reflected in the LEED pattern by a characteristic spot splitting (Fig. S1a) that depends on the primary electron energy. The inset in Fig. S1a shows the extension of the spot splitting line (red dotted line) in the  $[5 \bar{1} \bar{4}]$ -direction (towards the  $[4 0 \bar{2}]$  spot). The width, the direction and the energy dependence of the splitting allow determination of the crystallographic orientation of the selected area.

Figure S1b shows the application of this concept to the present  $\mu$ -LEED data: first, the experimentally obtained spot existence regions (marked by white bars in the inset of Fig. S1b) were summarized in a diagram. Then, the Ewald geometric construction was composed, where

the tilted black lines result from the atomic step-edges and the blue bars result from the terraces which, as mentioned above, have an extended width in the real space, in contrary to step-edges. The resulting construction provides the  $[14\ 10\ 8]$ -direction as the best fit for the spot existence diagram in the inset of Fig. 1Sb, which corresponds to a  $(7\ 5\ 4)$  surface orientation for the studied  $\mu\text{-m}$ -sized surface region. Fig. S1c displays a corresponding ball model of the Rh $(7\ 5\ 4)$  surface. Notably, the SMART instrument uses an electrostatic lens system without image rotation well-known for systems with magnetic lenses, i.e. the step orientation obtained from the  $\mu\text{-LEED}$  can be unambiguously associated with the LEEM images. In order to ensure the homogeneity of the studied surfaces,  $\mu\text{-LEED}$  patterns were recorded for several  $\mu\text{-m}$ -sized surface areas placed at distances of a few  $\mu\text{m}$  in the region displayed in Figs. 3 and 4 (Fig. S1d-f).

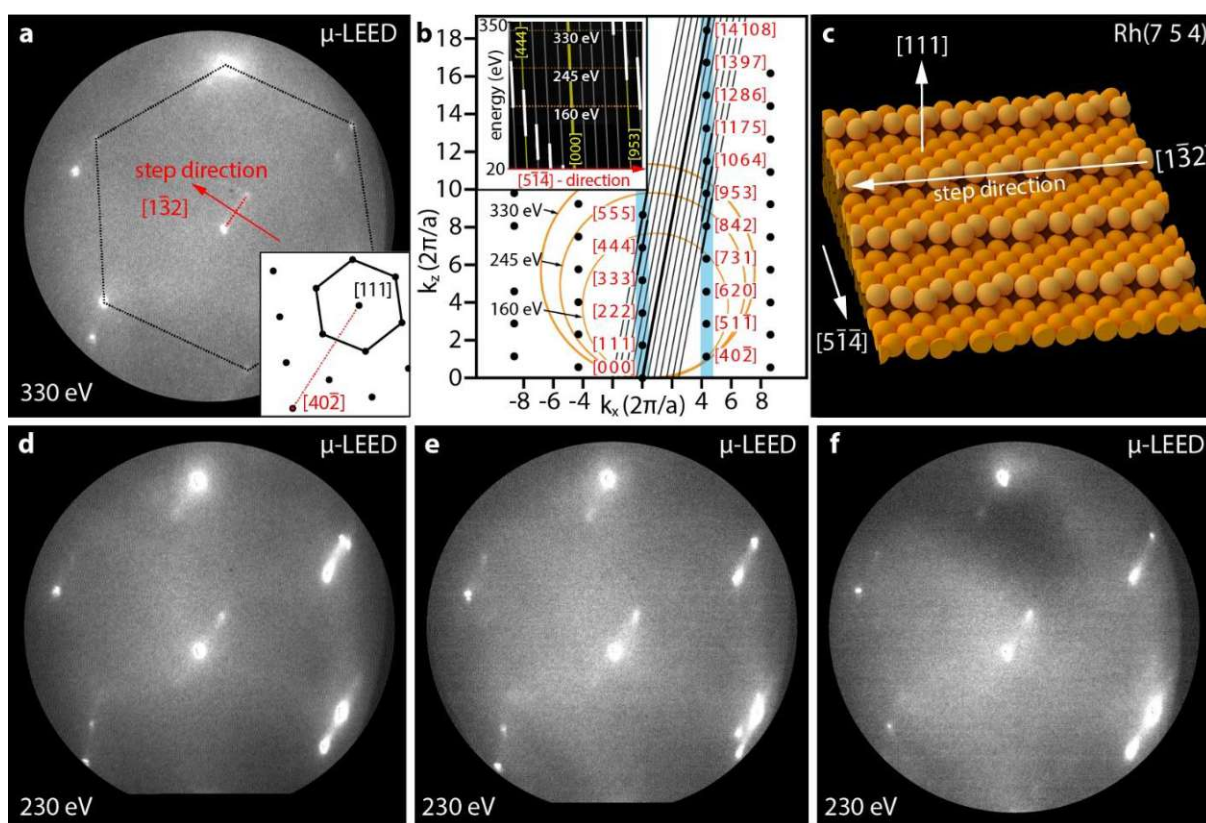


**Figure S1.** Determination of the local crystallographic orientation by  $\mu\text{-LEED}$ : (a) hexagonal  $\mu\text{-LEED}$  pattern obtained from the selected region on the Rh domain studied by LEEM (electron energy 330 eV). Spot splitting is well visible (exemplarily marked by the red dotted line), the inset schematically shows the spot splitting direction; (b) geometric Ewald construction of electron diffraction. Projections of Ewald spheres for 160, 245 and 330 eV are shown as orange lines. The inset shows the spot existence diagram in the energy range from 20 to 350 eV. The horizontal orange dotted lines correspond to the electron energies, for which the Ewald spheres are drawn; (c) ball model of the Rh $(7\ 5\ 4)$  surface with the step direction indicated; (d) the same as in (a) but with an electron energy of 230 eV; (e) the same as in (d) but for a  $\mu\text{-m}$ -sized region located 5  $\mu\text{m}$  to the right of (d); (f) the same as in (d) but for a  $\mu\text{-m}$ -sized region located 5  $\mu\text{m}$  below (e).

## Model simulations

The modeling approach used for the present simulations of pattern formation during the self-sustaining oscillations in hydrogen oxidation on rhodium is based on the Langmuir-Hinshelwood mechanism that is well established for this catalytic reaction (S10). The local formation and depletion of subsurface oxygen acts as feedback mechanism, governing the transitions from the inactive to the active state of the local catalytic activity and vice versa (S11–S15). The oscillation cycle can be described as follows: Presence of molecular hydrogen and oxygen in the gas phase results in their competitive coadsorption on rhodium surface. As the initial sticking coefficient of oxygen is much higher than that of hydrogen, at the experimental partial pressures  $p_{H_2} = 4.5 \times 10^{-7}$  mbar and  $p_{O_2} = 5.0 \times 10^{-7}$  mbar, oxygen preferentially adsorbs to the surface via a molecular precursor, which dissociates into two chemisorbed oxygen atoms. Since hydrogen adsorption is generally blocked by adsorbed oxygen at these conditions (S16), this results in a catalytically inactive state (Fig. S2; 1). After a dense oxygen coverage is formed, adsorbed oxygen atoms can migrate under the topmost rhodium layer, forming subsurface oxygen (Fig. S2; 2). The presence of subsurface oxygen reduces the sticking coefficient of oxygen, increasing the probability of hydrogen adsorption. This leads, upon surpassing a critical threshold of subsurface oxygen coverage, to a switch in the competitive coadsorption in favor of hydrogen and thus to a kinetic transition to the catalytically active state. In the active state, both hydrogen and oxygen can adsorb on the surface, where they react and form water which immediately desorb from the surface at the present conditions (Fig. S2; 3). Due to the continuous formation of water, the surface coverage of both hydrogen and oxygen remains low, thus subsurface oxygen can now migrate back to the surface.

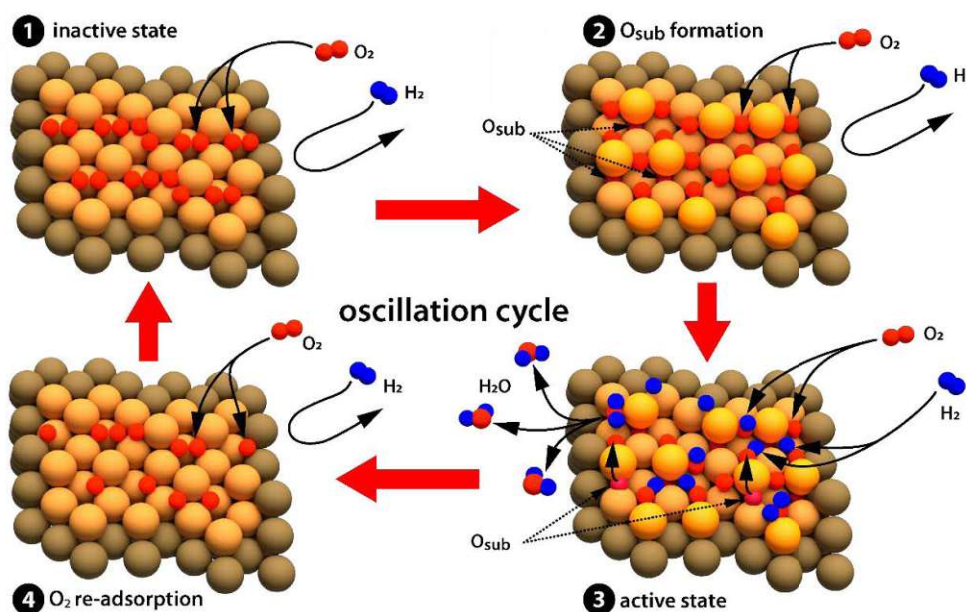


**Figure S2:** Schematic illustration of the oscillation mechanism for the catalytic hydrogen oxidation on rhodium. Color code: golden – Rh, red – O, blue – H.

The depletion of the subsurface oxygen depot leads to a recovery of the oxygen sticking, thus raising the favorability of oxygen adsorption (Fig. S2; 4). Eventually, oxygen again adsorbs preferentially and covers the surface, returning the system to its initial inactive state and closing the oscillation cycle.

The key role in the above oscillating process is played by the formation/depletion of subsurface oxygen: surpassing a high critical amount of subsurface oxygen causes a transition to the active catalytic state, while a fall below a certain low subsurface oxygen coverage induces a transition to the inactive state. The rate of the subsurface oxygen formation/depletion, which depends on the surface structure, governs, as a feedback mechanism, the frequency of the oscillations.

Based on this view of catalytic hydrogen oxidation, the present model was developed as a hybrid between micro-kinetic modeling (MKM) and Monte Carlo simulations (MC). The goal of our approach was to achieve a model description of the observed phenomena which can directly be compared to experiments.

The model approach assumes that kinetic transitions between states of catalytic activity can be narrowed down to two options: internal “self-induced” transitions through adsorption based on the local coverage of subsurface oxygen ( $\theta_S^i$ ) as described above, and externally induced transitions, caused by propagation of reaction/diffusion fronts from adjacent surface sites. Both of these transitions can be described by a MC approach, with the probabilities for each local transition event to occur in a MC step based on the local amount of  $\theta_S^i$ . Both the local coverage of subsurface oxygen and the local transition probabilities are updated before each MC step by MKM calculations, with a time interval ( $\Delta t$ ) of 40 ms between each MC step used for the calculations.

As a grid for the Monte Carlo simulation, a 400 x 400 hexagonal tiling grid was chosen, representing the (1 1 1) fcc surface structure of the terraces forming the Rh(7 5 4) surface. Due to the close-packing of the 160000 grid tiles, this results in a rectangular model field of view. To realistically simulate the experimental LEEM observations, the size of this field of view was set to 40 x 34.6  $\mu\text{m}^2$ , so each of the grid tiles contains a surface area of about 8660  $\text{nm}^2$ , or roughly 86600 surface sites, under the assumption of a surface site area of 0.10  $\text{nm}^2$  (S10). Based on the above-mentioned view of the mechanism of the reaction, it is reasonable to assign each grid tile a state of catalytic activity, active or inactive, each represented by a distinct set of surface coverages (inactive – high oxygen coverage, few empty adsorption sites; active – low oxygen and hydrogen coverage, many empty adsorption sites, see Tab. S3).

The local formation and depletion of subsurface oxygen can be accurately described via micro-kinetic modelling, as has been previously applied (S10–S15, S17). This deterministic approach is also suitable to describe the local subsurface oxygen coverage of each grid tile. The rate of the subsurface oxygen formation and depletion at the present conditions is sufficiently high to be accurately calculated by a numerical integration of the MKM differential equations, even disregarding the stochastic part of the local subsurface oxygen formation/depletion on each surface site of the grid tile.

In our model, the subsurface oxygen coverage  $\theta_S^i$  of each grid tile  $i$  is described by the following kinetic equation:

$$\frac{d\theta_S^i}{dt} = k_{ox}\theta_O^i(1 - \theta_S^i) - k_{red}^i\theta_S^i\theta_*^i, \quad (\text{Eq. S1})$$

where  $\theta_O^i$  is the local oxygen coverage and  $\theta_*^i$  represents the coverage of empty surface sites. The rate and coupling constants are given by

$$k_{ox} = k_{ox}^0 e^{-\beta E_{ox}^i}, \quad (\text{Eq. S2})$$

$$k_{red}^i = k_{red}^0 e^{-\beta(E_{red}^i + A_{red}^s \theta_S^i)}, \quad (\text{Eq. S3})$$

where  $\beta = 1/k_B T$ . The values of the kinetic parameters used in the present calculations are given in Tab. S3 and are based on the work of McEwen *et al.* (S10, S17). The rate of subsurface oxygen formation/depletion depends on the local activation energy for the formation of subsurface oxygen ( $E_{ox}^i$  in the model equations) and thus on the crystallographic orientation of the surface (S11–S15). Each grid tile is originally assigned the  $E_{ox}^i$  value of the crystallographically regular surface, with local deviations due to local defects of the crystallographic surface structure, randomly distributed across the surface. The occurrence rate of such modified  $E_{ox}^i$  values, as well as the  $E_{ox}^i$  value of the regular surface, are given in Tab. S1. For all calculations, the same distribution of  $E_{ox}^i$  values was used.

**Table S1.** Surface distribution probabilities of the local activation energy  $E_{ox}^i$  for the formation of subsurface oxygen.

occurrence rate	$E_{ox}^i$ (eV)
regular surface	1.25
$6.3 \times 10^{-6}$	1.15
$5.3 \times 10^{-2}$	1.172
$2.5 \times 10^{-3}$	1.30

The local activation energy for the depletion of subsurface oxygen  $E_{red}^i$  was calculated from the respective  $E_{ox}^i$ , utilizing the linear relation from Suchorski *et al.* (S12)

$$E_{red}^i = 0.293 + 0.776 E_{ox}^i. \quad (\text{Eq. S4})$$

The two possibilities for local transition events to occur (internally via the adsorption, mediated by the formation and depletion of subsurface oxygen, or externally via a reaction/diffusion front from neighboring grid tiles) are incorporated in the MC simulation model as follows: Although the adsorption of hydrogen is generally blocked on the oxygen covered surface, there still exists a certain probability of hydrogen adsorption due to a few stochastically appearing empty sites on

the surface. The local internal transition to the active state is governed by the probability of hydrogen adsorption  $\varphi_{Hads}$  on the oxygen covered grid tile. This probability is assumed to be proportional to the rate of hydrogen adsorption that can also be derived from the MKM (S10, S17) by

$$\varphi_{Hads,t} = \int_t^{t+\Delta t} 2k_a^H p_{H_2} \theta_*^i{}^2 dt, \quad (\text{Eq. S5})$$

with

$$k_a^H = S_0^H a_s / \sqrt{2\pi m_{H_2} / \beta}, \quad (\text{Eq. S6})$$

where  $S_0^H$  corresponds to the initial sticking coefficient of hydrogen,  $a_s$  denotes the area of a surface site and  $m_{H_2}$  is the average molecular mass of hydrogen. The probability for a transition to the active state is

$$\chi_{Hads,t} = N \cdot q_H \cdot \varphi_{Hads,t} \cdot \rho_H, \quad (\text{Eq. S7})$$

where  $N$  is the number of surface sites per grid tile. The adsorption of hydrogen and the following reaction to water leaves empty surface sites. These empty sites can subsequently be occupied by hydrogen, leading, after reaction to water, to even more empty surface sites, and thereby to an autocatalytic reaction and a kinetic transition to the active state. However, the empty surface sites can instead also be refilled by adsorbing oxygen, returning the surface coverage to its initial state.  $q_H$  is a parameter describing the probability that hydrogen adsorption on an oxygen covered grid tile leads to a successful kinetic transition.  $\rho_H$  is a factor describing the dependence of the probability of a hydrogen caused transition to the active state on the local subsurface oxygen coverage, which is written as

$$\rho_H = \ln \left( \frac{A_1 \cdot \theta_s^i}{A_{lim}} - A_1 + 1 \right) / \ln \left( -A_1 + 1 + \frac{A_1}{A_{lim}} \right), \quad (\text{Eq. S8})$$

where  $A_{lim}$  is the subsurface oxygen limit needed for a transition to the active state, and  $A_1$  is a factor describing the exponential dependence of the transition probability on  $\theta_s^i$ . For a saturated subsurface coverage,  $\rho_H$  becomes equal to one.

The same can also be done for the internal transition to the inactive state, caused by the favored adsorption of oxygen. The probability of oxygen adsorption on a surface site of the grid tile is derived from the MKM as

$$\varphi_{Oads,t} = \int_t^{t+\Delta t} \frac{2 \cdot k_a^O K^i p_{O_2} \theta_*^i{}^2}{1 + K^i \theta_*^i{}^2} dt, \quad (\text{Eq. S9})$$

with

$$k_a^O = S_0^O a_s / \sqrt{2\pi m_{O_2} / \beta}, \quad (\text{Eq. S10})$$



$$K^i = K_0 e^{-\beta(E_K + A_K^O \theta_0^i + A_K^S \theta_S^i)}, \quad (\text{Eq. S11})$$

where the parameters  $S_0^O$  and  $m_{O_2}$  represent the initial sticking coefficient of oxygen and its molecular mass, respectively. The probability for a transition to the active state is

$$\chi_{Oads,t} = N \cdot q_O \cdot \varphi_{Oads,t} \cdot \rho_O, \quad (\text{Eq. S12})$$

where  $q_O$  is a parameter describing the probability that the amount of adsorbed oxygen on a grid tile is sufficient for a kinetic transition to the inactive state, despite it being partially consumed in the reaction until the completed kinetic transition.  $\rho_O$  is a factor describing the dependence of the transition probability on the local subsurface concentration as

$$\rho_O = \ln\left(\frac{-B_1 \cdot \theta_S^i}{B_{lim}} + B_1 + 1\right) / \ln(B_1 + 1), \quad (\text{Eq. S13})$$

where  $B_{lim}$  is the subsurface oxygen limit needed for a transition to the active state, and  $B_1$  is a parameter describing the exponential dependence of the transition probability on  $\theta_S^i$ . When no subsurface oxygen is present,  $\rho_O$  becomes equal to one.

Apart from these adsorption-induced kinetic transitions, externally induced transitions are possible via reaction/diffusion fronts. In the kinetic transition to the active state, the hydrogen front propagation can be considered as propagation from one grid tile to a neighboring tile with a certain front velocity. In the model, this is represented by a local *event of front propagation*, in which a grid tile adopts the state of catalytic activity of its neighbor. For such a transition to occur, it is necessary that at least one neighboring grid tile is in a *front state*, meant as state of a tile immediately after the kinetic transition to the active state. The probability of an event of front propagation which induces a transition for the nearest neighboring grid tile determines the local velocity of the front, which can be extracted from the experimental observations. The corresponding relation between the probability for an inactive grid tile to turn active and the front velocity is then

$$\chi_{H,fr} = v_H \cdot n_{H,fr} \cdot X_{H,fr} \cdot \Delta t, \quad (\text{Eq. S14})$$

where  $v_H$  is the front velocity parameter of the hydrogen front and  $n_{H,fr}$  is the number of neighboring grid tiles being already in an active state front state.  $X_{H,fr}$  is a factor based on  $n_{H,fr}$ , given in Tab. S2.

Analogously, the corresponding relation between the probability for an active grid tile to turn inactive via oxygen front propagation and the front velocity is

$$\chi_{O,fr} = v_O \cdot n_{O,fr} \cdot X_{O,fr} \cdot \Delta t, \quad (\text{Eq. S15})$$

where  $v_O$  is the front velocity parameter of the oxygen front,  $n_{O,fr}$  is the number of neighboring grid tiles in an inactive front state and  $X_{O,fr}$  is a factor based on  $n_{O,fr}$ , also given in Tab. S2.

**Table S2.** Front propagation factors for the hydrogen and oxygen fronts based on the number of front state neighbors.

$n$	1	2	3	4	5	6
$X_{H,fr}$	0.9	1.8	3.5	8	14	20
$X_{O,fr}$	1	1.5	2.5	6	16	25

By choosing the size of each grid tile and the grid resolution, as well as the time delay for the numerical integration of the MKM differential equations, the chosen spatial resolution as well as time resolution can be directly assigned to each calculated MC model step, thereby generating time-series of surface images which can be interpreted as series of frames of a *simulated virtual surface microscopy* (see Fig. 5 in the main text and supporting movies 4-6).

**Table S3.** Micro-kinetic model parameters and Monte Carlo simulation parameters used in the present simulations of the LEEM patterns. Energies are given in eV, rate constants in 1/s and  $v_H$  and  $v_O$  in grid tiles/s.

symbol	parameter description	T = 428 K	T = 433 K	T = 468 K
$k_{ox}^0$	pre-factor for oxygen diffusion from surface to subsurface sites	$1.00 \times 10^{12}$	$1.00 \times 10^{12}$	$1.00 \times 10^{12}$
$k_{red}^0$	pre-factor for oxygen diffusion from subsurface to surface sites	$3.00 \times 10^{12}$	$3.00 \times 10^{12}$	$3.00 \times 10^{12}$
$A_{red}^s$	subsurface oxygen coverage dependence of the activation energy for subsurface oxygen depletion	-0.0200	-0.0200	-0.0200
$S_0^H$	initial sticking coefficient of H	0.300	0.300	0.300
$q_H$	pre-factor for transition to the active state	$1.37 \times 10^{-4}$	$1.37 \times 10^{-4}$	$1.37 \times 10^{-4}$
$K_0$	pre-factor for oxygen dissociation equilibrium constant	0.2525	0.2525	0.2525
$E_k$	activation energy for oxygen dissociation equilibrium constant	-0.178	-0.178	-0.178
$A_K^O$	coverage dependence of adsorbed oxygen on the activation energy of oxygen dissociation	0.158	0.158	0.158
$A_K^s$	coverage dependence of subsurface oxygen on the activation energy of oxygen dissociation	0.082	0.082	0.082
$S_0^O$	initial sticking coefficient of O	0.600	0.600	0.600
$q_O$	pre-factor for transition to the inactive state	$2.25 \times 10^{-7}$	$2.25 \times 10^{-7}$	$2.25 \times 10^{-7}$
$\theta_O^{act}$	surface coverage of O in the active state	0.0500	0.0500	0.0500
$\theta_*^{act}$	empty sites in the active state	0.950	0.950	0.950
$\theta_O^{inact}$	surface coverage of O in the inactive state	0.850	0.830	0.750

Table S3. (continued)

symbol	parameter description	T = 428 K	T = 433 K	T = 468 K
$\theta_*^{inact}$	empty sites in the inactive state	0.150	0.170	0.250
$A_1$	dependence on $\theta_S^i$ for the transition probability to the active state	-3.00	-3.00	-3.00
$A_{lim}$	subsurface oxygen limit needed for a transition to the active state	0.740	0.735	0.600
$B_1$	dependence on $\theta_S^i$ for the transition probability to the inactive state	10.0	10.0	10.0
$B_{lim}$	subsurface oxygen limit needed for a transition to the inactive state	0.100	0.100	0.020
$v_H$	front velocity parameter of the hydrogen front	0.00300	0.00700	0.225
$v_O$	front velocity parameter of the oxygen front	0.00300	0.00300	0.00300

## References

- (S1) Fink, R.; Weiss, M. R.; Umbach, E.; Preikszas, D.; Rose, H.; Spehr, R.; Hartel, P.; Engel, W.; Degenhardt, R.; Wichtendahl, R.; Kuhlenbeck, H.; Erlebach, W.; Ihmann, K.; Schlögl, R.; Freund, H.-J.; Bradshaw, A. M.; Lilienkamp, G.; Schmidt, Th.; Bauer, E.; Benner, G. SMART: A Planned Ultrahigh-Resolution Spectromicroscope for BESSY II. *J. Electron Spectrosc. Relat. Phenom.* **1997**, *84* (1–3), 231–250. DOI: 10.1016/S0368-2048(97)00016-9.
- (S2) Wichtendahl, R.; Fink, R.; Kuhlenbeck, H.; Preikszas, D.; Rose, H.; Spehr, R.; Hartel, P.; Engel, W.; Schlögl, R.; Freund, H.-J.; Bradshaw, A. M.; Lilienkamp, G.; Schmidt, Th.; Bauer, E.; Benner, G.; Umbach, E. SMART: An Aberration-Corrected XPEEM/LEEM with Energy Filter. *Surf. Rev. Lett.* **1998**, *05* (06), 1249–1256. DOI: 10.1142/S0218625X98001584.
- (S3) Weatherup, R. S.; Shahani, A. J.; Wang, Z.-J.; Mingard, K.; Pollard, A. J.; Willinger, M.-G.; Schloegl, R.; Voorhees, P. W.; Hofmann, S. In Situ Graphene Growth Dynamics on Polycrystalline Catalyst Foils. *Nano Lett.* **2016**, *16* (10), 6196–6206. DOI: 10.1021/acs.nanolett.6b02459.
- (S4) König, U.; Davepon, B. Microstructure of Polycrystalline Ti and Its Microelectrochemical Properties by Means of Electron-Backscattering Diffraction (EBSD). *Electrochimica Acta* **2001**, *47* (1–2), 149–160. DOI: 10.1016/S0013-4686(01)00572-2.
- (S5) Daviddi, E.; Shkirskiy, V.; Kirkman, P. M.; Robin, M. P.; Bentley, C. L.; Unwin, P. R. Nanoscale Electrochemistry in a Copper/Aqueous/Oil Three-Phase System: Surface Structure–Activity–Corrosion Potential Relationships. *Chem. Sci.* **2021**, *12* (8), 3055–3069. DOI: 10.1039/D0SC06516A.
- (S6) Humphreys, F. J. Review: Grain and Subgrain Characterisation by Electron Backscatter Diffraction. *J. Mater. Sci.* **2001**, *36* (16), 3833–3854. DOI: 10.1023/A:1017973432592.

- (S7) Ellis, W. P.; Schwobel, R. L. LEED from Surface Steps on UO<sub>2</sub> Single Crystals. *Surf. Sci.* **1968**, *11* (1), 82–98. DOI: 10.1016/0039-6028(68)90040-X.
- (S8) Henzler, M. LEED-Investigation of Step Arrays on Cleaved Germanium (111) Surfaces. *Surf. Sci.* **1970**, *19* (1), 159–171. DOI: 10.1016/0039-6028(70)90115-9.
- (S9) Wagner, F. T.; Ross, P. N. LEED Spot Profile Analysis of the Structure of Electrochemically Treated Pt(100) and Pt(111) Surfaces. *Surf. Sci.* **1985**, *160* (1), 305–330. DOI: 10.1016/0039-6028(85)91044-1.
- (S10) McEwen, J.-S.; Gaspard, P.; de Bocarmé, T. V.; Kruse, N. Electric Field Induced Oscillations in the Catalytic Water Production on Rhodium: A Theoretical Analysis. *Surf. Sci.* **2010**, *604* (17–18), 1353–1368. DOI: 10.1016/j.susc.2010.04.007.
- (S11) Suchorski, Y.; Datler, M.; Bespalov, I.; Zeininger, J.; Stöger-Pollach, M.; Bernardi, J.; Grönbeck, H.; Rupprechter, G. Visualizing Catalyst Heterogeneity by a Multifrequential Oscillating Reaction. *Nat. Commun.* **2018**, *9* (1), 600. DOI: 10.1038/s41467-018-03007-3.
- (S12) Suchorski, Y.; Datler, M.; Bespalov, I.; Zeininger, J.; Stöger-Pollach, M.; Bernardi, J.; Grönbeck, H.; Rupprechter, G. Surface-Structure Libraries: Multifrequential Oscillations in Catalytic Hydrogen Oxidation on Rhodium. *J. Phys. Chem. C* **2019**, *123* (7), 4217–4227. DOI: 10.1021/acs.jpcc.8b11421.
- (S13) Suchorski, Y.; Zeininger, J.; Buhr, S.; Raab, M.; Stöger-Pollach, M.; Bernardi, J.; Grönbeck, H.; Rupprechter, G. Resolving Multifrequential Oscillations and Nanoscale Interfacet Communication in Single-Particle Catalysis. *Science* **2021**, *372* (6548), 1314–1318. DOI: 10.1126/science.abf8107.
- (S14) Winkler, P.; Zeininger, J.; Raab, M.; Suchorski, Y.; Steiger-Thirsfeld, A.; Stöger-Pollach, M.; Amati, M.; Gregoratti, L.; Grönbeck, H.; Rupprechter, G. Coexisting Multi-States in Catalytic Hydrogen Oxidation on Rhodium. *Nat. Commun.* **2021**, *12* (1), 6517. DOI: 10.1038/s41467-021-26855-y.
- (S15) Zeininger, J.; Suchorski, Y.; Raab, M.; Buhr, S.; Grönbeck, H.; Rupprechter, G. Single-Particle Catalysis: Revealing Intraparticle Pacemakers in Catalytic H<sub>2</sub> Oxidation on Rh. *ACS Catal.* **2021**, *11* (15), 10020–10027. DOI: 10.1021/acscatal.1c02384.
- (S16) Padowitz, D. F.; Sibener, S. J. Kinetics of Hydrogen Oxidation to Water on the Rh(111) Surface Using Multiple Source Modulated Molecular Beam Techniques. *Surf. Sci.* **1991**, *254* (1–3), 125–143. DOI: 10.1016/0039-6028(91)90645-9.
- (S17) McEwen, J.-S.; Gaspard, P.; Visart de Bocarmé, T.; Kruse, N. Oscillations and Bistability in the Catalytic Formation of Water on Rhodium in High Electric Fields. *J. Phys. Chem. C* **2009**, *113* (39), 17045–17058. DOI: 10.1021/jp901975w.

# 5

---

## How the anisotropy of surface oxide formation influences the transient activity of a surface reaction

Surface oxides and partially oxidized surfaces are important in many areas of technology [117–121] and have also received significant interest in heterogeneous catalysis, because, depending on the reaction conditions, in industrial reactors, an initially metallic surface may oxidize, possibly changing its catalytic activity [123, 124]. When studying catalytic H<sub>2</sub> oxidation on rhodium and attempting to bridge the pressure gap between model catalytic studies and industrial catalytic reactors (section 1.3), it is therefore crucial to consider the possible oxidation of Rh and its influence on the catalytic properties.

Therefore, correlative microscopy studies using scanning photoelectron microscopy (SPEM, section 2.2) and UV photoemission electron microscopy (UV-PEEM, section 2.3) on the initial oxidation of Rh (section 1.9) and its influence on the catalytic activity in H<sub>2</sub> oxidation were performed. A polycrystalline Rh foil was used as a library of well-defined high-Miller-index surface structures (section 2.7), with SPEM allowing spatially resolved chemical analysis of the oxidation process and UV-PEEM providing visualization of the ongoing chemical reaction and kinetic data (e.g., kinetic phase diagrams, section 1.7). The surface oxide formation was summarized in an oxidation map and quantitatively explained by the novel step density (SDP) and step edge (SEP) parameters, which describe the atomic structure of the surface. This revealed anisotropy of the oxidation process, i.e., dependence on the atomic surface structure. *In situ* PEEM imaging of the ongoing H<sub>2</sub> oxidation enabled directly comparing the local reactivity of metallic and oxidized surfaces, demonstrating the effect of Rh surface oxides. Using the velocity of propagating reaction fronts as indicator for surface reactivity, a high transient activity of Rh surface oxides in

H<sub>2</sub> oxidation was observed. The corresponding velocity map revealed the structure-dependence of such activity, representing a direct imaging of a structure-activity relation for plenty of well-defined surface structures within a single sample.

The results of these studies were published in *Nature Communications* as given below. For this work, I performed the SPEM experiments in collaboration with J. Zeininger, P. Zeller, M. Amati, L. Gregoratti and G. Rupprechter, analyzed the SPEM data, performed the PEEM experiments in collaboration with J. Zeininger, analyzed the PEEM data and prepared the manuscript in collaboration with J. Zeininger, Y. Suchorski and G. Rupprechter.







The following pages give an unmodified reproduction of the manuscript “How the anisotropy of surface oxide formation influences the transient activity of a surface reaction” by P. Winkler, J. Zeininger, Y. Suchorski, M. Stöger-Pollach, P. Zeller, M. Amati, L. Gregoratti, and G. Rupprechter, published in 2021 in *Nature Communications*, **vol. 12**, article no. 69, and its supplementary material. The article and supplementary material are licensed under a Creative Commons Attribution 4.0 International License, available at <http://creativecommons.org/licenses/by/4.0/>.

## ARTICLE


<https://doi.org/10.1038/s41467-020-20377-9>

OPEN

# How the anisotropy of surface oxide formation influences the transient activity of a surface reaction

 P. Winkler <sup>1</sup>, J. Zeininger <sup>1</sup>, Y. Suchorski <sup>1</sup>, M. Stöger-Pollach<sup>2</sup>, P. Zeller<sup>3</sup>, M. Amati <sup>3</sup>, L. Gregoratti <sup>3</sup> & G. Rupprechter <sup>1</sup>✉

Scanning photoelectron microscopy (SPEM) and photoemission electron microscopy (PEEM) allow local surface analysis and visualising ongoing reactions on a  $\mu\text{m}$ -scale. These two spatio-temporal imaging methods are applied to polycrystalline Rh, representing a library of well-defined high-Miller-index surface structures. The combination of these techniques enables revealing the anisotropy of surface oxidation, as well as its effect on catalytic hydrogen oxidation. In the present work we observe, using locally-resolved SPEM, structure-sensitive surface oxide formation, which is summarised in an *oxidation map* and quantitatively explained by the novel step density (SDP) and step edge (SEP) parameters. In situ PEEM imaging of ongoing  $\text{H}_2$  oxidation allows a direct comparison of the local reactivity of metallic and oxidised Rh surfaces for the very same different stepped surface structures, demonstrating the effect of Rh surface oxides. Employing the velocity of propagating reaction fronts as indicator of surface reactivity, we observe a high transient activity of Rh surface oxide in  $\text{H}_2$  oxidation. The corresponding *velocity map* reveals the structure-dependence of such activity, representing a direct imaging of a structure-activity relation for plenty of well-defined surface structures within one sample.

 Die approbierte gedruckte Originalversion dieser Dissertation ist an der TU Wien Bibliothek verfügbar.  
 The approved original version of this doctoral thesis is available in print at TU Wien Bibliothek.

<sup>1</sup>Institute of Materials Chemistry, TU Wien, Getreidemarkt 9, 1060 Vienna, Austria. <sup>2</sup>University Service Center for Transmission Electron Microscopy, TU Wien, Wiedner Hauptstraße 8-10, 1040 Vienna, Austria. <sup>3</sup>Elettra-Sincrotrone Trieste S.C.p.A., SS14 - km 163.5 in Area Science Park, 34149 Trieste, Italy.  
✉email: [guenther.rupprechter@tuwien.ac.at](mailto:guenther.rupprechter@tuwien.ac.at)

Oxide surfaces are important in many areas of technology, including fuel and energy generation/storage (reforming, syngas, fuel cells, electrolyzers and batteries), corrosion, sensors, exhaust gas cleaning, and others<sup>1–5</sup>. Intensive experimental and theoretical research during the last decade has led to the discovery that the transition from the metal to the bulk oxide proceeds via the formation of ultrathin oxide films, which are termed surface oxides<sup>6</sup>. Such surface oxides, with the topmost metal layer sandwiched between two atomic layers of oxygen, can even be considered a new class of materials, as they may exhibit novel unexpected properties<sup>7–9</sup>. The growth of such surface oxides was observed for Rh<sup>7,9–12</sup>, Ru<sup>13</sup>, Pd<sup>6,14,15</sup> and Pt<sup>15</sup>, which is of academic interest, but also has practical impact on the technologies mentioned.

Much of the atomistic understanding of surface oxidation originates from studies of well-defined model systems in ultrahigh vacuum (UHV)<sup>6–15</sup>. Combined with DFT calculations, these studies identified the atomic structures of surface oxides formed on smooth (low-Miller-index) single crystals of several noble metals<sup>7,11–18</sup>. Usually, surface oxides are explored in time-consuming sequential one-sample-after-another experiments on multiple single crystal samples. However, surface oxidation exhibits anisotropy, so that the local oxidation rates on crystallographically different technologically relevant less-ideal surfaces vary substantially. This important point was not considered until now.

As an alternative approach to sequential experiments, polycrystalline surfaces can be employed as model systems. If the crystallographic orientation of each surface domain is known, polycrystalline surfaces turn into surface structure libraries, since hundreds of domains with different orientations are present on a 1 cm<sup>2</sup> sample<sup>19</sup>. This concept, in combination with a spatially resolving experimental technique, allows studying surface processes on different surface structures simultaneously<sup>20,21</sup>. In the present work, surface structure libraries are for the first time applied to examine the anisotropy of surface oxidation, exploiting their essential advantage, namely guaranteeing the same oxygen exposures, temperatures and temperature ramps for differently oriented domains. This identity of conditions can hardly be met by traditional sequential experiments. Furthermore, the domains on a polycrystalline sample are not limited to low-Miller-index crystallographic orientations. Typically, several stepped high-index domains are present, resembling rough surfaces or nanoparticles in typical catalytic applications<sup>22</sup>, and these stepped Rh surfaces are in the focus of the present work. Synchrotron-based scanning photoelectron microscopy (SPEM), using a 0.13 μm diameter X-ray microprobe, is used to obtain spatially resolved chemical information and for chemical imaging<sup>23</sup>.

Surface oxides have also received significant attention in heterogeneous catalysis, e.g. in the context of exhaust cleaning or combustion, because depending on reaction conditions an initially metallic surface may be in oxidised or reduced state, significantly changing its activity<sup>10,14</sup>. This shows the strong need for in situ studies of catalytic reactions once surface oxides are involved. For well-defined surface oxides the focus was so far mostly on CO oxidation<sup>13,24,25</sup>. For example, high CO oxidation activity was attributed to a trilayer surface oxide on Rh(111)<sup>25–27</sup>, whereas continued surface oxidation produced an inactive double-trilayer (ORhO-4L<sup>28</sup>) and thicker bulk-like oxides, leading to catalyst deactivation<sup>29</sup>.

To further examine the effect of surface oxides in catalysis, we have chosen the prototypical hydrogen oxidation as a “litmus paper” test. On platinum group metals this surface reaction has been intensively studied since the times of Döbereiner<sup>30</sup> and Faraday<sup>31</sup>, and even contributed to the introduction of the term “catalysis” by Berzelius<sup>32</sup>. Currently, the societal and

technological importance of catalytic H<sub>2</sub> oxidation increases, due to applications for fuel cells, catalytic heat production, elimination of hydrogen via catalytic recombination and hydrogen sensors<sup>33–36</sup>. On metallic surfaces, numerous atomic scale studies provided deep insights into the reaction mechanism<sup>37–39</sup>, whereas corresponding studies on surface oxides are rare<sup>40,41</sup>. The present work provides such study focusing on the role of the trilayer surface oxide, when large amounts of oxygen are incorporated into the Rh crystal lattice. This is in significant difference to previous studies<sup>21,42,43</sup> of H<sub>2</sub> oxidation on metallic Rh, when only small amounts of subsurface oxygen were involved.

The experimental approach is illustrated in Fig. 1: The crystallography of each μm-sized Rh(hkl) domain of the polycrystalline surface was characterised by electron backscatter diffraction (EBSD; Fig. 1a, see the Methods section below and the details in the SI). The polycrystalline Rh foil was oxidised in the range of 10<sup>−4</sup> mbar O<sub>2</sub> and the oxidised surface studied by locally resolved SPEM, resulting in an “oxidation map” (Fig. 1b). Photoemission electron microscopy (PEEM), with a resolution of ~1 μm, was then employed to visualise the ongoing H<sub>2</sub> oxidation in situ (Fig. 1c). Using the recently-developed kinetics by imaging approach<sup>44</sup>, the local reaction kinetics of individual Rh(hkl) domains can be extracted from real-time PEEM-video-files (Fig. 1c). An “activity map” was created based on hydrogen front propagation. The very same Rh sample was used in the EBSD, SPEM and PEEM experiments, and even the same field of view was monitored, allowing a direct correlation between the local crystallographic structure and SPEM and PEEM data of local oxidation and reaction kinetics, respectively. This combination of SPEM and PEEM is also promising for application to supported particles, enabling spatio-temporal monitoring of

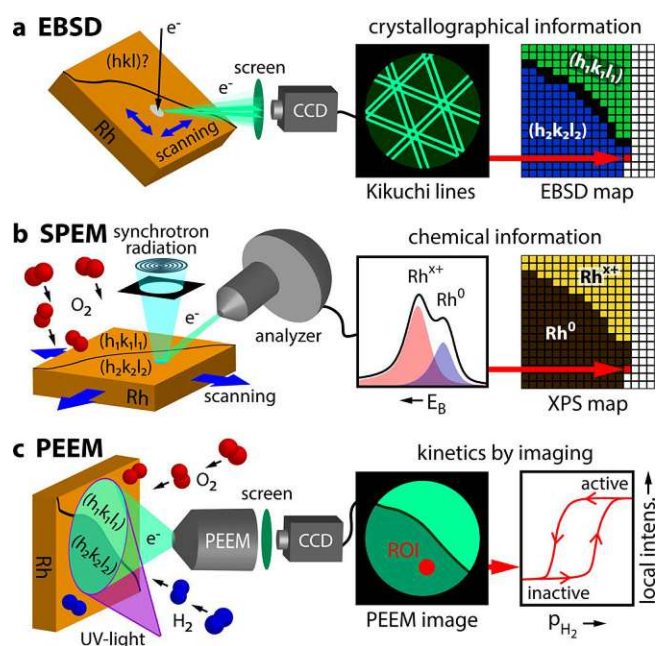


**Fig. 1 Experimental approach.** **a** EBSD: the backscattered electrons of a focused electron beam form Kikuchi lines on a phosphorous screen, enabling determination of the crystallographic orientation of each μm-sized Rh domain; **b** SPEM: an oxidised polycrystalline Rh sample is raster-scanned by a sub-μm-sized X-ray spot, with the emitted photoelectrons providing local XPS spectra. By processing the XPS spectra, the local Rh oxide components can be identified and displayed in a chemical map; **c** PEEM: the ongoing H<sub>2</sub> oxidation reaction is visualised in situ by PEEM, with the analysis of the local PEEM intensities providing spatially resolved local reaction kinetics.



structure, composition and reactivity of technological catalysts, which is mostly performed by e.g. X-Ray, infrared, Raman, magnetic resonance or electron microscopies<sup>45–51</sup>.

In the present work, the anisotropy of surface oxide formation on Rh and its influence on catalytic H<sub>2</sub> oxidation is studied using the powerful combination of two surface-imaging techniques: SPEM and PEEM. SPEM, yielding spatially resolved chemical information, reveals the correlation of initial surface structures and the formation of surface oxides. PEEM, in turn, is used to image H<sub>2</sub> oxidation reaction kinetics of the different highly stepped surface structures. This provides us immediate insight into the role of Rh surface oxides in catalytic H<sub>2</sub> oxidation. The velocities of reaction fronts propagating across the surface serve as an indicator for surface reactivity, revealing a high transient activity of Rh surface oxide.

## Results and discussion

**Mapping anisotropic Rh surface oxidation.** The surface oxidation of Rh and the structure of the resulting surface oxides has been previously studied via various experimental methods, focusing on well-defined Rh single crystal surfaces of mainly low-Miller-index orientations. Techniques such as low energy electron diffraction (LEED), scanning tunnelling microscopy (STM), surface X-ray diffraction (SXRD) and X-ray photoelectron spectroscopy (XPS)<sup>7,11,12,52</sup> were applied. The acquired XPS spectra and STM/SXRD-derived atomic structures were corroborated and explained by ab initio calculations<sup>7,11,12</sup>. Herein, we present the first spatially resolved comparative study of the oxidation of high-Miller-index Rh surfaces.

Figure 2a shows the EBSD map of a polycrystalline Rh foil, consisting of well-defined Rh(hkl) domains, as listed in Fig. 2b. After oxidation at  $T = 623$  K,  $p_{\text{O}_2} = 2.5 \times 10^{-4}$  mbar,  $t = 90$  min, i.e., under conditions similar to those reported for trilayer oxide growth on single crystals<sup>7,11,12</sup>, local XPS spectra (exemplarily shown in Fig. 2c, d) were measured for a  $0.13 \mu\text{m}$  diameter spot on each  $8 \times 8 \mu\text{m}^2$  sample area by SPEM. Due to the chosen photon energy of  $\sim 650$  eV, the kinetic energy of the Rh 3d photoelectrons was in the range of 340–350 eV. In combination with the grazing collection angle, this provides high surface sensitivity with a probing depth of  $\sim 1.5$  nm. The deconvolution of the measured Rh 3d spectra allows determining the metallic, oxidic and interfacial (i.e. the Rh atoms at the interface between the Rh bulk and the trilayer oxide) contributions for each Rh(hkl) domain in the field of view. The resulting peak positions are in quantitative agreement with XPS results for Rh surface oxides formed on low-Miller-index surfaces<sup>7,11,12</sup>, but differ from thicker bulk-like oxides<sup>10</sup> and metallic Rh with adsorbed oxygen<sup>7</sup>.

Figure 2c shows the spectrum deconvolution for the Rh(111) domain (position 1 in Fig. 2a) with 26%, 64 and 10% contributions by metallic, oxidic and interface Rh, respectively (see the SI for details). Corresponding results for the Rh(1391) domain (position 2 in Fig. 2a) with 10%, 78% and 12% of Rh, RhO<sub>x</sub> and interfacial Rh, respectively, are shown in Fig. 2d. Note that the trilayer oxide structures formed on Rh(111), Rh(100) and Rh(110) exhibit the same hexagonal symmetry, differing slightly by the lattice constant (3.02 Å, 3.08 Å and 3.04 Å, respectively<sup>7,11,12</sup>), while their Rh 3d peak positions are identical<sup>7,11,12</sup>. This is also the case for the present Rh(111) surface, consisting of (111) fcc terraces, and Rh(1391), consisting of (110) fcc terraces.

The XPS results for each Rh(hkl) domain in the field of view ( $512 \times 600 \mu\text{m}^2$ , Fig. 2a) are summarised as a chemical map of the surface oxide contribution (Fig. 2e), directly illustrating the anisotropy of the surface oxidation of different stepped Rh(hkl) surfaces. As the formed surface oxides are structurally nearly

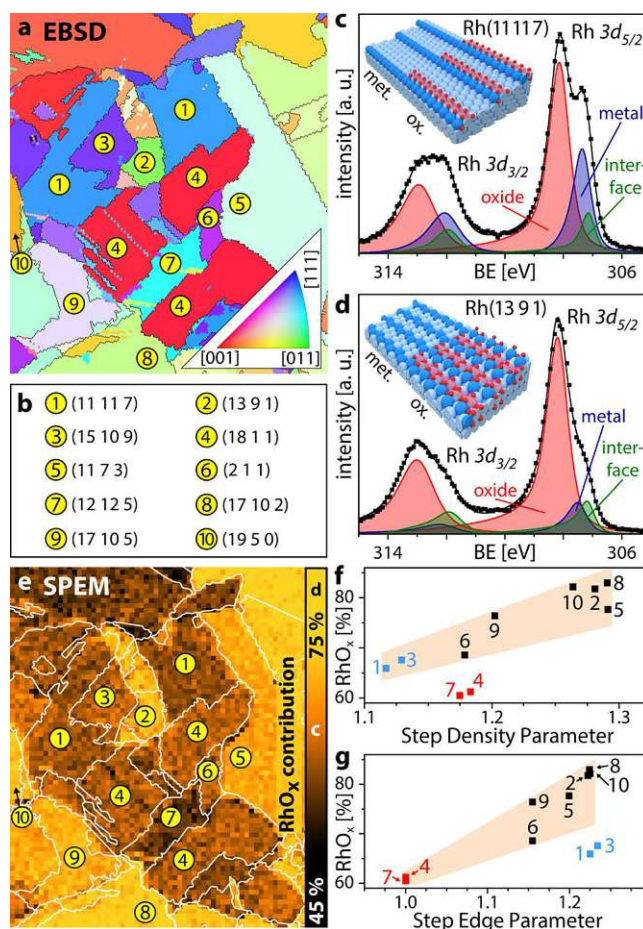


**Fig. 2 Mapping anisotropic Rh surface oxidation.** **a** EBSD image of the polycrystalline Rh foil ( $512 \times 600 \mu\text{m}$ ); **b** crystallographic orientations (Miller indices) of the Rh(hkl) domains indicated in **a** and **e**; **c**, **d** examples of local XPS spectra and ball models of the metallic and oxidised Rh(111) and Rh(1391) domains, respectively. Squares: measured values; solid lines: sum of the deconvoluted components; **e** oxidation map of the region displayed in **a** after oxidation in O<sub>2</sub> ( $T = 623$  K,  $p_{\text{O}_2} = 2.5 \times 10^{-4}$  mbar,  $t = 90$  min), with the right edge of the map displaying the colour scale for the RhO<sub>x</sub> contribution; **f**, **g** show the RhO<sub>x</sub> contribution versus the step density parameter (SDP) and step edge parameter (SEP), respectively (see SI for a detailed description of SDP and SEP). Squares: measured values (see text for the highlighted data points); shaded areas serve as a guide for the eye.

identical (see SI), the differences in the oxide contributions may thus result from different extent of oxide coverage on the metallic substrate. In this respect, we refer to recent STM results, which revealed a stripe-like growth of the Rh surface oxide: patches of the O-Rh-O trilayer were first formed along the step edges, before extending to the Rh(111) terraces<sup>53</sup>. Kinetic limitations of stripe-like growth, predicted by DFT, result in only partial coverage of wider terraces by surface oxide (see schematic models in Fig. 2c, d). Thus, domains differing in the width of their terraces will be covered by surface oxide to a different extent, leading to differing metal/oxide area ratios. Consequently, the RhO<sub>x</sub> contribution to the XPS signal depends on the step density. In addition, the atomic structure of the step edges (e.g. the number of kinks) modifies the kinetic barriers for surface oxide formation<sup>54</sup>. This will result in differing shapes of the oxide stripes, again varying the RhO<sub>x</sub> contribution to the XPS signal. To analyse the dependence of surface oxide formation on a particular surface orientation (structure), both the step density and step edge

configurations must be considered. Thus, we have developed a numerical description of these two relevant aspects, introducing the dimensionless step density parameter (SDP) and step edge parameter (SEP). Both parameters are based on the surface free energy in relation to the smooth close-packed (111) fcc surface. The SDP, characterising the density of atomic steps, is calculated from a model surface having the same terrace structure and width as the considered surface, but simplified non-kinked step edges. The SEP, in turn, is calculated from a model surface formed by the step edge rows of the considered surface and thus describes the particular atomic configuration of the step edges. Further details on the calculation of SDP and SEP are given in the SI.

Plots of the surface oxide contribution versus SDP and SEP are shown in Fig. 2f, g, respectively, displaying a clear trend of higher  $\text{RhO}_x$  extent for increasing SDP and SEP. A qualitative trend of stronger surface oxidation for higher atomic roughness (due to steps and kinks) has been reported in literature<sup>53</sup>, but, to our knowledge, the present SDP/SEP evaluation is the first to address both factors quantitatively. Even the apparent outliers (i.e. data points outside of the shaded areas in Fig. 2f, g) can be explained by this concept: the lower  $\text{RhO}_x$  contribution of Rh(18 1 1) and Rh(12 12 5) (red squares, positions 4 and 7 in Fig. 2f) is due to their position on the SEP axis (see Fig. 2g). Similarly, Rh(11 11 7) and Rh(15 10 9) (blue squares, positions 1 and 3 in Fig. 2g) have lower  $\text{RhO}_x$  contribution due to their position on the SDP axis (see Fig. 2f). For more details concerning the interrelation of SDP and SEP see the SI.

### Impact of surface oxidation anisotropy on catalytic $\text{H}_2$ oxidation.

In the following, catalytic  $\text{H}_2$  oxidation is used as a probe to indicate the effect of the surface oxidation anisotropy. For catalytic  $\text{H}_2$  oxidation on Rh, both reactants need to adsorb to the catalyst surface before the reaction can take place (Langmuir-Hinshelwood mechanism)<sup>42,55</sup>. At low  $p_{\text{H}_2}/p_{\text{O}_2}$  ratio the reaction system is in an inactive steady-state (adsorbed oxygen blocks the adsorption of hydrogen). Increasing the  $p_{\text{H}_2}/p_{\text{O}_2}$  ratio at constant temperature lets the system switch to an active steady-state at a certain  $p_{\text{H}_2}/p_{\text{O}_2}$  ratio. This, as well as the reverse switch, occur via a kinetic transition, a process similar to a phase transition in equilibrium thermodynamics (whereas kinetic transitions in catalysis are topics of non-equilibrium thermodynamics<sup>56</sup>). Such kinetic transitions can be visualised by PEEM, as the brightness of the PEEM image results from the photoemission yield governed by the work function of the imaged surface, which, in turn, depends on the surface coverage. For example, the inactive oxygen-covered Rh surface has a higher work function than the adsorbate free Rh surface and thus appears dark in PEEM contrast. Vice versa, the catalytically active surface with low  $\text{H}_{\text{ads}}$  and  $\text{O}_{\text{ads}}$  coverage is characterised by lower work function and thus appears bright. These image contrast differences are the basis of the kinetics by imaging approach in  $\text{H}_2$  oxidation on Rh<sup>21,57</sup> and allow extracting the local kinetic information from in situ recorded PEEM video-sequences (for details see the SI). In the present studies, the same Rh sample as in the SPEM experiments was used. The PEEM chamber was filled with gaseous  $\text{O}_2$  and  $\text{H}_2$  in the  $10^{-6}$  mbar pressure range and operated like a flow reactor, and the reaction on the Rh sample was visualised and video-recorded in real time, as summarised in Fig. 3. The fields of view in the SPEM and PEEM experiments are almost completely overlapping (cf. EBSD maps in Figs. 2a and 3a, a comparison is shown in the SI).

Catalytic experiments both on metallic and oxidised Rh always started from the inactive O-covered state (Fig. 3b). Increasing  $p_{\text{H}_2}$  at constant  $p_{\text{O}_2}$  and T leads to a kinetic transition to the active state at a particular  $p_{\text{H}_2}$  value  $\tau_A$ . The transition was

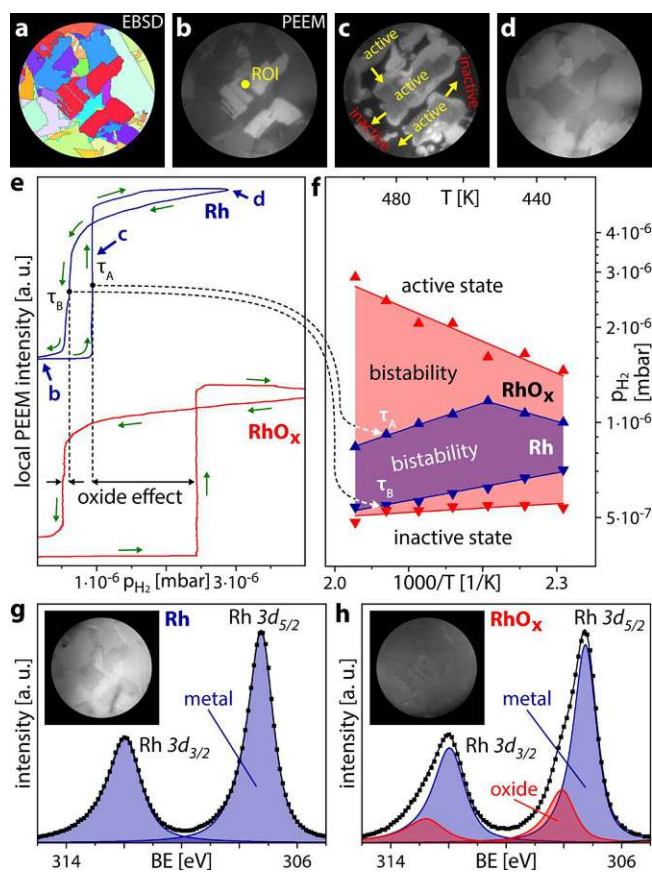


**Fig. 3** Imaging catalytic  $\text{H}_2$  oxidation on metallic and oxidised Rh. **a** EBSD map of the chosen Rh sample region (diameter 550  $\mu\text{m}$ , cf. Fig. 2a); **b** the same region imaged by PEEM (oxygen-covered metallic Rh surface), the contrast reflects the work function differences between different Rh(hkl) domains; **c** in situ PEEM image of an ongoing kinetic transition during  $\text{H}_2$  oxidation, arrows show directions of propagating reaction fronts, bright areas correspond to the catalytically active surface; **d** PEEM image of the catalytically active steady-state resulting from the transition depicted in **c**; **e** hysteresis curves registered by processing the local PEEM intensity of the ROI shown in **b** during cyclewise variation of the  $\text{H}_2/\text{O}_2$  pressure ratio from 0.1 to 6.5 at constant  $\text{O}_2$  pressure of  $7.7 \times 10^{-7}$  mbar and temperature of 483 K. The upper and lower hysteresis curves correspond to the metallic and oxidised Rh surface, respectively; **f** kinetic phase diagrams for  $\text{H}_2$  oxidation on the metallic (shaded blue) and oxidised (shaded red) Rh surface; **g, h** Rh 3d XPS spectra obtained by lab-XPS (excitation energy 1253.6 eV), for the metallic and oxidised Rh surface, respectively. Squares: measured values; solid lines: sum of the deconvoluted components. The insets show corresponding PEEM images.

accompanied by  $\text{H}_{\text{ads}}$  fronts spreading over the entire field of view (Fig. 3c), and resulted in the catalytically active nearly adsorbate-free state (Fig. 3d). Subsequently decreasing the  $\text{H}_2$  partial pressure caused the reverse kinetic transition at a  $p_{\text{H}_2}$  value  $\tau_B$ , with  $\tau_B$  being significantly lower than  $\tau_A$ .

From the recorded video-sequences, the local PEEM image intensity can be read out for regions of interest (ROIs) placed at arbitrarily chosen locations on the surface. As an example for metallic Rh, the local intensity evaluated within the ROI marked in Fig. 3b is plotted versus the  $\text{H}_2$  partial pressure ( $T = 483$  K,  $p_{\text{O}_2} = 7.7 \times 10^{-7}$  mbar), yielding the blue trace in Fig. 3e. The curve shows a pronounced hysteresis between the kinetic transition points  $\tau_A$  and  $\tau_B$ , indicating a bistability of the reaction: between  $\tau_A$  and  $\tau_B$ , the system can exist either in its active or inactive state, depending solely on the sample prehistory<sup>42,57</sup>.

To examine the effect of the Rh trilayer oxide on catalytic  $H_2$  oxidation, the Rh sample was oxidised at the same conditions as described for the SPEM experiments (Fig. 2). To ensure the same oxidation state of the Rh sample before each catalytic experiment, a laboratory XPS system, directly connected to the PEEM chamber, was used. Exemplary Rh 3d spectra and corresponding PEEM images of the clean and oxidised surfaces are shown in Fig. 3g, h, respectively. In comparison to the synchrotron SPEM (photon energy 650 eV, take-off angle  $60^\circ$ , probing depth  $\sim 1.5$  nm) the lab-XPS (photon energy 1253.6 eV, take-off angle  $0^\circ$ ), provides reduced surface sensitivity (due to the higher probing depth of  $\sim 5$  nm) and energy resolution (0.8 eV versus 0.3 eV in the SPEM experiments). This necessitates a different deconvolution procedure and hampers the discrimination of the interface and metallic components, but the surface oxide component relevant in the present study can still be reliably discerned.

After Rh surface oxidation, the  $H_2$  oxidation reaction was again monitored by PEEM and the local image intensity was evaluated. The red trace in Fig. 3e shows the exemplary result for the same ROI as for the metallic surface. Again, a hysteresis was observed, but with much wider hysteresis loop for the oxidised Rh surface than for metallic Rh:  $\tau_A$  is shifted to significantly higher  $pH_2$ , while  $\tau_B$  is shifted to slightly smaller  $pH_2$ . Such experiments were repeated at different temperatures in the range of 433–493 K and the transition points are summarised in a kinetic phase diagram, shown in Fig. 3f, both for the metallic (shaded blue) and the oxidised (shaded red) Rh surface. The same trends were observed in the whole temperature region studied, i.e. the region of bistability is generally wider for oxidised Rh.

To rationalise the different catalytic behaviour of metallic and oxidised Rh we refer to recent STM and high-resolution XPS studies, complemented by calculations performed via the Johnson-Mehl-Avrami-Kolmogoroff (JMAK) theory<sup>58</sup>. As shown in that study,  $H_2$  hardly adsorbs on Rh trilayer oxide and the reduction almost exclusively started at steps providing sites for dissociative  $H_2$  adsorption. In our experiments, particularly the step edges were covered by surface oxide (see the insets in Fig. 2c, d), so significantly higher  $H_2$  pressures ( $\tau_A$  values) were needed to initiate dissociative  $H_2$  adsorption, e.g. at a step edge or a terrace defect. For the reverse kinetic transition at  $\tau_B$ , the relevant sites on the step edges were already oxide-free. Accordingly, the kinetic transitions to the inactive state occurred at a  $H_2$  pressures  $\tau_B$  close to that of the metallic Rh surface. Therefore, the entire bistability region in the phase diagram for oxidised Rh in Fig. 3f is wider than that for metallic Rh. Clearly, exposures to reducing conditions may partially reduce the Rh oxide surface and modify the hysteresis loop (see the SI for details).

Due to the fast diffusion of atomic hydrogen on metallic and oxidic Rh surfaces, also across grain boundaries, the reaction is not confined to particular domains (in contrary to CO oxidation on Pt and Pd<sup>20</sup>). As a result, kinetic transitions initiated at a specific location quickly spilled-over to neighbouring domains and finally across the entire sample. At first glance, this seems to wipe out the main advantage of a surface structure library, namely the access to structure-sensitivity. However, a detailed view on exploiting the parallel imaging principle of PEEM reveals an interesting additional feature: PEEM provides simultaneous monitoring of the front propagation on different Rh(hkl) domains, allowing a direct comparison of the front velocities and their association with crystallographic orientations of particular Rh(hkl) domains.

This is illustrated in Fig. 4a–c, analysing the reaction front propagation on metallic Rh during the kinetic transition from the inactive to the active steady state (transition  $\tau_A$  in Fig. 3e,  $pH_2/pO_2 = 1.2$ ). Exemplarily, a rectangular ROI ( $15 \times 50 \mu m^2$ ) is placed on the Rh(11 7 3) domain (Fig. 4a), with the position of

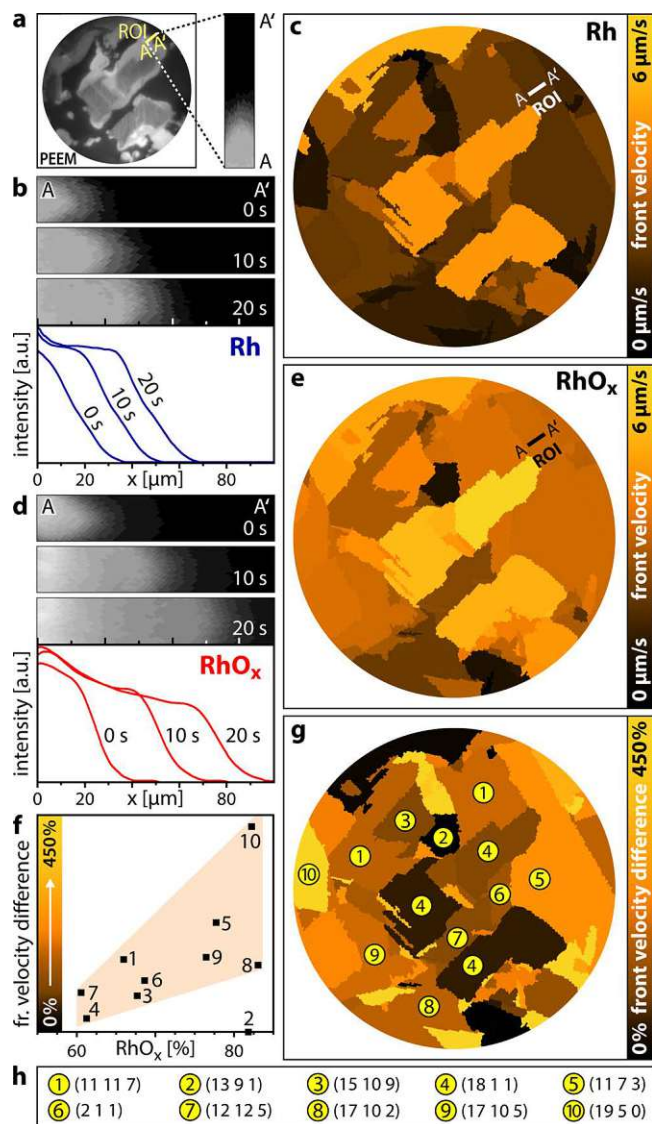


**Fig. 4** Mapping reaction front propagation in  $H_2$  oxidation on Rh. **a** in situ PEEM image during an ongoing kinetic transition from the inactive to the active steady state on metallic Rh ( $T = 483$  K,  $pO_2 = 7.7 \times 10^{-7}$  mbar,  $pH_2 = 9.2 \times 10^{-7}$  mbar) and a magnified ROI ( $15 \times 50 \mu m^2$ ); **b** consecutive PEEM snapshots (10 s interval) for the ROI marked in **a** and respective intensity profiles for the front propagation on metallic Rh; **c** the corresponding front velocity map of metallic Rh, the colour scale is placed on the right; **d** and **e** are analogous to **b** and **c**, but for the oxidised Rh surface ( $T = 483$  K,  $pO_2 = 7.7 \times 10^{-7}$  mbar,  $pH_2 = 2.4 \times 10^{-6}$  mbar); **f** front velocity difference for selected domains of the oxidised Rh surface relative to metallic Rh. Squares: measured values; the shaded area illustrates the trend; **g** velocity difference map, the colour scale (numerically corresponding to the ordinate in **f**), is placed on the right; **h** crystallographic orientations (Miller indices) of the Rh(hkl) domains indicated in **g**.

the reaction front being clearly visible as dividing line between the active (bright) and inactive (dark) Rh surface. The local front velocity was evaluated from the time dependence of the front position, as shown in three exemplary cut-outs of PEEM snapshots (10 s interval) and corresponding intensity profiles in Fig. 4b.

For the different domains, a front velocity map can then be constructed, with the values averaged over the particular  $\mu m$ -sized Rh(hkl) domains (Fig. 4c). Such velocity map clearly shows a pronounced structure-sensitivity of the front

propagation velocity ranging between 0.77  $\mu\text{m/s}$  for Rh(19 5 0) and 4.40  $\mu\text{m/s}$  for Rh(18 1 1).

To study how the surface oxide affected the reaction front propagation, the analogous kinetic transition was analysed for the oxidised Rh(hkl) surfaces at the same  $T$  and  $p\text{O}_2$ . Due to the presence of the surface oxide, the transition occurred at somewhat higher hydrogen pressure of  $2.4 \times 10^{-6}$  mbar (Fig. 3e,  $p\text{H}_2/p\text{O}_2 = 3.1$ ). The exemplary intensity profiles and the *front velocity map* are depicted in Fig. 4d, e, respectively. We note that also for the oxidised Rh(hkl) surfaces the structure-sensitivity of the front propagation is maintained. Comparing the results for metallic and oxidised surfaces reveals that the front propagation velocity is generally higher for the oxidised surfaces.

At first, one is tempted to attribute this to the higher  $p\text{H}_2$  required to initiate the kinetic transition on the oxidised surface. However, the different degree of increase in front velocity for differing Rh(hkl) domains indicates that this is not the main reason (Fig. 4e is not simply a brighter version of Fig. 4c). Indeed, previous experiments on surface oxidised Rh(110) reported an easier reduction of the oxide trilayer (especially of on-surface oxygen), whereas reduction of chemisorbed oxygen on Rh metal required a 40K higher temperature<sup>59</sup>. For the reaction on the oxidised Rh sample, in the initial inactive state,  $\text{RhO}_x$  stripes along the step edges alternate with stripes of  $\text{O}_{\text{ads}}$ -covered metallic Rh terraces (Fig. 2c, d). The hydrogen front then propagates significantly faster over the surface oxide than over the  $\text{O}_{\text{ads}}$ -covered metallic surface. As a result, the higher the extent of the surface oxide is, the faster the reaction front propagates over the domains.

To prove this relation between the extent of surface oxidation (as determined by SPEM) and the front propagation velocity (as determined by PEEM), ten different Rh(hkl) domains were analysed in detail, indeed revealing a correlation between the  $\text{RhO}_x$  contribution and the front velocity (Fig. 4f). The only exception is Rh(13 9 1) (number 2), which can be explained by the strong (110) component of its surface structure: the reaction front acceleration on the oxide is compensated by plenty atomic furrows on the terraces.

The results on the front propagation are summarised in a *velocity difference map* (Fig. 4g), depicting the structure-dependence of the velocity difference between Rh oxide and metal. We note that the *velocity difference map* strongly resembles the *oxidation map* in Fig. 2e: domains with a higher surface oxide contribution exhibit a stronger effect on the front propagation. This once more emphasises the intrinsic relation between the presence and extent of Rh surface oxide and the reaction front propagation, the latter transmitting kinetic transitions between the catalytically active and inactive states of the catalyst surface<sup>60,61</sup>. Compared to  $\text{O}_{\text{ads}}$  on metallic Rh, the oxygen atoms of the trilayer oxide have lower average binding energy, resulting from the distortion of the Rh lattice upon oxygen incorporation into the subsurface<sup>62,63</sup>. As a result, the surface oxygen atoms can be removed more easily, effectively lowering the activation barrier for the oxidation reaction (similar as calculated for CO oxidation<sup>17</sup>). The fronts move faster and the *front velocity map* directly reflects the increased activity. After  $\text{RhO}_x$  has been reduced, the active steady state in  $\text{H}_2$  oxidation is metallic Rh with low adsorbate coverage. However, the simultaneous real-time collection of data for different crystallographic orientations allows insight even into temporary catalytic phases, i.e. provides a direct visualisation of the transient surface oxide activity.

In the present study we demonstrate the combined power of two surface-imaging techniques, when applied to the very same sample regions: scanning photoelectron microscopy (SPEM) allows local XPS chemical analysis on a sub- $\mu\text{m}$ -scale, while photoemission electron microscopy (PEEM), based on the

parallel imaging principle, allows simultaneously monitoring reactions on different regions. When applied to a polycrystalline sample, representing a library of different well-defined surface structures, this specific combination enables a direct correlation between initial surface structures, the formation of surface oxides, and their resulting catalytic properties. SPEM revealed the effect of the step and kink density of different Rh(hkl) domains on the extent of Rh surface oxide formation, with the step density (SDP) and step edge (SEP) parameters enabling quantitative correlations.

In turn, PEEM imaged the  $\text{H}_2$  oxidation reaction kinetics of different highly stepped surface structures, both for metallic and oxidised surfaces of the very same sample region. The parallel imaging principle of PEEM enabled us to simultaneously register the local reactivity of dozens of domains with differing surface structures. This allowed mapping of reactivity on a  $\mu\text{m}$ -scale, providing immediate insight into the role of surface structure and surface oxidation, and to address the role of Rh surface oxides in catalytic  $\text{H}_2$  oxidation. Using the velocity of reaction fronts propagating across the surface during kinetic transitions as indicators of surface reactivity, a high transient activity of Rh surface oxide was detected. Since the local activity enhancement appeared to be structure-dependent, one can consider this a direct imaging of a structure-activity relation for plenty of well-defined structures combined within one sample.

## Methods

**Preparation and characterisation of the Rh sample.** A polished Rh foil (10  $\times$  12  $\text{mm}^2$ , 0.2 mm thickness, 99.99% purity, MaTeck) was used as polycrystalline Rh sample. The sample was cleaned in UHV by repeated cycles of  $\text{Ar}^+$  ion sputtering at 1 keV at 300 K, annealing to 1073–1173 K and consecutive chemical treatment in oxygen ( $p\text{O}_2 = 5 \times 10^{-7}$  mbar at 773 K) and hydrogen ( $p\text{H}_2 = 5 \times 10^{-6}$  mbar at 773 K). Cleanliness of the sample was verified before each experiment by SPEM or lab-XPS. The foil temperature was measured by a Type K thermocouple spot-welded to its front. Characterisation of the sample crystallography was performed by electron backscatter diffraction (EBSD), providing the crystallographic orientation of each  $\mu\text{m}$ -sized domain by scanning the sample surface with a focused electron beam and recording the diffraction patterns generated by the back-scattered electrons. EBSD measurements were performed in a field emission scanning electron microscope (FEI Quanta 200 F) using standard EBSD conditions and evaluation procedures<sup>64</sup>, more details are given in the SI.

**Surface oxidation of Rh.** Experiments on the surface oxidation of Rh were performed at the ESCA Microscopy beamline of the Elettra synchrotron facility, which has been described in detail elsewhere<sup>65</sup>. Summarising, the end station consists of three UHV sub-chambers: the sample is introduced to the system via a fast-entry load lock attached to the first chamber. Using magnetic transfer arms and wobble sticks, the sample can be transferred in UHV to a preparation chamber, which is equipped with facilities for  $\text{Ar}^+$  ion sputtering, annealing, high purity gas supply ( $\text{H}_2$ : 99.999%,  $\text{O}_2$ : 99.999%) and Auger Electron Spectroscopy (AES) for checking sample composition and cleanliness. Afterwards, the sample is transferred in UHV to the SPEM chamber, hosting the zone plate optical system, which provides the X-ray microprobe, a piezo specimen positioning and scanning system and a hemispherical energy analyser equipped with a 48-channel detector.

The SPEM was operated with a lateral resolution of 0.13  $\mu\text{m}$  in the micro-spectroscopy mode and data recorded for a 0.13- $\mu\text{m}$  spot on each  $8 \times 8 \mu\text{m}^2$  sample area in the spectro-microscopy mode with 0.3 eV energy resolution<sup>66</sup>. Due to the setup geometry, electrons emitted at an angle of 60° to the surface normal were registered. The surfaces were oxidised in the preparation chamber and the sample immediately transferred to the SPEM chamber. Spectra were taken at a photon energy of 650.9 eV and measured in a background pressure of  $1 \times 10^{-7}$  mbar  $\text{O}_2$  at 300 K, in order to prevent oxide reduction by residual gas ( $\text{CO}$  or  $\text{H}_2$ ). Calibration of the SPEM magnification was achieved by comparing the Rh  $3d$  elemental maps, displaying topographic contrast, with optical micrographs of the polycrystalline Rh sample.

**Catalytic  $\text{H}_2$  oxidation on metallic and oxidised Rh.** Experiments of catalytic  $\text{H}_2$  oxidation on metallic and oxidised Rh surfaces were conducted in a UHV setup consisting of separate chambers for PEEM and XPS, interconnected by a sample transfer tunnel. The PEEM chamber is equipped with sample cleaning facilities, a PEEM (Staib Instruments PEEM 150), a deuterium discharge UV lamp (Heraeus D200F, photon energy ~6.5 eV), a quadrupole mass spectrometer (MKS e-Vision 2) and a high purity gas supply system ( $\text{H}_2$ : 99.9995%,  $\text{O}_2$ : 99.9999%). In addition to similar sample cleaning and gas dosing facilities, the XPS chamber is equipped

with a twin anode X-ray source (Specs XR-50) and a hemispherical energy analyser (Specs Phoibos 100).

The ongoing H<sub>2</sub> oxidation reaction was visualised in situ by PEEM and the images were recorded by a high-speed CCD camera (Hamamatsu C11440-42U30). Calibration of the PEEM magnification was done by comparison of PEEM images with optical micrographs of the polycrystalline Rh sample. Apart from assessing the cleanliness of the sample, XPS was mainly used to verify the oxidation state of the Rh sample before performing PEEM experiments on the oxidised Rh surfaces. The XPS spectra were acquired from the centre of the sample (circular area of 100 µm in diameter), using Mg K<sub>α</sub> X-ray radiation, with the energy analyser oriented perpendicular to the sample surface (take-off angle 0°).

**Reporting summary.** Further information on research design is available in the Nature Research Reporting Summary linked to this article.

### Data availability

The data that support the findings of this study are available from the corresponding author upon reasonable request.

Received: 1 September 2020; Accepted: 30 November 2020;

Published online: 04 January 2021

### References

- Henrich, V. E. & Cox, P. A. *The Surface Science of Metal Oxides* (Cambridge University Press, 1994).
- Singhal, S. C. & Kendal, K. (eds) *High Temperature and Solid Oxide Fuel Cells: Fundamentals, Design and Applications* (Elsevier Science, 2003).
- Schmuki, P. From Bacon to barriers: a review on the passivity of metals and alloys. *J. Solid State Electrochem.* **6**, 145–164 (2002).
- Day, A. Semiconductor metal oxide gas sensors: a review. *Mater. Sci. Eng. B* **229**, 206–217 (2018).
- Bowker, M. Automotive catalysis studied by surface science. *Chem. Soc. Rev.* **37**, 2204–2211 (2008).
- Lundgren, E. et al. Two-Dimensional Oxide on Pd(111). *Phys. Rev. Lett.* **88**, 246103 (2002).
- Dri, C. et al. Initial oxidation of the Rh(110) surface: ordered adsorption and surface oxide structures. *J. Chem. Phys.* **125**, 094701 (2006).
- Diebold, U., Li, S.-C. & Schmid, M. Oxide surface science. *Annu. Rev. Phys. Chem.* **61**, 129–148 (2010).
- Mittendorfer, F. Low-dimensional surface oxides in the oxidation of Rh particles. *J. Phys. Condens. Matter* **22**, 393001 (2010).
- Blomberg, R. et al. A high pressure X-ray photoelectron spectroscopy study of oxidation and reduction of Rh(100) and Rh nanoparticles. *Surf. Sci.* **628**, 153–158 (2014).
- Gustafson, J. et al. Structure of a thin oxide film on Rh(100). *Phys. Rev. B* **71**, 115442 (2005).
- Gustafson, J. et al. Self-limited growth of a thin oxide layer on Rh(111). *Phys. Rev. Lett.* **92**, 126102 (2004).
- Flege, J. I., Hrbek, J. & Sutter, P. Structural imaging of surface oxidation and oxidation catalysis on Ru(0001). *Phys. Rev. B* **78**, 165407 (2008).
- Westerström, R. et al. Oxidation of Pd(553) from ultrahigh vacuum to atmospheric pressure. *Phys. Rev. B* **76**, 155410 (2007).
- Lundgren, E. et al. Surface oxides on close-packed surfaces of late transition metals. *J. Phys. Condens. Matter* **18**, R481–R499 (2006).
- Reuter, K., Stampfl, C., Ganduglia-Pirovano, M. V. & Scheffler, M. Atomistic description of oxide formation on metal surfaces: the example of ruthenium. *Chem. Phys. Lett.* **352**, 311–317 (2002).
- Todorova, M. et al. Role of subsurface oxygen in oxide formation at transition metal surfaces. *Phys. Rev. Lett.* **89**, 096103 (2002).
- Jelic, J., Reuter, K. & Meyer, R. The role of surface oxides in NO<sub>x</sub> storage reduction catalysts. *ChemCatChem* **2**, 658–660 (2010).
- Suchorski, Y. & Rupprechter, G. Heterogeneous surfaces as structure and particle size libraries of model catalysts. *Catal. Lett.* **148**, 2947–2956 (2018).
- Vogel, D. et al. Local catalytic ignition during CO oxidation on low-index Pt and Pd surfaces: a combined PEEM, MS, and DFT study. *Angew. Chem. Int. Ed.* **51**, 10041–10044 (2012).
- Suchorski, Y. et al. Visualizing catalyst heterogeneity by a multifrequential oscillating reaction. *Nat. Commun.* **9**, 1–6 (2018).
- Rioux, R. M., Song, H., Yang, P. & Somorjai, G. A. *Metal Nanoclusters in Catalysis and Materials Science: The Issue of Size Control* Ch. 7 (Elsevier B. V., 2008).
- Amati, M. et al. Characterization of catalytic materials with scanning photoelectron microscopy: present and future. *Surf. Sci.* **652**, 20–25 (2016).
- Gustafson, J. et al. The role of oxides in catalytic CO oxidation over rhodium and palladium. *ACS Catal.* **8**, 4438–4445 (2018).
- Gustafson, J. et al. Structure and catalytic reactivity of Rh oxides. *Catal. Today* **145**, 227–235 (2009).
- Westerström, R. et al. Structure and reactivity of a model catalyst alloy under realistic conditions. *J. Phys. Condens. Matter* **20**, 184018 (2008).
- Grass, M. E. et al. A reactive oxide overlayer on rhodium nanoparticles during CO oxidation and its size dependence studied by in situ ambient-pressure X-ray photoelectron spectroscopy. *Angew. Chem. Int. Ed.* **47**, 8893–8896 (2008).
- Flege, J. I. & Sutter, P. In situ structural imaging of CO oxidation catalysis on oxidized Rh(111). *Phys. Rev. B* **78**, 153402 (2008).
- Peden, C. H. F. et al. Kinetics of carbon monoxide oxidation by oxygen or nitric oxide on rhodium (111) and rhodium (100) single crystals. *J. Phys. Chem.* **92**, 1563–1567 (1988).
- Döbereiner, J. W. Propriétés nouvelles et remarquables reconnues au sus-oxide de platine, au sulphure oxidé et à la poussiere du même metal. *Ann. Chim. Phys.* **24**, 91–96 (1823).
- Faraday, M. Experimental researches in electricity. Sixth series. *Philos. Trans.* **124**, 55–76 (1834).
- Berzelius, J. J. Einige Ideen über eine bei der Bildung organischer Verbindungen in der lebenden Natur wirksame aber bisher nicht bemerkte Kraft. *Jahresber. Fortsch. Phys. Wiss.* **15**, 237–248 (1836).
- Yu, W., Yu, X. & Tu, S.-T. Oxidation of hydrogen off-gas from a fuel cell using a microstructured reactor with hydrophobic Pt-Al<sub>2</sub>O<sub>3</sub> catalyst coating. *Energy Proc.* **61**, 2854–2857 (2014).
- Saint-Just, J. & Etemad, S. *Compendium of Hydrogen Energy Volume 3: Hydrogen Energy Conversion* Ch. 10 (Elsevier, 2016).
- Steffen, P.-M. et al. Operational behavior of a passive auto-catalytic recombiner under low pressure conditions. *Fusion Eng. Des.* **124**, 1281–1286 (2017).
- Hübner, T., Boon-Brett, L., Black, G. & Banacha, U. Hydrogen sensors – a review. *Sens. Actuat. B Chem.* **157**, 329–352 (2011).
- Völkening, S., Bedürftig, K., Jacobi, K., Wintterlin, J. & Ertl, G. Dual-path mechanism for catalytic oxidation of hydrogen on platinum surfaces. *Phys. Rev. Lett.* **83**, 2672–2675 (1999).
- Mitsui, T., Rose, M. K., Fomin, E., Ogletree, D. F. & Salmeron, M. A scanning tunneling microscopy study of the reaction between hydrogen and oxygen to form water on Pd(111). *J. Chem. Phys.* **117**, 5855–5858 (2002).
- Michaelides, A. & Hu, P. Catalytic water formation on platinum: a first-principles study. *J. Am. Chem. Soc.* **123**, 4235–4242 (2001).
- Africh, C. et al. Two-step reaction on a strained, nanoscale segmented surface. *Phys. Rev. Lett.* **93**, 126104 (2004).
- Africh, C. et al. Effects of lattice expansion on the reactivity of a one-dimensional oxide. *J. Am. Chem. Soc.* **131**, 3253–3259 (2009).
- Schaak, A. & Imbihl, R. Bistability and formation of low work function areas in the O<sub>2</sub>+H<sub>2</sub> reaction on a Rh(111) surface. *J. Chem. Phys.* **113**, 9822–9829 (2000).
- Suchorski, Y. et al. Surface-structure libraries: multifrequential oscillations in catalytic hydrogen oxidation on rhodium. *J. Phys. Chem. C* **123**, 4217–4227 (2019).
- Suchorski, Y. & Rupprechter, G. Local reaction kinetics by imaging. *Surf. Sci.* **643**, 52–58 (2016).
- Barroo, C., Wang, Z.-J., Schlögl, R. & Willinger, M.-G. Imaging the dynamics of catalysed surface reactions by in situ scanning electron microscopy. *Nat. Catal.* **3**, 30–39 (2020).
- Chen, G. et al. Bimetallic effect of single nanocatalysts visualized by super-resolution catalysis imaging. *ACS Cent. Sci.* **3**, 1189–1197 (2017).
- Gross, E. Challenges and opportunities in IR nanospectroscopy measurements of energy materials. *Nano Res.* **12**, 2200–2210 (2019).
- Grunwaldt, J.-D., Wagner, J. B. & Dunin-Borkowski, R. E. Imaging catalysts at work: a hierarchical approach from the macro- to the meso- and nano-scale. *ChemCatChem* **5**, 62–80 (2013).
- Mutschler, R. et al. Imaging catalysis: operando investigation of the CO<sub>2</sub> hydrogenation reaction dynamics by means of infrared thermography. *ACS Catal.* **10**, 1721–1730 (2020).
- Ni, G. X. et al. Nanoscale infrared spectroscopy and imaging of catalytic reactions in Cu<sub>2</sub>O crystals. *ACS Photon.* **7**, 576–580 (2020).
- Weckhuysen, B. M. Chemical imaging of spatial heterogeneities in catalytic solids at different length and time scales. *Angew. Chem. Int. Ed.* **48**, 4910–4943 (2009).
- Zhan, R. R., Vesselli, E., Baraldi, A., Lizzit, S. & Comelli, G. The Rh oxide ultrathin film on Rh(100): an x-ray photoelectron diffraction study. *J. Chem. Phys.* **133**, 214701 (2010).
- Farber, R. G. et al. The quest for stability: structural dependence of Rh(111) on oxygen coverage at elevated temperature. *J. Phys. Chem. C* **121**, 10470–10475 (2017).
- Klikovits, J. et al. Step-orientation-dependent oxidation: from 1D to 2D oxides. *Phys. Rev. Lett.* **101**, 266104 (2008).

55. Yates, J. T. Jr, Thiel, P. A. & Weinberg, W. H. Reactions at surfaces: the catalytic reaction between adsorbed oxygen and hydrogen on Rh(111). *Surf. Sci.* **82**, 45–68 (1979).
56. Nicolis, G. & Prigogine I. *Self-Organization in Nonequilibrium Systems* (New York, John Wiley & Sons, 1977).
57. Datler, M. et al. Hydrogen oxidation on stepped Rh surfaces:  $\mu\text{m}$ -scale versus nanoscale. *Cat. Lett.* **146**, 1867–1847 (2016).
58. Klikovits, J. et al. Kinetics of the reduction of the Rh(111) surface oxide: linking spectroscopy and atomic-scale information. *J. Phys. Chem. B* **110**, 9966–9975 (2006).
59. Dudin, P. et al. Initial oxidation of a Rh(110) surface using atomic or molecular oxygen and reduction of the surface oxide by hydrogen. *J. Phys. Chem. B* **109**, 13649–13655 (2005).
60. Suchorski, Y. et al. The role of metal/oxide interfaces for long-range metal particle activation during CO oxidation. *Nat. Mater.* **17**, 519–522 (2018).
61. Suchorski, Y. et al. Transmitting metal-oxide interaction by solitary chemical waves:  $\text{H}_2$  oxidation on  $\text{ZrO}_2$  supported Rh. *Surf. Sci.* **679**, 163–168 (2019).
62. Ganduglia-Pirovano, M. V., Reuter, K. & Scheffler, M. Stability of subsurface oxygen at Rh (111). *Phys. Rev. B* **65**, 245426 (2003).
63. Gong, X.-Q., Liu, Z.-P., Raval, R. & Hu, P. A systematic study of CO oxidation on metals and metal oxides: density functional theory calculations. *J. Am. Chem. Soc.* **126**, 8–9 (2004).
64. Humphreys, F. J. Grain and subgrain characterisation by electron backscatter diffraction. *J. Mater. Sci.* **36**, 3833–3854 (2001).
65. Casalis, L. et al. ESCA microscopy beamline at ELETTRA. *Rev. Sci. Instrum.* **66**, 4870–4875 (1995).
66. Zeller, P. et al. Scanning photoelectron spectro-microscopy: a modern tool for the study of materials at the nanoscale. *Phys. Status Solidi A* **215**, 180308 (2018).

### Acknowledgements

This work was supported by the Austrian Science Fund (FWF) (P 32772-N and SFB F45 FOXSI) and by the project CALIPSOplus under Grant Agreement 730872 from the EU Framework Programme for Research and Innovation HORIZON 2020.

### Author contributions

M.S.-P. performed the EBSD characterisation. M.A., L.G., G.R., P.W., J.Z. and P.Z. performed the SPEM measurements. P.W. and J.Z. performed the PEEM measurements.

G.R. and Y.S. supervised the experimental work and were involved in the analysis of the experimental data. G.R., Y.S., P.W. and J.Z. prepared the manuscript. All authors contributed to the discussion and approved the manuscript.

### Competing interests

The authors declare no competing interests.

### Additional information

Supplementary information is available for this paper at <https://doi.org/10.1038/s41467-020-20377-9>.

Correspondence and requests for materials should be addressed to G.R.

Peer review information *Nature Communications* thanks Qiang Fu and the other, anonymous, reviewer(s) for their contribution to the peer review of this work.

Reprints and permission information is available at <http://www.nature.com/reprints>

Publisher's note Springer Nature remains neutral with regard to jurisdictional claims in published maps and institutional affiliations.



**Open Access** This article is licensed under a Creative Commons Attribution 4.0 International License, which permits use, sharing, adaptation, distribution and reproduction in any medium or format, as long as you give appropriate credit to the original author(s) and the source, provide a link to the Creative Commons license, and indicate if changes were made. The images or other third party material in this article are included in the article's Creative Commons license, unless indicated otherwise in a credit line to the material. If material is not included in the article's Creative Commons license and your intended use is not permitted by statutory regulation or exceeds the permitted use, you will need to obtain permission directly from the copyright holder. To view a copy of this license, visit <http://creativecommons.org/licenses/by/4.0/>.

© The Author(s) 2021

## **How the anisotropy of surface oxide formation influences the transient activity of a surface reaction**

P. Winkler<sup>1</sup>, J. Zeininger<sup>1</sup>, Y. Suchorski<sup>1</sup>, M. Stöger-Pollach<sup>2</sup>, P. Zeller<sup>3</sup>, M. Amati<sup>3</sup>,  
L. Gregoratti<sup>3</sup>, and G. Rupprechter<sup>1\*</sup>

<sup>1</sup>*Institute of Materials Chemistry, TU Wien, Getreidemarkt 9, 1060 Vienna, Austria*

<sup>2</sup>*University Service Center for Transmission Electron Microscopy, TU Wien,  
Wiedner Hauptstraße 8-10, 1040 Vienna, Austria*

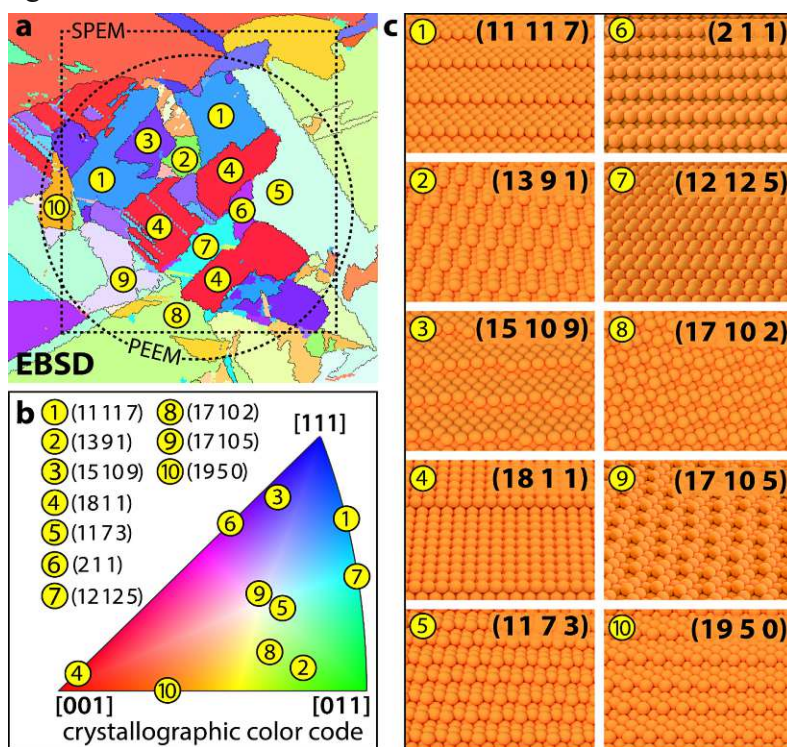
<sup>3</sup>*Elettra–Sincrotrone Trieste S.C.p.A., SS14 - km 163.5 in Area Science Park,  
34149 Trieste, Italy*

## ***Supplementary Information***

## Supplementary Note 1: EBSD characterisation of the Rh sample

In order to study processes such as adsorption, surface oxidation and reaction on individual  $\mu$ -sized domains of the polycrystalline Rh foil and, particularly, to uncover the anisotropy of these processes, the crystallographic orientations of particular Rh(hkl) domains need to be determined first. In the present study, this was carried out by electron backscatter diffraction (EBSD). EBSD is a well-established crystallographic microstructural characterisation technique based on scanning electron microscopy. In EBSD experiments, backscattered electrons of an electron beam, focused on a particular region of a sample, form a backscatter Kikuchi diffraction pattern (BKDP), which corresponds to each of the diffracting crystal lattice planes [1, 2]. EBSD is commonly used in studies of crystalline or polycrystalline materials, e.g. in metallurgy, to understand recrystallisation and grain-growth processes [3, 4]. EBSD was also successfully applied to polycrystalline foils, e.g. to correlate microstructure with electrochemical properties [5] or with catalytic properties of platinum group metals [6, 7, 8]. In the present study, the EBSD measurements were performed by a field emission scanning electron microscope (FEI Quanta 200F) using standard EBSD conditions and evaluation procedures [9].

The corresponding results are shown as a color-coded map in Supplementary Fig. 1a, the dashed lines indicate the regions studied in the SPEM (rectangular region) and PEEM (circular region) experiments. In order to quantify the influence of structural features (e.g. atomic steps and kinks) a set of ten domains (indicated by numbers in Supplementary Fig. 1a) was selected from the studied region, aiming at a resulting broad variety of surface structures. In Supplementary Fig. 1b these domains and their corresponding Miller indices are listed and marked on the colour key (the latter used for colouring the domains in the EBSD map in Supplementary Fig. 1a). Atomic ball models of the crystallographically different stepped Rh surfaces are given in Supplementary Fig. 1c.

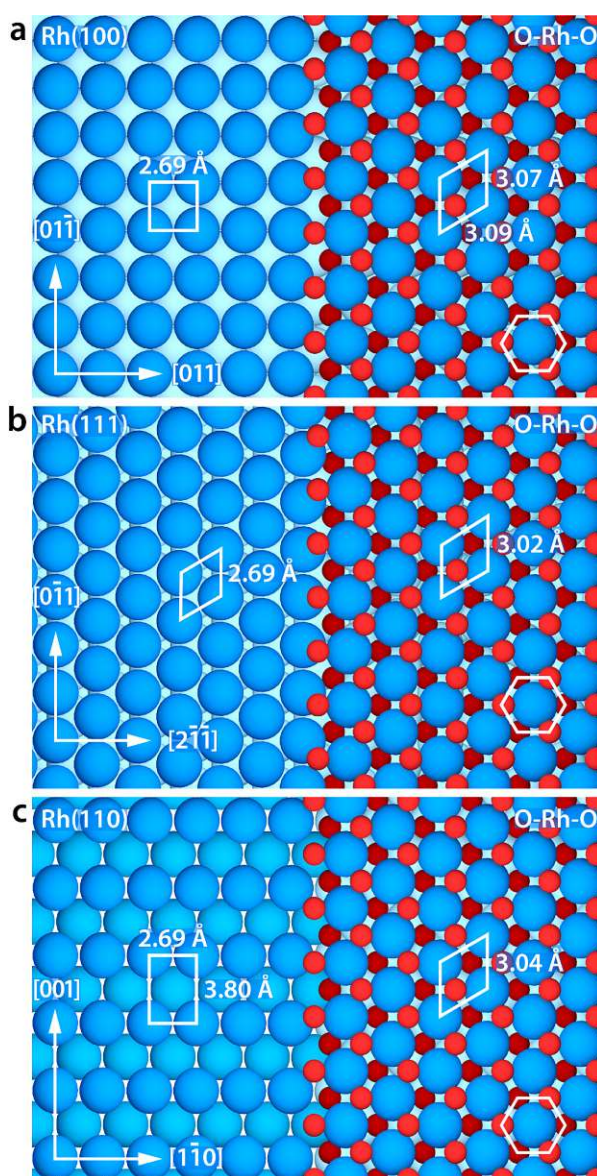


**Supplementary Figure 1.** Determination of the crystallographic orientation and surface structure of individual domains of a polycrystalline Rh foil: (a) EBSD color-coded map of the studied region; the areas imaged by SPEM and PEEM are indicated by dashed lines; (b) Miller indices of ten domains indicated in (a), selected in order to study structural effects, and their location on the EBSD colour key; (c) atomic ball models of the selected set of domains shown in (a) and (b).



## Supplementary Note 2: Surface oxides of Rh

The surface oxidation of rhodium has been studied using various techniques such as X-ray photoelectron spectroscopy (XPS), surface X-ray diffraction (SXRD) and scanning tunnelling microscopy (STM), in combination with ab-initio calculations for mostly simple single crystal surfaces such as (100) [10], (111) [11, 12] and (110) [13]. These studies revealed that at the used oxygen partial pressures ( $10^{-5} < p_{\text{O}_2} < 10^{-3}$  mbar) the formation of a trilayer surface oxide takes place, while the formation of thicker, bulk-like oxide is kinetically hindered. It is important to note that the atomic structure of the surface oxide is similar for all the mentioned low-Miller-index substrate structures. It consists of a hexagonal arrangement of Rh atoms sandwiched between two layers of oxygen atoms, differing just slightly by their lattice constant (3.07/3.09 Å, 3.02 Å and 3.04 Å for Rh(100), Rh(111) and Rh(110), respectively [10, 11, 13]) and by a minimal distortion in the case of Rh(100). Illustrating these findings, Supplementary Fig. 2 shows atomic ball models of the metallic and respective trilayer oxide structures for Rh(100) (Supplementary Fig. 2a), Rh(111) (Supplementary Fig. 2b) and Rh(110) (Supplementary Fig. 2c) and the corresponding surface unit cells, constructed from literature data [10, 11, 13].



**Supplementary Figure 2.** Atomic ball models of the trilayer oxide structures on (a) Rh(100), (b) Rh(111) and (c) Rh(110), in comparison to the corresponding metallic surface structures and their respective surface unit cells. Based on data in Refs. [10, 11, 13].

A typical Rh  $3d_{5/2}$  XPS spectrum of the Rh surface oxide obtained by scanning photoelectron microscopy (SPEM) in the present experiments reveals three components (Fig. 2 in the main article): (i) a bulk (metallic) component; (ii) a component shifted by about 0.3 eV to lower binding energies respective to the bulk, which is attributed to the interface Rh layer between the metal bulk and surface oxide and (iii) a component shifted by about 0.8 eV to higher binding energies, which corresponds to the Rh layer in the surface oxide. Supplementary Table 1 summarises typical binding energies from literature in comparison to the present data. In addition to the synchrotron-based XPS, we also performed lab-XPS measurements in the course of the catalytic experiments. The lower spectral resolution in our lab-XPS setup unfortunately impedes differentiation between the metallic and interface components, therefore the corresponding spectra (Fig. 3 in the main article) just show two components. Nevertheless, distilling of the surface oxide contribution is still possible, thus proving the presence of surface oxide (the oxidation procedure was the same as in the synchrotron-based experiments). All spectra in the present work were deconvoluted using a pseudo-Voigt lineshape [14] in combination with a Shirley background [15]. The energy scales were calibrated against the energy of the Au  $4f_{7/2}$  peak with a binding energy of 84.0 eV.

**Supplementary Table 1.** Binding energies (in eV) of Rh  $3d_{5/2}$  components for the Rh trilayer surface oxide on different Rh(hkl) substrates. The conditions for surface oxide formation and values for the  $\text{Rh}_2\text{O}_3$  and  $\text{RhO}_2$  bulk oxides are listed for comparison.

Substrate	T [K]	$p_{\text{O}_2}$ [mbar]	Binding energy [eV]			Ref.
			Bulk	Oxide	Interface	
Rh(111)	650	$2 \times 10^{-4}$	307.2	308.0	307.0	S11
Rh(110)	750	$> 10^{-4}$	307.2	307.9	306.9	S13
Rh(100)	700	$5 \times 10^{-5}$	307.2	308.0	306.9	S10
Rh(553)	823	$1 \times 10^{-3}$	307.2	308.0	307.0	S46
Rh(poly)	623	$2.5 \times 10^{-4}$	307.3	308.1	307.1	this work
$\text{Rh}_2\text{O}_3$				308.3		S47
$\text{RhO}_2$				308.6		S47

The surface oxidation of rhodium is known to start at the lower coordinated Rh atoms at atomic steps, especially at kink sites via the formation of  $\text{RhO}_2$  mono- and dimers [16]. Subsequently, a chain of oxygen atoms at the step edges and Rh ridges is formed [17, 18]. The oxidation process continues via diffusion of oxygen under the step edges [11, 18, 19], which poses a kinetic hindrance after reaching a penetration depth of several atomic layers [18, 19]. This results in patches of oxide extending into the step edges but not covering the whole terrace, even after continued oxygen exposure. Furthermore, it was shown that the atomic structure of the step edge determines the kinetic barrier for oxygen penetration [18] and thus also the width and/or shape of the oxide patches. As a result, the ratio of oxide covered and metallic areas varies with the atomic structure of the surfaces. As the atomic structures of the trilayer oxide are identical for all low-Miller-index surfaces (and as a result also for the terraces of any high-Miller-index surface), the XPS peak positions and relative intensities are nearly identical (Supplementary Tab. 1). The observed variation in relative peak intensity between the studied surfaces can thus only stem from the varying ratios of oxide covered and metallic areas. Therefore, evaluation of the XPS spectra for areas of different crystallographic orientation (i.e. different domains of a polycrystalline sample) oxidised at identical conditions allow comparison of the extent of the Rh surface oxide formation for surfaces of differing atomic structures.

### Supplementary Note 3: Introduction of SDP and SEP parameters

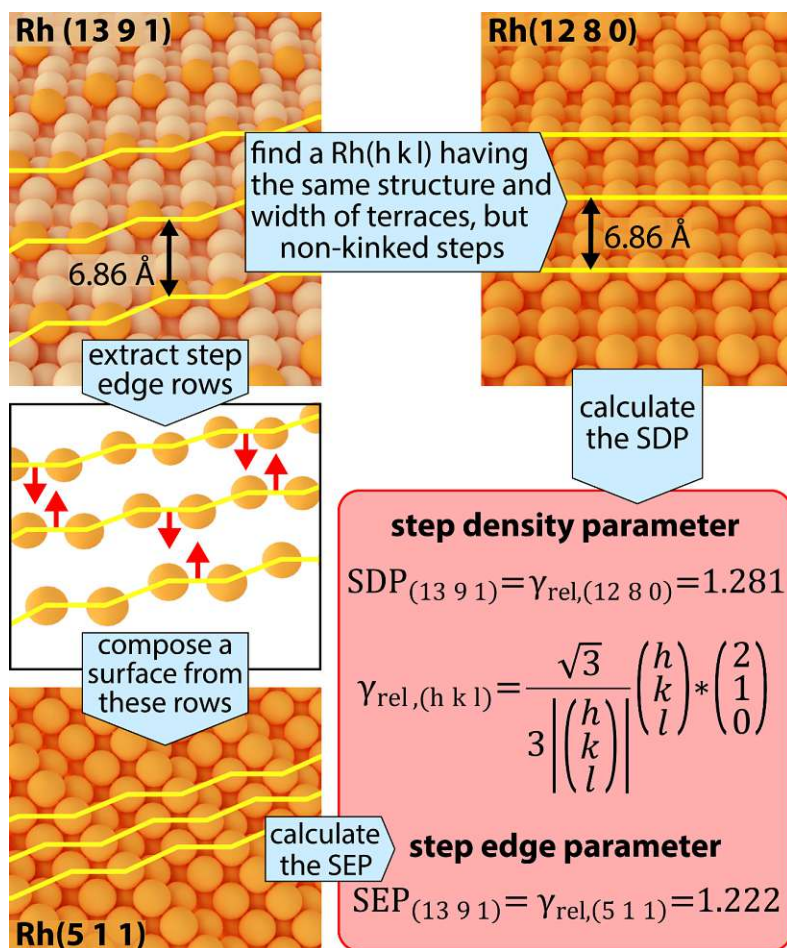
As detailed in Supplementary Note 2, the surface oxidation of rhodium is essentially determined by the presence of atomic steps (and their density) and the atomic structure of the step edges [17-19]. In order to enable quantitative interpretation of the obtained data on surface oxidation, the studied surfaces have to be numerically characterised with respect to these features. The Terrace-Step-Kink (TSK) model [20, 21] provides a suitable framework for interpretation of the atomic structure of a given surface and serves as a basis for the proposed numerical description. Previously used criteria (e.g. geometric step and kink densities [22, 23] or a weighted average number of nearest neighbours [24, 25]) were insufficient for the current purpose, however. The insufficiency results from neglecting essential features such as the particular structure of a terrace or its step edge (in the case of the geometric step and kink densities, respectively) or because the relative contributions of step density and step edge structure (in the case of an average number of nearest neighbours) are not accurately considered. As it is important to consider both the step density and step edge structure, we have developed a set of parameters describing these features, namely the step density parameter (SDP) and the step edge parameter (SEP), respectively. Both parameters are based on the concept of the surface free energy  $\gamma_{(hkl)}$ , which has previously been used e.g. for calculating equilibrium shapes of crystals according to the Wulff theorem [26-28] or to study the structural effects of surface defects [29, 30]. A first approximation of the surface free energy is given by calculating the average number of broken bonds for a given surface [31]. For fcc crystals, such as rhodium, the surface free energy  $\gamma_{(hkl)}$  of the (hkl) surface according to the broken bond model is calculated in Ref. [32]. By normalising the results to the (111) surface, yielding the relative surface free energy  $\gamma_{rel,(hkl)}$ , one circumvents the need for physical properties in the calculation. Equation 1 gives the result of such normalisation for a given (hkl) surface, where  $h$ ,  $k$  and  $l$  denote the corresponding Miller indices.

$$\gamma_{rel,(hkl)} = \frac{\gamma_{(hkl)}}{\gamma_{(111)}} = \frac{\sqrt{3}}{3\sqrt{h^2+k^2+l^2}} \begin{pmatrix} h \\ k \\ l \end{pmatrix} * \begin{pmatrix} 2 \\ 1 \\ 0 \end{pmatrix} \quad (1)$$

Both SDP and SEP are calculated by first constructing a surface, which is equivalent to the described surface in one aspect, but simplifies other aspects. The equivalent surface for calculation of the SDP is characterised by having the exactly same terrace structure and width, but simplified non-kinked step edges (i.e. the steps are of (111)-, (110)- or (100)-type). Calculating  $\gamma_{rel,(hkl)}$  according to Eq. 1, using the Miller indices of this first equivalent surface, yields the SDP. For the SEP, in turn, the equivalent surface is constructed by extracting the step edge rows from the original surface and composing a new surface from these rows (i.e. pushing these rows together). This yields a surface which exactly describes the step edge structure, but totally neglects the terraces present in the original surface. The SEP is obtained by calculating  $\gamma_{rel,(hkl)}$  according to Eq. 1 using the Miller indices of this second equivalent surface.

The process is exemplarily shown for Rh(13 9 1) in Supplementary Fig. 3. Searching for the equivalent surface for calculation of the SDP yields the Rh(12 8 0) surface, which also has

(110)-type terraces of similar width, but plain (111)-type step edges. This results in an SDP of 1.281 for Rh(13 9 1) by calculating  $\gamma_{\text{rel},(hkl)}$  for Rh(12 8 0) using Eq. 1. Constructing the equivalent surface for the SEP produces the Rh(5 1 1) surface, corresponding to an SEP of 1.222 for Rh(13 9 1) by calculating  $\gamma_{\text{rel},(hkl)}$  for Rh(5 1 1) using Eq. 1.



**Supplementary Figure 3.** Step density (SDP) and step edge (SEP) parameters for the Rh(13 9 1) surface. The SDP is calculated as the relative surface free energy  $\gamma_{h,(hkl)}$  of a surface with the same terrace structure and width as Rh(13 9 1), but having non-kinked step edges. In the present case a surface constructed in this way results in a Rh(12 8 0) structure. The SEP is calculated as the relative surface free energy of a surface consisting only of the step edge rows extracted from the Rh(13 9 1) surface (resulting in a Rh(5 1 1) structure in the present case).

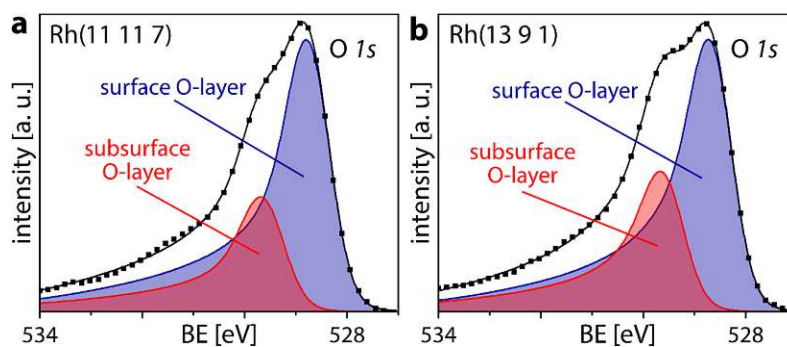
The above procedure has been applied to the whole set of domains studied in the SPEM and PEEM experiments and their structures are shown as atomic ball models in Supplementary Fig. 1c. Supplementary Table 2 lists the Miller indices and the relevant equivalent surfaces for calculation of SDP and SEP, as well as the calculation results for the above-mentioned set of ten domains.

**Supplementary Table 2.** Equivalent surfaces and calculated atomic structure parameters for the set of ten different surface structures shown in Supplementary Fig. 1 and studied in detail in the SPEM and PEEM experiments (Equiv. surf.: equivalent surface, SDP: step density parameter, SEP: step edge parameter).

Number	Miller indices	Step density		Step edge	
		Equiv. surf.	SDP	Equiv. surf.	SEP
1	(11 11 7)	(11 11 7)	1.117	(1 1 0)	1.225
2	(13 9 1)	(12 8 0)	1.281	(5 1 1)	1.222
3	(15 10 9)	(14 9 9)	1.129	(6 1 0)	1.234
4	(18 1 1)	(18 1 1)	1.183	(1 1 1)	1.000
5	(11 7 3)	(8 4 0)	1.290	(7 3 3)	1.199
6	(2 1 1)	(2 1 1)	1.179	(1 0 0)	1.155
7	(12 12 5)	(12 12 5)	1.175	(1 1 1)	1.000
8	(17 10 2)	(15 8 0)	1.291	(9 2 2)	1.224
9	(17 10 5)	(12 5 5)	1.202	(2 2 1)	1.154
10	(19 5 0)	(19 5 0)	1.264	(1 1 0)	1.225

### Supplementary Note 4: O 1s spectra of the oxidised Rh foil

The characteristic fingerprint in the Rh 3d XPS spectra (Fig. 2 in the main article) allows reliably identifying the  $\text{RhO}_x$  formed in the present study as the trilayer oxide described in Supplementary Note 2. However, the spectroscopic evidence can be complemented by O 1s spectra. Supplementary Fig. 4 exemplarily shows such spectra after oxidation in molecular oxygen ( $T = 623 \text{ K}$ ,  $p_{\text{O}_2} = 2.5 \times 10^{-4} \text{ mbar}$ ,  $t = 90 \text{ min}$ ) for the Rh (11 11 7) domain (domain number 1 in Supplementary Fig. 1) and the Rh(13 9 1) domain (domain number 2 in Supplementary Fig. 1). As described in literature [10, 11, 13], a typical O 1s spectrum of Rh trilayer oxide reveals two components: (i) a component corresponding to the topmost oxygen atoms (i.e. the surface oxygen layer) and (ii) a component corresponding to the oxygen atoms sandwiched between the first two Rh layers (i.e. the ordered subsurface oxygen layer), the latter shifted by about 1.1 eV to higher binding energies. As described in the main text and in Supplementary Note 2, the trilayer oxide forms stripes, but does not fully cover wider terraces due to kinetic limitations at the present conditions. As a result, some metallic stripes remain covered by adsorbed oxygen, which contributes to the O 1s component of the topmost atoms in the trilayer oxide.



**Supplementary Figure 4.** O 1s spectra of the oxidised Rh foil: (a) O 1s spectrum measured locally for the Rh(11 11 7) domain after oxidation in  $\text{O}_2$  ( $T = 623 \text{ K}$ ,  $p_{\text{O}_2} = 2.5 \times 10^{-4} \text{ mbar}$ ,  $t = 90 \text{ min}$ ), the corresponding Rh 3d spectrum is shown in Fig. 2c in the main article; (b) the same as in (a), but for the Rh(13 9 1) domain, the corresponding Rh 3d spectrum is shown in Fig. 2d in the main article. Squares: measured values; solid lines: sum of the deconvoluted components.

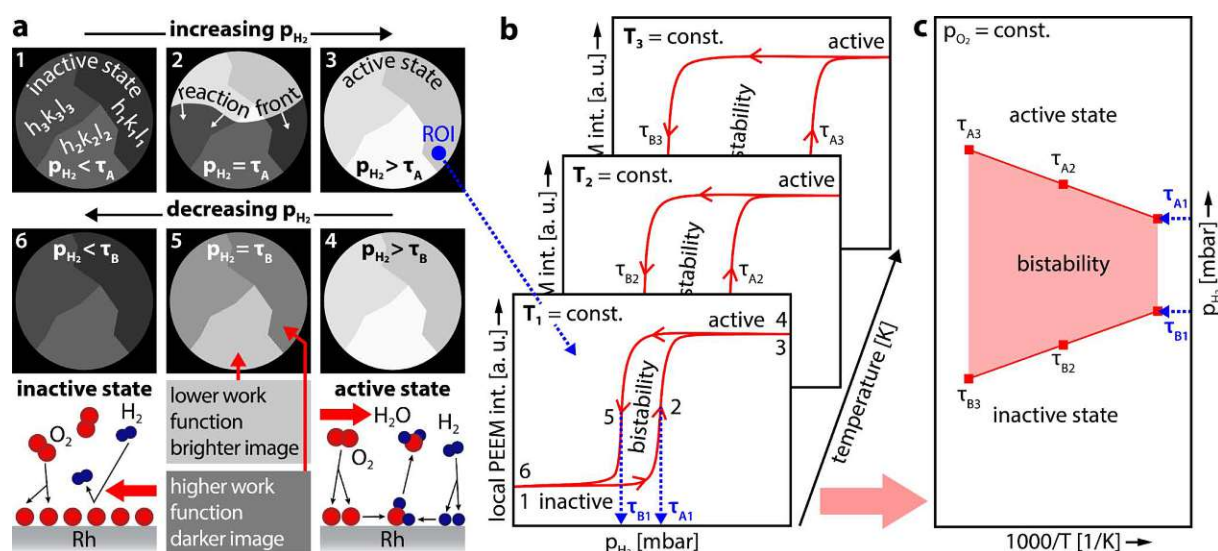
The peak positions match the literature reports on trilayer surface oxide well [10, 11, 13]. Certain deviations of the peak area ratios between the two components can be traced back to the presence of adsorbed oxygen on those parts of terraces which remain uncovered by the oxide stripes in the present experiments.

### Supplementary Note 5: Visualisation of catalytic H<sub>2</sub> oxidation by PEEM

Catalytic hydrogen oxidation on platinum group metal surfaces, such as Rh, proceeds via the Langmuir-Hinshelwood mechanism and the reaction rate is thus determined primarily by the competitive dissociative co-adsorption of hydrogen and oxygen [33-35]. At low H<sub>2</sub>/O<sub>2</sub> partial pressure ratios, the surface is saturated by oxygen, inhibiting the adsorption of hydrogen and the system is in an inactive steady state (so-called oxygen poisoning [17, 36], corresponding ball model in Supplementary Fig. 5a). Upon increasing the H<sub>2</sub>/O<sub>2</sub> ratio, small surface areas with adsorbed H atoms can be observed, where OH islands are formed [17, 36]. The surface density is higher for OH species than for oxygen [17], creating free sites for hydrogen adsorption and H<sub>2</sub>O is produced. These catalytically active areas spatially extend over the whole surface via a reaction front, with hydrogen adsorption being blocked ahead and occurring behind it. Due to the high reaction rate, the surface behind the front exhibits both low hydrogen and low oxygen coverage. Impinging hydrogen and oxygen react off, forming immediately desorbing H<sub>2</sub>O and the system remains in the active steady state (corresponding ball model in Supplementary Fig. 5a).

Using photoemission electron microscopy (PEEM), the above-mentioned states can be identified in situ during the ongoing reaction. In PEEM, the image intensity is determined by the local work function of the imaged surface, i.e. by the coverage of reactants. The reaction rate in turn also depends on the surface coverage of the reactants, dark image contrast (high work function, oxygen covered surface) thus corresponds to the catalytically inactive state. In turn, areas of bright image contrast (low work function, nearly adsorbate-free surface) are corresponding to high catalytic activity, thus the PEEM image brightness reflects the local catalytic activity. Proven quantitatively by averaging over the whole field of view [33], the relationship between image brightness and catalytic activity can be scaled down to each single pixel in the PEEM image. Resulting from the spatial distribution of the work function over the sample surface, the local PEEM intensity reflects the local H<sub>2</sub>O production rate [37]. This procedural method known as local kinetics by imaging approach, was recently successfully applied to different model systems and different length scales [6, 8, 25, 38].

Supplementary Fig. 5a, showing schematically drawn PEEM images, explains this approach for the present PEEM experiments with cyclewise variation of  $p_{\text{H}_2}$  at constant  $T$  and  $p_{\text{O}_2}$ . Starting from the inactive oxygen covered surface (frame 1) and increasing  $p_{\text{H}_2}$ , a kinetic transition, accompanied by spreading reaction fronts (frame 2) to the catalytically active state (frame 3) takes place at a certain  $p_{\text{H}_2} = \tau_{\text{A}}$ . Upon decreasing the hydrogen partial pressure back from the active state (frame 4, identical to frame 3), the reverse kinetic transition takes place at a  $p_{\text{H}_2} = \tau_{\text{B}}$  (frame 5) to the catalytically inactive state (frame 6). The value of  $\tau_{\text{B}}$  appears to be significantly lower than  $\tau_{\text{A}}$ , i.e. a hysteresis is observed (Supplementary Fig. 5b).



**Supplementary Figure 5.** Principle of the catalytic PEEM experiments: (a) frames 1 to 6 show schematic PEEM images upon cyclewise variation of  $p_{H_2}$  at constant  $T$  and  $p_{O_2}$ . A graphics of the catalytically inactive and active states is shown below; (b) schematic hysteresis curves resulting from the local PEEM image brightness in a selected region of interest (ROI) as a function of the hydrogen partial pressure; (c) kinetic phase diagram resulting from the hysteresis curves and summarising the kinetic transition points at different temperatures, showing the states of low and high catalytic activity and bistability.

This hysteresis-like behaviour is a result of the unequal adsorption properties of the reactants [33] and is reflected in the local PEEM image brightness plotted against the hydrogen partial pressure (Supplementary Fig. 5b). The resulting plots are typical for a bistable character of the reaction, i.e. two steady states (high and low catalytic activity) can exist at the same set of external parameters and the actual state is determined solely by the prehistory of the system [39].

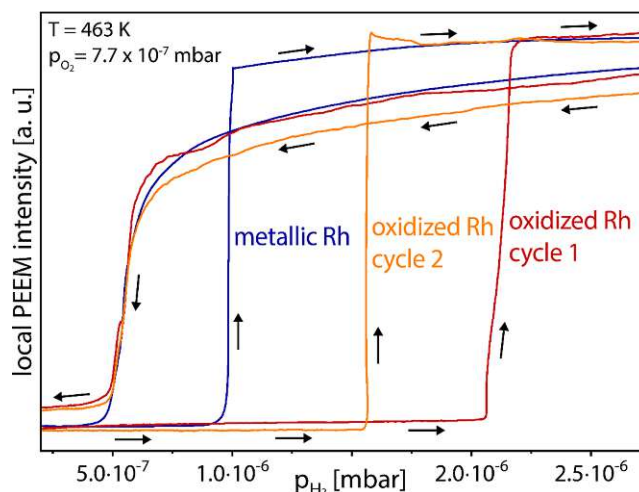
Upon repeating the described experiment at different temperatures, a set of transition points can be collected and summarised in a kinetic phase diagram, as shown in Supplementary Figs. 5b and 5c. A detailed discussion concerning the term kinetic phase diagram can be found elsewhere [40-43]. Such diagrams show areas of high and low catalytic activity and bistability at one glance and allow comparison of the performance of different catalysts, as well as the prediction of temperatures and partial pressures of kinetic transitions.

### Supplementary Note 6: Partial reduction of surface oxide during $H_2$ oxidation

The Rh surface oxide can be reduced during exposure to a reducing atmosphere [44, 45]. Therefore, the surface oxide formed in our experiments will be inevitably reduced to some extent in the catalytically active steady state. During the cyclewise variation of the  $H_2$  pressure in the PEEM experiments on the oxidised Rh surface, the reduction may start immediately after the increasing  $p_{H_2}$  reaches  $\tau_A$  (Supplementary Fig. 5). This has, of course, an effect on the hysteresis loop “on the way back”, i.e. during the following decrease of  $p_{H_2}$ , and this also influences the position of the resulting  $\tau_B$  transition. To shed light on this effect, we performed

experiments consisting of serial cycles of increasing and decreasing the hydrogen partial pressure, one right after the other.

Supplementary Fig. 6 exemplarily shows the hysteresis curves obtained in such experiments during cyclewise variation of  $p_{\text{H}_2}$  from  $1.0 \times 10^{-7}$  to  $5.0 \times 10^{-6}$  mbar and vice versa, at a constant temperature of 463 K and constant  $p_{\text{O}_2}$  of  $7.7 \times 10^{-7}$  mbar. The surface region for which the PEEM intensity curves were registered corresponds to the one analysed in Fig. 3b in the main article.



**Supplementary Figure 6.** Hysteresis curves of the local PEEM intensity registered in serial (“one right after the other”) cyclewise variations of  $p_{\text{H}_2}$  at constant  $p_{\text{O}_2} = 7.7 \times 10^{-7}$  mbar and  $T = 463$  K. In addition, the hysteresis curve for the metallic Rh surface is shown for comparison (which shows no changes when repeated).

The experiments reveal that indeed reduction of the surface oxide takes place during the catalytically active period. However, reduction is only partial in the first cycle, since the kinetic transition  $\tau_A$  during the second cycle still occurs at significantly higher hydrogen pressure than for the metallic surface. It is therefore justified to assume that surface oxide survives at least one hysteresis cycle, i.e. the results summarised in the phase diagrams (Fig. 3 in the main article) and velocity map (Fig. 4 in the main article) definitely concern the Rh surface oxide.



## Supplementary References

- [1] Dingley, D. J., Baba-Kishi, K. Z. & Randle V. *Atlas of Backscattering Kikuchi Diffraction Patterns* (IOP Publishing, 1995).
- [2] Baba-Kishi, K. Z. Review Electron backscatter Kikuchi diffraction in the scanning electron microscope for crystallographic analysis. *J. Mater. Sci.* **37**, 1715–1746 (2002).
- [3] Dingley, D. J. & Randle, V. Microtexture determination by electron back-scatter diffraction. *J. Mater. Sci.* **27**, 4545–4566 (1992).
- [4] Schwartz, A. J., Kumar, M., Adams, B. L. & Field, D. P. (eds.) *Electron Backscatter Diffraction in Materials Science* (Springer US, 2009).
- [5] König, U. & Davepon, B. Microstructure of polycrystalline Ti and its micro-electrochemical properties by means of electron-backscattering diffraction (EBSD). *Electrochim. Acta.* **47**, 149–160 (2001).
- [6] Vogel, D. *et al.* The Role of Defects in the Local Reaction Kinetics of CO Oxidation on Low-Index Pd Surfaces. *J. Phys. Chem. C* **117**, 12054–12060 (2013).
- [7] Weatherup, R. S. *et al.* In Situ Graphene Growth Dynamics on Polycrystalline Catalyst Foils. *Nano Lett.* **16**, 6196–6206 (2016).
- [8] Suchorski, Y. *et al.* Visualizing catalyst heterogeneity by a multifrequential oscillating reaction. *Nat. Commun.* **9**, 600:1–6 (2018).
- [9] Humphreys, F. J. Grain and subgrain characterisation by electron backscatter diffraction. *J. Mater. Sci.* **36**, 3833–3854 (2001).
- [10] Gustafson, J. *et al.* Structure of a thin oxide film on Rh(100). *Phys. Rev. B* **71**, 115442-1–9 (2005).
- [11] Gustafson, J. *et al.* Self-Limited Growth of a Thin Oxide Layer on Rh(111). *Phys. Rev. Lett.* **92**, 126102-1–4 (2004).
- [12] Blomberg, S. *et al.* Structure of the Rh<sub>2</sub>O<sub>3</sub>(0001) surface. *Surf. Sci.* **606**, 1416–1421 (2012).
- [13] Dri, C. *et al.* Initial oxidation of the Rh(110) surface: Ordered adsorption and surface oxide structures. *J. Chem. Phys.* **125**, 094701-1–9 (2006).
- [14] Evans, S. Curve Synthesis and Optimization Procedures for X-ray Photoelectron Spectroscopy. *Surf. Interface. Anal.* **17**, 85–93 (1991).
- [15] Shirley, D. A. High-Resolution X-Ray Photoemission Spectrum of the Valence Bands of Gold. *Phys. Rev. B* **5**, 4709–4714 (1972).
- [16] Mittendorfer, F. *et al.* Oxygen-Stabilized Rh Adatoms: 0D Oxides on a Vicinal Surface. *J. Phys. Chem. Lett.* **2**, 2747–2751 (2011).
- [17] Africh, C. *et al.* Two-Step Reaction on a Strained, Nanoscale Segmented Surface. *Phys. Rev. Lett.* **93**, 126104-1–4 (2004).
- [18] Klikovits, J. *et al.* Step-Orientation-Dependent Oxidation: From 1D to 2D Oxides. *Phys. Rev. Lett.* **101**, 266104-1–4 (2008).
- [19] Farber, R. G. *et al.* The Quest for Stability: Structural Dependence of Rh(111) on Oxygen Coverage at Elevated Temperature. *J. Phys. Chem. C* **121**, 10470–10475 (2017).
- [20] Kossel, W. Zur Theorie des Kristallwachstums. *Nachr. Ges. Wiss. Göttingen, Math.-Phys. Klasse* **1927**, 135–143 (1927).
- [21] Stranski, I. N. Zur Theorie des Kristallwachstums. *Z. Phys. Chem.* **136U**, 259–278 (1928).
- [22] Gruber, E. E. & Mullins W. W. On the theory of anisotropy of crystalline surface tension. *J. Phys. Chem. Solids* **28**, 875–887 (1967).

- [23] Böller, B., Durner K. M. & Wintterlin J. The active sites of a working Fischer–Tropsch catalyst revealed by operando scanning tunnelling microscopy. *Nat. Catal.* **2**, 1027–1034 (2019).
- [24] Calle-Vallejo, F., Martinez, J. I., Garcia-Lastra, J. M., Sautet, P. & Loffreda, D. Fast Prediction of Adsorption Properties for Platinum Nanocatalysts with Generalized Coordination Numbers. *Angew. Chem. Int. Edit.* **53**, 8316–8319 (2014).
- [25] Suchorski, Y. *et al.* CO Oxidation on Stepped Rh Surfaces:  $\mu\text{m}$ -Scale Versus Nanoscale. *Cat. Lett.* **150**, 605–612 (2020).
- [26] Wulff, G. XXV. Zur Frage der Geschwindigkeit des Wachstums und der Auflösung der Krystallflächen. *Z. Kristallogr.* **34**, 449–530 (1901).
- [27] v. Laue, M. XXV. Der Wulffsche Satz für die Gleichgewichtsform von Kristallen. *Z. Kristallogr.* **105**, 124–133 (1943).
- [28] Barmparis, G. D., Lodziana, Z., Lopez, N. & Remediakis I. N. Nanoparticle shapes by using Wulff constructions and first-principles calculations. *Beilstein J. Nanotech.* **6**, 361–368 (2015).
- [29] Bonzel, H. P. Surface Morphologies: Transient and Equilibrium Shapes. *Interface. Sci.* **8**, 21–34 (2001).
- [30] Grochola, G., du Plessis, J., Snook, I. K. & Russo, S. P. On the computational calculation of adatom, vacancy and early stage surface nucleation island free energies on the (1 1 1) copper surface. *Surf. Sci.* **591**, 32–37 (2005).
- [31] Stranski, I. N. Forms of equilibrium of crystals. *Discuss. Faraday Soc.* **5**, 13–21 (1949).
- [32] Mackenzie, J. K., Moore, A. J. W. & Nicholas, J. F. Bonds broken at atomically flat crystal surfaces—I: Face-centred and body-centred cubic crystals. *J. Phys. Chem. Solids* **23**, 185–196 (1962).
- [33] Schaak, A. & Imbihl, R. Bistability and formation of low work function areas in the  $\text{O}_2+\text{H}_2$  reaction on a Rh(111) surface. *J. Chem. Phys.* **113**, 9822–9829 (2000).
- [34] Ertl, G. Reactions at Surfaces: From Atoms to Complexity (Nobel Lecture). *Angew. Chem. Int. Edit.* **47**, 3524–3535 (2008) and references therein.
- [35] Yates, J. T. Jr., Thiel, P. A. & Weinberg, W. H. Reactions at Surfaces: The catalytic reaction between adsorbed oxygen and hydrogen on Rh(111). *Surf. Sci.* **82**, 45–68 (1979).
- [36] Sachs, C., Hildebrand, M., Völkening, S., Wintterlin, J. & Ertl, G. Reaction fronts in the oxidation of hydrogen on Pt(111): Scanning tunneling microscopy experiments and reaction–diffusion modeling. *J. Chem. Phys.* **116**, 5759–5773 (2002).
- [37] Suchorski, Y. & Rupprechter, G. Local reaction kinetics by imaging. *Surf. Sci.* **643**, 52–58 (2016).
- [38] Datler, M. *et al.* Hydrogen Oxidation on Stepped Rh Surfaces:  $\mu\text{m}$ -Scale versus Nanoscale. *Cat. Lett.* **146**, 1867–1847 (2016).
- [39] Vogel, D. *et al.* Mapping the local reaction kinetics by PEEM: CO oxidation on individual (100)-type grains of Pt foil. *Surf. Sci.* **605**, 1999–2005 (2011).
- [40] Zhdanov, V. P. & Kasemo B. Kinetic phase transitions in simple reactions on solid surfaces. *Surf. Sci. Rep.* **20**, 113–189 (1994).
- [41] Schlögl, F. Chemical reaction models for non-equilibrium phase transitions. *Z. Phys.* **253**, 147–161 (1972).
- [42] Schlögl, F. What Can we Learn about Dissipative Structures by Model Reactions. *Berich. Bunsen Gesell.* **84**, 351–357 (1980).

- [43] Ehsais, M. *et al.* A reactive phase diagram of CO oxidation on Pd(110): Steady and oscillatory states. *J. Chem. Phys.* **98**, 9177–9184 (1993).
- [44] Lundgren, E. *et al.* The surface oxide as a source of oxygen on Rh(1 1 1). *J. Electron Spectrosc.* **144-147**, 364–372 (2005).
- [45] Dudin, P. *et al.* Initial Oxidation of a Rh(110) Surface Using Atomic or Molecular Oxygen and Reduction of the Surface Oxide by Hydrogen. *J. Phys. Chem. B* **109**, 13649–13655 (2005).
- [46] Gustafson, J. *et al.* Oxygen-induced step bunching and faceting of Rh(553): Experiment and ab initio calculations. *Phys. Rev. B* **74**, 035401-1–7 (2006).
- [47] Abe, Y., Kato, K., Kawamura, M. & Sasaki, K. Rhodium and Rhodium Oxide Thin Films Characterized by XPS. *Surf. Sci. Spec.* **8**, 117–125 (2001).



# 6

---

## Imaging interface and particle size effects by *in situ* correlative microscopy of a catalytic reaction

The various studies presented in the previous chapters were performed on individual domains of a polycrystalline Rh foil sample, i.e., on a library of flat well-defined surface structures. Typical catalysts used in industrial processes are, however, often complex systems of metal nanoparticles on an oxidic support material, sometimes also in combination with other species acting as promoters. The results obtained for such idealized systems might therefore not be perfectly applicable to real world catalysts (materials gap, section 1.3). In an attempt to bridge this materials gap, the system complexity was increased and a sample comprising  $\mu\text{m}$ -sized Rh particles of different sizes and on different support materials was prepared.

The catalytic behavior of Rh particles supported on a Rh foil, i.e., a quasi-unsupported system, a Au foil, i.e., a system comparable to, e.g., Au-modified Ni-based steam reforming catalysts [267], and an oxidized Zr foil, i.e., a system resembling oxide supported metal particles, was studied *in situ* by correlative UV photoemission electron microscopy (UV-PEEM, section 2.3) and scanning photoelectron microscopy (SPEM, section 2.2). Kinetic transitions between the catalytically inactive and active steady states (section 1.7) were monitored and self-sustaining kinetic oscillations (section 1.8) on supported Rh particles were observed for this reaction for the first time. The catalytic performance could be shown to be dependent on the support material and Rh particle size and the oscillations varied from particle-size independent (Rh/Rh), via size dependent (Rh/ZrO<sub>2</sub>) to fully inhibited (Rh/Au). Using the SPEM data, for Rh/Au, the formation of a surface alloy could be identified as being responsible for these effects, whereas for Rh/ZrO<sub>2</sub> the formation of substoichiometric Zr oxides on the Rh surface, enhanced oxygen bonding, Rh oxidation and hydrogen spillover onto the ZrO<sub>2</sub> support were identified as the causes. The experimental observations were complemented by micro-kinetic model simulations, in which the

hydrogen adsorption and oxygen binding properties were modified in accordance with the experimental data. The results demonstrate how correlative *in situ* surface microscopy enables linking local structure, composition and catalytic performance.

A manuscript containing the results of these studies was prepared and submitted for publication in *Nature Communications* as given below. For this work, I performed the PEEM experiments and evaluated the PEEM data in collaboration with L.M. Rois, performed the SPEM measurements in collaboration with M. Raab, J. Zeininger, M. Amati, R. Parmar, L. Gregoratti, and G. Rupprechter, evaluated the SPEM data, performed the TEM measurements and TEM data analysis in collaboration with M. Stöger-Pollach and prepared the manuscript in collaboration with Y. Suchorski and G. Rupprechter.

The following is an unmodified reproduction of the manuscript “Imaging interface and particle size effects by *in situ* correlative microscopy of a catalytic reaction” by P. Winkler, M. Raab, J. Zeininger, L.M. Rois, Y. Suchorski, M. Stöger-Pollach, M. Amati, R. Parmar, L. Gregoratti, and G. Rupprechter, submitted for publication in *Nature Communications* on the 25<sup>th</sup> of November 2022, reproduced here with permission of all authors.

# Imaging interface and particle size effects by *in situ* correlative microscopy of a catalytic reaction

Philipp Winkler<sup>1</sup>, Maximilian Raab<sup>1</sup>, Johannes Zeininger<sup>1</sup>, Lea M. Rois<sup>1</sup>, Yuri Suchorski<sup>1</sup>,  
Michael Stöger-Pollach<sup>2</sup>, Matteo Amati<sup>3</sup>, Rahul Parmar<sup>3</sup>, Luca Gregoratti<sup>3</sup>,  
and Günther Rupprechter<sup>1, \*</sup>

<sup>1</sup> Institute of Materials Chemistry, TU Wien, Getreidemarkt 9, 1060 Vienna, Austria

<sup>2</sup> University Service Center for Transmission Electron Microscopy, TU Wien,  
Wiedner Hauptstraße 8-10, 1040 Vienna, Austria

<sup>3</sup> Elettra-Sincrotrone Trieste S.C.p.A., km 163.5 in AREA Science Park, 34149 Trieste, Italy

\* E-Mail: guenther.rupprechter@tuwien.ac.at

**The catalytic behavior of Rh particles supported by three different materials (Rh, Au, ZrO<sub>2</sub>) in H<sub>2</sub> oxidation has been studied *in situ* by correlative photoemission electron microscopy (PEEM) and scanning photoemission electron microscopy (SPEM). Kinetic transitions between the inactive and active steady states were monitored and self-sustaining oscillations on supported Rh particles were observed for this reaction for the first time. Catalytic performance differed depending on the support and Rh particle size. Oscillations varied from particle-size independent (Rh/Rh) via size dependent (Rh/ZrO<sub>2</sub>) to fully inhibited (Rh/Au). For Rh/Au, the formation of a surface alloy induced such effects, whereas for Rh/ZrO<sub>2</sub> the formation of substoichiometric Zr oxides on the Rh surface, enhanced oxygen bonding, Rh oxidation, and hydrogen spillover onto the ZrO<sub>2</sub> support were held responsible. The experimental observations were complemented by micro-kinetic simulations, based on variations of hydrogen adsorption and oxygen binding. The results demonstrate how correlative *in situ* surface microscopy enables linking local structure, composition and catalytic performance.**

## Main

Size and support effects of catalytically active metal particles have been among the most studied phenomena in heterogeneous catalysis for over 50 years<sup>1-4</sup>. A vast number of *ex situ* and *in situ* studies have been carried out by spectroscopic, diffractive, or imaging techniques, both on technological as well as on model catalytic systems<sup>5-7</sup>. Low-coordinated step/edge sites and interfaces were often found most active<sup>8-14</sup>. In the present work, we study the effect of various metal/support interfaces on catalytic H<sub>2</sub> oxidation on Rh by *in situ* correlative microscopy, i.e., the same area of the same sample is imaged under identical reaction conditions by different microscopies, providing real-time complementary information. Accordingly, interface phenomena and particle size effects can be directly observed by

spatially-resolved evaluation of surface structure, surface composition and catalytic performance.

The correlative microscopy concept stems from biological research, where the same cell/tissue structures were studied by light and electron microscopy already in the 70ies<sup>15,16</sup>. This has been extended to other imaging techniques such as atomic force microscopy, single molecule fluorescence, x-ray tomography or scanning electron microscopy<sup>17,18</sup> and has made huge impact in materials research<sup>19,20</sup>. In catalysis, correlative microscopy has also been applied, e.g. by combining transmission electron microscopy (TEM) with fluorescence microscopy, atom probe tomography (APT) with scanning transmission x-ray microscopy, scanning photoelectron microscopy (SPEM) with APT or optical microscopy with confocal and x-ray fluorescence microscopy<sup>21–25</sup>.

On planar Rh samples, catalytic H<sub>2</sub> oxidation has been studied in a correlative way by various combinations of (UV or x-ray) photoemission electron microscopy ((UV or X)PEEM), SPEM, or low energy electron microscopy<sup>26–28</sup>. Apart from the known steady states of high and low activity and bistability<sup>29–32</sup>, this allowed revealing spatio-temporal phenomena such as mono- and multifrequential self-sustaining oscillations<sup>12,33,34</sup> and coexisting multi-states<sup>35</sup>. For supported Rh particles, such an approach has not yet been applied. Based on the thorough understanding of the mechanism of hydrogen oxidation, it can be used to benchmark interface and size effects in different catalysts.

Here we present the first correlative microscopy study of catalytic H<sub>2</sub> oxidation on Rh powder aggregates (size of ~5-30 μm) supported by different materials: A *single* sample comprising of Rh aggregates supported either by Rh, Au or ZrO<sub>2</sub> was studied *in situ* by combining PEEM (providing *local reaction kinetics*) and SPEM (providing *local chemical information*). The Rh/Rh system represents a reference for unmodified (quasi-unsupported) Rh, with particles nonetheless having the same curved/stepped surface morphology as in the Au and Zr-oxide supported systems. Rh/Au was prepared to provide an inert support, but finally served as a model system for active particles modified by an inactive second metal, possibly by active site blocking<sup>36</sup> or surface alloying. This configuration is comparable to, e.g., Au- or Cu-modified Ni-based steam reforming catalysts<sup>37,38</sup> or Au-modified Cu-based catalysts for water gas shift<sup>39</sup>. As an example for oxide supported metals, the Rh/ZrO<sub>2</sub> system was used, which is catalytically active in steam reforming<sup>40</sup>, CO and CO<sub>2</sub> hydrogenation<sup>41</sup> or H<sub>2</sub> oxidation<sup>32,42</sup>. Late transition metals (including platinum group metals) supported on various oxides (including ZrO<sub>2</sub>) are well-known for *strong metal-support interaction* (SMSI)<sup>43–51</sup>, i.e. fully or partially oxide decorated metal surfaces. In the present study, we demonstrate that the mechanisms of surface modification are very different, affecting both steady state and oscillatory hydrogen oxidation, but the modification of steps was crucial in both cases.

Experiments are illustrated in Fig. 1: H<sub>2</sub> oxidation occurring simultaneously on the three sample regions (Rh/Rh, Rh/Au, Rh/ZrO<sub>2</sub>) was visualized *in situ* by PEEM. The sample is illuminated by UV-light and the emitted photoelectrons form an image on a fluorescent screen. The image brightness depends on the adsorbate coverage via the work function and is thus directly related to catalytic activity (kinetics by imaging<sup>52</sup>). Therefore, spatially-resolved reaction kinetics, e.g., hysteresis curves and kinetic phase diagrams, can be extracted by analyzing PEEM video-sequences.



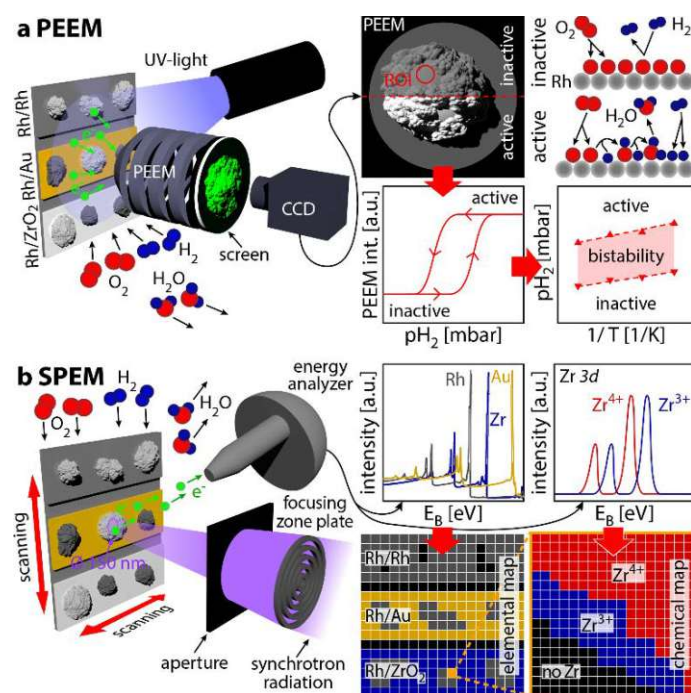


**Figure 1.** Correlative microscopy approach. **(a)** In PEEM, the sample is illuminated by UV-light and the photoemitted electrons form an image on a fluorescent screen. The image brightness is related to the states of catalytic activity shown in the schematic ball models. From the PEEM video-sequences, hysteresis curves and kinetic phase diagrams can be obtained for selected regions (ROIs). **(b)** In SPEM, the sample is raster-scanned under a sub- $\mu\text{m}$  synchrotron x-ray beam and energy analysis of the emitted photoelectrons provides local x-ray photoelectron spectra (XPS) and elemental/chemical maps on various length scales.

To complement local kinetics with spatially-resolved chemical information, the same sample regions were studied *in situ* by SPEM under identical reaction conditions, with the sample raster-scanned under a focused sub- $\mu\text{m}$  synchrotron x-ray photon probe. The energy of the emitted photoelectrons is measured, resulting in high-resolution x-ray photoelectron spectra (XPS) and elemental/chemical maps on a  $\mu\text{m}$ -scale.

### Kinetic PEEM studies

PEEM studies were carried out in an ultrahigh vacuum (UHV) setup operated as flow reactor (for details see Methods). First, the kinetic transitions between the steady states of catalytic activity in H<sub>2</sub> oxidation were studied on Rh/Rh. The reaction follows the Langmuir-Hinshelwood mechanism<sup>29,53</sup>, i.e., both reactants adsorb on the catalyst before reacting. At low pO<sub>2</sub>/pH<sub>2</sub> the system is in an inactive steady state (adsorbed oxygen blocks the hydrogen adsorption, ball model in Fig. 1a). Upon increasing pO<sub>2</sub>/pH<sub>2</sub>, the system switches to a catalytically active steady state. This, and the reverse, occur via kinetic transitions, which can be visualized due to the dependence of the PEEM image intensity on surface coverage: The catalytically inactive oxygen-covered Rh surface has a higher work function than adsorbate-free Rh, resulting in dark PEEM contrast. In turn, the catalytically active surface with low adsorbate coverage appears much brighter. These image contrast variations allow extracting local kinetic information from *in situ* recorded PEEM videos (kinetics by imaging<sup>31,33,52</sup>).

The observed kinetic transitions are illustrated in Fig. 2: Experiments always started from the catalytically inactive state (shown for Rh particles on Rh foil in Fig. 2a). Upon increasing  $p_{H_2}$  at constant  $p_{O_2}$  and  $T$ , a kinetic transition to the catalytically active state takes place at a certain  $p_{H_2}$  value  $\tau_A$ . On Rh/Rh this is accompanied by  $H_{ads}$  fronts nucleating at the perimeter of the particles<sup>32</sup> and spreading over the whole field of view (Fig. 2b). After the kinetic transition, the system stays in the active steady state (Fig. 2c). Upon decreasing  $p_{H_2}$ , a reverse kinetic transition to the inactive state will take place at a certain  $p_{H_2}$  value  $\tau_B$  (Fig. 2d), which differs from  $\tau_A$ , exhibiting a hysteresis indicating bistability<sup>29–32</sup>.

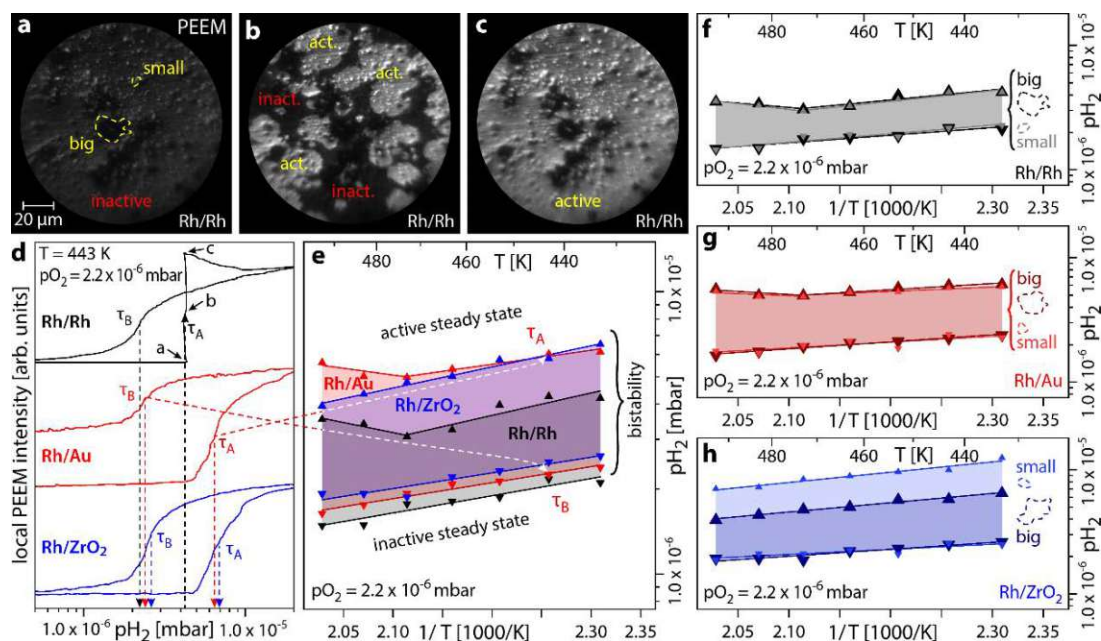


**Figure 2.** Support and particle size effects in  $H_2$  oxidation on supported Rh particles. **(a)** PEEM image of oxygen-covered catalytically inactive Rh particles on Rh support; **(b)** *in situ* PEEM image of an ongoing kinetic transition to the catalytically active state at  $T = 443$  K,  $p_{O_2} = 2.2 \times 10^{-6}$  mbar,  $p_{H_2} = 4.2 \times 10^{-6}$  mbar. Dark areas correspond to a catalytically inactive surface, while the bright areas spreading from the Rh particle boundaries indicate a catalytically active Rh surface; **(c)** the catalytically active surface resulting from the kinetic transition depicted in **(b)**; **(d)** hysteresis curves registered during cyclewise variation of  $p_{H_2}$  from  $5.0 \times 10^{-7}$  mbar to  $2.0 \times 10^{-5}$  mbar at constant  $T = 443$  K and  $p_{O_2} = 2.2 \times 10^{-6}$  mbar, obtained by processing the local PEEM intensity of a selected ROI on similarly sized Rh particles on Rh foil (black trace, ROI marked in **(a)**), Au (red trace) and  $ZrO_2$  (blue trace) support. Conditions of frames **(a)**-**(c)** are marked by arrows. The dashed lines illustrate the construction of a kinetic phase diagram; **(e)** kinetic phase diagram for  $H_2$  oxidation in the temperature range from 433 K to 493 K at constant  $p_{O_2} = 2.2 \times 10^{-6}$  mbar for similarly sized Rh particles supported by Rh (black), Au (red) and  $ZrO_2$  (blue); **(f)** the same as in **(b)** but for two differently sized Rh particles (big, black diagram; small, grey diagram) on Rh support; **(g)** the same as in **(f)** but for two differently sized Rh particles on Au support; **(h)** the same as in **(f)** but for two differently sized Rh particles on  $ZrO_2$  support.

From recorded video-sequences, the local PEEM intensity can be read out for an arbitrarily placed region of interest (ROI). For Rh/Rh, a ROI was placed, e.g., on the “big” particle in the middle (marked in Fig. 2a) and the local PEEM intensity vs.  $p_{H_2}$  upon cyclewise variation of  $p_{H_2}$  is shown as black trace in Fig. 2d. The curve exhibits the expected pronounced hysteresis

between the kinetic transition points  $\tau_A$  and  $\tau_B$ . To examine the effect of different supports, identical experiments were performed for Rh/Au and Rh/ZrO<sub>2</sub>. Similarly sized Rh particles (diameter  $\sim 20 \mu\text{m}$ ) were selected for analysis and results for Rh/Au (red) and Rh/ZrO<sub>2</sub> (blue) are shown in Fig. 2d. A hysteresis was observed for both, but with a much wider and shifted loop.

By experiments at different temperatures and plotting the measured  $\tau_A$  and  $\tau_B$  values vs. the inverse temperature, kinetic phase diagrams can be constructed. For Rh/Rh (Fig. 2e, black), the unexpected sharp bend in the  $\tau_A$  line can be attributed to oxygen induced surface Rh restructuring and corresponding roughness changes at a certain temperature, reported for several single crystals<sup>54-57</sup>, Rh nanoparticles<sup>44,58</sup> or needle-shaped specimens<sup>59</sup>. Due to the rounded shape of the Rh particles/aggregates, exposing plenty of differently oriented stepped surfaces (Extended Data Fig. 3), similar behavior can be expected.

The kinetic phase diagram of Rh/Au (red) is similar to the one of Rh/Rh, but  $\tau_A$  and  $\tau_B$  are both shifted to higher  $p\text{H}_2$ . Since (bulk) Au is catalytically inactive in H<sub>2</sub> oxidation due to the lack of dissociative adsorption of the reactants<sup>60,61</sup>, and no interaction between the Rh particles and the Au support is expected, this seems unusual and will be explained below. For Rh/ZrO<sub>2</sub> (blue diagram), the  $\tau_A$  and  $\tau_B$  values are also shifted to higher  $p\text{H}_2$  in comparison to Rh/Rh, but also the bistability area does not exhibit a sharp bend in  $\tau_A$ . The shift towards higher  $p\text{H}_2$  has been discussed in our previous work<sup>32</sup>. Due to the electron density jump across the metal/oxide interface, the binding energy for oxygen is modified in close vicinity of the interface. Since the energetics govern the adsorption kinetics, the local oxygen/hydrogen adsorption equilibrium is shifted towards oxygen, necessitating compensation by higher  $p\text{H}_2$  to induce kinetic transitions. Furthermore, it appears that the presence of the metal/oxide interface inhibits the oxygen induced restructuring of Rh/Rh and Rh/Au.

Besides the “big” Rh particles, other differently sized particles are present in the field of view (Fig. 2a-c) and the *in situ* recorded video-sequences contain kinetic information for all particles at inherently identical conditions, allowing the addressing of size effects. Figures 2f-g show kinetic phase diagrams analogous to Fig. 2e, but additionally for a set of “small” particles ( $\sim 5 \mu\text{m}$ ). The corresponding PEEM images are shown in Extended Data Fig. 1. Comparison of diagrams for differently sized particles reveals interesting features: For Rh/Rh, the kinetic phase diagrams are identical within experimental accuracy, which is expected as there are no interface effects between the Rh particles and Rh support. The same seems true for Rh/Au, but the shift in comparison to Rh/Rh remains to be explored below. In contrary, for Rh/ZrO<sub>2</sub>, there is a clear particle size effect: The  $\tau_A$  values of the “small” particle are shifted towards higher  $p\text{H}_2$ , while the  $\tau_B$  values remain basically identical. This demonstrates the contribution of the particle/support interface to the catalytic activity. For smaller particles, the ratio of perimeter/interface length to surface area is higher than for bigger particles: smaller particles are stronger influenced by the interface than bigger ones.

PEEM results unambiguously show interface and particle size effects, but lack detailed chemical information. Especially the behavior of the Rh/Au system cannot be explained by PEEM alone, calling for a chemically sensitive technique.

### Chemically-resolved SPEM studies

Therefore, SPEM experiments, with the SPEM chamber also operated as flow reactor, were performed using a photon energy of 720 eV at the ESCA Microscopy beamline (Elettra synchrotron), as described in detail in Methods.

In Fig. 3, the same “big” Rh particle on Au as in PEEM was probed in the catalytically active state (the Rh/Rh system provides no chemical contrast). Figure 3a shows high-resolution *in situ* Au  $4f_{7/2}$  spectra of the two spots marked in Fig. 3d: Spot A on the support and spot B on the Rh particle. While spot A shows expected bulk Au, significant Au amounts are detected on the Rh particle as well. There are three possible reasons: First, the cleaning procedure includes  $\text{Ar}^+$ -ion sputtering, possibly leading to deposition of support material onto the Rh particles. Second, Au adatoms can diffuse on platinum group metals at temperatures as low as 300 K<sup>62,63</sup>. Third, kinetic transitions in a surface reaction may cause a large scale redistribution of adsorbed Au<sup>64</sup>. Furthermore, the spectra show two distinct Au species, bulk Au (support material, red) and another one only on the Rh particle (green). We attribute this second component to the formation of a RhAu surface alloy, in analogy to studies of thin Au films on Al, Rh or Ru<sup>65–67</sup>.

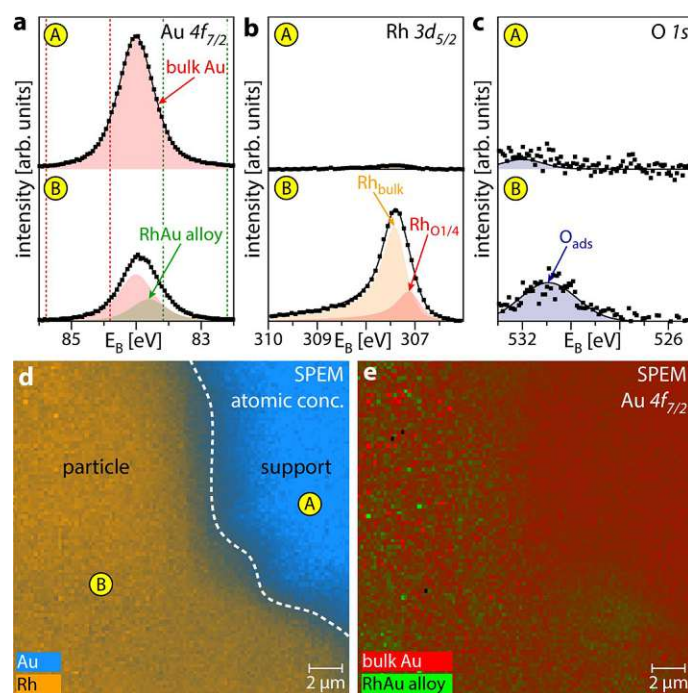


**Figure 3.** Surface alloying on a Au supported Rh particle in the catalytically active state at  $T = 453$  K,  $p\text{O}_2 = 2.2 \times 10^{-6}$  mbar,  $p\text{H}_2 = 4.0 \times 10^{-6}$  mbar. **(a)** local Au  $4f_{7/2}$  XPS spectra at spots A and B indicated in (d); the red component is related to bulk Au, while the green component is related to the formation of a RhAu surface alloy; **(b)** local Rh  $3d_{5/2}$  XPS spectra at the spots A and B indicated in (d). The orange component corresponds to bulk Rh, while the red component is related to Rh bound to adsorbed oxygen; **(c)** local O  $1s$  XPS spectra at the points A and B indicated in (d). The single blue component corresponds to adsorbed oxygen; **(d)** SPEM chemical map of the atomic concentrations of Au (blue) and Rh (orange) at the boundary of a Rh particle; the particle boundary is indicated by a white dashed line; **(e)** Au  $4f$  SPEM chemical map of the distribution of the two different Au species. The field of view is identical to (e). The energy windows used for constructing the map are indicated by dashed red and green lines in (c) and given in Extended Data Table 1.

The corresponding Rh  $3d_{5/2}$  spectra (Fig. 3b) indicate no presence of Rh on the support material. We conclude that the presence of Au on the Rh particles is caused by a combination of the effects mentioned above: Au atoms are deposited on the Rh particle in close vicinity to the interface due to sputtering, from where they diffuse and migrate, covering the whole particle. The spectrum on the particle, deconvoluted following a previously established procedure<sup>35</sup>, consists of a bulk Rh component ( $Rh_{\text{bulk}}$ , orange) and a component related to oxygen-bound Rh ( $Rh_{O_{1/4}}$ , red), which unambiguously indicates the catalytically active state<sup>35</sup>. The O  $1s$  spectra (Fig. 3c) highlight that the Au support does not take part in the reaction (no oxygen present in spot A), while the spectrum for the Rh particle (spot B) agrees with our previous observations<sup>35</sup>.

Using the Au  $4f_{7/2}$  and Rh  $3d_{5/2}$  signals after correction for the different inelastic mean free paths and x-ray cross-sections, a chemical map of the atomic concentrations of Au (blue) and Rh (orange) was constructed (Fig. 3d). The map reveals that there is hardly any gradient in the Au concentration on the Rh particle with the entire particle covered. A Au  $4f_{7/2}$  chemical map detailing the lateral distribution of the two different Au species is displayed in Fig. 3e, completing the picture and supporting our component assignment of RhAu on the particle.

Based on SPEM, the unexpected behavior of Rh/Au in PEEM can be explained: Au atoms migrated onto the Rh particle are very likely located at the Rh step edges, in line with previous observations on Pt, Rh or Ru<sup>36,63,67</sup>. Since the Rh step sites are crucial for dissociative hydrogen adsorption<sup>68</sup> and thus for switching to the active state, their lower activity due to RhAu alloy formation must be compensated by a higher  $pH_2$ , shifting the kinetic phase diagram as observed.

In analogy to Rh/Au, *in situ* SPEM of the “big” Rh particle on  $ZrO_2$  in the active state is shown in Fig. 4. In Figs. 4a, 4b, and 4c high-resolution Zr  $3d$ , Rh  $3d_{5/2}$  and O  $1s$  XPS spectra are displayed for spots A to E placed along a line from the oxide support to the Rh particle center. The Zr  $3d$  spectra (Fig. 4a) display three different  $Zr^{x+}$  species ( $Zr^{4+}$  bulk-oxide, red;  $Zr^{3+}$  sub-oxide, green; and  $Zr^{2+}$  sub-oxide, blue), identified based on previous XPS studies of thin  $ZrO_x$  islands/films on Rh(111)<sup>43</sup> or Pt(111)<sup>50</sup> and of the initial oxidation of Zr<sup>69,70</sup>. Similarly, detailed analysis of the Rh  $3d_{5/2}$  spectra (Fig. 4b) reveals the presence of bulk Rh ( $Rh_{\text{bulk}}$ , orange), two components associated with oxygen-bound Rh ( $Rh_{O_{1/4}}$ , red and  $Rh_{O_{2/3}}$ , green) as well as a component related to Rh surface oxide ( $Rh_{O_x}$ , blue), in accordance with our previous work<sup>27,35</sup>. The O  $1s$  spectra (Fig. 4c) complete the picture: One component is associated with bulk  $ZrO_2$  (red), one component is related to the Zr sub-oxides (green) and one component represents oxygen adsorbed on Rh (blue).

Combining all information yields the following: At spot A (i.e., on the support, several  $\mu\text{m}$  away from the particle), there is bulk-like  $ZrO_2$ . At spot B, still on the support, but near the metal/oxide interface, Zr sub-oxides are present in addition, but there are no significant amounts of Rh. This can be understood by partial reduction of  $ZrO_2$ , possibly by hydrogen spillover, as, e.g., observed for Rh or Pt particles on  $ZrO_2$ <sup>43,71,72</sup>. Computational studies have shown that reduction of nano-sized  $ZrO_2$  is facilitated in comparison to bulk  $ZrO_2$ , making partial reduction feasible at the present conditions<sup>73</sup>. On the Rh particle near the metal/oxide interface (spot C), significant amounts of zirconia are present mostly as Zr sub-oxides, while the  $Rh_{O_{1/4}}$  component again indicates the active state. Further towards the particle center (spot

D), the amount of Zr sub-oxides decreases and the Rh  $3d_{5/2}$  spectrum reveals an unexpected shoulder due to a distinct Rh surface oxide. It seems that small amounts of Zr sub-oxides locally enhance the oxidation of Rh, probably as a result of the stronger oxygen binding close to the metal/oxide interface<sup>32,74</sup>. Even more towards the particle center (spot E), there is no Zr present and the Rh surface is in the active state.

Based on reports that the growth of  $ZrO_x$  2D-islands preferentially started at step and defect sites of a Pt substrate<sup>75,76</sup>, it can be suggested that the  $ZrO_x$  layers on Rh near the interface may originate from a limited mobility of Zr-O species at temperatures around 450 K. However, the observed formation of small  $ZrO_x$  islands closer to the Rh center rather takes place by sputter-induced support deposition on the Rh particles, where it forms small, hardly mobile oxide islands.

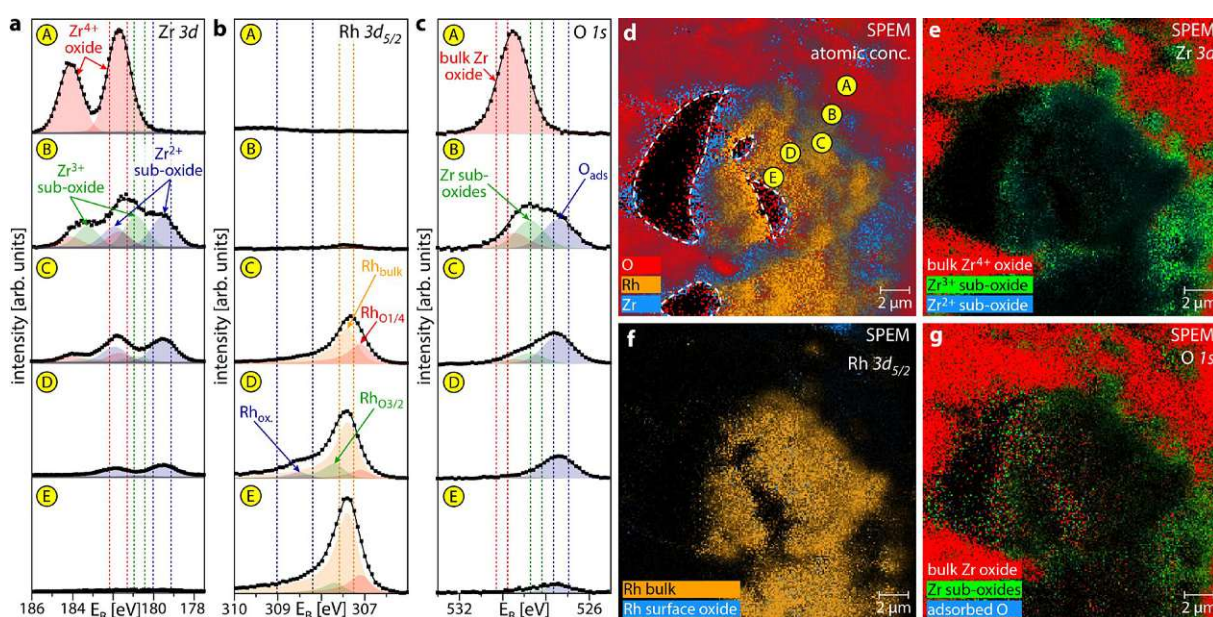


**Figure 4.** Metal/oxide interface effects on  $ZrO_2$  supported Rh particles in the catalytically active state at  $T = 453$  K,  $p_{O_2} = 2.2 \times 10^{-6}$  mbar,  $p_{H_2} = 4.0 \times 10^{-6}$  mbar. **(a)** local Zr  $3d$  XPS spectra for spots A to E indicated in **(d)**, revealing several oxide components (bulk oxide – red;  $Zr^{3+}$  sub-oxide – green;  $Zr^{2+}$  sub-oxide – blue); **(b)** local Rh  $3d_{5/2}$  XPS spectra for spots A to E indicated in **(d)**. In addition to bulk Rh (orange) and Rh surface oxide (blue), two components related to differently oxygen-bound Rh are present (green and red); **(c)** local O  $1s$  XP spectra for spots A to E indicated in **(d)**, showing different oxygen species (bulk Zr oxide – red; Zr sub-oxides – green; adsorbed oxygen – blue); **(d)** SPEM chemical map of the atomic concentrations of O (red), Rh (orange) and Zr (blue). The white dashed lines indicate areas not imaged due to the setup geometry; **(e)** Zr  $3d$  SPEM chemical map for different Zr-oxide species. The field of view is identical to **(d)**. The spectra components correspond to the species in **(a)**, where the dashed lines indicate the energy windows used for constructing the map; **(f)** Rh  $3d$  SPEM chemical map for different Rh species (bulk Rh – orange; Rh surface oxide – blue). The field of view is identical to **(d)**. The energy windows used for constructing the map are indicated by dashed lines in **(b)**; **(g)** O  $1s$  SPEM chemical map for different oxygen species. The field of view is identical to **(d)**. The spectra components correspond to the species in **(c)**, where the dashed lines indicate the energy windows used for constructing the map. All energy windows for constructing the chemical maps are given in Extended Data Table 1.

A chemical map (Fig. 4d) of the atomic concentrations of O (red), Rh (orange) and Zr (blue) was constructed from the O  $1s$ , Rh  $3d_{5/2}$  and Zr  $3d$  signals. The map shows a significant coverage of  $ZrO_x$  on the Rh particle. The island density of  $ZrO_x$  is, however, not as uniform as for Au on Rh, but decreases towards the particle center, which remains free of  $ZrO_x$ . In addition, the Zr/O atomic ratio differs up to 50 % between the support (appearing purple) and near the interface (appearing blue). This is also reflected in the Zr  $3d$  chemical map (Fig. 4f), constructed using the same three components as in the spectra (Fig. 4a). The Rh  $3d_{5/2}$  chemical map (Fig. 4f) reveals mainly bulk metallic Rh (orange) being present on the “big” particle, while small patches of Rh surface oxide (blue dots) are also formed. Smaller particles (e.g., in the top right corner) appear to be strongly oxidized. The corresponding O  $1s$  chemical map (Fig. 4g) shows the expected gradient between support (appearing mainly red), interface region (appearing green) and the center region (appearing in a slight blueish tint).

SPEM results demonstrate an unexpected complexity of the seemingly simple metal/support interfaces: Due to the mobility of Au atoms, the Rh particles were decorated by significant amounts of Au, strongly modifying the catalytic properties by RhAu alloy formation. In the Rh/ $ZrO_2$  system, due to the formation of  $ZrO_x$  islands, a complex interface region spanning several  $\mu\text{m}$  has been formed, resembling strong metal-support interaction (SMSI) states observed on several platinum group metal nanoparticles on various oxides<sup>43–46,48,50,51,77</sup>. Furthermore, the previously identified modification of binding energies at the metal/oxide interface<sup>32,74</sup> appears to be complemented by the formation of substoichiometric Zr oxides, hydrogen spillover onto the  $ZrO_x$  support near the particle and a narrow region where Rh surface oxide is present, altogether resulting in the observed support-induced modifications of the catalytic properties (Fig. 2).

### The oscillating reaction mode

Catalytic  $H_2$  oxidation may exhibit self-sustaining oscillations between the active and inactive state at particular constant reaction parameters, as observed on polycrystalline Rh foils<sup>33–35</sup> and hemispherical apexes of nm- and  $\mu\text{m}$ -sized Rh specimens<sup>12,13,78</sup>. The oscillation frequency and the parameter window for oscillations are very sensitive to surface structure and composition<sup>12,33–35</sup>, turning the oscillating  $H_2$  oxidation on Rh into a sensitive probe. The well-established mechanism of oscillations (Extended Data Fig. 2) is based on formation and depletion of subsurface oxygen<sup>33–35</sup>. However, as for supported Rh particles self-sustained oscillations in  $H_2$  oxidation were so far not observed, their existence and parameter space should be explored.

At constant external parameters oscillations were visualized by PEEM for Rh/Rh and Rh/ $ZrO_2$  (but did not occur for Rh/Au). For Rh/Rh, selected PEEM image cut-outs for the “big” and “small” particles already studied in the steady states and corresponding local PEEM intensity curves are shown in Fig. 5a. Both particles exhibit the same oscillation frequency within the experimental accuracy. It is important to note that while the Rh substrate acts as excitable medium and therefore also exhibits oscillations, the nucleation of the reaction fronts transmitting the oscillations always takes place on the Rh particle perimeters acting as pacemakers<sup>13,74</sup>.

For Rh/Au, PEEM images and local intensity curves are displayed in Fig. 5b. No oscillations occur, with the particles remaining in the inactive state. This can be explained in light of SPEM experiments and the mechanism of oscillations: Au atoms migrated onto the Rh particle are located preferentially at/in steps, hindering the formation of subsurface oxygen and thus the switch to the active state.

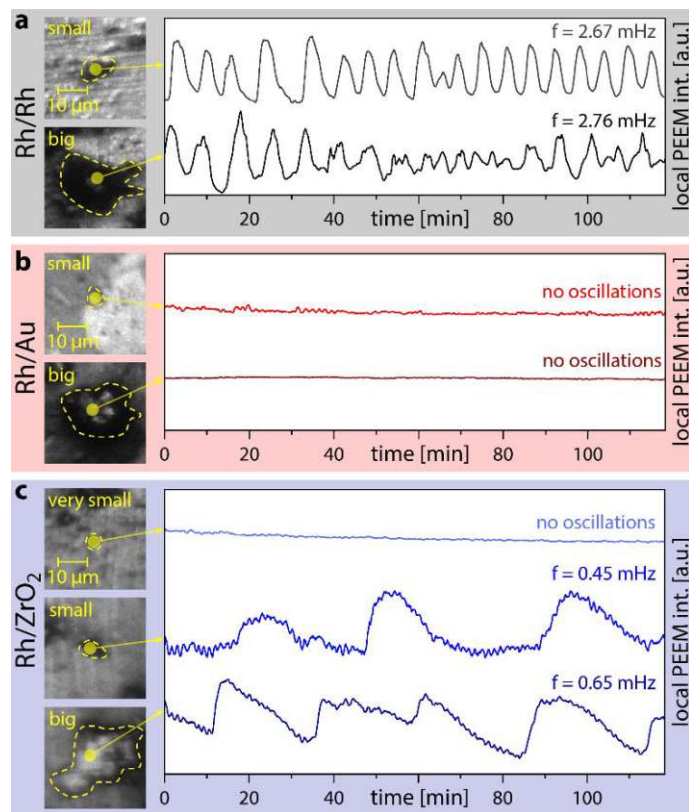


**Figure 5.** Visualizing support and particle size effects by the oscillating mode of catalytic  $\text{H}_2$  oxidation on Rh particles at  $T = 453 \text{ K}$ ,  $p_{\text{O}_2} = 2.2 \times 10^{-6} \text{ mbar}$ ,  $p_{\text{H}_2} = 1.7 \times 10^{-6} \text{ mbar}$ . **(a)** PEEM image cut-outs (left) and local PEEM intensity time series (right) for differently sized Rh particles supported on Rh. The ROIs for constructing the time series are indicated in the cut-outs; **(b)** the same as in (a) but for Rh particles on Au support; **(c)** the same as in (a) but for Rh particles on  $\text{ZrO}_2$  support.

In Fig. 5c, corresponding results for Rh/ $\text{ZrO}_2$  are shown. In addition to the “big” and “small” particles, even a “very small” one was studied, for which no oscillations were observed, apparently due to its oxidized state resulting from  $\text{ZrO}_x$  promoted Rh oxidation. Oscillations observed for “small” and “big” Rh particles exhibited significantly lower frequency than for Rh/Rh, which depended on particle size. We attribute this to the Rh steps being partly blocked by  $\text{ZrO}_x$  and the resulting stronger oxygen bonding. Accordingly, the oscillation cycle slows down. Differently sized Rh particles are differently affected and thus exhibit different oscillation frequencies, due to their different ratios of  $\text{ZrO}_x$ -modified (interfacial) vs. -unmodified Rh surface areas.

In order to assess the curved/stepped particle shape and structure, post-reaction TEM analysis (Extended Data Fig. 3) was performed on cross-sections of some of the studied particles. The composition of particle surfaces and metal/support interface regions was characterized by combined scanning-TEM/energy dispersive x-ray fluorescence (EDX), confirming the *in situ* results.



### Micro-kinetic model simulations

To better understand the experiments, micro-kinetic model simulations of H<sub>2</sub> oxidation were performed, based on the Langmuir-Hinshelwood mechanism and adapting a model of McEwen et al.<sup>78,79</sup>

For representing Rh/Rh, similar parameters as in our previous works were used<sup>12,33–35</sup>. Reflecting PEEM and SPEM results to model Rh/Au, the hydrogen sticking coefficient was adjusted to simulate hindered dissociative hydrogen adsorption and the parameter corresponding to surface “roughness” was decreased, both resulting from RhAu surface alloy formation. To model Rh/ZrO<sub>2</sub>, parameters were modified to simulate the stronger oxygen binding/adsorption<sup>32</sup> and the changed energetics of subsurface oxygen formation in the metal/oxide interface regions (for details see Methods).

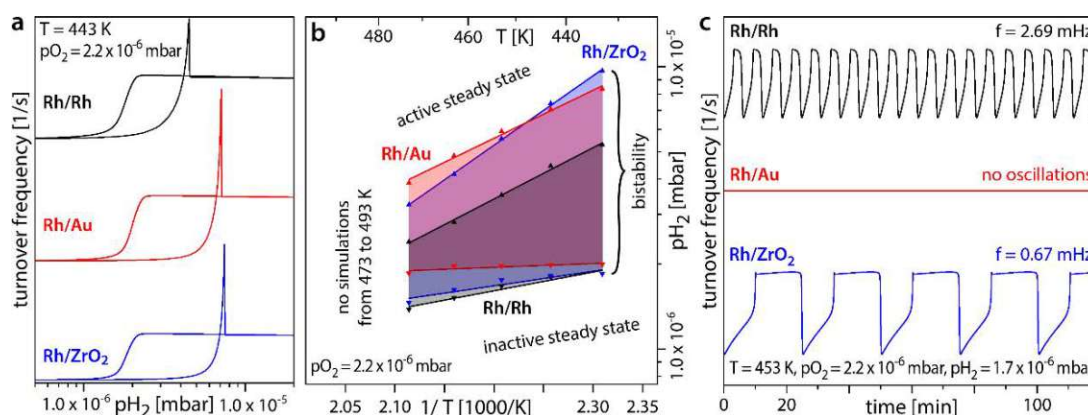


**Figure 6.** Results of the micro-kinetic model simulations. **(a)** simulated turnover frequency curves upon cyclewise variation of  $p_{\text{H}_2}$  from  $5.0 \times 10^{-7}$  mbar to  $2.0 \times 10^{-5}$  mbar at constant  $T = 443$  K and  $p_{\text{O}_2} = 2.2 \times 10^{-6}$  mbar for three model configurations representing Rh/Rh (black), Rh/Au (red) and Rh/ZrO<sub>2</sub> (blue); **(b)** simulated kinetic phase diagram for H<sub>2</sub> oxidation in the temperature range from 433 K to 473 K at constant  $p_{\text{O}_2} = 2.2 \times 10^{-6}$  mbar for the same model configurations as in (a); **(c)** simulations of the oscillating reaction mode at constant  $T = 453$  K,  $p_{\text{O}_2} = 2.2 \times 10^{-6}$  mbar,  $p_{\text{H}_2} = 1.7 \times 10^{-6}$  mbar for the same model configurations as in (a).

Figure 6 presents results of the micro-kinetic model simulations: In Fig. 6a, traces of the reaction rate (turnover frequency; TOF) upon cyclewise variation of  $p_{\text{H}_2}$  are displayed for the three different model configurations, i.e. Rh/Rh (black), Rh/Au (red) and Rh/ZrO<sub>2</sub> (blue). Simulations were performed for the external parameters of the PEEM experiments, allowing a direct comparison (Fig. 2d). By repeating simulations for different temperatures, a kinetic phase diagram can be constructed (Fig. 6b), similar to the experimental diagram in Fig. 2e. Simulations were performed only for 433–473 K, because oxygen-induced surface restructuring was not included in the model. Simulations of the oscillating mode were also performed for all three configurations. The simulated TOF time series are shown in Fig. 6c, corresponding to the big Rh particles in Fig. 5.

The calculations/simulations reproduce the experimental behavior well: Realistic variations of hydrogen adsorption and oxygen binding, mimicking the effects of the various Rh/support interfaces, quantitatively reproduce the shifts in the kinetic phase diagrams as well as the alteration of the oscillatory behavior (oscillation frequency, inhibition of oscillations).

In summary, the catalytic behavior of stepped Rh particles supported by three different materials (Rh, Au, ZrO<sub>2</sub>) in H<sub>2</sub> oxidation has been visualized *in situ* by PEEM. Kinetic transitions between the catalytically inactive and active steady states were studied and self-sustaining oscillations on supported Rh particles were observed for this reaction for the first time. Supported Rh particles show different catalytic properties in H<sub>2</sub> oxidation, depending on the support material and particle size. The oscillating reaction mode varies from particle-size independent (Rh/Rh) via size dependent (Rh/ZrO<sub>2</sub>) to fully inhibited oscillations (Rh/Au).

To interpret the PEEM results, *in situ* SPEM studies were performed for the same sample under the same reaction conditions, i.e. in a correlative way. The SPEM results identified the presence of support material on the Rh particles during the reaction to cause their different behavior. For Rh/Au, the formation of a RhAu surface alloy and for Rh/ZrO<sub>2</sub>, the formation of substoichiometric Zr oxides, hydrogen spillover onto the ZrO<sub>2</sub> support and a narrow region of enhanced Rh oxidation were detected. Combining the real time PEEM data and chemical information from SPEM, the catalytic properties of Rh particles on different supports can be explained, underpinning the effectiveness of the correlative approach. The experimental observations were complemented by micro-kinetic model simulations of kinetic phase diagrams and oscillating time series for catalytic H<sub>2</sub> oxidation on various Rh surfaces. Through realistic variations of hydrogen adsorption and oxygen binding, resulting from the observed modification of stepped Rh surfaces, the experimental findings could be confirmed.

## Methods

### Sample Preparation

The sample was fabricated from a Rh foil (10 x 3 mm, thickness 0.2 mm, MaTeck, 99.9%), an Au foil (10 x 3 mm, thickness 0.2 mm, MaTeck, 99.9%) and an oxidized Zr foil (10 x 3 mm, thickness 0.2 mm, MaTeck, 99.8%), all mounted onto a Ta foil (10 x 12 mm, thickness 0.2 mm, MaTeck, 99.9%) for mechanical stability. The Rh powder aggregates ("Rh black", 5-30 μm size, Alfa Aesar, 99.9%) were suspended in acetone and mechanically pressed on the substrates after solvent evaporation.

The sample was cleaned in UHV by repeated cycles of Ar<sup>+</sup> ion sputtering ( $p_{\text{Ar}} = 5.0 \times 10^{-6}$  mbar, ion energy 1 keV, T = 300 K) and consecutive chemical treatment in oxygen ( $p_{\text{O}_2} = 5 \times 10^{-7}$  mbar, T = 773 K) and hydrogen ( $p_{\text{H}_2} = 5 \times 10^{-6}$  mbar, T = 773 K). Cleanliness of the sample was verified before each experiment by lab-XPS or by SPEM. The sample temperature was measured by a K-type thermocouple spot-welded to its front.

### PEEM experiments

The PEEM experiments were carried out in a multipurpose UHV setup consisting of separate chambers for PEEM and XPS, interconnected by a sample transfer tunnel. The PEEM chamber is equipped with sample cleaning facilities, a deuterium discharge UV lamp (Heraeus D200F, photon energy ~6.5 eV), a PEEM (Staib Instruments PEEM 150), a quadrupole mass spectrometer (MKS e-Vision 2) and a high-purity gas supply (Ar, H<sub>2</sub>, O<sub>2</sub>: 99.999%). In addition to similar sample cleaning and gas dosing-facilities, the XPS chamber is equipped with a twin anode x-ray source (SPECS XR-50) and a hemispherical energy analyzer (SPECS Phoibos 100).

The ongoing H<sub>2</sub> oxidation reaction was monitored by PEEM and the images recorded by a high-speed CCD camera (Hamamatsu C11440-42U30). Calibration of the PEEM magnification was performed by comparison of PEEM images with optical micrographs of the same sample areas. To prove sample cleanliness, XPS spectra were acquired from one circular spot of 500 μm diameter per support material using Mg K<sub>α</sub> radiation with the energy analyzer axis oriented perpendicular to the sample surface (take-off angle 0°).

### SPEM experiments

The SPEM experiments were performed at the “ESCA Microscopy” beamline of the Elettra synchrotron facility, which has been described in detail elsewhere<sup>80</sup>. Summarizing, the end station consists of three connected UHV sub-chambers: the sample is introduced to the system via a fast-entry load lock attached to the first chamber. Using magnetic transfer arms and wobble sticks, the sample can be moved under UHV to a preparation chamber, which is equipped with facilities for Ar<sup>+</sup> ion sputtering, a high purity gas supply (Ar, H<sub>2</sub>, O<sub>2</sub>: 99.999%) and an Auger electron spectrometer for checking the sample cleanliness. After preparation, the sample is moved in UHV to the SPEM chamber. A zone plate optical system provides a small focused photon probe (spot diameter 0.13 μm) on the sample surface, while the analyzed surface region is selected by a piezo specimen positioning and scanning system. The emitted photoelectrons are collected within an 8 eV kinetic energy window by a hemispherical energy analyzer equipped with a 48 channel detector.

The SPEM was operated in two modes: in the microspectroscopy mode, an XPS spectrum was collected from a single microspot on the sample surface, while in the imaging mode, the sample surface was mapped by synchronized-scanning the sample with respect to the photon probe. In the imaging mode, a 48 points XPS spectrum covering the chosen energy window was recorded for each pixel in the image. This allows determination of the spatial distribution of different chemical species<sup>81</sup> and thus the creation of chemical maps and spatial profiles. The overall energy resolution of the system is 0.3 eV<sup>82</sup> and due to the setup geometry, electrons emitted at an angle of 60° from the surface normal are registered. Spectra were taken at a photon energy of 720.2 eV and the energy scale was calibrated against the energy of the Au 4f<sub>7/2</sub> peak with a binding energy of 84.0 eV on the Au part of the sample. The absence of drifts in photon energy and photon flux was verified at regular intervals between the experiments by Au 4f<sub>7/2</sub> spectra on the Au part of the sample.

All spectra in the present work are representative examples of the described states and were deconvoluted using a pseudo-Voigt line shape<sup>83</sup> in combination with a Shirley background<sup>84</sup>. The spectral components are based on literature data (see details in the corresponding parts of the results section above) and were refined by considering a whole ensemble of spectra, including reference spectra of the clean, catalytically active and catalytically inactive surfaces.

### (S)TEM/EDX characterization

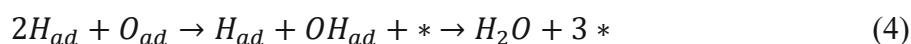
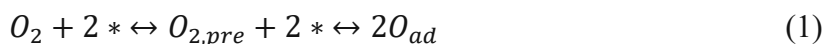
The (S)TEM/EDX characterization of the Rh/Au and Rh/ZrO<sub>2</sub> particles was performed at the University Service Center for Transmission Electron Microscopy (USTEM) at TU Wien after the PEEM and SPEM experiments. Cross-sections of the “big” particles were prepared by focused ion beam (FIB) milling (using Ga<sup>+</sup> ions at 30 keV) in a FEI Quanta 200 3D dual beam electron microscope. The cross-sections were investigated in a FEI Tecnai G<sup>2</sup>20 S-TWIN

transmission electron microscope operated at 200 kV, which is equipped with a Gatan Orius 600 camera for imaging and diffraction imaging and an EDAX-AMETEK Octane T Elite plus detector for EDX.

### Micro-kinetic model simulations

The mean-field micro-kinetic model applied in our simulations is based on the Langmuir-Hinshelwood mechanism, which is well established for H<sub>2</sub> oxidation on Rh surfaces<sup>85</sup>, and the previously established mechanism of kinetic oscillations<sup>12,33–35</sup>.

The reaction network is described by four equations (1)-(4), where \* denotes an empty surface site and \*<sub>sub</sub> denotes an empty subsurface site:



The formation of water takes place via an OH<sub>ad</sub> intermediate, where the formation of the intermediate from O<sub>ad</sub> and H<sub>ad</sub> is the rate-limiting step in comparison to the subsequent reaction with a second H<sub>ad</sub> species. Alternative ways of water formation (e.g., by OH<sub>ad</sub> disproportioning) can be neglected<sup>79</sup> and the reaction product water immediately desorbs at the present conditions<sup>86</sup>. The coverages for oxygen  $\theta_O$ , subsurface oxygen  $\theta_S$  and hydrogen  $\theta_H$  can then be described by three kinetic equations (5)-(7), where the empty sites  $\theta_*$  are given by  $\theta_* = 1 - \theta_H - \theta_O$ .

$$\frac{d\theta_O}{dt} = \frac{2}{1+K\theta_*^2} (k_a^O K p_{O_2} \theta_*^2 - k_d^O \theta_O^2) - k_{ox} \theta_O (1 - \theta_S) + k_{red} \theta_S \theta_* - k_r \theta_H \theta_O \quad (5)$$

$$\frac{d\theta_S}{dt} = k_{ox} \theta_O (1 - \theta_S) - k_{red} \theta_S \theta_* \quad (6)$$

$$\frac{d\theta_H}{dt} = 2k_a^H p_{H_2} \theta_*^2 - 2k_d^H \theta_H^2 - 2k_r \theta_H \theta_O \quad (7)$$

The rate constants in (5)-(7) are given by expressions (8)-(15), where  $\beta = 1/k_B T$ . The symbols are explained in Methods Table 1.

$$k_a^H = S_0^H a_s / \sqrt{2\pi m_{H_2} k_B T} \quad (8)$$

$$k_a^O = S_0^O a_s / \sqrt{2\pi m_{O_2} k_B T} \quad (9)$$

$$k_d^H = k_{d0}^H e^{-\beta E_d^H} \quad (10)$$

$$K = K_0 e^{-\beta(E_K + A_K^O \theta_O + A_K^S \theta_S)} \quad (11)$$

$$k_d^O = k_{d0}^O e^{-\beta(E_d^O + A_d^O \theta_O + B_d^O \theta_O^2)} \quad (12)$$

$$k_{ox} = k_{ox}^0 e^{-\beta E_{ox}} \quad (13)$$

$$k_{red} = k_{red}^0 e^{-\beta(E_{red} + A_{red}^S \theta_S)} \quad (14)$$

$$k_r = k_r^0 e^{-\beta(E_r + A_r^H \theta_H + A_r^O \theta_O)} \quad (15)$$

In order to model the three different systems studied in the experiments (Rh/Rh, Rh/Au and Rh/ZrO<sub>2</sub>), three parameter sets were used. The set for Rh/Rh is closely related to the one used for the step edge sites on Rh(110) in our recent studies on coexisting multi-states in H<sub>2</sub> oxidation on Rh<sup>35</sup>, as the Rh particles are expected to expose surface structures of similar roughness. The set differs slightly only in the choice of  $S_0^O$ ,  $A_K^S$ ,  $A_{red}^S$  and  $E_d^H$  which have been adjusted to account for the particles exposing a mixture of several different surface structures. For modeling the hinderance of dissociative hydrogen adsorption by the RhAu surface alloy and a resulting “smoothing” of the particle shape,  $S_0^H$ ,  $E_{ox}$  and  $E_{red}$  were modified in the parameter set for the Rh/Au system. For modeling Rh/ZrO<sub>2</sub>,  $E_d^O$ ,  $A_K^O$ ,  $A_K^S$ ,  $E_{ox}$ ,  $E_{red}$  and  $E_r$  were modified in comparison to the Rh/Rh parameter set, in line with the stronger binding of oxygen in the vicinity of the metal/oxide interface and a slight reduction of the surface roughness due to partially blocked step edges. All model parameters are summarized in Methods Table 1.

**Methods Table 1.** Parameter sets used in the micro-kinetic model simulations of the Rh/Rh, Rh/Au and Rh/ZrO<sub>2</sub> systems. Energies are given in eV, the area of a surface site in Å<sup>2</sup> and rate constants in 1/s. When no value is given, the same value as for Rh/Rh was used.

symbol	description	Rh/Rh	Rh/Au	Rh/ZrO <sub>x</sub>
$a_s$	area of a surface site	10		
$S_0^O$	initial sticking coefficient of O	0.82		
$k_{dO}^O$	pre-factor for oxygen desorption	$6.0 \times 10^{13}$		
$E_d^O$	desorption energy of O	3.20		3.70
$A_d^O$	dependence of oxygen desorption energy on adsorbed oxygen coverage	-0.5		
$B_d^O$	dependence of oxygen desorption energy on molecular oxygen coverage	-0.7		
$K_0$	pre-factor for oxygen dissociation equilibrium constant	0.2525		
$E_k$	activation energy for oxygen dissociation equilibrium constant	-0.178		
$A_K^O$	dependence of oxygen dissociation on adsorbed oxygen coverage	0.158		0.125
$A_K^S$	dependence of oxygen dissociation on sub-surface oxygen coverage	0.088		0.089
$k_{ox}^O$	pre-factor for oxygen diffusion from surface to sub-surface sites	$5.0 \times 10^{11}$		
$E_{ox}$	activation energy for oxygen diffusion from surface to sub-surface sites	1.193	1.247	1.221
$k_{red}^O$	pre-factor for oxygen diffusion from sub-surface to surface sites	$1.85 \times 10^{13}$		
$E_{red}$	activation energy for oxygen diffusion from sub-surface to surface sites	1.220	1.261	1.241

$A_{red}^s$	dependence of sub-surface oxygen reduction on sub-surface oxygen coverage	0.36	
$S_0^H$	initial sticking coefficient of H	0.40	0.37
$k_{d0}^h$	pre-factor for hydrogen desorption	$3.0 \times 10^{10}$	
$E_d^H$	desorption energy of H	0.75	
$k_r^0$	pre-factor for water formation	$7.0 \times 10^{12}$	
$E_r$	activation energy for water formation	0.79	0.80
$A_r^H$	dependence of activation energy of water formation on H coverage	-0.27	
$A_r^O$	dependence of activation energy of water formation on O coverage	-0.145	

In addition to the already well-established simulations of the oscillating reaction mode at constant external parameters, in the present work kinetic transitions were modeled as well. For this, the  $p_{H_2}$  parameter was ramped from  $5.0 \times 10^{-7}$  mbar to  $2.0 \times 10^{-5}$  mbar and back at constant T and  $p_{O_2}$  parameters. The kinetic transition points were then extracted from the turnover frequency vs.  $p_{H_2}$  data series by determining the respective inflection points.

### Data availability

The data of this study are available from the corresponding author upon reasonable request and will be available from an open-source online repository (zenodo®) upon publication.

### Code availability

All the code or mathematical algorithm files within this paper are available from the corresponding author upon reasonable request.

### References

1. Boudart, M. Catalysis by Supported Metals. in *Advances in Catalysis* vol. 20 153–166 (Elsevier, 1969).
2. Hayek, K., Kramer, R. & Paál, Z. Metal-support boundary sites in catalysis. *Appl. Catal. Gen.* **162**, 1–15 (1997).
3. Tuxen, A. *et al.* Size-Dependent Dissociation of Carbon Monoxide on Cobalt Nanoparticles. *J. Am. Chem. Soc.* **135**, 2273–2278 (2013).
4. van Deelen, T. W., Hernández Mejía, C. & de Jong, K. P. Control of metal-support interactions in heterogeneous catalysts to enhance activity and selectivity. *Nat. Catal.* **2**, 955–970 (2019).
5. Besenbacher, F., Lauritsen, J. V. & Wendt, S. STM studies of model catalysts. *Nano Today* **2**, 30–39 (2007).
6. Mattevi, C. *et al.* In-situ X-ray Photoelectron Spectroscopy Study of Catalyst–Support Interactions and Growth of Carbon Nanotube Forests. *J. Phys. Chem. C* **112**, 12207–12213 (2008).

7. Liu, J. J. Advanced Electron Microscopy of Metal-Support Interactions in Supported Metal Catalysts. *ChemCatChem* **3**, 934–948 (2011).
8. Silvestre-Albero, J., Rupprechter, G. & Freund, H. Atmospheric pressure studies of selective 1,3-butadiene hydrogenation on well-defined Pd/Al<sub>2</sub>O<sub>3</sub>/NiAl(110) model catalysts: Effect of Pd particle size. *J. Catal.* **240**, 58–65 (2006).
9. Jørgensen, M. & Grönbeck, H. Scaling Relations and Kinetic Monte Carlo Simulations To Bridge the Materials Gap in Heterogeneous Catalysis. *ACS Catal.* **7**, 5054–5061 (2017).
10. Jørgensen, M. & Grönbeck, H. The Site-Assembly Determines Catalytic Activity of Nanoparticles. *Angew. Chem. Int. Ed.* **57**, 5086–5089 (2018).
11. Vogt, C. *et al.* Unravelling structure sensitivity in CO<sub>2</sub> hydrogenation over nickel. *Nat. Catal.* **1**, 127–134 (2018).
12. Suchorski, Y. *et al.* Resolving multifrequential oscillations and nanoscale interfacet communication in single-particle catalysis. *Science* **372**, 1314–1318 (2021).
13. Zeininger, J. *et al.* Single-Particle Catalysis: Revealing Intraparticle Pacemakers in Catalytic H<sub>2</sub> Oxidation on Rh. *ACS Catal.* **11**, 10020–10027 (2021).
14. Zeininger, J. *et al.* Reaction Modes on a Single Catalytic Particle: Nanoscale Imaging and Micro-Kinetic Modeling. *ACS Catal.* **12**, 12774–12785 (2022).
15. Osborn, M., Webster, R. & Weber, K. Individual microtubules viewed by immunofluorescence and electron microscopy in the same PtK2 cell. *J. Cell Biol.* **77**, R27 (1978).
16. Webster, R. E., Osborn, M. & Weber, K. Visualization of the same PtK2 cytoskeletons by both immunofluorescence and low power electron microscopy. *Exp. Cell Res.* **117**, 47–61 (1978).
17. Odermatt, P. D. *et al.* High-Resolution Correlative Microscopy: Bridging the Gap between Single Molecule Localization Microscopy and Atomic Force Microscopy. *Nano Lett.* **15**, 4896–4904 (2015).
18. Carlson, D. B., Gelb, J., Palshin, V. & Evans, J. E. Laboratory-Based Cryogenic Soft X-Ray Tomography with Correlative Cryo-Light and Electron Microscopy. *Microsc. Microanal.* **19**, 22–29 (2013).
19. Povstugar, I. *et al.* Correlative Atom Probe Tomography and Transmission Electron Microscopy Analysis of Grain Boundaries in Thermally Grown Alumina Scale. *Microsc. Microanal.* **25**, 11–20 (2019).
20. Albu, M., Fitzek, H., Moser, D., Kothleitner, G. & Hofer, F. Multiscale and Correlative Analytical Electron Microscopy of Extraterrestrial Minerals. *Front. Astron. Space Sci.* **7**, 544331 (2020).
21. Weckhuysen, B. M. Chemical Imaging of Spatial Heterogeneities in Catalytic Solids at Different Length and Time Scales. *Angew. Chem. Int. Ed.* **48**, 4910–4943 (2009).
22. Hendriks, F. C. *et al.* Integrated Transmission Electron and Single-Molecule Fluorescence Microscopy Correlates Reactivity with Ultrastructure in a Single Catalyst Particle. *Angew. Chem. Int. Ed.* **57**, 257–261 (2018).
23. Schmidt, J. E. *et al.* Probing the Location and Speciation of Elements in Zeolites with Correlated Atom Probe Tomography and Scanning Transmission X-Ray Microscopy. *ChemCatChem* **11**, 488–494 (2019).
24. Schweinar, K. *et al.* Probing catalytic surfaces by correlative scanning photoemission electron microscopy and atom probe tomography. *J. Mater. Chem. A* **8**, 388–400 (2020).

25. Gambino, M. *et al.* Mimicking industrial aging in fluid catalytic cracking: A correlative microscopy approach to unravel inter-particle heterogeneities. *J. Catal.* **404**, 634–646 (2021).
26. Marbach, H. *et al.* Ordered phases in alkali redistribution during a catalytic surface reaction. *Phys Chem Chem Phys* **5**, 2730–2735 (2003).
27. Winkler, P. *et al.* How the anisotropy of surface oxide formation influences the transient activity of a surface reaction. *Nat. Commun.* **12**, 69 (2021).
28. Zeininger, J. *et al.* Pattern Formation in Catalytic H<sub>2</sub> Oxidation on Rh: Zooming in by Correlative Microscopy. *ACS Catal.* 11974–11983 (2022) doi:10.1021/acscatal.2c03692.
29. Schaak, A. & Imbihl, R. Bistability and formation of low work function areas in the O<sub>2</sub>+H<sub>2</sub> reaction on a Rh(111) surface. *J. Chem. Phys.* **113**, 9822–9829 (2000).
30. Visart de Bocarmé, T., Bär, T. & Kruse, N. In situ dynamic study of hydrogen oxidation on rhodium. *Ultramicroscopy* **89**, 75–82 (2001).
31. Datler, M. *et al.* Hydrogen Oxidation on Stepped Rh Surfaces: μm-Scale versus Nanoscale. *Catal. Lett.* **146**, 1867–1874 (2016).
32. Suchorski, Y. *et al.* Transmitting metal–oxide interaction by solitary chemical waves: H<sub>2</sub> oxidation on ZrO<sub>2</sub> supported Rh. *Surf. Sci.* **679**, 163–168 (2019).
33. Suchorski, Y. *et al.* Visualizing catalyst heterogeneity by a multifrequential oscillating reaction. *Nat. Commun.* **9**, 600 (2018).
34. Suchorski, Y. *et al.* Surface-Structure Libraries: Multifrequential Oscillations in Catalytic Hydrogen Oxidation on Rhodium. *J. Phys. Chem. C* **123**, 4217–4227 (2019).
35. Winkler, P. *et al.* Coexisting multi-states in catalytic hydrogen oxidation on rhodium. *Nat. Commun.* **12**, 6517 (2021).
36. Dahl, S. *et al.* Role of Steps in N<sub>2</sub> Activation on Ru(0001). *Phys. Rev. Lett.* **83**, 1814–1817 (1999).
37. Besenbacher, F. *et al.* Design of a Surface Alloy Catalyst for Steam Reforming. *Science* **279**, 1913–1915 (1998).
38. H. Larsen, J. From fundamental studies of reactivity on single crystals to the design of catalysts. *Surf. Sci. Rep.* **35**, 163–222 (1999).
39. Santos, J. L., Reina, T. R., Ivanova, S., Centeno, M. A. & Odriozola, J. A. Gold promoted Cu/ZnO/Al<sub>2</sub>O<sub>3</sub> catalysts prepared from hydrotalcite precursors: Advanced materials for the WGS reaction. *Appl. Catal. B Environ.* **201**, 310–317 (2017).
40. Igarashi, A., Ohtaka, T., Honnma, T. & Fukuhara, C. The Role of Zirconium Dioxide in the Activation of Water and as the Catalytic Site for Low-Temperature Steam Reforming Over Rh/ZrO<sub>2</sub>. in *Studies in Surface Science and Catalysis* vol. 75 2083–2086 (Elsevier, 1993).
41. Boffa, A., Lin, C., Bell, A. T. & Somorjai, G. A. Promotion of CO and CO<sub>2</sub> Hydrogenation over Rh by Metal Oxides: The Influence of Oxide Lewis Acidity and Reducibility. *J. Catal.* **149**, 149–158 (1994).
42. Frey, H., Beck, A., Huang, X., van Bokhoven, J. A. & Willinger, M. G. Dynamic interplay between metal nanoparticles and oxide support under redox conditions. *Science* **376**, 982–987 (2022).
43. Lackner, P., Choi, J. I. J., Diebold, U. & Schmid, M. Substoichiometric ultrathin zirconia films cause strong metal–support interaction. *J. Mater. Chem. A* **7**, 24837–24846 (2019).



44. Rupprechter, G., Hayek, K. & Hofmeister, H. Electron Microscopy of Thin-Film Model Catalysts: Activation of Alumina-Supported Rhodium Nanoparticles. *J. Catal.* **173**, 409–422 (1998).
45. Bernal, S. *et al.* Some recent results on metal/support interaction effects in NM/CeO<sub>2</sub> (NM: noble metal) catalysts. *Catal. Today* **50**, 175–206 (1999).
46. Bernal, S. Nanostructural evolution of high loading Rh/lanthana catalysts through the preparation and reduction steps. *Catal. Today* **52**, 29–43 (1999).
47. Fu, Q., Wagner, T., Olliges, S. & Carstanjen, H.-D. Metal–Oxide Interfacial Reactions: Encapsulation of Pd on TiO<sub>2</sub> (110). *J. Phys. Chem. B* **109**, 944–951 (2005).
48. Willinger, M. G. *et al.* A Case of Strong Metal-Support Interactions: Combining Advanced Microscopy and Model Systems to Elucidate the Atomic Structure of Interfaces. *Angew. Chem. Int. Ed.* **53**, 5998–6001 (2014).
49. Liu, Z. *et al.* Dry Reforming of Methane on a Highly-Active Ni-CeO<sub>2</sub> Catalyst: Effects of Metal-Support Interactions on C–H Bond Breaking. *Angew. Chem. Int. Ed.* **55**, 7455–7459 (2016).
50. Rameshan, C. *et al.* *In situ* NAP-XPS spectroscopy during methane dry reforming on ZrO<sub>2</sub>/Pt(111) inverse model catalyst. *J. Phys. Condens. Matter* **30**, 264007 (2018).
51. Li, Y., Zhang, Y., Qian, K. & Huang, W. Metal–Support Interactions in Metal/Oxide Catalysts and Oxide–Metal Interactions in Oxide/Metal Inverse Catalysts. *ACS Catal.* **12**, 1268–1287 (2022).
52. Suchorski, Y. & Rupprechter, G. Local reaction kinetics by imaging. *Surf. Sci.* **643**, 52–58 (2016).
53. Yates, J. T., Thiel, P. A. & Weinberg, W. H. The catalytic reaction between adsorbed oxygen and hydrogen on Rh(111). *Surf. Sci.* **82**, 45–68 (1979).
54. Bowker, M., Guo, Q. & Joyner, R. CO and O<sub>2</sub> adsorption on Rh(110). *Surf. Sci.* **253**, 33–43 (1991).
55. Murray, P. W. *et al.* Scanning-tunneling-microscopy study of the oxygen-induced reconstruction of Rh(110). *Phys. Rev. B* **47**, 12976–12979 (1993).
56. Hoogers, G. & King, D. A. Adsorbate-induced step-doubling reconstruction of a vicinal metal surface: oxygen on Rh {332}. *Surf. Sci.* **286**, 306–316 (1993).
57. Voss, C., Gaussmann, A. & Kruse, N. Oxygen-induced reconstruction of Rh{110} and {113} single crystal planes. *Appl. Surf. Sci.* **67**, 142–146 (1993).
58. Nolte, P. *et al.* Shape Changes of Supported Rh Nanoparticles During Oxidation and Reduction Cycles. *Science* **321**, 1654–1658 (2008).
59. Voss, C. & Kruse, N. Morphological changes of Rh crystallites in the presence of adsorbed oxygen. *Surf. Sci.* **409**, 252–257 (1998).
60. Sault, A. G., Madix, R. J. & Campbell, C. T. Adsorption of oxygen and hydrogen on Au(110)-(1 × 2). *Surf. Sci.* **169**, 347–356 (1986).
61. Deng, X., Min, B. K., Guloy, A. & Friend, C. M. Enhancement of O<sub>2</sub> Dissociation on Au(111) by Adsorbed Oxygen: Implications for Oxidation Catalysis. *J. Am. Chem. Soc.* **127**, 9267–9270 (2005).
62. Bassett, D. W. & Webber, P. R. Diffusion of single adatoms of platinum, iridium and gold on platinum surfaces. *Surf. Sci.* **70**, 520–531 (1978).
63. Berg, C., Venvik, H. J., Strisland, F., Ramstad, A. & Borg, A. Nucleation and growth of Au overlayers on Pt(100)-hex-R0.7° studied by STM and photoelectron spectroscopy. *Surf. Sci.* **409**, 1–15 (1998).

64. Locatelli, A., Heun, S. & Kiskinova, M. Direct observation of reaction-induced lateral redistribution of sub-monolayers of Au deposited on a Rh(110) surface. *Surf. Sci.* **566–568**, 1130–1136 (2004).
65. Fuggle, J. C., Källne, E., Watson, L. M. & Fabian, D. J. Electronic structure of aluminum and aluminum-noble-metal alloys studied by soft-x-ray and x-ray photoelectron spectroscopies. *Phys. Rev. B* **16**, 750–761 (1977).
66. Kuhn, M., Bzowski, A., Sham, T. K., Rodriguez, J. A. & Hrbek, J. Ru-promoted alloying of Au and Cu ultrathin films: photoemission studies. *Thin Solid Films* **283**, 209–220 (1996).
67. Óvári, L. *et al.* The growth and thermal properties of Au deposited on Rh(111): formation of an ordered surface alloy. *Phys. Chem. Chem. Phys.* **18**, 25230–25240 (2016).
68. Africh, C. *et al.* Two-Step Reaction on a Strained, Nanoscale Segmented Surface. *Phys. Rev. Lett.* **93**, 126104 (2004).
69. Bespalov, I. *et al.* Initial stages of oxide formation on the Zr surface at low oxygen pressure: An in situ FIM and XPS study. *Ultramicroscopy* **159**, 147–151 (2015).
70. Ma, W., Herbert, F. W., Senanayake, S. D. & Yildiz, B. Non-equilibrium oxidation states of zirconium during early stages of metal oxidation. *Appl. Phys. Lett.* **106**, 101603 (2015).
71. Jóźwiak, W. K. Influence of reoxidation temperature on TPR of zirconia supported rhodium. *React. Kinet. Catal. Lett.* **30**, 345–351 (1986).
72. Hoang, D.-L., Berndt, H. & Lieske, H. Hydrogen spillover phenomena on Pt/ZrO<sub>2</sub>. *Catal. Lett.* **31**, 165–172 (1995).
73. Ruiz Puigdollers, A., Tosoni, S. & Pacchioni, G. Turning a Nonreducible into a Reducible Oxide via Nanostructuring: Opposite Behavior of Bulk ZrO<sub>2</sub> and ZrO<sub>2</sub> Nanoparticles Toward H<sub>2</sub> Adsorption. *J. Phys. Chem. C* **120**, 15329–15337 (2016).
74. Suchorski, Y. *et al.* The role of metal/oxide interfaces for long-range metal particle activation during CO oxidation. *Nat. Mater.* **17**, 519–522 (2018).
75. Meinel, K., Schindler, K.-M. & Neddermeyer, H. Growth, structure and annealing behaviour of epitaxial ZrO<sub>2</sub> films on Pt(111). *Surf. Sci.* **532–535**, 420–424 (2003).
76. Meinel, K., Eichler, A., Schindler, K.-M. & Neddermeyer, H. STM, LEED, and DFT characterization of epitaxial ZrO<sub>2</sub> films on Pt(111). *Surf. Sci.* **562**, 204–218 (2004).
77. Hayek, K., Fuchs, M., Klötzer, B., Reichl, W. & Rupprechter, G. Studies of metal–support interactions with “real” and “inverted” model systems: reactions of CO and small hydrocarbons with hydrogen on noble metals in contact with oxides. *Top. Catal.* **13**, 55–66 (2000).
78. McEwen, J.-S., Gaspard, P., de Bocarmé, T. V. & Kruse, N. Nanometric chemical clocks. *Proc. Natl. Acad. Sci.* **106**, 3006–3010 (2009).
79. McEwen, J.-S., Gaspard, P., Visart de Bocarmé, T. & Kruse, N. Oscillations and Bistability in the Catalytic Formation of Water on Rhodium in High Electric Fields. *J. Phys. Chem. C* **113**, 17045–17058 (2009).
80. Casalis, L. *et al.* ESCA microscopy beamline at ELETTRA. *Rev. Sci. Instrum.* **66**, 4870–4875 (1995).
81. Gregoratti, L. *et al.* 48-Channel electron detector for photoemission spectroscopy and microscopy. *Rev. Sci. Instrum.* **75**, 64–68 (2004).
82. Zeller, P. *et al.* Scanning Photoelectron Spectro-Microscopy: A Modern Tool for the Study of Materials at the Nanoscale. *Phys. Status Solidi A* **215**, 1800308 (2018).

83. Evans, S. Curve synthesis and optimization procedures for X-ray photoelectron spectroscopy. *Surf. Interface Anal.* **17**, 85–93 (1991).
84. Shirley, D. A. High-Resolution X-Ray Photoemission Spectrum of the Valence Bands of Gold. *Phys. Rev. B* **5**, 4709–4714 (1972).
85. Zum Mallen, M. P., Williams, W. R. & Schmidt, L. D. Steps in hydrogen oxidation on rhodium: hydroxyl desorption at high temperatures. *J. Phys. Chem.* **97**, 625–632 (1993).
86. Gregoratti, L. *et al.* Structural effects on water formation from coadsorbed H + O on Rh(100). *Surf. Sci.* **340**, 205–214 (1995).

## Acknowledgements

This work was supported by the Austrian Science Fund (FWF) (P 32772-N and F81-P08). We acknowledge Elettra Sincrotrone Trieste for providing access to its synchrotron radiation facilities and for financial support under the IUS internal project. The authors are grateful to Prof. Henrik Grönbeck for helpful discussions on micro-kinetic modeling.

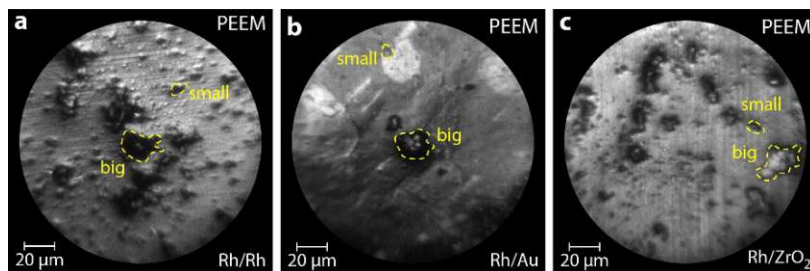
## Author Contributions

P.W. and L.M.R. performed the PEEM measurements and evaluated the data. P.W., J.Z., M.R., M.A., L.G., R.P. and G.R. performed the SPEM measurements and P.W. evaluated the data. P.W. and M.S.-P. performed TEM and data evaluation. M.R. performed the micro-kinetic model simulations. Y.S. and G.R. supervised the work. P.W., Y.S. and G.R. prepared the manuscript. All authors contributed to the discussion and approved the manuscript.

## Competing Interests

The authors declare no competing interests.

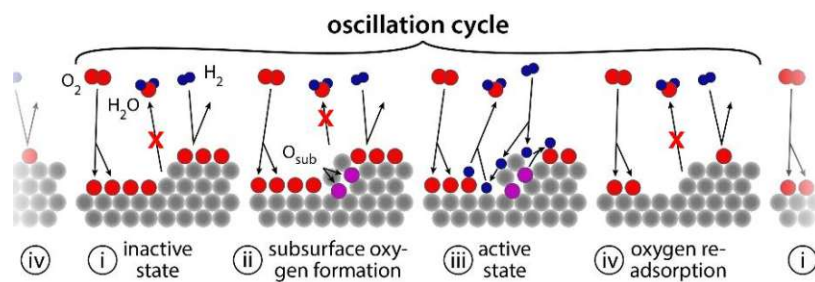
## Extended data



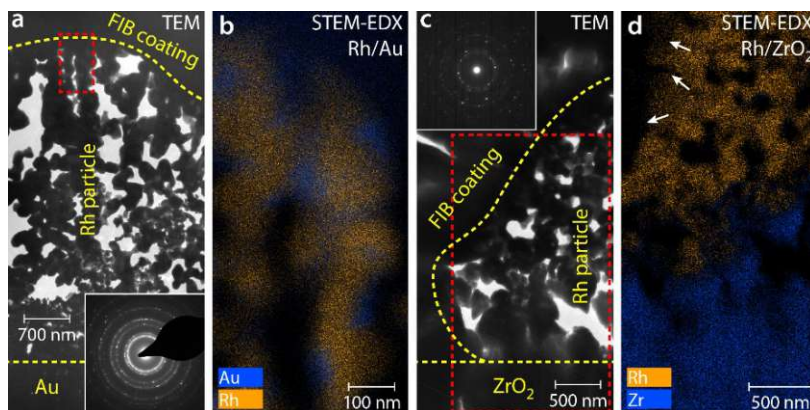
**Extended Data Figure 1.** PEEM images of the clean Rh particles on the three different supporting materials with the “big” and “small” particles marked. **(a)** Rh/Rh; **(b)** Rh/Au; **(c)** Rh/ZrO<sub>2</sub>.

**Extended Data Table 1.** Energy windows used in constructing the chemical maps in Figs. 3 and 4.

	Species	Lower binding energy boundary [eV]	Upper binding energy boundary [eV]
<b>Rh/Au: Au <math>4f_{7/2}</math></b> (Fig. 3e)	Au bulk	84.40	85.39
	RhAu alloy	82.60	83.58
<b>Rh/ZrO<sub>2</sub>: Zr <math>3d</math></b> (Fig. 4e)	bulk Zr <sup>4+</sup> oxide	181.30	182.18
	Zr <sup>3+</sup> sub-oxide	180.43	180.96
	Zr <sup>2+</sup> sub-oxide	179.15	180.03
<b>Rh/ZrO<sub>2</sub>: Rh <math>3d_{5/2}</math></b> (Fig. 4f)	Rh bulk	308.20	309.02
	Rh surface oxide	307.26	307.59
<b>Rh/ZrO<sub>2</sub>: O <math>1s</math></b> (Fig. 4g)	bulk Zr oxide	529.77	530.30
	Zr sub-oxides	528.18	528.71
	adsorbed O	526.95	527.65



**Extended Data Figure 2.** The oscillation cycle in catalytic H<sub>2</sub> oxidation on Rh. (i) the cycle starts from the catalytically inactive state, where preferential adsorption of oxygen at the step edges hinders dissociative adsorption of hydrogen and thus hampers catalytic activity; (ii) because of the dense oxygen coverage, oxygen starts to penetrate the Rh surface at kink or step sites. Some Rh atoms get dislocated, increasing the local surface roughness and creating favorable conditions for dissociative hydrogen adsorption; (iii) a switch to the catalytically active state takes place, where both hydrogen and oxygen adsorb, and then form water. Eventually, subsurface oxygen will diffuse to surface sites and react. Oxygen will once again be preferred at the step edges, resulting in a lack of hydrogen supply and the surface switches back to the catalytically inactive state; (iv) oxygen at the surface is replenished during the last stage and the cycle restarts.



**Extended Data Figure 3.** Transmission electron microscopy (TEM) and energy-dispersive X-ray fluorescence (EDX) of selected particles studied before by PEEM and SPEM. **(a)** cross-section TEM image of the “big” Rh particle on Au, prepared by focused ion beam (FIB). The yellow dashed lines indicate the boundaries of the Au support and the Rh particle. The inset shows a diffraction pattern obtained from within the Rh region, highlighting the polycrystalline nature of the Rh particle; **(b)** STEM-EDX compositional map of the area marked by the red dashed rectangle in (a), i.e., near the particle surface (blue: Au; orange: Rh), indicating decoration by Au; **(c)** cross-section TEM image of the metal/support boundary area of the “big” Rh particle on ZrO<sub>2</sub> prepared by FIB. The yellow dashed lines mark the boundaries of the ZrO<sub>2</sub> support and the Rh particle. The inset shows a diffraction pattern from within the Rh region; **(d)** STEM-EDX compositional map of the area indicated by the red dashed rectangle in (c), indicating ZrO<sub>x</sub> species mainly near the metal/support boundary (orange: Rh, blue: Zr). Small oxide patches on Rh surface are marked by white arrows.



---

## List of Figures

1.1	Working principle of a catalyst . . . . .	3
1.2	The pressure and materials gap . . . . .	6
1.3	Crystal structures of rhodium and Rh(hkl) surfaces . . . . .	8
1.4	Woods notation for adsorbate structures . . . . .	9
1.5	The Langmuir-Hinshelwood mechanism of catalytic H <sub>2</sub> oxidation on platinum group metals . . . . .	13
1.6	The steady states of catalytic activity, bistability and kinetic phase diagrams in catalytic H <sub>2</sub> oxidation on Rh . . . . .	14
1.7	The feedback mechanism in the oscillating catalytic H <sub>2</sub> oxidation on Rh . . . . .	16
2.1	The photoelectric effect and its application in UPS and XPS . . . . .	22
2.2	The universal mean free path curve . . . . .	24
2.3	Working principles of the essential components of an XPS setup . . . . .	26
2.4	The working principle of SPEM . . . . .	28
2.5	The working principle of UV-PEEM . . . . .	30
2.6	Schematic layout of the Spectromicroscope for All Relevant Techniques (SMART) . . . . .	32
2.7	The working principle of EBSD . . . . .	34
2.8	The kinetics by imaging approach . . . . .	36





---

## List of Tables

1.1	Adsorption phases observed for hydrogen on various Rh(hkl) surfaces . . . . .	10
1.2	Adsorption phases observed for oxygen on various Rh(hkl) surfaces . . . . .	11



---

## Bibliography

- (1) McGovern, P. E.; Zhang, J.; Tang, J.; Zhang, Z.; Hall, G. R.; Moreau, R. A.; Nuñez, A.; Butrym, E. D.; Richards, M. P.; Wang, C.-s.; Cheng, G.; Zhao, Z.; Wang, C. *Proceedings of the National Academy of Sciences* **2004**, *101*, 17593–17598.
- (2) In *Catalysis: An Integrated Approach to Homogeneous, Heterogeneous and Industrial Catalysis*, Moulijn, J., van Leeuwen, P., Van Santen, R., Eds.; Studies in Surface Science and Catalysis, Vol. 79; Elsevier: 1993, pp 3–21.
- (3) Berzelius, J. *Jahresbericht über die Fortschritte der physischen Wissenschaften* **1836**, *15*, 237–245.
- (4) Davy, H. *Philosophical Transactions of the Royal Society of London* **1817**, *107*, 77–85.
- (5) Döbereiner *Annalen der Physik und der physikalischen Chemie* **1823**, *74*, 269–273.
- (6) Henry, W. *Philosophical Transactions of the Royal Society of London* **1824**, *114*, 266–289.
- (7) Faraday, M. *Philosophical Transactions of the Royal Society of London* **1834**, *124*, 55–76.
- (8) Van 't Hoff, J., *Etudes de Dynamique Chimique*; Frederik Muller & Co.: Amsterdam, The Netherlands, 1884.
- (9) Ostwald, W. *Zeitschrift für Physikalische Chemie* **1894**, *15U*, 705–706.
- (10) Sabatier, P., *La Catalyse en Chimie Organique*; Encyclopédie de Science Chimique Appliquée; C. Béranger: Paris, Liège, 1913.
- (11) Haber, F. *Die Naturwissenschaften* **1922**, *10*, 1041–1049.
- (12) Erisman, J. W.; Sutton, M. A.; Galloway, J.; Klimont, Z.; Winiwarter, W. *Nature Geoscience* **2008**, *1*, 636–639.
- (13) Gandhi, H. S.; Piken, A. G.; Shelef, M.; Delosh, R. G. In 1976, p 760201.
- (14) Monte, R. D.; Kašpar, J. *Topics in Catalysis* **2004**, *28*, 47–57.
- (15) Nehrir, M. H.; Wang, C. In *Electric Renewable Energy Systems*; Elsevier: 2016, pp 92–113.
- (16) Badwal, S.; Foger, K. *Ceramics International* **1996**, *22*, 257–265.

- (17) Antolini, E. *Energy & Environmental Science* **2009**, 2, 915.
- (18) Rego de Vasconcelos, B.; Lavoie, J.-M. *Frontiers in Chemistry* **2019**, 7, 392.
- (19) Saint-Just, J.; Etemad, S. In *Compendium of Hydrogen Energy*; Elsevier: 2016, pp 263–287.
- (20) Yu, W.; Yu, X.; Tu, S.-T. *Energy Procedia* **2014**, 61, 2854–2857.
- (21) Steffen, P.-M.; Reinecke, E.-A.; Meynet, N.; Bentaib, A.; Chaumeix, N.; Allelein, H.-J. *Fusion Engineering and Design* **2017**, 124, 1281–1286.
- (22) Karimov, E. K.; Karimov, O. K.; Kasyanova, L. Z.; Movsumzade, E. M.; Dmitriev, Y. K. *Key Engineering Materials* **2016**, 685, 764–767.
- (23) Hübert, T.; Boon-Brett, L.; Black, G.; Banach, U. *Sensors and Actuators B: Chemical* **2011**, 157, 329–352.
- (24) Schubert, M. M.; Hackenberg, S.; van Veen, A. C.; Muhler, M.; Plzak, V.; Behm, R. *Journal of Catalysis* **2001**, 197, 113–122.
- (25) Freund, H.-J.; Bäumer, M.; Libuda, J.; Risse, T.; Rupprechter, G.; Shaikhutdinov, S. *Journal of Catalysis* **2003**, 216, 223–235.
- (26) Rupprechter, G. In *Advances in Catalysis*; Elsevier: 2007; Vol. 51, pp 133–263.
- (27) Rupprechter, G. *Catalysis Today* **2007**, 126, 3–17.
- (28) Rupprechter, G. In *Surface and Interface Science*, Wandelt, K., Ed., 1st ed.; Wiley: 2016, pp 459–528.
- (29) Langmuir, I. *Trans. Faraday Soc.* **1922**, 17, 607–620.
- (30) Livingstone, S. E., *The chemistry of ruthenium, rhodium, palladium, osmium, iridium and platinum*, Reprinted, with corr; Comprehensive inorganic chemistry Ch. 43; Pergamon Press: Oxford, 1975.
- (31) White, G. K.; Woods, S. B. *Canadian Journal of Physics* **1957**, 35, 248–257.
- (32) Heidingsfeldová, M.; Čapka, M. *Journal of Applied Polymer Science* **1985**, 30, 1837–1846.
- (33) Halligudi, S. B.; Bajaj, H. C.; Bhatt, K. N.; Krishnaratnam, M. *Reaction Kinetics & Catalysis Letters* **1992**, 48, 547–552.
- (34) Devendra, B. K.; Praveen, B.; Tripathi, V.; Nagaraju, G.; Nagaraju, D.; Nayana, K. *Inorganic Chemistry Communications* **2021**, 134, 109065.
- (35) Renner, H. et al. In *Ullmann's Encyclopedia of Industrial Chemistry*, Wiley-VCH Verlag GmbH & Co. KGaA, Ed., 1st ed.; Wiley: 2018, pp 1–73.
- (36) Amatayakul, W.; Ramnäs, O. *Journal of Cleaner Production* **2001**, 9, 395–403.
- (37) Heck, R. M.; Farrauto, R. J. *Applied Catalysis A: General* **2001**, 221, 443–457.
- (38) Castner, D.; Sexton, B.; Somorjai, G. *Surface Science* **1978**, 71, 519–540.
- (39) Ehsasi, M.; Christmann, K. *Surface Science* **1988**, 194, 172–198.

- (40) Yates, J.; Thiel, P.; Weinberg, W. *Surface Science* **1979**, *84*, 427–439.
- (41) Nichtl-Pecher, W.; Stammer, W.; Heinz, K.; Müller, K. *Physical Review B* **1991**, *43*, 6946–6951.
- (42) Payne, S.; Kreuzer, H.; Frie, W.; Hammer, L.; Heinz, K. *Surface Science* **1999**, *421*, 279–295.
- (43) Hammer, L.; Nichtl-Pecher, W.; Elbel, N.; Stammer, W.; Heinz, K.; Müller, K. *Surface Science* **1993**, 287–288, 84–88.
- (44) Matsushima, T. *Journal of Catalysis* **1984**, *85*, 98–104.
- (45) Salanov, A.; Savchenko, V. *Surface Science* **1993**, *296*, 393–399.
- (46) Schwarz, E.; Lenz, J.; Wohlgemuth, H.; Christmann, K. *Vacuum* **1990**, *41*, 167–170.
- (47) Bowker, M.; Guo, Q.; Joyner, R. *Surface Science* **1991**, *253*, 33–43.
- (48) Comelli, G.; Dhanak, V.; Kiskinova, M.; Pangher, N.; Paolucci, G.; Prince, K.; Rosei, R. *Surface Science* **1992**, *260*, 7–13.
- (49) Fisher, G. B.; Schmieg, S. J. *Journal of Vacuum Science & Technology A: Vacuum, Surfaces, and Films* **1983**, *1*, 1064–1069.
- (50) Thiel, P.; Yates, J.; Weinberg, W. *Surface Science* **1979**, *82*, 22–44.
- (51) Logan, A.; Datsy, A.; Houston, J. *Surface Science* **1991**, *245*, 280–288.
- (52) Oed, W.; Dötsch, B.; Hammer, L.; Heinz, K.; Müller, K. *Surface Science* **1988**, *207*, 55–65.
- (53) Baraldi, A.; Dhanak, V. R.; Comelli, G.; Prince, K. C.; Rosei, R. *Physical Review B* **1997**, *56*, 10511–10517.
- (54) Baraldi, A.; Cerdá, J.; Martín-Gago, J. A.; Comelli, G.; Lizzit, S.; Paolucci, G.; Rosei, R. *Physical Review Letters* **1999**, *82*, 4874–4877.
- (55) Norris, A. G.; Schedin, F.; Thornton, G.; Dhanak, V. R.; Turner, T. S.; McGrath, R. *Physical Review B* **2000**, *62*, 2113–2117.
- (56) Comelli, G.; Dhanak, V.; Kiskinova, M.; Prince, K.; Rosei, R. *Surface Science Reports* **1998**, *32*, 165–231.
- (57) Dri, C.; Africh, C.; Esch, F.; Comelli, G.; Dubay, O.; Köhler, L.; Mittendorfer, F.; Kresse, G.; Dudin, P.; Kiskinova, M. *The Journal of Chemical Physics* **2006**, *125*, 094701.
- (58) Gibson, K. D.; Viste, M.; Sanchez, E. C.; Sibener, S. J. *The Journal of Chemical Physics* **1999**, *110*, 2757–2760.
- (59) Derouin, J.; Farber, R. G.; Killelea, D. R. *The Journal of Physical Chemistry C* **2015**, *119*, 14748–14755.
- (60) Hoogers, G.; King, D. *Surface Science* **1993**, *286*, 306–316.
- (61) Belton, D. N.; Fisher, G. B.; DiMaggio, C. L. *Surface Science* **1990**, *233*, 12–26.

- (62) Leibsle, F. M.; Murray, P. W.; Francis, S. M.; Thornton, G.; Bowker, M. *Nature* **1993**, *363*, 706–709.
- (63) Dhanak, V. R.; Prince, K. C.; Rosei, R.; Murray, P. W.; Leibsle, F. M.; Bowker, M.; Thornton, G. *Physical Review B* **1994**, *49*, 5585–5590.
- (64) Dudin, P.; Barinov, A.; Gregoratti, L.; Kiskinova, M.; Esch, F.; Dri, C.; Africh, C.; Comelli, G. *The Journal of Physical Chemistry B* **2005**, *109*, 13649–13655.
- (65) Barroo, C.; Gilis, N.; Lambeets, S.; Devred, F.; Visart de Bocarmé, T. *Applied Surface Science* **2014**, *304*, 2–10.
- (66) Medvedev, V. K.; Suchorski, Y.; Voss, C.; Visart de Bocarmé, T.; Bär, T.; Kruse, N. *Langmuir* **1998**, *14*, 6151–6157.
- (67) Wider, J.; Greber, T.; Wetli, E.; Kreutz, T.; Schwaller, P.; Osterwalder, J. *Surface Science* **1998**, *417*, 301–310.
- (68) Schwegmann, S.; Over, H.; De Renzi, V.; Ertl, G. *Surface Science* **1997**, *375*, 91–106.
- (69) Peterlinz, K. A.; Sibener, S. J. *The Journal of Physical Chemistry* **1995**, *99*, 2817–2825.
- (70) Monine, M.; Schaak, A.; Rubinstein, B.; Imbihl, R.; Pismen, L. *Catalysis Today* **2001**, *70*, 321–330.
- (71) Schaak, A.; Imbihl, R. *The Journal of Chemical Physics* **2000**, *113*, 9822–9829.
- (72) Hennig, D.; Wilke, S.; Löber, R.; Methfessel, M. *Surface Science* **1993**, *287-288*, 89–93.
- (73) Löber, R.; Hennig, D. *Physical Review B* **1997**, *55*, 4761–4765.
- (74) Ferrin, P.; Kandoi, S.; Nilekar, A. U.; Mavrikakis, M. *Surface Science* **2012**, *606*, 679–689.
- (75) Gurney, B. A.; Ho, W. *The Journal of Chemical Physics* **1987**, *87*, 1376–1391.
- (76) Kiss, J.; Solymosi, F. *Surface Science* **1986**, *177*, 191–206.
- (77) Wagner, F.; Moylan, T. *Surface Science* **1987**, *191*, 121–146.
- (78) Gorodetskii, V.; Nieuwenhuys, B.; Sachtler, W.; Boreskov, G. *Applications of Surface Science* **1981**, *7*, 355–371.
- (79) Visart de Bocarmé, T.; Beketov, G.; Kruse, N. *Surface and Interface Analysis* **2004**, *36*, 522–527.
- (80) Anton, A.; Cadogan, D. C. *Surface Science* **1990**, *239*, L548–L560.
- (81) Fogelberg, J.; Petersson, L.-G. *Surface Science* **1996**, *350*, 91–102.
- (82) Zhdanov, V.; Kasemo, B. *Surface Science Reports* **1994**, *20*, 113–189.
- (83) Mikhailov, A. S., *Foundations of Synergetics I*; Haken, H., Ed.; Springer Series in Synergetics, Vol. 51; Springer Berlin Heidelberg: Berlin, Heidelberg, 1994.
- (84) Cencini, M.; Lopez, C.; Vergni, D. In *The Kolmogorov Legacy in Physics*, Beig, R. et al., Eds., Series Title: Lecture Notes in Physics; Springer Berlin Heidelberg: Berlin, Heidelberg, 2003; Vol. 636, pp 187–210.

- (85) Vogel, D.; Spiel, C.; Suchorski, Y.; Trincherro, A.; Schlögl, R.; Grönbeck, H.; Rupprechter, G. *Angewandte Chemie International Edition* **2012**, *51*, 10041–10044.
- (86) Datler, M.; Bespalov, I.; Rupprechter, G.; Suchorski, Y. *Catalysis Letters* **2015**, *145*, 1120–1125.
- (87) Suchorski, Y.; Bespalov, I.; Zeininger, J.; Raab, M.; Datler, M.; Winkler, P.; Rupprechter, G. *Catalysis Letters* **2020**, *150*, 605–612.
- (88) Bray, W. C. *Journal of the American Chemical Society* **1921**, *43*, 1262–1267.
- (89) Fechner, M. *Journal für Chemie und Physik* **1828**, *53*, 129–151.
- (90) Zaikin, A. N.; Zhabotinsky, A. M. *Nature* **1970**, *225*, 535–537.
- (91) Zhang, D.; Györgyi, L.; Peltier, W. R. *Chaos: An Interdisciplinary Journal of Nonlinear Science* **1993**, *3*, 723–745.
- (92) Hugo, P. *Berichte der Bunsengesellschaft für physikalische Chemie* **1970**, *74*, 121–127.
- (93) Hugo, P.; Jakubith, M. *Chemie Ingenieur Technik - CIT* **1972**, *44*, 383–387.
- (94) Takoudis, C. G.; Schmidt, L. D. *The Journal of Physical Chemistry* **1983**, *87*, 964–968.
- (95) Cox, M. P.; Ertl, G.; Imbihl, R. *Physical Review Letters* **1985**, *54*, 1725–1728.
- (96) Ertl, G. *Science* **1991**, *254*, 1750–1755.
- (97) Imbihl, R.; Ertl, G. *Chemical Reviews* **1995**, *95*, 697–733.
- (98) Yamamoto, S. Y.; Surko, C. M.; Maple, M. B.; Pina, R. K. *The Journal of Chemical Physics* **1995**, *102*, 8614–8625.
- (99) Imbihl, R. *Progress in Surface Science* **1993**, *44*, 185–343.
- (100) Carlsson, P.-A.; Zhdanov, V. P.; Skoglundh, M. *Physical Chemistry Chemical Physics* **2006**, *8*, 2703.
- (101) Saidi, G.; Tsotsis, T. *Surface Science* **1985**, *161*, L591–L596.
- (102) Tsai, P. *Journal of Catalysis* **1986**, *101*, 142–152.
- (103) Gorodetskii, V.; Sametova, A.; Matveev, A.; Tapilin, V. *Catalysis Today* **2009**, *144*, 219–234.
- (104) Lovis, F.; Smolinsky, T.; Locatelli, A.; Niño, M. Á.; Imbihl, R. *The Journal of Physical Chemistry C* **2012**, *116*, 4083–4090.
- (105) Smolinsky, T.; Homann, M.; Imbihl, R. *Physical Chemistry Chemical Physics* **2016**, *18*, 970–973.
- (106) Li, Y. E.; Gonzalez, R. D. *Catalysis Letters* **1988**, *1*, 229–235.
- (107) McEwen, J.-S.; Gaspard, P.; Visart de Bocarmé, T.; Kruse, N. *The Journal of Physical Chemistry C* **2009**, *113*, 17045–17058.
- (108) Suchorski, Y.; Datler, M.; Bespalov, I.; Zeininger, J.; Stöger-Pollach, M.; Bernardi, J.; Grönbeck, H.; Rupprechter, G. *Nature Communications* **2018**, *9*, 600.

- (109) Suchorski, Y.; Zeininger, J.; Buhr, S.; Raab, M.; Stöger-Pollach, M.; Bernardi, J.; Grönbeck, H.; Rupprechter, G. *Science* **2021**, *372*, 1314–1318.
- (110) Zeininger, J.; Suchorski, Y.; Raab, M.; Buhr, S.; Grönbeck, H.; Rupprechter, G. *ACS Catalysis* **2021**, *11*, 10020–10027.
- (111) Noyes, R. M. In *Temporal Order*, Haken, H., Rensing, L., Jaeger, N. I., Eds., Series Title: Springer Series in Synergetics; Springer Berlin Heidelberg: Berlin, Heidelberg, 1985; Vol. 29, pp 13–23.
- (112) Imbihl, R.; Cox, M. P.; Ertl, G.; Müller, H.; Brenig, W. *The Journal of Chemical Physics* **1985**, *83*, 1578–1587.
- (113) Suchorski, Y.; Drachsel, W.; Gorodetskii, V.; Medvedev, V.; Weiss, H. *Surface Science* **2006**, *600*, 1579–1585.
- (114) Suchorski, Y.; Datler, M.; Bespalov, I.; Zeininger, J.; Stöger-Pollach, M.; Bernardi, J.; Grönbeck, H.; Rupprechter, G. *The Journal of Physical Chemistry C* **2019**, *123*, 4217–4227.
- (115) Horn, F. J. M.; Lin, R. C. *Industrial & Engineering Chemistry Process Design and Development* **1967**, *6*, 21–30.
- (116) Wolff, J.; Papathanasiou, A. G.; Kevrekidis, I. G.; Rotermund, H. H.; Ertl, G. *Science* **2001**, *294*, 134–137.
- (117) Henrich, V. E.; Cox, P. A., *The surface science of metal oxides*, 1. ed. (with corrections) - transferred to digital printing 2000; Cambridge University Press: Cambridge, 2000.
- (118) Schmuki, P. *Journal of Solid State Electrochemistry* **2002**, *6*, 145–164.
- (119) *High-temperature solid oxide fuel cells: fundamentals, design, and applications*; Singhal, S. C., Kendall, K., Eds.; Elsevier Advanced Technology: New York, 2003.
- (120) Bowker, M. *Chemical Society Reviews* **2008**, *37*, 2204.
- (121) Dey, A. *Materials Science and Engineering: B* **2018**, *229*, 206–217.
- (122) Gabasch, H.; Knop-Gericke, A.; Schlögl, R.; Borasio, M.; Weilach, C.; Rupprechter, G.; Penner, S.; Jenewein, B.; Hayek, K.; Klötzer, B. *Physical Chemistry Chemical Physics* **2007**, *9*, 533–540.
- (123) Westerström, R.; Gustafson, J.; Resta, A.; Mikkelsen, A.; Andersen, J. N.; Lundgren, E.; Seriani, N.; Mittendorfer, F.; Schmid, M.; Klikovits, J.; Varga, P.; Ackermann, M. D.; Frenken, J. W. M.; Kasper, N.; Stierle, A. *Physical Review B* **2007**, *76*, 155410.
- (124) Blomberg, S.; Westerström, R.; Martin, N.; Lundgren, E.; Andersen, J.; Messing, M.; Gustafson, J. *Surface Science* **2014**, *628*, 153–158.
- (125) Lundgren, E.; Kresse, G.; Klein, C.; Borg, M.; Andersen, J. N.; De Santis, M.; Gauthier, Y.; Konvicka, C.; Schmid, M.; Varga, P. *Physical Review Letters* **2002**, *88*, 246103.
- (126) Gustafson, J.; Mikkelsen, A.; Borg, M.; Lundgren, E.; Köhler, L.; Kresse, G.; Schmid, M.; Varga, P.; Yuhara, J.; Torrelles, X.; Quirós, C.; Andersen, J. N. *Physical Review Letters* **2004**, *92*, 126102.



- (127) Gustafson, J.; Mikkelsen, A.; Borg, M.; Andersen, J. N.; Lundgren, E.; Klein, C.; Hofer, W.; Schmid, M.; Varga, P.; Köhler, L.; Kresse, G.; Kasper, N.; Stierle, A.; Dosch, H. *Physical Review B* **2005**, *71*, 115442.
- (128) Mittendorfer, F. *Journal of Physics: Condensed Matter* **2010**, *22*, 393001.
- (129) Flege, J. I.; Hrbek, J.; Sutter, P. *Physical Review B* **2008**, *78*, 165407.
- (130) Lundgren, E.; Mikkelsen, A.; Andersen, J. N.; Kresse, G.; Schmid, M.; Varga, P. *Journal of Physics: Condensed Matter* **2006**, *18*, R481–R499.
- (131) Diebold, U.; Li, S.-C.; Schmid, M. *Annual Review of Physical Chemistry* **2010**, *61*, 129–148.
- (132) Blomberg, S.; Lundgren, E.; Westerström, R.; Erdogan, E.; Martin, N.; Mikkelsen, A.; Andersen, J.; Mittendorfer, F.; Gustafson, J. *Surface Science* **2012**, *606*, 1416–1421.
- (133) Mittendorfer, F.; Franz, T.; Klikovits, J.; Schmid, M.; Merte, L. R.; Shah Zaman, S.; Varga, P.; Westerström, R.; Resta, A.; Andersen, J. N.; Gustafson, J.; Lundgren, E. *The Journal of Physical Chemistry Letters* **2011**, *2*, 2747–2751.
- (134) Africh, C.; Esch, F.; Li, W. X.; Corso, M.; Hammer, B.; Rosei, R.; Comelli, G. *Physical Review Letters* **2004**, *93*, 126104.
- (135) Klikovits, J.; Schmid, M.; Merte, L. R.; Varga, P.; Westerström, R.; Resta, A.; Andersen, J. N.; Gustafson, J.; Mikkelsen, A.; Lundgren, E.; Mittendorfer, F.; Kresse, G. *Physical Review Letters* **2008**, *101*, 266104.
- (136) Farber, R. G.; Turano, M. E.; Oskorep, E. C. N.; Wands, N. T.; Iski, E. V.; Killelea, D. R. *The Journal of Physical Chemistry C* **2017**, *121*, 10470–10475.
- (137) Kellogg, G. *Surface Science* **1986**, *171*, 359–376.
- (138) Tolia, A.; Smiley, R.; Delgass, W.; Takoudis, C.; Weaver, M. *Journal of Catalysis* **1994**, *150*, 56–70.
- (139) Kibis, L. S.; Stadnichenko, A. I.; Koscheev, S. V.; Zaikovskii, V. I.; Boronin, A. I. *The Journal of Physical Chemistry C* **2016**, *120*, 19142–19150.
- (140) Ahmadi, M.; Mistry, H.; Roldan Cuenya, B. *The Journal of Physical Chemistry Letters* **2016**, *7*, 3519–3533.
- (141) Barbero, J. *Catalysis Letters* **2003**, *87*, 211–218.
- (142) Campbell, C. T. *Accounts of Chemical Research* **2013**, *46*, 1712–1719.
- (143) Claeys, M.; Dry, M. E.; van Steen, E.; van Berge, P. J.; Booyens, S.; Crous, R.; van Helden, P.; Labuschagne, J.; Moodley, D. J.; Saib, A. M. *ACS Catalysis* **2015**, *5*, 841–852.
- (144) Farmer, J. A.; Campbell, C. T. *Science* **2010**, *329*, 933–936.
- (145) Luches, P.; Pagliuca, F.; Valeri, S.; Illas, F.; Preda, G.; Pacchioni, G. *The Journal of Physical Chemistry C* **2012**, *116*, 1122–1132.
- (146) Matos, J.; Ono, L. K.; Behafarid, F.; Croy, J. R.; Mostafa, S.; DeLaRiva, A. T.; Datye, A. K.; Frenkel, A. I.; Roldan Cuenya, B. *Physical Chemistry Chemical Physics* **2012**, *14*, 11457.

- (147) Novotný, Z.; Argentero, G.; Wang, Z.; Schmid, M.; Diebold, U.; Parkinson, G. S. *Physical Review Letters* **2012**, *108*, 216103.
- (148) Brune, H.; Bromann, K.; Röder, H.; Kern, K.; Jacobsen, J.; Stoltze, P.; Jacobsen, K.; No/rskov, J. *Physical Review B* **1995**, *52*, R14380–R14383.
- (149) Henry, C. R. *Progress in Surface Science* **2005**, *80*, 92–116.
- (150) Pedersen, M.; Helveg, S.; Ruban, A.; Stensgaard, I.; Lægsgaard, E.; Nørskov, J.; Besenbacher, F. *Surface Science* **1999**, *426*, 395–409.
- (151) Günter, M.; Ressler, T.; Bems, B.; Büscher, C.; Genger, T.; Hinrichsen, O.; Muhler, M.; Schlögl, R. *Catalysis Letters* **2001**, *71*, 37–44.
- (152) Yudanov, I. V.; Genest, A.; Schauer mann, S.; Freund, H.-J.; Rösch, N. *Nano Letters* **2012**, *12*, 2134–2139.
- (153) Müller, P.; Kern, R. *Surface Science* **2000**, *457*, 229–253.
- (154) Iddir, H.; Komanicky, V.; Ögüt, S.; You, H.; Zapol, P. *The Journal of Physical Chemistry C* **2007**, *111*, 14782–14789.
- (155) Bruix, A.; Rodriguez, J. A.; Ramírez, P. J.; Senanayake, S. D.; Evans, J.; Park, J. B.; Stacchiola, D.; Liu, P.; Hrbek, J.; Illas, F. *Journal of the American Chemical Society* **2012**, *134*, 8968–8974.
- (156) Yang, X.; Kattel, S.; Senanayake, S. D.; Boscoboinik, J. A.; Nie, X.; Graciani, J.; Rodriguez, J. A.; Liu, P.; Stacchiola, D. J.; Chen, J. G. *Journal of the American Chemical Society* **2015**, *137*, 10104–10107.
- (157) Roberts, S.; Gorte, R. J. *The Journal of Chemical Physics* **1990**, *93*, 5337–5344.
- (158) Harding, C.; Habibpour, V.; Kunz, S.; Farnbacher, A. N.-S.; Heiz, U.; Yoon, B.; Landman, U. *Journal of the American Chemical Society* **2009**, *131*, 538–548.
- (159) Shao, X.; Prada, S.; Giordano, L.; Pacchioni, G.; Nilus, N.; Freund, H.-J. *Angewandte Chemie International Edition* **2011**, *50*, 11525–11527.
- (160) Roldán, A.; Ricart, J. M.; Illas, F.; Pacchioni, G. *The Journal of Physical Chemistry C* **2010**, *114*, 16973–16978.
- (161) Hu, C. H.; Chizallet, C.; Mager-Maury, C.; Corral-Valero, M.; Sautet, P.; Toulhoat, H.; Raybaud, P. *Journal of Catalysis* **2010**, *274*, 99–110.
- (162) Lykhach, Y.; Kozlov, S. M.; Skála, T.; Tovt, A.; Stetsovych, V.; Tsud, N.; Dvořák, F.; Johánek, V.; Neitzel, A.; Mysliveček, J.; Fabris, S.; Matolín, V.; Neyman, K. M.; Libuda, J. *Nature Materials* **2016**, *15*, 284–288.
- (163) Tauster, S. J.; Fung, S. C.; Garten, R. L. *Journal of the American Chemical Society* **1978**, *100*, 170–175.
- (164) Tauster, S. J. *Accounts of Chemical Research* **1987**, *20*, 389–394.
- (165) Tauster, S. J.; Fung, S. C.; Baker, R. T. K.; Horsley, J. A. *Science* **1981**, *211*, 1121–1125.
- (166) Dallagnol, C. *Journal of Catalysis* **1985**, *96*, 106–114.

- (167) Bennett, R.; Stone, P.; Bowker, M. *Catalysis Letters* **1999**, *59*, 99–105.
- (168) Caballero, A.; Holgado, J. P.; Gonzalez-de-laCruz, V. M.; Habas, S. E.; Herranz, T.; Salmeron, M. *Chemical Communications* **2010**, *46*, 1097–1099.
- (169) Linsmeier, C.; Taglauer, E. *Applied Catalysis A: General* **2011**, *391*, 175–186.
- (170) Hardacre, C.; Ormerod, R. M.; Lambert, R. M. *The Journal of Physical Chemistry* **1994**, *98*, 10901–10905.
- (171) Sun, Y.-N.; Qin, Z.-H.; Lewandowski, M.; Carrasco, E.; Sterrer, M.; Shaikhutdinov, S.; Freund, H.-J. *Journal of Catalysis* **2009**, *266*, 359–368.
- (172) Senanayake, S. D.; Ramírez, P. J.; Waluyo, I.; Kundu, S.; Mudiyansele, K.; Liu, Z.; Liu, Z.; Axnanda, S.; Stacchiola, D. J.; Evans, J.; Rodriguez, J. A. *The Journal of Physical Chemistry C* **2016**, *120*, 1778–1784.
- (173) Carrero, A.; Calles, J.; Vizcaíno, A. *Chemical Engineering Journal* **2010**, *163*, 395–402.
- (174) Ciambelli, P.; Palma, V.; Ruggiero, A. *Applied Catalysis B: Environmental* **2010**, *96*, 18–27.
- (175) Choong, C. K.; Zhong, Z.; Huang, L.; Wang, Z.; Ang, T. P.; Borgna, A.; Lin, J.; Hong, L.; Chen, L. *Applied Catalysis A: General* **2011**, *407*, 145–154.
- (176) Teichner, S. J. *Applied Catalysis* **1990**, *62*, 1–10.
- (177) Conner, W. C.; Falconer, J. L. *Chemical Reviews* **1995**, *95*, 759–788.
- (178) Rozanov, V. V.; Krylov, O. V. *Russian Chemical Reviews* **1997**, *66*, 107–119.
- (179) Wang, J. B.; Tai, Y.-L.; Dow, W.-P.; Huang, T.-J. *Applied Catalysis A: General* **2001**, *218*, 69–79.
- (180) Xu, W.; Liu, Z.; Johnston-Peck, A. C.; Senanayake, S. D.; Zhou, G.; Stacchiola, D.; Stach, E. A.; Rodriguez, J. A. *ACS Catalysis* **2013**, *3*, 975–984.
- (181) Remediakis, I. N.; Lopez, N.; Nørskov, J. K. *Angewandte Chemie International Edition* **2005**, *44*, 1824–1826.
- (182) Behrens, M.; Studt, F.; Kasatkin, I.; Kühn, S.; Hävecker, M.; Abild-Pedersen, F.; Zander, S.; Girgsdies, F.; Kurr, P.; Knief, B.-L.; Tovar, M.; Fischer, R. W.; Nørskov, J. K.; Schlögl, R. *Science* **2012**, *336*, 893–897.
- (183) Shi, J.; Li, H.; Genest, A.; Zhao, W.; Qi, P.; Wang, T.; Rupprechter, G. *Applied Catalysis B: Environmental* **2022**, *301*, 120789.
- (184) Ono, L. K.; Behafarid, F.; Cuenya, B. R. *ACS Nano* **2013**, *7*, 10327–10334.
- (185) Bliem, R.; van der Hoeven, J.; Zavodny, A.; Gamba, O.; Pavelec, J.; de Jongh, P. E.; Schmid, M.; Diebold, U.; Parkinson, G. S. *Angewandte Chemie International Edition* **2015**, *54*, 13999–14002.
- (186) Hertz, H. *Annalen der Physik und Chemie* **1887**, *267*, 983–1000.
- (187) Hallwachs, W. *Annalen der Physik und Chemie* **1888**, *269*, 301–312.

- (188) Einstein, A. *Annalen der Physik* **1905**, 322, 132–148.
- (189) Reilman, R. F.; Msezane, A.; Manson, S. T. *Journal of Electron Spectroscopy and Related Phenomena* **1976**, 8, 389–394.
- (190) Seah, M. P.; Dench, W. A. *Surface and Interface Analysis* **1979**, 1, 2–11.
- (191) Innes, P. *Proceedings of the Royal Society of London. Series A, Containing Papers of a Mathematical and Physical Character* **1907**, 79, 442–462.
- (192) Nordling, C.; Sokolowski, E.; Siegbahn, K. *Physical Review* **1957**, 105, 1676–1677.
- (193) Caciuffo, R.; Melone, S.; Rustichelli, F.; Boeuf, A. *Physics Reports* **1987**, 152, 1–71.
- (194) Bubert, H.; Rivière, J. C.; Werner, W. S. M. In *Surface and Thin Film Analysis*, Friedbacher, G., Bubert, H., Eds., 1st ed.; Wiley: 2011, pp 7–41.
- (195) Casalis, L. et al. *Review of Scientific Instruments* **1995**, 66, 4870–4875.
- (196) Zeller, P.; Amati, M.; Sezen, H.; Scardamaglia, M.; Struzzi, C.; Bittencourt, C.; Lantz, G.; Hajlaoui, M.; Papalazarou, E.; Marino, M.; Fanetti, M.; Ambrosini, S.; Rubini, S.; Gregoratti, L. *physica status solidi (a)* **2018**, 215, 1800308.
- (197) Gregoratti, L.; Barinov, A.; Benfatto, E.; Cautero, G.; Fava, C.; Lacovig, P.; Lonza, D.; Kiskinova, M.; Tommasini, R.; Mähl, S.; Heichler, W. *Review of Scientific Instruments* **2004**, 75, 64–68.
- (198) Amati, M.; Aleman, B.; Bozzini, B.; Gregoratti, L.; Sezen, H.; Kiskinova, M. *Surface Science* **2016**, 652, 20–25.
- (199) *Der lichtelektrische Effekt und seine Anwendungen*; Simon, H., Suhrmann, R., Eds.; Springer Berlin Heidelberg: Berlin, Heidelberg, 1958.
- (200) Brüche, E. *Zeitschrift für Physik* **1933**, 86, 448–450.
- (201) Engel, W.; Kordesch, M.; Rotermund, H.; Kubala, S.; von Oertzen, A. *Ultramicroscopy* **1991**, 36, 148–153.
- (202) Rotermund, H.; Nettesheim, S.; von Oertzen, A.; Ertl, G. *Surface Science* **1992**, 275, L645–L649.
- (203) Rotermund, H. *Surface Science* **1993**, 283, 87–100.
- (204) Ehsasi, M.; Seidel, C.; Ruppender, H.; Drachsel, W.; Block, J.; Christmann, K. *Surface Science Letters* **1989**, 210, L198–L208.
- (205) Kordesch, M. E.; Engel, W.; Zeitler, E.; Bradshaw, A. M. *Journal of Physics: Condensed Matter* **1989**, 1, SB1–SB6.
- (206) Rotermund, H. H.; Engel, W.; Kordesch, M.; Ertl, G. *Nature* **1990**, 343, 355–357.
- (207) Ertl, G. *Angewandte Chemie International Edition* **2008**, 47, 3524–3535.
- (208) Bauer, E.; Mundschau, M.; Swiech, W.; Teliëps, W. *Ultramicroscopy* **1989**, 31, 49–57.
- (209) Teliëps, W.; Bauer, E. *Ultramicroscopy* **1985**, 17, 57–65.
- (210) Mundschau, M.; Bauer, E.; Świech, W. *Journal of Applied Physics* **1989**, 65, 581–584.

- (211) Fink, R. et al. *Journal of Electron Spectroscopy and Related Phenomena* **1997**, *84*, 231–250.
- (212) Wichtendahl, R. et al. *Surface Review and Letters* **1998**, *05*, 1249–1256.
- (213) Rausenberger, B.; Świech, W.; Engel, W.; Bradshaw, A.; Zeitler, E. *Surface Science* **1993**, 287–288, 235–240.
- (214) Schmidt, T.; Marchetto, H.; Lévesque, P.; Groh, U.; Maier, F.; Preikszas, D.; Hartel, P.; Spehr, R.; Lilienkamp, G.; Engel, W.; Fink, R.; Bauer, E.; Rose, H.; Umbach, E.; Freund, H.-J. *Ultramicroscopy* **2010**, *110*, 1358–1361.
- (215) Schmidt, T.; Sala, A.; Marchetto, H.; Umbach, E.; Freund, H.-J. *Ultramicroscopy* **2013**, *126*, 23–32.
- (216) Dingley, D. J.; Baba-Kishi, K. Z.; Randle, V., *Atlas of backscattering Kikuchi diffraction patterns*; Microscopy in materials science series; Institute of Physics Pub: Bristol, Eng.; Philadelphia, Pa, 1995.
- (217) Baba-Kishi, K. Z. *Journal of Materials Science* **2002**, *37*, 1715–1746.
- (218) Nishikawa, S.; Kikuchi, S. *Nature* **1928**, *121*, 1019–1020.
- (219) Krieger Lassen, N. C.; Juul Jensen, D.; Conradsen, K. *Scanning Microscopy* **1992**, *6*, 115–121.
- (220) Alam, M.; Blackman, M.; Pashley, D. *Proceedings of the Royal Society of London. Series A. Mathematical and Physical Sciences* **1954**, *221*, 224–242.
- (221) Venables, J. A.; Harland, C. J. *Philosophical Magazine* **1973**, *27*, 1193–1200.
- (222) Venables, J. A.; Bin-jaya, R. *The Philosophical Magazine: A Journal of Theoretical Experimental and Applied Physics* **1977**, *35*, 1317–1332.
- (223) Harland, C. J.; Akhter, P.; Venables, J. A. *Journal of Physics E: Scientific Instruments* **1981**, *14*, 175–182.
- (224) Baba-Kishi, K. Z.; Dingley, D. J. *Scanning* **1989**, *11*, 305–312.
- (225) Wright, S. I.; Adams, B. L. *Metallurgical Transactions A* **1992**, *23*, 759–767.
- (226) Dingley, D. J.; Randle, V. *Journal of Materials Science* **1992**, *27*, 4545–4566.
- (227) *Electron Backscatter Diffraction in Materials Science*; Schwartz, A. J., Kumar, M., Adams, B. L., Field, D. P., Eds.; Springer US: Boston, MA, 2009.
- (228) König, U.; Davepon, B. *Electrochimica Acta* **2001**, *47*, 149–160.
- (229) Vogel, D.; Spiel, C.; Schmid, M.; Stöger-Pollach, M.; Schlögl, R.; Suchorski, Y.; Rupprechter, G. *The Journal of Physical Chemistry C* **2013**, *117*, 12054–12060.
- (230) Weatherup, R. S.; Shahani, A. J.; Wang, Z.-J.; Mingard, K.; Pollard, A. J.; Willinger, M.-G.; Schloegl, R.; Voorhees, P. W.; Hofmann, S. *Nano Letters* **2016**, *16*, 6196–6206.
- (231) Johansson, M.; Hoffmann Jørgensen, J.; Chorkendorff, I. *Review of Scientific Instruments* **2004**, *75*, 2082–2093.

- (232) Kraemer, K.; Menzel, D. *Berichte der Bunsengesellschaft für physikalische Chemie* **1975**, *79*, 649–653.
- (233) Suchorski, Y.; Rupprechter, G. *Surface Science* **2016**, *643*, 52–58.
- (234) Suchorski, Y.; Rupprechter, G. *Topics in Catalysis* **2020**, *63*, 1532–1544.
- (235) Vogel, D.; Spiel, C.; Suchorski, Y.; Urich, A.; Schlögl, R.; Rupprechter, G. *Surface Science* **2011**, *605*, 1999–2005.
- (236) Datler, M.; Bepalov, I.; Buhr, S.; Zeininger, J.; Stöger-Pollach, M.; Bernardi, J.; Rupprechter, G.; Suchorski, Y. *Catalysis Letters* **2016**, *146*, 1867–1874.
- (237) Ertl, G. *Topics in Catalysis* **1994**, *1*, 305–314.
- (238) King, D. A. *Surface Science* **1994**, *299-300*, 678–689.
- (239) Somorjai, G. A. *Annual Review of Physical Chemistry* **1994**, *45*, 721–751.
- (240) Suchorski, Y.; Rupprechter, G. *Catalysis Letters* **2018**, *148*, 2947–2956.
- (241) Sander, M.; Bassett, M.; Imbihl, R.; Ertl, G. *Vacuum* **1990**, *41*, 272–274.
- (242) Ortega, J. E.; Vasseur, G.; Piquero-Zulaica, I.; Matencio, S.; Valbuena, M. A.; Rault, J. E.; Schiller, F.; Corso, M.; Mugarza, A.; Lobo-Checa, J. *New Journal of Physics* **2018**, *20*, 073010.
- (243) Lawton, T.; Pushkarev, V.; Broitman, E.; Reinicker, A.; Sykes, E.; Gellman, A. *The Journal of Physical Chemistry C* **2012**, *116*, 16054–16062.
- (244) De Alwis, A.; Holsclaw, B.; Pushkarev, V.; Reinicker, A.; Lawton, T.; Blecher, M.; Sykes, E.; Gellman, A. *Surface Science* **2013**, *608*, 80–87.
- (245) Suchorski, Y.; Kozlov, S. M.; Bepalov, I.; Datler, M.; Vogel, D.; Budinska, Z.; Neyman, K. M.; Rupprechter, G. *Nature Materials* **2018**, *17*, 519–522.
- (246) Suchorski, Y.; Datler, M.; Bepalov, I.; Freytag, C.; Zeininger, J.; Rupprechter, G. *Surface Science* **2019**, *679*, 163–168.
- (247) Brückner, A. *Catalysis Reviews* **2003**, *45*, 97–150.
- (248) Tinnemans, S. J.; Mesu, J. G.; Kervinen, K.; Visser, T.; Nijhuis, T. A.; Beale, A. M.; Keller, D. E.; van der Eerden, A. M.; Weckhuysen, B. M. *Catalysis Today* **2006**, *113*, 3–15.
- (249) Iglesias-Juez, A.; Beale, A. M.; Maaijen, K.; Weng, T. C.; Glatzel, P.; Weckhuysen, B. M. *Journal of Catalysis* **2010**, *276*, 268–279.
- (250) Osborn, M.; Webster, R.; Weber, K. *Journal of Cell Biology* **1978**, *77*, R27.
- (251) Webster, R. E.; Osborn, M.; Weber, K. *Experimental Cell Research* **1978**, *117*, 47–61.
- (252) Jun, S.; Ro, H.-J.; Bharda, A.; Kim, S. I.; Jeoung, D.; Jung, H. S. *The Protein Journal* **2019**, *38*, 609–615.
- (253) Carlson, D. B.; Gelb, J.; Palshin, V.; Evans, J. E. *Microscopy and Microanalysis* **2013**, *19*, 22–29.

- (254) Odermatt, P. D.; Shivanandan, A.; Deschout, H.; Jankele, R.; Nievergelt, A. P.; Feletti, L.; Davidson, M. W.; Radenovic, A.; Fantner, G. E. *Nano Letters* **2015**, *15*, 4896–4904.
- (255) Povstugar, I.; Weber, J.; Naumenko, D.; Huang, T.; Klinkenberg, M.; Quadackers, W. J. *Microscopy and Microanalysis* **2019**, *25*, 11–20.
- (256) Albu, M.; Fitzek, H.; Moser, D.; Kothleitner, G.; Hofer, F. *Frontiers in Astronomy and Space Sciences* **2020**, *7*, 544331.
- (257) Fitzek, H.; Wewerka, K.; Schmidt, U.; Schröttner, H.; Zankel, A. *Micron* **2021**, *143*, 103029.
- (258) Weckhuysen, B. M. *Angewandte Chemie International Edition* **2009**, *48*, 4910–4943.
- (259) Schmidt, J. E.; Ye, X.; van Ravenhorst, I. K.; Oord, R.; Shapiro, D. A.; Yu, Y.-S.; Bare, S. R.; Meirer, F.; Poplawsky, J. D.; Weckhuysen, B. M. *ChemCatChem* **2019**, *11*, 488–494.
- (260) Schweinar, K.; Nicholls, R. L.; Rajamathi, C. R.; Zeller, P.; Amati, M.; Gregoratti, L.; Raabe, D.; Greiner, M.; Gault, B.; Kasian, O. *Journal of Materials Chemistry A* **2020**, *8*, 388–400.
- (261) Gambino, M.; Nieuwelink, A.; Reints, F.; Veselý, M.; Filez, M.; Ferreira Sanchez, D.; Grolimund, D.; Nesterenko, N.; Minoux, D.; Meirer, F.; Weckhuysen, B. *Journal of Catalysis* **2021**, *404*, 634–646.
- (262) Hendriks, F. C.; Mohammadian, S.; Ristanović, Z.; Kalirai, S.; Meirer, F.; Vogt, E. T. C.; Bruijninx, P. C. A.; Gerritsen, H. C.; Weckhuysen, B. M. *Angewandte Chemie International Edition* **2018**, *57*, 257–261.
- (263) Marbach, H.; Lilienkamp, G.; Wei, H.; Günther, S.; Suchorski, Y.; Imbihl, R. *Physical Chemistry Chemical Physics* **2003**, *5*, 2730–2735.
- (264) Günther, S.; Liu, H.; Menteş, T. O.; Locatelli, A.; Imbihl, R. *Physical Chemistry Chemical Physics* **2013**, *15*, 8752.
- (265) Marbach, H.; Günther, S.; Neubrand, T.; Imbihl, R. *Chemical Physics Letters* **2004**, *395*, 64–69.
- (266) Lilienkamp, G.; Wei, H.; Maus-Friedrichs, W.; Kempter, V.; Marbach, H.; Günther, S.; Suchorski, Y. *Surface Science* **2003**, *532-535*, 132–136.
- (267) Besenbacher, F.; Chorkendorff, I.; Clausen, B. S.; Hammer, B.; Molenbroek, A. M.; Nørskov, J. K.; Stensgaard, I. *Science* **1998**, *279*, 1913–1915.





# CURRICULUM VITAE

Dipl.-Ing. Philipp Winkler, BSc

---

## PERSONAL DATA

Address TU Wien  
Institute of Materials Chemistry  
Getreidemarkt 9  
1060 Vienna  
Austria

Phone +43 (0) 1 58801 165143

E-Mail philipp.winkler@tuwien.ac.at

Date and place of birth 9<sup>th</sup> of January, 1994 in Vienna, Austria

Nationality Austrian

## OVERVIEW

Trained in materials science, experience in UV and x-ray photoemission electron microscopy (UV-/X-PEEM), X-ray photoelectron spectroscopy (XPS), scanning photoelectron microscopy (SPEM), low energy electron microscopy (LEEM), field electron emission microscopy (FEM) and field ion microscopy (FIM). Proficient in development of customized experimental equipment, microcontroller programming (C/C++) and MATLAB.

## RESEARCH INTERESTS

Interested in catalysis on the  $\mu\text{m}$ - and  $\text{nm}$ -scales, spatiotemporal pattern formation in catalytic surface reactions, study of catalytic model systems, *in situ* reaction imaging (UV-/X-PEEM, SPEM, LEEM, FEM, FIM) and surface analysis (SPEM, XPS).

---

## EDUCATION

Since Jan. 2019 Doctoral programme in Technical Sciences, Chemistry  
TU Wien, Austria

Dec. 2018 MSc in Technical Chemistry, with distinction  
TU Wien, Austria  
*Thesis:* "Instability phenomena in catalytic hydrogen oxidation studied on a nano-scale by a field electron microscope"  
*Advisor:* Prof. Yuri Suchorski

Oct. 2016 BSc in Technical Chemistry  
TU Wien, Austria

Jun. 2012 Matura, with distinction (equivalent to British A-Levels)  
Sir Karl Popper Schule am Wiedner Gymnasium, Vienna, Austria

## RESEARCH EXPERIENCE

- Since Jan. 2019                      University assistant in the group of Profs. Rupprechter/Suchorski  
Institute of Materials Chemistry, TU Wien, Austria
- Dec. 2016 - Dec. 2018              Trainee in the group of Prof. Suchorski  
Institute of Materials Chemistry, TU Wien, Austria

## TEACHING EXPERIENCE

- Fall 2020 - Fall 2022                  Undergraduate Teaching Assistant, TU Wien, Austria  
*Course: Physical Chemistry II, Lecture*
- Fall 2019 - Fall 2022                  Undergraduate Teaching Assistant, TU Wien, Austria  
*Course: Physical Chemistry, Laboratory Course*
- Spring 2019                              Undergraduate Teaching Assistant, TU Wien, Austria  
*Course: Fundamentals of Chemistry, Laboratory Course*  
co-supervision of undergraduate students (3 interns, 1 Bachelor student)

## OTHER SKILLS

### LANGUAGES

- German                                      Native language
- English                                      Advanced (CEFRL scale)
- Spanish                                      Intermediate (CEFRL scale)

### TECHNICAL SKILLS

- C/C++ programming                  Advanced
- MATLAB programming                Advanced
- Adobe Creative Suite: Illustrator, InDesign, Photoshop
- Development of microcontroller-based specialized experimental equipment

## LIST OF PUBLICATIONS

### PUBLICATIONS IN SCIENTIFIC JOURNALS

1. P. Winkler, M. Raab, J. Zeininger, L.M. Rois, Y. Suchorski, M. Stöger-Pollach, M. Amati, R. Parmar, L. Gregoratti, G. Rupprechter\*:  
*“Imaging interface and particle size effects by in situ correlative microscopy of a catalytic reaction”*  
Nature Communications (2022), submitted
2. J. Zeininger<sup>†</sup>, P. Winkler<sup>†</sup>, M. Raab, Y. Suchorski, M.J. Prieto, L.C. Tănase, L. de Souza Caldas, A. Tiwari, T. Schmidt, M. Stöger-Pollach, A. Steiger-Thirsfeld, B. Roldan Cuenya, G. Rupprechter\*:  
*“Pattern Formation in Catalytic H<sub>2</sub> Oxidation on Rh: Zooming in by Correlative Microscopy”*  
ACS Catalysis **12** (2022) 11974

3. P. Winkler, J. Zeininger, M. Raab, Y. Suchorski, A. Steiger-Thirsfeld, M. Stöger-Pollach, M. Amati, L. Gregoratti, H. Grönbeck, G. Rupprechter\*:  
*“Coexisting multi-states in catalytic hydrogen oxidation on rhodium”*  
 Nature Communications **12** (2021) 6517
4. P. Winkler, J. Zeininger, Y. Suchorski, M. Stöger-Pollach, P. Zeller, M. Amati, L. Gregoratti, G. Rupprechter\*:  
*“How the anisotropy of surface oxide formation influences the transient activity of a surface reaction”*  
 Nature Communications **12** (2021) 69
5. Y. Suchorski, I. Bepalov, J. Zeininger, M. Raab, M. Datler, P. Winkler, G. Rupprechter\*:  
*“CO oxidation on stepped Rh surfaces:  $\mu\text{m}$ -scale versus nanoscale”*  
 Catalysis Letters **150** (2020) 605
6. P. Winkler, J. Zeininger, M. Raab, G. Rupprechter, Y. Suchorski\*:  
*“A novel wireless sample temperature control system for field ion, field electron and atom probe techniques”*  
 Review of Scientific Instruments **91** (2020) 013705
7. L. Felgitsch, P. Baloh, J. Burkart, M. Mayr, E. Momken, T.M. Seifried, P. Winkler, D. G. Schmale III, H. Grothe\*:  
*“Birch leaves and branches as a source of ice-nucleating macromolecules”*  
 Atmospheric Chemistry and Physics **18** (2018) 16063

## ORAL COMMUNICATIONS

1. P. Winkler, J. Zeininger, M. Stöger-Pollach, J. Bernardi, P. Zeller, M. Amati, L. Gregoratti, Y. Suchorski, G. Rupprechter\*:  
*“Structure dependence of the initial oxidation of Rh and its effect on catalytic H<sub>2</sub> oxidation”*  
 Symposium on Surface Science 2020, St. Christoph am Arlberg, Austria; 01.-07.03.2020
2. C. Freytag\*, P. Winkler, G. Rupprechter, Y. Suchorski:  
*“Catalytic hydrogen oxidation on metallic, oxidized and oxide supported Rh surfaces”*  
 2<sup>nd</sup> FemChem Scientific Workshop, Vienna, Austria; 04.10.2019
3. M. Trzcinski\*, P. Winkler, C. Freytag, A. Bukaluk, G. Rupprechter, Y. Suchorski:  
*“Structure sensitivity of the initial oxidation of Rh: XPS and PEEM studies”*  
 9<sup>th</sup> International Workshop on Surface Physics, Trzebnica, Poland; 24.-28.06.2019
4. P. Winkler\*, C. Freytag, M. Trzcinski, A. Bukaluk, M. Stöger-Pollach, J. Bernardi, G. Rupprechter, Y. Suchorski:  
*“Structure dependent initial oxidation of rhodium: XPS and PEEM studies”*  
 8<sup>th</sup> Annual FOXSI PhD Workshop, Haus im Ennstal, Austria; 20.-23.03.2019
5. A. Bukaluk\*, M. Trzcinski, P. Winkler, C. Freytag, G. Rupprechter, Y. Suchorski:  
*“Orientation dependent oxidation of rhodium: XPS and PEEM studies”*  
 International Conference on Catalysis and Surface Chemistry, Kraków, Poland; 18.-23.03.2018

6. J. Zeininger\*, S. Buhr, P. Winkler, G. Rupprechter, Y. Suchorski:  
*"Hydrogen oxidation on a  $\mu$ m-sized curved rhodium crystal"*  
 7<sup>th</sup> Annual FOXSI PhD Workshop, Haus im Ennstal, Austria; 31.01.-03.02.2018

## POSTER PRESENTATIONS

1. P. Winkler, J. Zeininger, M. Raab, Y. Suchorski, A. Steiger-Thirsfeld, M. Stöger-Pollach, M. Amati, L. Gregoratti, H. Grönbeck, G. Rupprechter\*:  
*"In-Situ Imaging of Multi-States in a Catalytic Surface Reaction"*  
 Photoelectron spectroscopy and the future of surface analysis: Faraday Discussion, London, United Kingdom; 20.04.2022 - 22.04.2022
2. P. Winkler\*, J. Zeininger, M. Raab, Y. Suchorski, A. Steiger-Thirsfeld, M. Stöger-Pollach, G. Rupprechter:  
*"Anisotropic surface oxide formation and its role in the catalytic hydrogen oxidation on Rh"*  
 TAming COmplexity in Materials Modeling (TACO) - 1<sup>st</sup> Annual PhD Workshop, Schladming, Austria; 03.04.2022 - 06.04.2022.
3. M. Raab\*, J. Zeininger, P. Winkler, G. Rupprechter, Y. Suchorski:  
*"Kinetic instabilities in  $H_2$  oxidation on Rh: chaos on a nm-scale"*  
 International FOXSI Conference 2019, Vienna, Austria; 04.-06.12.2019
4. P. Winkler\*, C. Freytag, J. Zeininger, M. Stöger-Pollach, J. Bernardi, G. Rupprechter, Y. Suchorski:  
*"Hydrogen oxidation on rhodium: metallic surface versus surface oxide"*  
 International FOXSI Conference 2019, Vienna, Austria; 04.-06.12.2019
5. P. Winkler\*, J. Zeininger, M. Raab, G. Rupprechter, Y. Suchorski:  
*"Nanoscale model catalytic studies in UHV: bridging the high voltage gap"*  
 11<sup>th</sup> Symposium on Vacuum based Science and Technology, Kolobrzeg, Poland; 19.-21.11.2019
6. J. Zeininger\*, M. Raab, P. Winkler, G. Rupprechter, Y. Suchorski:  
*"Nanoscale model catalytic studies in UHV: contribution to bridging the materials gap"*  
 11<sup>th</sup> Symposium on Vacuum based Science and Technology, Kolobrzeg, Poland; 19.-21.11.2019
7. C. Freytag\*, P. Winkler, M. Trzcinski, A. Bukaluk, J. Zeininger, G. Rupprechter, Y. Suchorski:  
*"Hydrogen oxidation on partially oxidized Rh: in situ PEEM studies"*  
 8<sup>th</sup> Annual FOXSI PhD Workshop, Haus im Ennstal, Austria; 20.-23.03.2019
8. M. Raab\*, J. Zeininger, P. Winkler, G. Rupprechter, Y. Suchorski:  
*"Kinetic instabilities in  $H_2$  oxidation on Rh: road to chaos"*  
 8<sup>th</sup> Annual FOXSI PhD Workshop, Haus im Ennstal, Austria; 20.-23.03.2019
9. M. Trzcinski\*, A. Bukaluk, P. Winkler, C. Freytag, M. Stöger-Pollach, J. Bernardi, G. Rupprechter, Y. Suchorski:  
*"Oxidation of stepped Rh surfaces: PEEM and XPS studies"*  
 34<sup>th</sup> European Conference on Surface Science, Aarhus, Denmark; 26.-31.08.2018

10. P. Winkler\*, J. Zeininger, S. Buhr, G. Rupprechter, Y. Suchorski:  
"Extracting information from high voltage environment: WiFi is the best isolator"  
7<sup>th</sup> Annual FOXSI PhD Workshop, Haus im Ennstal, Austria; 31.01.-03.02.2018
11. S. Buhr\*, J. Zeininger, M. Datler, C. Freytag, P. Winkler, G. Rupprechter, Y. Suchorski:  
"H<sub>2</sub> Oxidation on Rh: Mapping the nm- and μm-Sized Reaction Fronts"  
8<sup>th</sup> International Workshop on Surface Physics, Trzebnica, Poland; 26.-30.06.2017
12. M. Datler\*, J. Zeininger, C. Freytag, S. Buhr, P. Winkler, G. Rupprechter, Y. Suchorski:  
"H<sub>2</sub> Oxidation on Rh: Guiding Reaction Instabilities Through Surface Geometry"  
8<sup>th</sup> International Workshop on Surface Physics, Trzebnica, Poland; 26.-30.06.2017
13. S. Buhr\*, J. Zeininger, M. Datler, C. Freytag, P. Winkler, G. Rupprechter, Y. Suchorski:  
"H<sub>2</sub> oxidation on Rh: Mapping the nm- and μm-sized reaction fronts"  
International FOXSI Conference 2017, Vienna, Austria; 15.-17.05.2017
14. P. Winkler\*, J. Zeininger, S. Buhr, G. Rupprechter, Y. Suchorski:  
"Adaptive control of samples under tens of kilovolts: a wireless solution"  
6<sup>th</sup> Annual FOXSI PhD Workshop, Haus im Ennstal, Austria; 01.-04.02.2017